Size dependent tuneability and intercoupling of physical properties of multiferroic nanomaterials

THESIS SUBMITTED TO THE

UNIVERSITY OF PUNE

FOR THE DEGREE OF

DOCTOR OF PHILOSOPHY

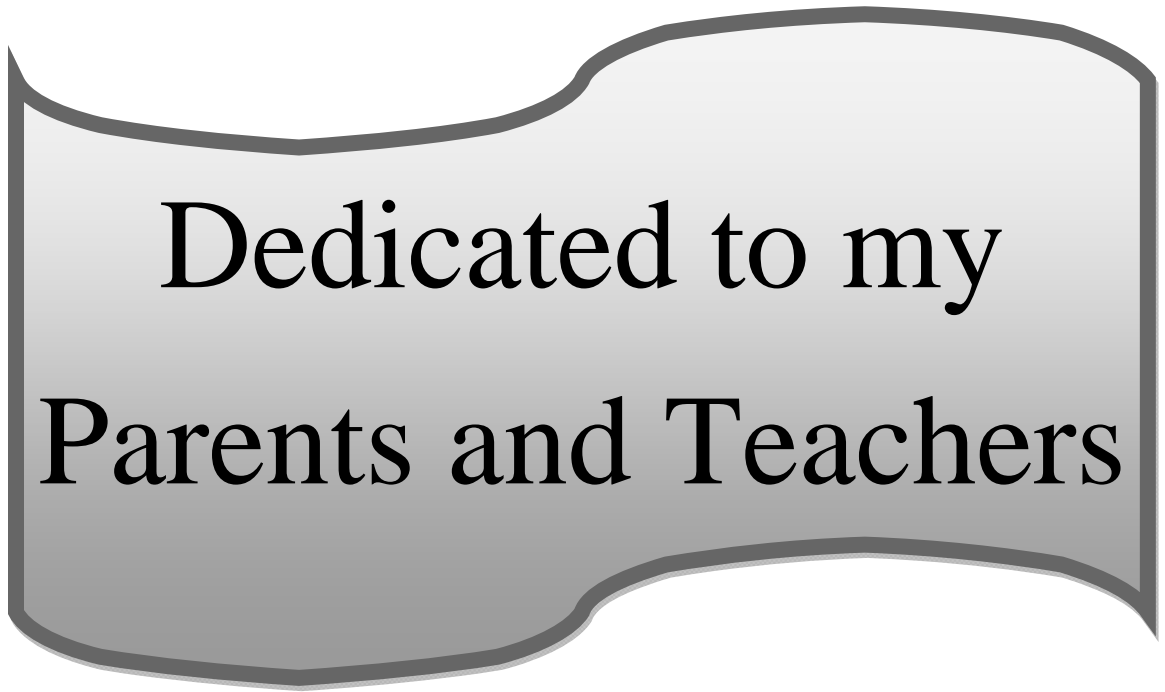**IN**

Chemistry

BY

Mr. Adhish Kumar Jaiswal

PHYSICAL CHEMISTRY DIVISION

NATIONAL CHEMICAL LABORATORY

PUNE – 411008

INDIA

SEPTEMBER 2011

Dedicated to my

Parents and Teachers

CERTIFICATE

This is to certify that the work discussed in the thesis entitled "**SIZE DEPENDENT TUNEABILITY AND INTERCOUPLING OF PHYSICAL PROPERTIES OF MULTIFERROIC NANOMATERIALS"** by **Mr. Adhish Kumar Jaiswal**, for the *degree of Doctor of Philosophy* in chemistry was carried out under my supervision in the Physical & Materials Chemistry Division of National Chemical Laboratory, Pune, India. Such material as has been obtained by other sources has been duly acknowledged in this thesis. To the best of my knowledge, the present work or any part thereof, has not been submitted to any other University for the award of any other degree or diploma.

Date: **Dr. Pankaj Poddar**

Place: Pune   (Research Guide)

DECLARATION

I hereby declare that the work incorporated in this thesis entitled "**SIZE DEPENDENT TUNEABILITY AND INTERCOUPLING OF PHYSICAL PROPERTIES OF MULTIFERROIC NANOMATERIALS**" submitted for the degree of *Doctor of Philosophy in Chemistry* has been carried out by me at the Physical & Materials Chemistry Divisions of the National Chemical Laboratory, Pune, India under the supervision of Dr. Pankaj Poddar. Such materials as have been obtained by other sources have been duly acknowledged in this thesis. The work is original and has not been submitted in part or full by me for award of any other degree or diploma in any other University.

Date: **Adhish Kumar jaiswal**

Place: Pune   (Research Student)

Acknowledgements

Adhish Jaiswal

Table of Contents

Chapter 1

Introduction

Chapter 2

Effect of Reduced Particle Size on the Magnetic, Raman & Dielectric Spectroscopy in Chemically Synthesized $BiFeO_3$ Nanocrystals: Signatures of Spin-Phonon and Magnetoelectric Coupling

Chapter 3

Surface Effects on Morin Transition, Exchange Bias Enchanced Spin Reorientation and Dielectric Spectroscopy in Chemically Synthesized DyFeO₃ Nanoparticles

Chapter 4

Optical, Magnetic, Dielectric and Raman Spectroscopic Study of GdCrO₃ Nanoparticles

Chapter 5

Outlook

List of Publications

Chapter 1

Introduction

Outline

This chapter provides an introduction to the thesis and starts with the motivation behind the work carried out in this thesis, followed by an overview of the basics of multiferroics including the magnetoelectric coupling and its application in memory devices. This chapter ends with a look to the properties of some rare earth ferrites and chromites.

Chapter 1

1.1 Ferroelectrics:

The formal definition of ferroelectric material is one which has a phase transition from high temperature phase that behaves as a normal dielectric to a low temperature phase that has a spontaneous polarisation. The direction of spontaneous polarisation can be switched by the direction of the applied electric field.[1, 2] The birth of ferroelectric material was traced back in 1921 when Valasek observed a nonlinear electrical properties in sodium tartrate tetrahydrate ($KNaC_4H_4O_6 \cdot 4H_2O$) which is commonly known as *Rochelle salt* and further confirmed that it is a hydrogen bonding in the materials which is responsible for the ferroelectricity.[3-5] Following this discovery, anomalous dielectric, piezoelectric, elastic, and phase transition behaviors have been reported in various materials.[6, 7] In 1930, ferroelectricity in KH_2PO_4 was discovered and theory of phase transition developed.[8] In 1945, a new type of ferroelectric material – barium titanate $BaTiO_3$- was discovered and had a more than one ferroelectric phase.[9-12] Ferroelectric materials have interesting physical properties which offer a broad range of applications including transducers and actuators due to its piezoelectric property, capacitors due to its high dielectric permittivity value and data storage devices due to its hysteresis loop.[13-15] Due to size dependent physical and chemical properties of ferroelectric materials, it offers flexibility to design new devices with new multiple functionality.[16-19] Furthermore, coupling between the two or three physical properties in single phase led to new discoveries which are important both from scientific and technological point of view. For example, break junction and ballistic electrons where the coupling between elastic and nanosized magnetic domains provides controlling parameter for new devices.[20].

1.1.1 Mechanism of ferroelectricity in BaTiO₃:

To explain the basic mechanism of ferroelectricity in perovskite structure, $BaTiO_3$ has been chosen as a model system. In the figure 1.1(a), we have shown the normal cubic perovskite structure of $BaTiO_3$ in which titanium occupies the center of the cube and barium share all the corner of the cube. In figure 1.1 (b), we have shown the distorted perovskite structure where the off centering of titanium ions generates ferroelectricity.[21] There are two opposite forces acting simultaneously in the $BaTiO_3$ structure at the transition temperature called Curie temperature. The first force which

favors non-ferroelectric symmetric phase is the short range repulsions between adjacent electron clouds of titanium and oxygen and another force which favors off-center distortion and stabilizes the ferroelectric phase is the covalent bonding between the titanium and oxygen. It is now well known that why the ferroelectricity is favored in perovskite structures like $BaTiO_3$. The reason is the ligand field stabilization energy, in which $2p$ orbital of oxygen donate its electron density to empty d orbital of
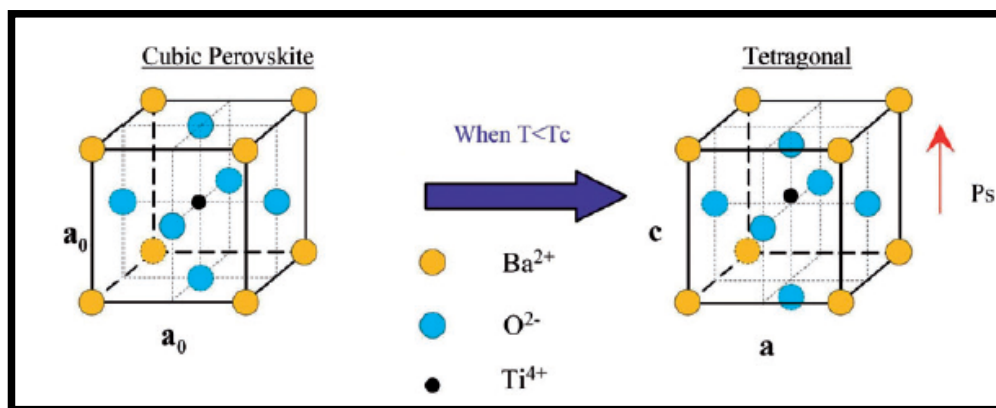
Figure 1.1 Lattice structures of the high-temperature paraelectric phase (left) and low temperature ferroelectric phase (right) of perovskite $BaTiO_3$. In the ferroelectric phase, the B site Ti ions shift from the centrosymmetric positions, generating a net polarization and thus ferroelectricity[21].

the transition metal cation, results off-centering of the titanium atom. Thus vacant d-orbital of the transition metal ions of appropriate energy range is the requirement to stabilize the ferroelectric phase. Today, there are about 1000 known ferroelectrics. A list of some ferroelectrics,[22] year of their discovery, and some important properties are given in Table 1.1.

Chapter 1

Table 1.1: A list of ferroelectric materials and their properties:

Compound	Year discovered	Curie Temperature $T_c(K)$	Remanant Polarisation $P_s(\mu C/cm^2)$	Crystal structure at room temperature
Rochelle salt $KNaC_4H_4O_6.4H_2O$	1921	255 & 297	0.25	Monoclinic between T_C orthorhombic at other temperature
KH_2PO_4	1935	123	6.1	Orthorhombic
$BaTiO_3$	1945	398	25	Tetragonal
$LiNbO_3$	1949	1415	10-30	Trigonal
$KNbO_3$	1949	400	20-40	Orthorhombic
$PbZr_{1-x}Ti_xO_3$	1949	Depend upon composition	20-97	Tetragonal for Ti rich, Rhombohedral for Zr rich
$PbTiO_3$	1950	763	20-96.5	Tetragonal
$PbZrO_3$	1951	503	20-50	Orthorhombic
$C(NH_2)_3Al(SO_4)_2.$ $6H_2O$	1955	473	0.5	Trigonal
$PbBi_2Nb_2O_9$	1959	833	3	Pseudotetragonal
$SrBi_2Ta_2O_9$	1960	600	30-70	Orthorhombic
$Ba_{0.73}Sr_{0.27}TiO_3$	1960	298	10-30	Tetragonal
$Bi_4Ti_3O_{12}$	1961	953	10-30	Orthorhombic

1.1.2 Requirement of ferroelectricity: "d^0-ness":

As we have stated above that to stabilize the ferroelectric phase in perovskite structure the empty *d* orbital of transition metal ions is the main requirement. Among the known perovskite materials, the materials containing transition metal ions like Ti^{4+}, Ta^{5+}, W^{6+}, etc have d^0 configuration and are able to make ternary oxides which show ferroelectric behavior. But the question arises why do we need empty *d* orbitals for ferroelectricity? As we have mentioned earlier that the empty *d* orbitals of the transition metal ions form a strong covalent bond with the surrounding *p* orbitals of oxygen which results in shifting of the transition metal ions from the centre of the octahedral towards one particular oxygen to form a covalent bond at the expense of weakening of the other oxygen bonds. This collective shifting of transition metal ions and oxygen inside a periodic lattice induces a bulk ferroelectric polarisation.

The mechanism of the covalent bonding in such a molecule is described by the virtual hopping of electrons from oxygen *2p* shell to *d* shell of the transition metal ions.[10, 23, 24] There are still some single phase materials like $BiFeO_3$ or $BiMnO_3$ where $Fe^{3+}(d^5)$ and $Mn^{3+}(d^4)$ cations are not in d^0 configuration but still they show simultaneously ferroelectric and magnetic ordering.[25-28] It seems that these two cases violate "d^0" requirement for ferroelectricity (FE) as discussed previously. Therefore, the requirement of d^0 shell is not the necessary condition to show ferroelectricity as in $BaTiO_3$. In the next section, I will describe that it is the lone pair of Bi ions in *6s* orbitals, in bismuth related perovskite compounds which is responsible for breaking of the centre of symmetry.[27] In addition, there are other materials also like $TbMnO_3$,[29, 30] $DyFeO_3$[31, 32] or $LuFe_2O_4$[33, 34] which don't fulfill the requirement of d^0 -ness but still they exhibit ferroelectricity. Therefore, depending upon the origin of breaking of centrosymmetric position, ferroelectric materials are divided into three broad categories. (1) Proper ferroelectricity[1] or displacive-type ferroelectricity, where relative displacement of cations and anions is responsible for macroscopic polarization eg. $BaTiO_3$, $BiFeO_3$ and $BiMnO_3$. (2) Order-disorder type ferroelectricity where ferroelectricity is generated by the cooperative alignment of permanent dipole moments. Hydrogen bond type ferroelectricity is often regarded as an order–disorder type eg Rochelle salt.[4, 5] (3) Improper ferroelectricity, where the electronic

interaction,[35] geometric frustration[36, 37] and electronic degree of freedom[38] are responsible for ferroelectricity eg $TbMnO_3$, $LuFe_2O_4$ and $DyFeO_3$. In the table 1.2, we have shown type of ferroelectricity with some examples.[39]

Table 1.2 Type of ferroelectricity

Type	Mechanism of inversion symmetry breaking	Materials
Proper	Covalent bonding between $3d^0$ transition metal(Ti) and oxygen	$BaTiO_3$
	Polariation of $6s^2$ lone pair of Bi or Pb	$BiMnO_3$, $BiFeO_3$, $Pb(Fe_{2/3}W_{1/3})O_3$
Improper	Structural transition	K_2SeO_4, Cs_2CdI_4,
	Geometric Ferroelectric	Hexagonal $RMnO_3$
	Charge ordering	$LuFe_2O_4$
	Electronic ferroelectrics	
Order-disorder	Hydrogen bond type ferroelectricity	Rochelle salt

1.2 Ferro and antiferromagnetism:

The occurrence of magnetic spin polarization has the opposite requirement than the ferroelectricity- there must be partially filled transition metal d states. According to the usual Stoner model, the fundamental driving force for local spin polarization is the exchange energy, which is minimized if all the electrons have the same spin. If the electrons have opposite spin alignment then it will increase the band energy by transferring electrons from the lowest band states (occupied equally with up- and down-spin electrons) to band states of higher energy. The exchange effect dominates over the band energy only in narrow bands, such as those arising from d electrons, that have a high density of states at the Fermi energy.[1] These materials are widely used for the application in transformer cores, permanent magnets, and electromagnets.

1.3 Ferroelasticity:

Ferroelastic materials display a spontaneous deformation that is stable and can be switched hysteretically by an applied stress.[40] When a stress is applied to a ferroelastic material, a phase change will occur in the material from one phase to an equally stable phase either of different crystal structure (e.g. cubic to tetragonal) or of different orientation.[41, 42]This stress-induced phase change results a spontaneous strain in the material. The shape memory effect and super elasticity is manifestations of ferroelasticity. Nitinol (nickel titanium), a common ferroelastic alloy, can display either super elasticity or the shape-memory effect at room temperature, depending on the nickel/titanium ratio.[43, 44]

1.4 Multiferroicity:

In 1994, Hans Schmid proposed the definition of multiferroics— "crystals can be defined as multiferroic when two or more of the primary ferroic properties ferromagnetism, - electricity and - elasticity coexisit in the same phase.[45] This means that they have a spontaneous magnetization that can be reoriented by an applied magnetic field, a spontaneous ferroelectric polarization that can be reoriented by an applied electric field, and a spontaneous elastic deformation that can be reoriented by an applied stress. Later on, neither the combination of antiferromagnetic and ferroelastic like $SrRuO_3$[46] nor ferroelastic and ferroelectrics like $BaTiO_3$ and $PbTiO_3$ are considered as a multiferroics. In practice, multiferroic materials are those which have simultaneously ferroelectric and one of the magnetic ordering, either ferromagnetic or antiferromagnetic as represented in figure1.2.[39, 47-53] Typical multiferroics belong to the group of the perovskite transition metal oxides, and include rare-earth manganites and ferrites (e.g. $TbMnO_3$, $HoMn_2O_5$[54], $LuFe_2O_4$[55-59]). Other examples are the bismuth compounds $BiFeO_3$[60-64] and $BiMnO_3$[27, 28, 65] and non-oxides such as $BaNiF_4$[66] and spinel chalcogenides, e.g. $ZnCr_2Se_4$[67]. Apart from single phase multiferroics, composites and heterostructures exhibiting more than one ferroic order parameter are studied extensively. Some examples include magnetic thin films on piezoelectric PMN-PT substrates.[68] Besides scientific interest in their physical and chemical properties, multiferroics have potential applications as multiple state

memory elements, electric-field-controlled ferromagnetic resonance devices, and transducers with magnetically modulated piezoelectricity.[69] Multiferroic materials are appealing not only because they have property of their parent compounds but also the ability to couple with either the magnetic or the electric polarization, offers an extra degree of freedom in the design of conventional actuators, transducers, and storage devices. A list of some multiferroics[21] and their properties has shown in table 1.3
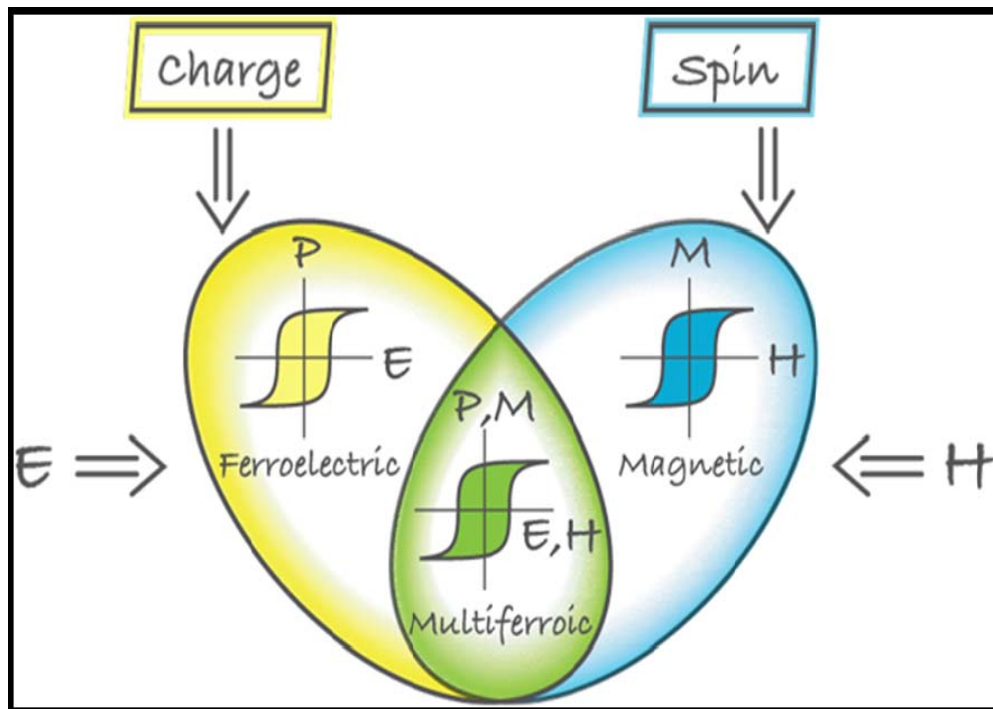
Figure 1.2: Multiferroics combine the properties of ferroelectrics and magnets. In the ideal case, the magnetization of a ferromagnet in a magnetic field displays the usual hysteresis (blue), and ferroelectrics have a similar response to an electric field (yellow). If we manage to create multiferroics that are simultaneously ferromagnetic and ferroelectric (green), then there is a magnetic response to an electric field, or, vice versa, the modification of polarization by magnetic field.[48]

Chapter 1

Table 1.3: A list of multiferroics

Compound	Crystal structure space group	Magnetic ions	Mechanism for multiferroics	Ps μC/cm^2	T$_C$ (K)	T$_N$ (K)
RFe$_3$(BO$_3$)$_4$ R= Gd, Tb	R32	R^{+3}, Fe^{+3}	Ferroelectric BO$_3$ group	9	38	37
BiFeO$_3$	R3c	Fe^{+3}	Lone pair at A- site	75	1103	643
BiMnO$_3$	C2	Mn^{+3}	Lone pair at A- site	20	800	100
BiFe$_{0.5}$Cr$_{0.5}$O$_3$	-	Cr^{+3}	Lone pair at A- site	60	-	-
(Y, Yb)MnO$_3$	Hexagonal P6$_3$cm	Mn^{+3}	Geometric ferroelectricity	6	950	77
HoMnO$_3$	Hexagonal P6$_3$cm	Mn^{+3}	Geometric ferroelectricity	5.6	875	76 for Mn 5 for Ho
InMnO$_3$	Hexagonal P6$_3$cm	Mn^{+3}	Geometric ferroelectricity	2	500	50
YCrO$_3$	P21	Cr^{+3}	Geometric ferroelectricity	2	475	140
Y(Ho)MnO$_3$	Orthorhom-bic	Mn^{+3}	E-type antiferromagnetism	100	28	28
LuFe$_2$O$_4$	R3m	Fe^{+2}, Fe^{+3}	Charge frustration	26	330	330
Pr$_{1-x}$Ca$_x$MnO$_3$	Pnma	Mn^{+3}, Mn^{+4}	Site and bond center charge ordering	4.4	230	230
RMn$_2$O$_5$ R=Y, Tb, Dy	Pbam	Mn^{+3}, Mn^{+4}	Charge ordering plus magnetostriction	40	38	T$_N$=43K T$_{CM}$=33K T$_{ICM}$=24K
DyFeO$_3$	Pbnm	Fe^{+3} Dy^{+3}	Magnetostriction	0.4	3.5	3.5 for Dy 645 for Fe
(Fe, Mn)TiO$_3$	R3c	Mn^{+3} Fe^{+3}	Polarization induced weak ferromagnetism	-	-	-

1.5 Magnetoelectric coupling:

There is an increasing interest from the last decades in the field of device miniaturisation, where the combination of magnetic and electronic properties produces multifunctional material which can perform more than one task simultaneously.[15, 70, 71] Multiferroic ME materials are particularly appealing not only because they have the properties of their parent compounds, but also because interactions between the magnetic and electric orders lead to additional functionalities[72-74] and allow additional degree of freedom in the device design. Other applications include multiple-state memory elements[74], in which data are stored both in the electric and magnetic polarizations, and novel memory media, which allow the writing of a ferroelectric data bit and reading of the magnetic data generated by association.[61, 63]Aside from the potential applications, the fundamental physics of multiferroic materials is rich and fascinating.

The general definition of magnetoelectric effect is the coupling between electric and magnetic field ie we can tune the magnetization not only by magnetic field but also electric field similarly electric polarization could be tuned not only by electric field but also by magnetic field.[72, 75, 76]

The first successful observation of the magnetoelectric effect was realized in Cr_2O_3.[77-79]Up to now, more than 100 compounds that exhibit the magnetoelectric effect have been discovered. In the table 1.4, we have shown a list of some magnetoelectric materials and their properties.[22]

The magnetoelectric effects can then easily be established in the form $P_i(H_j)$ or $M_i(E_j)$.[52]

$$P_i = \alpha_{ij} + \frac{\beta_{ijk}}{2} H_j H_k + \dots.$$

$$\mu_0 M_i = \alpha_{ji} E_j + \frac{\gamma_{ijk}}{2} E_j E_k + \dots.$$

Where P_i and M_i is the ith component of electrical polarisation and magnetisation, H_j and E_j is the Jth component of applied magnetic field and electric field. α_{ij} describe the linear magnetoelectric coupling and third rank tensor β_{ijk} and γ_{ijk} represent higher-order (quadratic) magnetoelectric coefficients.

Chapter 1

linear magnetoelectric coupling and third rank tensor β_{ijk} and γ_{ijk} represent higher-order (quadratic) magnetoelectric coefficients.

Table 1.4: Magnetoelectric coupling coefficients measured for various multiferroic single-phase materials. Some two-phase systems are also included for comparison.

Material	Magnetoelectric coefficient	
	$C_M = \mu_0 \delta M / \delta E (ps/m)$	$\alpha_E = \delta E / \delta H (mV/cm\ Oe)$
Cr_2O_3		20
$TbMn_2O_5$	21 (at 28 K)	
$LiCoPO_4$	30.6 (at 4.2 K)	
$LiNiPO_4$	1.7 (at 20 K)	
YIG	30 (at very low T)	
$TbPO_4$	36.7 (at 1.9 K)	
$BiFeO_3$		0.3 (at 20 K)
$La_{0.7}Sr_{0.3}MnO_3$/PMN-PT(001) bilayer	60000 (at 300 K)	
$La_{0.7}Sr_{0.3}MnO_3$/PZT laminated composite		32 (at 300 K)
$NiFe_2O_4$/PZT laminated composite		1500 (at 300 K)
LSMO/PZT laminated composite		60
$0.3NiFe_2O_4/0.7PZT$ ceramic composite		20-30
$BaTiO_3/CoFe_2O_4$ ceramic composite		up to 2540

Multiferroic magnetoelectric materials are divided into two categories on the basis of their constituents: (1) single phase[80] (2) composites.[81, 82] According to the previous definition, a single phase multiferroic material is one that possesses at least two of the 'ferroic' properties, such as ferroelectricity, ferromagnetism or ferroelasticity in one phase. While ME composites are multiphase materials composed of different phases and none of the phase have ME effect. In the figure 1.3, we have shown the relation between multiferroics and magnetoelectrics with some examples.[52] Unfortunately, the magnetoelectric effect in single-phase compounds is usually too small to be practically applicable (see table 1.4).[79] The breakthrough in terms of the giant magnetoelectric effect was achieved in composite materials.[82-85] The composite materials are made up of ferromagnetic piezomagnetic layer and a ferroelectric piezoelectric layer. These composites are acceptable for practical applications in a number of devices such as microwave components, magnetic field sensors and magnetic memories. For example, it was reported recently that the magnetoelectric composites can be used as probes in scanning probe microscopy to develop a near-field room temperature scanning magnetic probe microscope.[86]

Now, we will discuss those that are the limiting factors in preventing the simultaneous existence of magnetism and ferroelectricity.

1.5.1 Symmetry:

The point group symmetry is closely related with multiferroics and magnetoelectric effect. The ferroic property can be characterised by their behaviour under the space and time inversion. In the space inversion, direction of polarisation will be reversed while magnetisation remains same but in time inversion, the direction of magnetisation will be reversed while polarisation remains same.

	Space Invariant	**Space Variant**
Time Invariant	Ferroelastic	Ferroelectric
Time Variant	Ferromagnetic	Ferrotoroidic

Chapter 1

Magnetoelectric multiferroics require simultaneous violation of space and time inversion Symmetry.[87] In BiFeO$_3$, off-centering of bismuth ions gives rise to an electric polarization, while at a lower temperature additional magnetic ordering of iron ions breaks time-reversal symmetry. In general, a variety of mechanisms can cause lowering of symmetry resulting in multiferroicity.[48] The primary requirement of being ferroelectricity is the structural distortion which results breaking of the high symmetry phase to low symmetry phase. There are 31 point groups that allow a spontaneous electric polarization, P, and 31 that allow a spontaneous magnetic polarization, M. Therefore, Thirteen point groups (1, 2, 2', *m*, *m* ', 3, 3*m* ', 4, 4*m*'*m*', *m*'*m*2', *m*'*m*'2', 6, and 6*m*'*m*') are found in both sets, allowing both properties to exist in the same phase.[1]
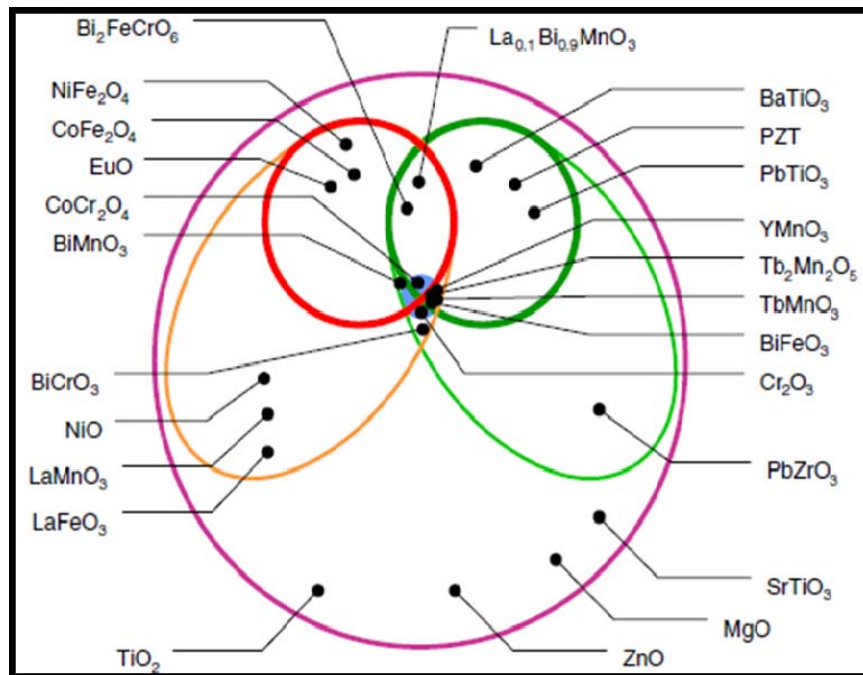
Figure 1.3: Ferromagnetic (red) and ferroelectric (dark green) form a subset of magnetically (orange) and electrically (light green) polarizable materials such as paramagnets and antiferromagnets or paraelectrics and antiferroelectrics. The intersection of ferromagnetic and ferroelectric loop represents materials that are multiferroic. Magnetoelectric coupling (blue) is an independent phenomenon that can, but need not, arise in any of the materials that are both magnetically and electrically polarizable. In practice, it is likely to arise in all such materials, either directly or via strain. [52]

Ph.D. Thesis   Adhish Kumar Jaiswal   University of Pune

1.5.2 Mechanisms for ferroelectric and magnetic integration:

In this respect the two mechanisms are not so dissimilar but the difference in the filling of the electron in *d* or *f* shells required for ferroelectricity and magnetism makes these two ordered states mutually exclusive. Then what are the other ways to combine these two properties? The first route was taken by the Russian groups[88]. They proposed the mixed system which contains magnetic ions with partially d shell and ferroelectric active transition metal ions with d^0 configuration. Each of the components then can do what they ''like'': magnetic ions give some magnetic ordering, and ferroelectric-active ions make a system FE.

To integrate both ferroelectric and magnetism, here, we have addressed some examples which contain separate functional group which is responsible for ferroelectricity and magnetic ordering. Usually, mixing of the two elements where one is creating magnetic ordering and another one, non center of symmetric units, is responsible for strong dielectric response and ferroelectricity. The best example in this category is $BiFeO_3$ and $BiMnO_3$ where, the A-sites are usually facilitated with cations of a $(ns)^2$ valence electron configuration, such as Bi^{3+}, which favour the stability of ferroelectrically distorted structures.[26] At the same time, the B-sites, iron ions, are facilitated with magnetic ions providing magnetic oredring.[89] This approach avoids the exclusion of ferroelectric and magnetism at the same site. Such simple approach does allow for ferroelectricity and magnetism in a single phase but it may not create strong magnetoelectric effect because the origin of both the properties are physically different.[60, 90] To produce strong magnetoelectric coupling in a single phase, the origin of ferroelectricity must come from the spin or charge ordering. This is not only enhanced the magnetoelectric coupling but also able to mutually control both the properties.[91] Fortunately, in the recent years, there is substantial progress in this area in which ferroelectricity is induced by a geometric distortion[37] and a helical/conical spin order,[92-94] as well as a charge-ordered (CO) structure.[95, 96] The details of these efforts and results are presented in the next section.

Chapter 1

Applications:

1.5.3 Magnetoelectric and multiferroic memories:

BiFeO$_3$ is a prime candidate for the application of magnetoelectric memories, A voltage V controls the ferroelectric state of BiFeO$_3$, and given the strong coupling between the antiferromagnetic plane and ferroelectric polarisation, switching the ferroelectric polarisation by 71^0 or 109^0 can change the antiferromagnetic planes, and thereby flip the direction of the lower ferromagnetic (FM, blue) layer through exchange bias if the coupling is strong enough. In the FM-Metal-FM trilayer the alignment of the FM layers can thus be controlled to be parallel or antiparallel by the ferroelectric state of the green BiFeO$_3$ layer. Parallel FM layers give a lower
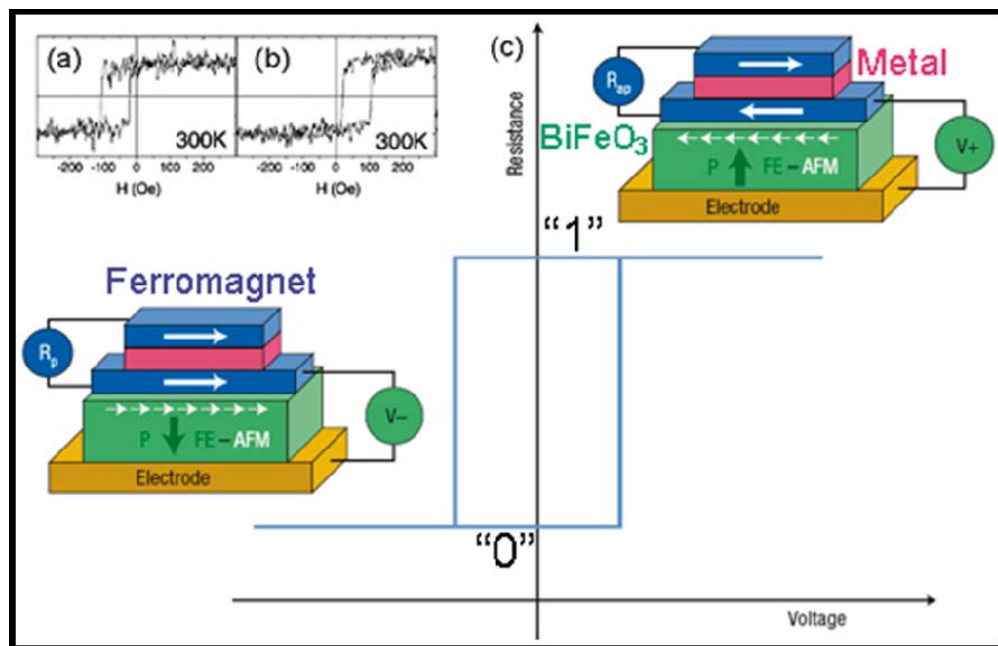
Figure 1.4 (a-b) Exchange biased magnetic hysteresis loops of ferromagnetic CoFeB (5 nm) grown on BiFeO$_3$ (35 nm) measured along opposite direction of ferroelectric polarisation in (a) and (b), (c) A concept for a MERAM element utilising BiFeO$_3$ (green) FE-AFM layer, ferroelectric ,antiferromagnetic.[74]

resistance across the FM-Metal-FM trilayer, corresponding to the binary state "0". Oppositely, antiparallel alignment of the FM layers give a higher resistance, corresponding to the binary state "1", as in conventional read-out of bits utilising

Giant Magnetoresistance. $BiFeO_3$ can also be used as a tunnelling barrier layer as it is ferroelectric down to 2 nm thickness. The ferroelectric state can control the direction of magnetisation in adjacent ferromagnetic layers, and thus the tunnelling magnetoresistance[73]. The direction of the polarisation can also directly control the tunnelling resistance, enabling non-destructive read-out of ferroelectric bits[98]. Four-state memories where both the polarisation and magnetisation can modulate the tunnelling resistance have been demonstrated[99].

1.6 Types of multiferroics:

The microscopic origin of magnetism is same in all the magnetic materials. It is the presence of partially filled *d* or *f* orbital of transition metal or rare earth ions which have a corresponding magnetic moment. There are several different microscopic sources of ferroelectricity, and accordingly one can have different types of multiferroics. Generally, there are two groups of multiferroics. The first group, called type-I multiferroics, where the source of magnetism and ferroeletricity is different though there is a coupling between these two order parameter. In these materials, ferroelectricity appears at high temperature compared to magnetic ordering and spontaneous polarization is quite large. Examples are $BiFeO_3$[25, 26], and $YMnO_3$[100]. The second group, which we can call type-II multiferroics, is the relatively recently discovered materials, in which magnetism causes ferroelectricity, implying a strong coupling between the two.[101] However, the polarization in these materials is usually much smaller.

1.7 Type I multiferroics:

1.7.1 Lone pair ferroelectricity:

The first exception from the exclusion rule which violate the d^0 requirment for ferroelectricity in the perovskite family is the $BiFeO_3$ and $BiMnO_3$ where Bi^{3+} plays the major role in the origin of ferroelectricity. Both the materials have magnetic ions like Fe^{+3} (d^5) and Mn^{+3}(d^4) and shows simultaneously magnetic and ferroelectric ordering. In both the case ferroelectricity is not driven from the B sites like in $BaTiO_3$ but from the A sites in this case Bi lone pairs. In general, the valance electronic configuration of Bi^{3+} is $6s^2$ where these two electrons in *s* orbital don't participate in

bonding. They are called the 'lone-pair' electrons or sometimes dangling bonds. Theoretical calculation indicate that this $6s^2$ lone pair is responsible for both stabilizing the ferromagnetism and inducing the ferroelectric distortion.[27] The particular orientation of these lone pairs, or dangling bonds, may create local dipoles and distort the monoclinic structure and results ferroelectricity. The $6s$ "lone pairs" on Bi are approximately spherically distributed around the Bi atoms forming orange rings of localization. It has been pointed out previously that spherically distributed lone pairs tend to be unstable and the tendency of the lone pair to localize into a lobe shape can be strong enough to drive a structural distortion. In Figure1.5, we again display the structure of monoclinic $BiMnO_3$ with black spheres representing Bi and cyan spheres (bonded to red O) representing Mn.[27] The transformation from a nearly spherical lone pair in the cubic phase to

Figure 1.5: Valence electron localization functions for monoclinic BiMnO₃. The blue end of the scale bar corresponds to no electron localization while the white end corresponds to a complete localization.[27]

a lobe-like lone pair in the monoclinic phase is perhaps the driving force for some of the structural distortions in this system. Further the coupling between ferroelectric and magnetic ordering leads to interesting magnetoelectric property.

1.7.2 Charge order ferroelectricity:

One more mechanism that can lead to ferroelectricity and type-I multiferroicity can be charge ordering, often observed in transition metal ions with different valence and with geometrical or magnetic frustration. We consider doped manganites of the type $R_{1-x}Ca_xMnO_3$, with R = La, Pr. Different types of magnetic charge orderings are observed in this class of compounds[102-104].
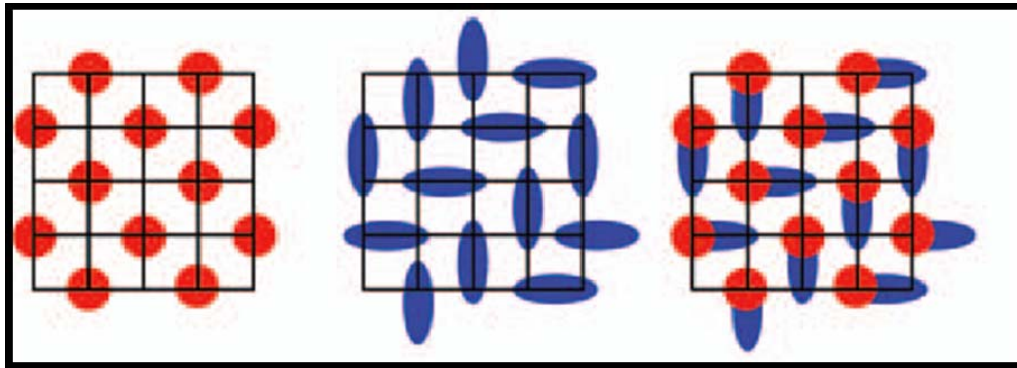
Figure 1.6: Three types of charge ordering. (a) Site-centred charge order; (b) bond-centred charge order (the Zener polaron state); and (c) a ferroelectric intermediate state. The charge-ordered structure in c lacks inversion symmetry.[104]

Charge-ordering pattern in these compounds is of a simple checkerboard type. There are three kind of charge ordering are possible in such a system. In figure 1.6(a), the check board is characterized by the alternation of Mn^{3+} and Mn^{4+} sites. We refer to such a pattern as Mn-centred (in general metal-, or site-centred) charge ordering (SCO).[95, 102, 103, 105] In figure 1.6(b), another kind of charge ordering is possible where the charge is localized not on sites but on bonds. In this situation the metal sites remain equivalent. In both kind of charge ordering there is a centre of symmetry but the unexpected outcome will come when we combined both the charge ordering features in one which results breaking of the centre of symmetry and result ferroelectricity. A corresponding mechanism can work in systems like $Pr_{1/2}Ca_{1/2}MnO_3$[95, 105] or in nickelates $RNiO_3$[106] with charge ordering. Magnetite Fe_3O_4 is one of the most famous insulating magnets.[107] Chemical formula is often written as $Fe^{3+}(Fe^{2+}Fe^{3+})O_4$ where equal amount of Fe^{2+} and Fe^{3+} occupy the so-called B sites in the spinal crystal structure with frustrated geometry. The well known phenomenon in this compound is the Verwey transition; a metal–insulator transition at around 120K which is believed to be the charge order transition of Fe^{2+} and Fe^{3+} in the spinal B sites.[107, 108] Below the Verwey transition, Fe_3O_4 shows magnetoelectric response which again explained by the spontaneous polarisation along the b axis. Since 2000, the Veywey transition and the associated charge order have been reinvestigated by the recently developed experimental techniques such as Combined powder neutron and x-ray diffraction study suggest an evidence of the charge ordering

where Fe valences are 2.4^+ and 2.6^+. A first-principle band structure calculation proposed that the ferroelectricity below the Verwey transition temperature is induced by the noncentrosymmetric charge order. In spite of these origin of the ferroelectricity, a detailed charge order pattern are still under debate.[96, 108, 109]

1.7.3 Geometrically frustrated ferroelectricity:

There exists another class of compounds, which violate the ''d^0-ness'' rule: hexagonal manganites $RMnO_3$ (R = Y or small rare earths). Several of the compounds from the rare earth manganite, chromite, and ferrite RBO_3 (R = rare earth ion, B = Cr, Mn, Fe) family are believed to show multiferroic properties and adopt two types of structures depending upon the radius of the rare earth atoms and synthesis conditions.[30, 37, 110, 111] In the case of R = La, Ce-Dy, the $RMnO_3$ compounds crystallize in the distorted orthorhombic perovskite structure.[30] On the other hand, for R = Ho-Lu, Y, Sc, a hexagonal structure(with a layered structure) is formed, where Mn^{3+} ions are coordinated by five oxide ions and form trigonal bipyramid geometry and the Y^{+3} is coordinated by eight oxide ions where six at equatorial position and two are apical position.[112, 113] These MnO_5 bipyramids tilt and shift with respect to the R^{3+} cations to form a noncentrosymmetric structure, resulting in the ferroelectric polarization along the *c* axis.[114] It is also possible to crystallize these hexagonal materials to orthorhombic structure either at very high pressure [115, 116] or by using low temperature soft chemical routes.[117] Geometric frustrated multiferroicity is related to a structural phase transition at high temperature. Several compounds belong to this important class of multiferros: K_2SeO_4[118], Cs_2CdI_4[119], hexagonal $RMnO_3$.[113] We consider a case realized in, for example, $YMnO_3$[80]. Along the hexagonal *c*-axis, the MnO_5 layers are separated by layers of Y^{3+} ions and below the ferroelectric curie temperature the MnO_5 bipyramids undergo a collective rotation that leads to unit cell tripling,[120] as shown in the right panel in figure 1.7. This tilting occurs just to provide close packing, and as a result the oxygen ions move closer to the rather small Y ions. Due to tilting of the bipiramidal structure, the bond length of Y with two oxide ions at the apical position changed leading to net polarisation.[121] In the recent years, careful structural study carried out and demonstrated that in this case the off-centre shifts of Mn^{3+} ions

Chapter 1

 from the centre of O_5 trigonal biprism are very small and difficult to analyze from any instruments. It is still under debate that the Y-O dipole not Mn-O dipole is responsible for the ferroelectricity. These systems are proto-typical multiferroics which can be understood by competition between local interactions on several ion sites. The mechanism of the ferroelectric ordering in hexagonal $RMnO_3$ is still questionable in scientific community whether geometric distortion or off-centring of Mn ions are responsible for the origin of ferroelectricity.[49] Geometric multiferroics are dominated by the behaviour of the *d*-shell electrons and of the rare earth elements with an unfilled *f*-shell. They have largest deviation from the perovskite structure due to the small size of rare-earth ion and they provide a unique set of physical properties, such as rich phase diagrams or multiple frustrations. Geometric frustrated ferroelectrics are prime candidates for device memory applications. In this case, the remarkable conclusion in geometric ferroelectricity is the absence of coupling

Figure 1.7: High-temperature centrosymmetric (left) and low temperature ferroelectric structure (right) of hexagonal $RMnO_3$. In the low-temperature structure the oxygen polyhedra undergo a collective rotation that leads to a unit cell tripling. This unit cell tripling is accompanied by displacements of the R cations (spheres) along the (0001) directions, which lead to an electric dipole moment. [120]

between magnetic and ferroelectric ordering, although certain coupling is always present and explore new functionality in applications.

1.8 Type II multiferroics:

The biggest achievement nowadays is the discovery of a novel class of multiferroics in which ferroelectricity exists only in a magnetically ordered state. For example, in $TbMnO_3$ magnetic ordering appears at T_{N1} = 41 K, and at a lower temperature, T_{N2} = 28 K, the magnetic structure changes.[29] It is only in the low temperature phase that a nonzero electric polarization appears. Similar behaviour occurs in $TbMn_2O_5$.[122, 123] From the point of view of the mechanism of multiferroic behavior, one can divide type-II multiferroics into two groups: those in which ferroelectricity is caused by a particular type of magnetic spiral and those in which ferroelectricity appears even for collinear magnetic structures.

1.8.1 Spiral spin ordering:

So far, we have shown various mechanism for being multiferroics but none of the above mechanism have a strong magnetoelectric coupling behaviour because the origin of magnetic and ferroelectric ordering in the previous examples is coming from different sublattice. The breakthrough in this area came when the ferroelectricity is generated by magnetic ordering. Since in a magnetoelectric system, we can produce an electric polarization by applying a external magnetic field or vice versa. If an external magnetic field can do it, is it not possible that the same polarisation can happen spontaneously, due to an internal magnetic field or due to certain magnetic ordering like spiral or cycloidal ordering? This is the case which has been observed in the recently discovered multiferroic materials $RMnO_3$ (with perovskite structure; R = Tb, Gd)[124], in RMn_2O_5 (R-different rare earths, such as Tb, Y etc.)[54], and in $Ni_3V_2O_8$ [125]. A list of multiferroics[21] with spiral spin ordering has been shown in table 1.5. The origin of ferroelectricity in these system appear in the certain magnetic ordered range. Therefore, the coupling between magnetic and electric ordering in them is especially strong, and one can expect giant magnetoelectric effects. The detailed microscopic mechanism of generation of ferroelectricity by magnetic ordering in these systems is actually not known. But one general idea seems to be
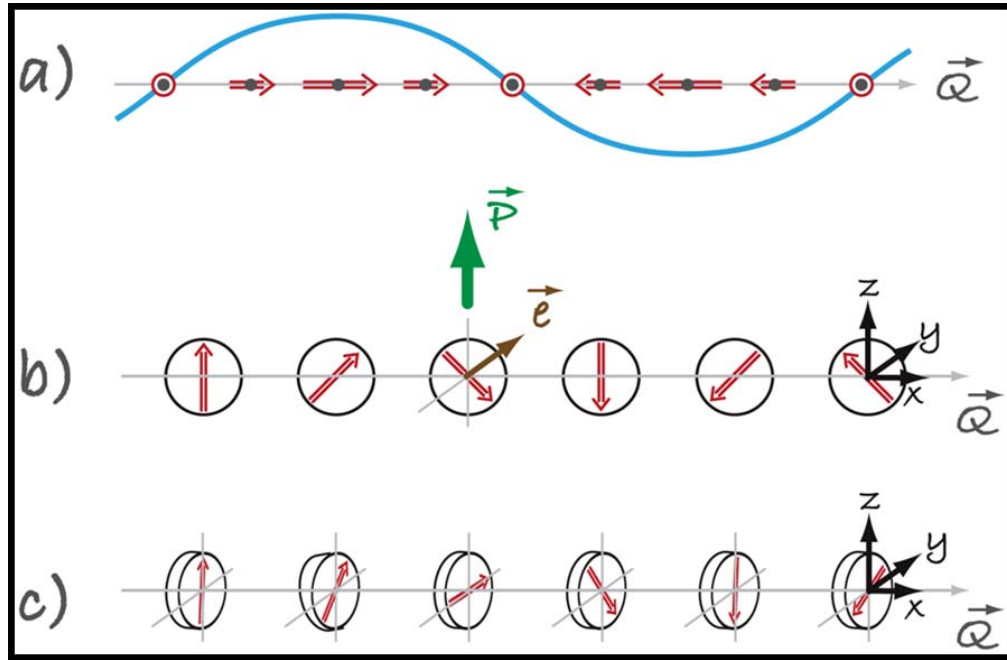
Figure 1.8: Different types of spin structures relevant for type-II multiferroics. (a) Sinusoidal spin density wave, in which spins point along one direction but vary in magnitude. This structure is centrosymmetic and consequently not ferroelectric. (b)The cycloidal spiral with the wave vector $Q = Qx$ and spins rotating in the (x,z)-plane. It is in this case where one finds nonzero polarization. (c) In a so-called "proper screw" the spins rotate in a plane perpendicular to Q. Here the inversion symmetry is broken, but most often it does not produce polarization.[48]

quite plausible.[126-128] In all these system multiferroics appears because of cycloid type structure[48] as in figure 1.8. When the spin of the adjacent atomic sides are canted from each other, the horizontal mirror plane symmetry is lost, meaning the possible generation of polarisation along the vertical direction. In other words spontaneous spin current will flow between the mutual canted spins, such a spin current produce the electric dipole. Theoretically it is shown that the overlapping of two atomic sites between the canted spins results ferroelectricity via spin-orbit coupling. When thespin forms a cycloidal modulation along the specific crystallographic direction then every nearest neighbour pair produce the local unidirectional polarisation.

Chapter 1

Table 1.5 A list of multiferroics with spiral spin-order-induced ferroelectricity.[21]

Compound	Crystal structure	Magnetic Ions	Ferroelectric temperature (K)	Spontanious polarization $\mu C/cm^2$
$LiCu_2O_2$	Orthorhombic(Pnma)	Cu^{+2}	< 23	Pc = 4
$LiCuVO_4$	Orthorhombic(Pnma)	Cu^{+2}	< 3	Pa= 20
$Ni_3V_2O_8$	Orthorhombic(mmm)	Ni^{+3}	3.9-6.3	Pb= 100
$RbFe(MoO_4)_2$	Triangular (P3m1)	Fe^{+3}	<3.8	Pc = 5.5
$CuCrO_2, AgCrO_2$	Delafossite (R3m)	Cr^{+3}	< 24	30^b
$NaCrO_2, LiCrO_2$	Ordered sock salt (R3m)	Cr^{+3}	< 60	Antiferro-electricity
$CuFeO_2$	Delafossite (R 3m)	Fe^{+3}	< 11	P=300($\perp$c) (H=6-13T)
$Cu(Fe,Al/Ga)O_2$	Delafossite (R 3m)	Fe^{+3}	< 7	$P_{[110]}$=50
$RMnO_3$ (R=Tb,Dy)	Orthorhombic(Pbnm)	Mn^{+3}	< 28	Pc=500
$CoCr_2O_4$	Cubic spinel (m3m)	Cr^{+3}	< 26	Pc=2
$AMSi_2O_6$(A=Na,Li) M=Fe,Cr)	Monoclinic (C2/c)	Fe^{+3}	< 6	Pb=14
$MnWO_4$	Monoclinic (Pc/2)	Mn^{+2}	7-12.5	Pb=55
CuO	Monoclinic (C2/c)	Cu^{+2}	213-230	Pb=150
$(Ba,Sr)_2Zn_2Fe_{12}O_{22}$	Rhomboheral Y-type hexaferrite	Fe^{+3}	< 325	150 (H=1T)
$Ba_2Mg_2Fe_{12}O_{22}$	Rhomboheral Y-type hexaferrite	Fe^{+3}	< 195	$P_{[120]}$=80
$ZnCr_2Se_4$	Cubic spinel	Cr^{+3}	< 20	-
Cr_2BeO_4	Orthorhombic	Cr^{+3}	< 28	3^b

The direction of the polarisation can be totally determined by the clockwise or counter clockwise rotation of the spin along the spiral propagation or spin helicity. The spiral spin states are widely seen in complex transition metal compounds like spinals and perovskite.

In these systems, neighbouring spins have competition of exchange interaction which finally produce spiral or modulated spin structure. In most of these systems, FE appears in magnetic phases with the spiral, or helicoidal magnetic structures and the spin structure which is responsible for ferroelectricity can be controlled by external magnetic field. In $TbMnO_3$, there is no electric polarization between 30-40K temperature where the magnetic structure is sinusoidal but nonzero P appears below 30 K, when magnetic structure changes from the sinusoidal to a helicoidal one as in figure 1.8(b).[101] Below 40K the magnetic structure is a sinusoidal spin-density wave, where all spins point in one direction, but the size of the local moment varies periodically in space (figure 1.8(a). More detail experiment shows that the existence of a spiral magnetic structure alone is not yet sufficient for generation of ferroelectricity. As is shown by Mostovoy[126], FE in spiral system can appear if the spin rotation axis e does not coincide with the wave vector of a spiral Q: the polarization P appears only if these two directions are different, and it is proportional to the vector product of e and Q,

$$\mathbf{P} \sim \mathbf{r}_{ij} \times [\mathbf{S}_i \times \mathbf{S}_j] \sim [\mathbf{Q} \times \mathbf{e}] \quad \text{--------------(1)}$$

where $\mathbf{r}_{ij}$ is the vector connecting neighbouring spins S_i and S_j, Q is the wave vector describing the spiral, and $e \sim [S_i \times S_j]$ is the spin rotation axis. One word of caution about Eq. (1): Its derivation assumes particular crystal symmetry, such as simple cubic or tetragonal. In these cases, Eq. (1) is indeed valid, and, for example, the polarization of a proper screw indicated in figure 1.8(c), in which spins rotate in the plane perpendicular to the wave vector of a spiral Q, would be zero. Magnetic frustration is the source of spiral magnetic ordering in an insulator. Therefore, these type-II multiferroics are usually found in frustrated systems. The effect of an external field H on a cycloid is analogous to the well-known spin-flop transition in an antiferromagnet. When a magnetic field forces the plane of a magnetic cycloid to flop by 90^0, the polarization P also flops: according to Eq. (1), P lies in the plane of spins but perpendicular to Q.

1.8.2 Collinear magnetic structures induce multiferroicity:

The second group of magnetically driven ferroelectrics are those in which ferroelectricity appears in collinear magnetic structures—that is all magnetic moments aligned along a particular axis—without the necessary involvement of the spin-orbit interaction. In these systems, magnetic coupling varies with the atomic position due to exchange striction results generation of polarisation. The simplest example, found in Ca_3CoMnO_6[129] where magnetic ordering, however, breaks inversion symmetry: the spins form a ↑↑↓↓ type magnetic structure. Due to an exchange striction the distance between magnetic ions with ferro and antiferromagnetic coupling is changed and end up in the situation where the material becomes ferroelectric[130].

1.8.3 Multiferroic with conical spin structure:

To realize the multiferroic phase with the use of spiral spin configuration, one may consider the conical spin structure that can be viewed as a sum of the ferromagnetic component and transverse spiral one[131] as in figure 1.9. A remarkable characteristic is expected for this kind of multiferroics is the electric (magnetic) reversal of the M (P) vector as shown in figure. The multiferroic of all spin origin may show the clamping of the ferromagnetic and ferroelectric domain walls.
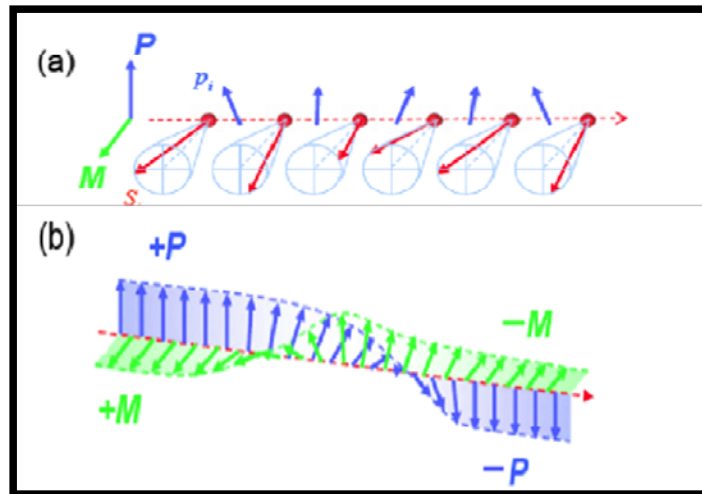
Figure 1.9: Spin conical structure as the candidate of multiferroics of all magnetic origin. P_i represents the local polarisation, the sum of which generates the macroscopic polarisation P. Thus, the magnetisation M of the conical spin is always orthogonal to P. (b) possible domain wall clamping of the multiferroics of the magnetic origin. [131]

Chapter 1

1.9 Properties of BiFeO₃:

Summarises the most important structural and physical properties of $BiFeO_3$, out of which some are elaborated below.

Property	Value	Ref
Crystal system	**Trigonal**	[132], [42]
	$a_{rh} = 5.6343$ Å, $\alpha_{rh} = 59.348°$	
	$a_{hex} = 5.5787$ Å, $c_{hex} = 13.8688$ Å	
	$a_{pc} = 3.965$ Å, $\alpha_{pc} = 89.35°$	
Space group	*R3c*,161	[132]
Polyhedral volume ratio	$V_A/V_B = 4.727$	[133]
Density	8.40 g/cm^3	
Thermal expansion	**Non-linear and anisotropic**	[134]
Ferroelectricity	$T_C = 820\text{-}830$ °C	[135]
Ferroelectric polarisation	$90\text{-}100$ μC/cm^2	[136]
Dielectric constant	$\varepsilon = 30$	[137]
Antiferromagnetism	**Canted G-type**, $T_N = 370$ °C	[138]
Piezoelectricity	$D_{33} = 15\text{-}60$ pm/V	[139]

1.9.1 Magnetic structure:

At room temperature, $BiFeO_3$ has a G-type antiferromagnetic ordering where each iron ion of spin-up configuration is surrounded by six nearest neighbours with spin-down configuration. Due to the size of the Bi ion, tilting of FeO_6 octahedra occurs to make a close packed structure which reduces the bond angle of Fe-O-Fe from 180^0 to $154\text{-}155^0$. If the Fe-O-Fe angle was 180^0 one would expect collinear antiferromagnetism. The antiparallel magnetic sublattices are also canted due to the Dzyaloshinskii-Moriya interaction[140,141] result of combination of exchange interaction and spin-orbit coupling. Canting of the iron sublattices yields a weak ferromagnetic moment, illustrated schematically in figure 1.10(b). The weak ferromagnetic moment is however cancelled on average due to a spiral modulation, or

spin cycloid, of the spin structure with a periodicity of 62 nm, incommensurate with the crystal lattice as in figure 1.10(c).
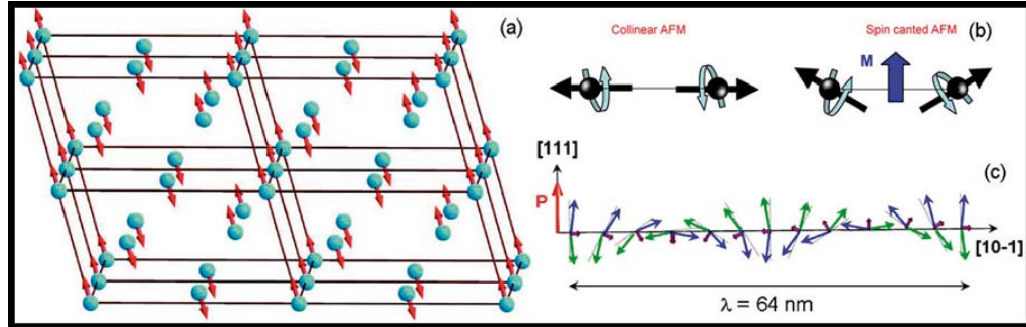
Figure 1.10:   (a) G-type antiferromagnetic ordering. (b) Weak ferromagnetic moment induced by canted spin sublattices caused by the Dzyaloshinskii-Moriya interaction. (c) Cycloidal modulation of the spin structure, directions are given with pseudocubic in indices[142, 143].

1.9.2 Ferroelectricity and Piezoelectrcity:

BiFeO$_3$ has spontaneous polarization P$_s$ along || [111]rh || [001]hex, due to the cooperative displacement of Bi^{3+} and Fe^{3+} ions. Early direct measurements of polarisation did however yield a small value of 6 μC/cm^2. Recent measurements on high quality thin films[144,145], single crystals[26], and ceramic polycrystals[146] have shown
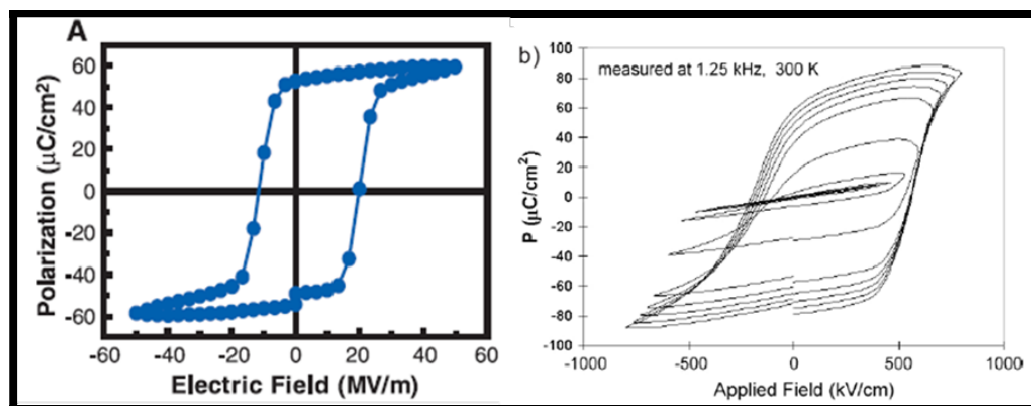
Figure 1.11 (A) ferroelectric hysteresis loop measured at a frequency of 15 kHz, which shows that the film is ferroelectric with Pr =55 μC/cm^2 by Wang et al[144].(B) P–E loops of BFO thin film measured at 300 K with Ps= 90 μC/cm^2 by Joonghoe Dho et al[147]

that P_S is 90-100 $\mu C/cm^2$ along the polar axis, in agreement with the a*b initio* studies by groups in Oslo[142] and Santa Barbara[26] also found a large spontaneous polarisation in the order of 90- 100 $\mu C/cm^2$. The spontaneous ferroelectric polarisation of $BiFeO_3$ is larger than those of the prototype ferroelectrics $BaTiO_3$ and $PbTiO_3$, in concordance with the more distorted crystal structure, larger polar displacements of cations and higher Curie temperature.

1.9.3 Magnetoelectric coupling:

The cycloidal modulation of the spin structure prevents a macroscopic weak ferromagnetic moment, and also exploitation of the linear magnetoelectric effect. This cycloidal modulation is suppressed and linear magnetoelectric coupling is possible only at large magnetic fields, above 20T.
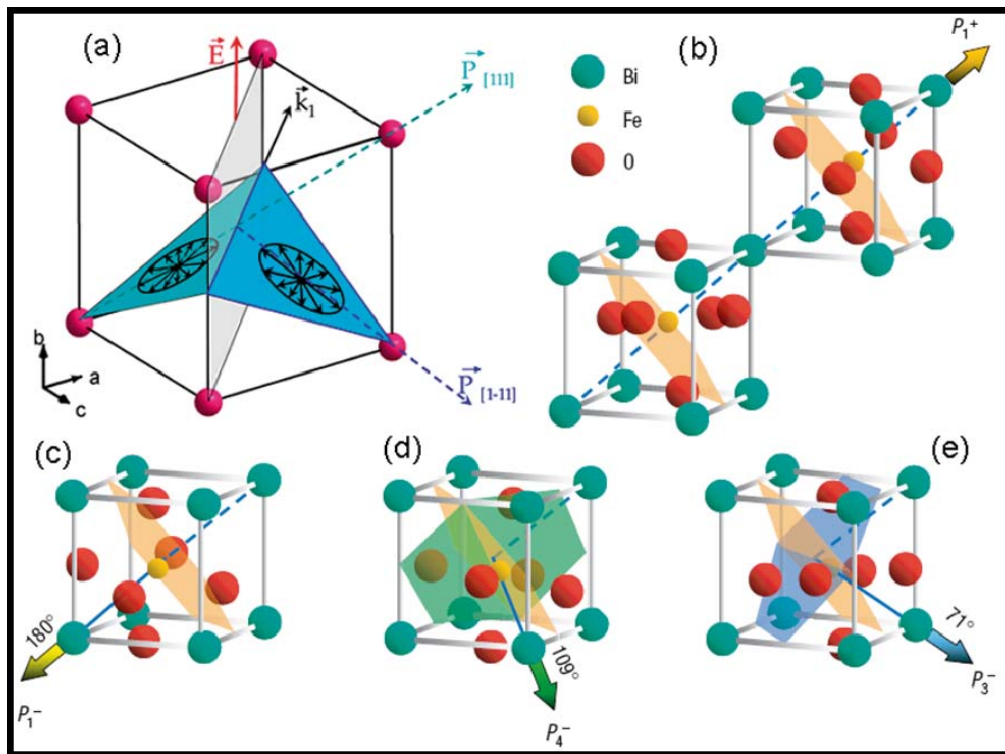
Figure 1.12: (a) 71^0 domain wall (light grey) and polarisation vectors with pseudocubic indices. The plane of spin rotation (Figure 1.12 (c)) is defined by the polarisation vector P and the propagation vector k_1. (b-d) The antiferromagnetic plane is normal to the polarisation and does not change with 180^0 switching (b) $\leftrightarrow$ (c), but rotates when the ferroelastic state is altered (d) and (e).[151]

Chapter 1

The origin of the cycloidal spin structure is believed to be the ferroelectric polarisation, as polarisation can couple to magnetisation gradients and induce the spin cycloid. This can be regarded as the opposite effect of the polarisation induced by spiral magnetic order in improper ferroelectric multiferroics.[148,149]Given that $BiFeO_3$ is a proper ferroelectric with only weak ferromagnetism due to the Dzyaloshinskii-Moriya interaction. Ferroelectric control of the magnetic structure is obviously more feasible than vice versa, as e.g. demonstrated in $TbMnO_3$.[150] A theoretical study of $BiFeO_3$ found that the direction of the weak ferromagnetic moment can be reversed by switching the direction of antiferro distortive rotation of the FeO_6 octahedra, but it is invariant under 180^0 switching of the direction of polar displacements of the Bi^{3+} and Fe^{3+} cations.[60] 180^0 ferroelectric switching does not affect neither the ferroelastic state of the material, nor the easy plane of magnetisation. Switching the ferroelectric polarisation by 71^0 or 109^0 changes the ferroelastic strain state of the domains for the rhombohedral structure, also changes both the easy plane of magnetisation and the direction of the weak ferromagnetic moment. This has been experimentally verified in rhombohedral 600 nm thick films without cycloidal modulation of the magnetic structure[151], as illustrated in figure 1.12. The antiferromagnetic domains coincide with the ferroelectric, illustrating the strong coupling of ferroelectric and magnetic order in $BiFeO_3$. This was the first demonstration of electric voltage control of magnetic order at room temperature.[152] Two independent neutron scattering studies of $BiFeO_3$ single crystals, with cycloidal spin structure, demonstrated that 71^0 switching of polarisation is accompanied by a 71^0 switching of the easy plane of magnetisation.[151,153] The microscopic origin of magnetoelectric coupling is not fully understood, and is expected to attract considerable attention in near future. Based on observations of phonon anomalies at T_N, and coupling of magnetic order to the ferroelastic domain state, Rovillain *et al.* proposed that the magnetoelectric coupling in $BiFeO_3$ is mediated by magnetostriction and piezoelectricity.[154]

1.10 Properties of DyFeO₃:

1.10.1 Crystal structure:

The $DyFeO_3$ structure is a distorted form of perovskite. The distortion mechanism is a tilting of essentially rigid FeO_6 octahedra. It occurs when the A-site cation is too small for its 12 coordinate cavity in the cubic perovskite structure like ABO_3.

The distortion has several consequences.

(1) It lowers the symmetry from cubic to orthorhombic.

(2) The unit cell dimensions are also expanded.

(3) The coordination number is effectively lowered from 12 to 8.

(4) The Fe-O-Fe bond, which is linear in the cubic perovskite structure, is bent.

1.10.2 Ferroelectricity and magnetoelectric coupling in DyFeO₃:

It has been known that in orthorhombic $DyAlO_3$ there exists a large linear magnetoelectric component.[155-157] However, the Al ions are diamagnetic at the ground state, and these materials do not show spontaneous polarization P and magnetization M. Substitution of a magnetic ion at the B-site may produce the multiferroic state. Recently, Y. Tokura group found existence of giant magnetoelectric coupling behaviour in $DyFeO_3$. The magnetic structures of $DyFeO_3$ are shown in Figure 1.13. Below reorientation temperature $T_r \sim 37$ K, the Fe spins align antiferromagnetically in configuration $A_x G_y C_z$ where the G-type and A-type components of Fe spins are direct towards the b-axis and a-axis respectively, while the C-type components are along the c-axis. Upon further cooling magnetization shows another anomaly around 4 K which correspond to the antiferromagnetic ordering of the Dy ion in $G_x A_y$ configuration. Below T_r if we apply a magnetic field which is greater than the magnetic field require
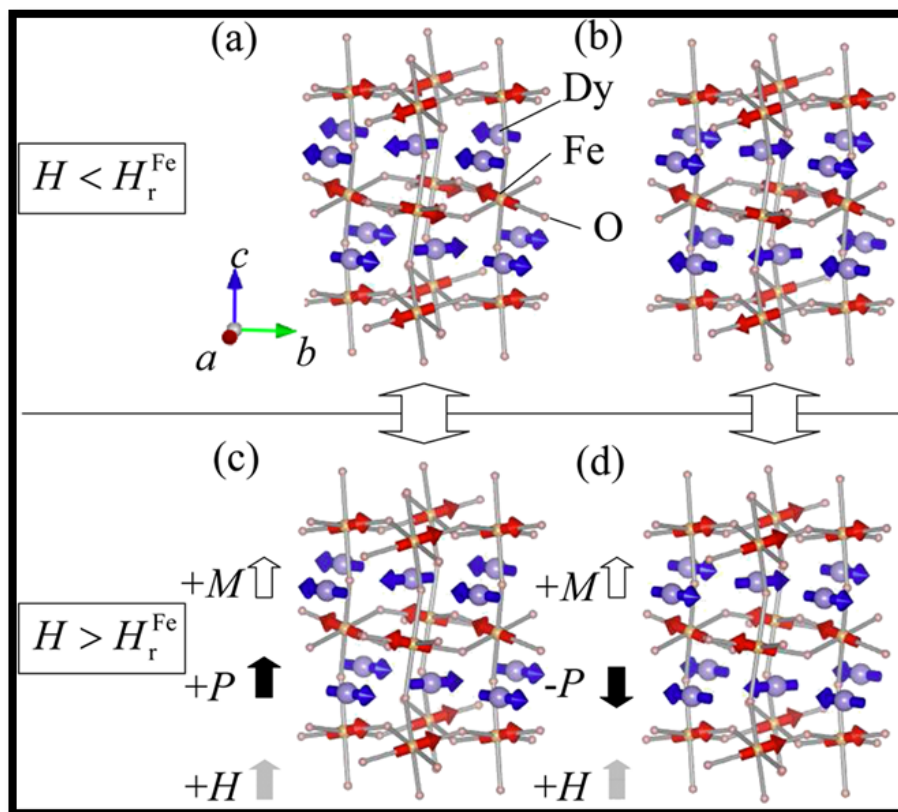
Figure 1.13: (Colour online) Magnetic structures of DyFeO₃ below T_N^{Dy} *under a magnetic field (along the c-axis)* $H < H_r^{Fe}$ *((a) and (b)) and* $H > H_r^{Fe}$ *((c) and (d)). In (b) and (d), the magnetic structures of Dy ions are different from (a) and (c), and then a reversed polarization appears in (d).*[31]

to reorient the iron spins below T_r, then it produce a weak ferromagnetism along the c axis. Moreover, a large polarisation below the 4K has been observed under the magnetic field 30 kOe along the c axis as shown in Figure 1.14(a). In the figure 1.14(b), as the magnetic field increases polarisation increases monotonically from zero, but shows a anomaly at H ~ 24 kOe. The extrapolated value of polarisation towards H=0 magnetic field is non zero shown by the dashed line in figure 1.14(b) which again confirm the existence of spontaneous polarisation. In fact, the multiferroic state can be further confirmed by the PE hysteresis loop, as shown in Figures 1.14(c) and (d).[31, 32] It is postulated that the exchange striction between those adjacent Fe^{3+} and Dy^{3+} layers with

the interlayer antiferromagnetic interaction (see Figures 1.13(c) and (d)) results in the multiferroic phase. The ferromagnetic sheets formed by Fe and Dy ions stack along the c-axis.
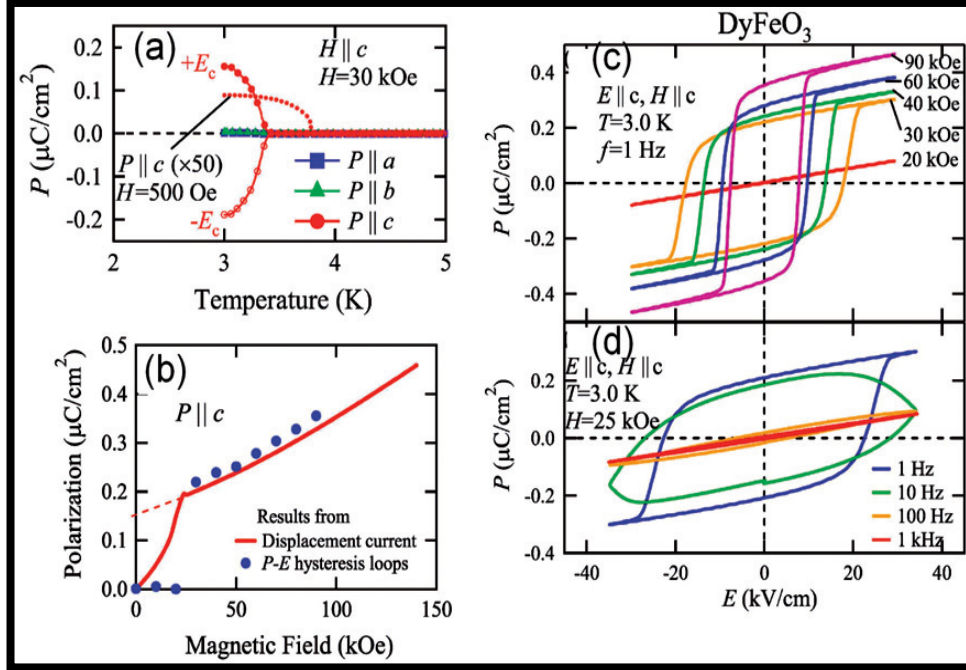
Figure 1.14: (a) Temperature dependence of polarization of DyFeO₃ along the a-axis, b-axis, c-axis under magnetic field of 30 kOe (> H_r^{Fe}) along the c-axis. The dotted line shows the polarization along the c-axis under a magnetic field of 500 Oe (<H_r^{Fe}). (b) Magnetic field (along the c-axis) dependence of the residual polarization obtained by P– E loops (filled circles)and the displacement current measurement (solid line) at T=3K. The dashed line is the extrapolated polarization curve in the regions of H > H_r^{Fe} towards H=0.(c),(d) Magnetic field(along the c axis) dependence of the P-E loops measured under H//c and E//c configuration with different frequencies by Sawyer-Tower bridge.[31]

The spins on the Fe layer become parallel to the moments on one of the nearest-neighbour Dy layers and antiparallel to those moments on another nearest-neighbour layer. As a result, the Dy layers should displace cooperatively toward the Fe layers with antiparallel spins, via the exchange striction. Then the polarization along the c-axis appears.[31]

Chapter 1

1.11 Properties of GdCrO₃ :

1.11.1 Crystal structure:

GdCrO$_3$ has been shown to crystallize in a distorted perovskite structure, space group Pbnm. The dimensions of the orthorhombic unit cell are a = 5.312Å, *b =*
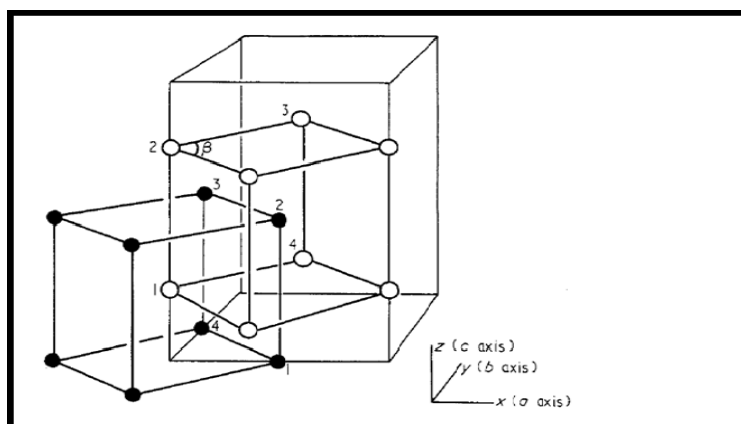
Figure 1.15: The crystal structure of GdCrO₃: O represents Gd atoms and ● represents Cr atoms. [158]

5.514Å, c = 7.611 Å**.** whilst the angle *β,* shown in figure 1.15, in the monoclinic cell is 91.1°. The Cr ions lie on undistorted positions relative to the orthorhombic cell, while the Gd ions are slightly removed from the special positions.[158]

1.11.2 Antiferromagnetic and weak ferromagnetic structure:

Orthorhombic *Gd*CrO$_3$, have a canted-antiferromagnetic order of localized Cr^{3+} moments ($3d^3$, μ_{eff} = 3.87 μ_B for a spin-only value) with Neel temperatures 170 K for GdCrO$_3$. It was found that below TN$_1$, a net magnetic moment (canted moment) of Cr^{3+} lies parallel to a crystallographic *c* axis. An antisymmetric exchange interaction or a psudodipolar interaction between Gd and Cr produces an effective magnetic "field at the Gd^{3+} ($4f^{\,7}$, μ_{eff} =7.94 μ_B site), whose direction is opposite to that of the canted Cr^{3+} moments.The interactions become important at low temperature where Cr moment shows a reorientation transition at 7K. At lower temperatures, a magnetic interaction between Gd becomes significant, which results in the order of the Gd^{3+} moments at 2.3 K.[158]

1.11.3 Magnetoelectric coupling:

Yamaguchi etal have predicted that the ME effect may be observed in RMO_3 such as $GdCrO_3$, $DyFeO_3$, and $DyCrO_3$ below the second Neel temperature due to the reordering of the rare-earth spins TN_2 , although any RMO_3 has no ME effect above TN_2.[157] $GdCrO_3$ are weak ferromagnets resulting from a small canting of the antiferromagnetic M^{3+} spins. Just below the first Neel temperature TN_1 (where the M^{3+} spins order), the M^{3+} sublattice moments and the net moment are observed to lie either along the a axis and the c axis, respectively, in most of RMO_3 , or along the c axis and the a axis in some $RCrO_3$ (R =Nd, Tb, Dy, Ho, Yb). The net moment of the R^{3+} spins is polarized parallel or antiparallel to the net M^{3+} moment by the M^{3+}–R^{3+} magnetic interactions. As the temperature is lowered, the R^{3+} moment increases and the spin reorientation occur at T_2 and T_1 (or at T_r) in most of RMO_3. Finally, below $TN_2 = 1$-4 K, a different configuration of R^{3+} spins is caused by the R^{3+}–R^{3+} interaction. The R^{3+} spin configuration below TN_2 can not be explained by the existing theory, which assumes that the magnetic symmetry group is the same for both above and below TN_2. Bertaut etal have investigated the R^{3+} spin configurations in some RMO_3 under the assumption that the magnetic unit cell is different from the paramagnetic one. Experiments on some RMO_3 near TN_2 have shown that the transition at TN_2 is of second order. Here, it should be noted that a phase transition is of second order if the symmetry of a crystal changes in such a way that the number of symmetry operations after the transition is reduced to half that before transition. Lowering symmetry can be realized either by (i) a doubling of the unit cell for a given crystal class, or by (ii) a halving of the number of rotations and reflections for a given unit cell. Yamaguchi etal show that case (ii) is more plausible than case (i) to describe the magnetic symmetry below TN_2 in RMO_3. Symmetry arguments and the calculation of the free energy show that two spin configurations are stable, in $GdCrO_3$ below TN_2. In $GdCrO_3$ with the Γ_{26} configuration, the ME polarization and magnetization are induced along the b axis (or the c axis) with the applied magnetic and electric field along the c axis (or the b axis). If $GdCrO_3$ has the Γ_{27} configuration, the role of the b axis in the Γ_{26} configuration is replaced by that of the a axis. Thus, measurements of the ME tensor determine which configuration $GdCrO_3$ has.

Chapter 1

1.12 References:

1. Hill, N. A., Why are there so few magnetic ferroelectrics? *Journal of Physical Chemistry B* **2000**, 104, (29), 6694-6709.

2. Cohen, R. E., Origin of ferroelectricity in perovskite oxides. *Nature* **1992**, 358, (6382), 136-138.

3. Valasek, J., Piezo-electric and allied phenomena in Rochelle salt. *Physical Review* 1921, 17, 475-481.

4. Fugiel, B., Transverse electric field effect in ferroelectrics with hydrogen bonds. *Physica B-Condensed Matter* **2003**, 325, (1-4), 256-258.

5. Konsin, P., Dynamic theory of ferroelectrics with asymmetrical hydrogen-bonds-application to Rochelle salt-type crystals. *Physica Status Solidi B-Basic Research* **1975**, 70, (2), 451-459.

6. Mueller, H., Influence of electrostatic fields or the elastic properties of Rochelle salt. *Physical Review* **1940**, 57, (9), 842-843.

7. Mueller, H., Properties of Rochelle salt. *Physical Review* **1940**, 57, (9), 829-839.

8. Slater, J. C., Theory of the transition in KH_2PO_4. *Journal of Chemical Physics* **1941**, 9, (1), 16-33.

9. Debretteville, A., 2nd order transition in $BaTiO_3$. *Physical Review* **1955**, 98, (5), 1563-1563.

10. Jaynes, E. T., Displacement of oxygen in $BaTiO_3$. *Physical Review* **1950**, 79, (6), 1008-1009.

11. Danielson, G. C.; Matthias, B. T.; Richardson, J. M., Dielectric behaviour of single domain crystals of $BaTiO_3$. *Physical Review* **1948**, 74, (8), 986-987.

12. Richardson, J. M.; Matthias, B. T., Theory of the dielectric behaviour of $BaTiO_3$. *Physical Review* **1948**, 74, (8), 987-988.

13. Jayachandran, K. P.; Guedes, J. M.; Rodrigues, H. C., Ferroelectric materials for piezoelectric actuators by optimal design. *Acta Materialia* **2011**, 59, (10), 3770-3778.

14. Shang, J. L.; Hu, G. J., Applications of Ferroelectric Materials in Optoelectronic Engineering. *Proceedings of the 7th National Conference on Chinese Functional Materials and Applications* **2001**, (1-3), 2121-2124.

15. Kumar, A.; Katiyar, R. S.; Scott, J. F., Novel Room Temperature Multiferroics for Random Access Memory Elements. IEEE Transactions on Ultrasonics Ferroelectrics and Frequency Control **2010**, 57, (10), 2237-2242.

16. Szwarcman, D.; Vestler, D.; Markovich, G., The Size-Dependent Ferroelectric Phase Transition in $BaTiO_3$ Nanocrystals Probed by Surface Plasmons. *ACS Nano* **2011**, 5, (1), 507-515.

17. Petzelt, J., Dielectric Grain-Size Effect in High-Permittivity Ceramics. *Ferroelectrics* **2010**, 400, 117-134.

18. Gharbi, M.; Sun, Z. H.; Sharma, P.; White, K., The origins of electromechanical indentation size effect in ferroelectrics. *Applied Physics Letters* **2009**, 95, (14), 142901.

19. Ahn, C. H.; Rabe, K. M.; Triscone, J. M., Ferroelectricity at the nanoscale: Local polarization in oxide thin films and heterostructures. *Science* **2004**, 303, (5657), 488-491.

20. Garcia, N.; Munoz, M.; Zhao, Y. W., Magnetoresistance in excess of 200% in ballistic Ni nanocontacts at room temperature and 100 Oe. *Physical Review Letters* **1999**, 82, (14), 2923-2926.

21. Wang, K. F.; Liu, J. M.; Ren, Z. F., Multiferroicity: the coupling between magnetic and polarization orders. *Advances in Physics* **2009**, 58, (4), 321-448.

22. Izyumskaya, N.; Alivov, Y.; Morkoc, H., Oxides, Oxides, and More Oxides: High- Oxides, Ferroelectrics, Ferromagnetics, and Multiferroics. *Critical Reviews in Solid State and Materials Sciences* **2009**, 34, (3-4), 89-179.

23. Miura, K.; Tanaka, M., Electronic structures of $PbTiO_3$: I. Covalent interaction between Ti and O ions. *Japanese Journal of Applied Physics Part 1-Regular Papers Short Notes & Review Papers* **1998**, 37, (12A), 6451-6459.

24. Miura, K.; Furuta, T.; Funakubo, H., Electronic and structural properties of BaTiO3: A proposal about the role of Ti 3s and 3p states for ferroelectricity. *Solid State Communications* **2010**, 150, (3-4), 205-208.

Chapter 1

25. Baek, S. H.; Folkman, C. M.; Park, J. W.; Lee, S. H.; Bark, C. W.; Tybell, T.; Eom, C. B., The Nature of Polarization Fatigue in $BiFeO_3$. *Advanced Materials* **2011**, 23, (14), 1621.

26. Neaton, J. B.; Ederer, C.; Waghmare, U. V.; Spaldin, N. A.; Rabe, K. M., First-principles study of spontaneous polarization in multiferroic BiFeO3. *Physical Review B* **2005**, 71, (1), 014113.

27. Seshadri, R.; Hill, N. A., Visualizing the role of Bi 6s "Lone pairs" in the off-center distortion in ferromagnetic $BiMnO_3$. *Chemistry of Materials* **2001**, 13, (9), 2892-2899.

28. Belik, A. A.; Takayama-Muromachi, E., Magnetic properties of $BiMnO_3$ studied with dc and ac magnetization and specific heat. *Inorganic Chemistry* **2006**, 45, 10224-10229.

29. Kenzelmann, M.; Harris, A. B.; Jonas, S.; Broholm, C.; Schefer, J.; Kim, S. B.; Zhang, C. L.; Cheong, S. W.; Vajk, O. P.; Lynn, J. W., Magnetic inversion symmetry breaking and ferroelectricity in $TbMnO_3$. *Physical Review Letters* **2005**, 95, (8).

30. Aliouane, N.; Prokhnenko, O.; Feyerherm, R.; Mostovoy, M.; Strempfer, J.; Habicht, K.; Rule, K. C.; Dudzik, E.; Wolter, A. U. B.; Maljuk, A.; Argyriou, D. N., Magnetic order and ferroelectricity in $RMnO_3$ multiferroic manganites: coupling between R- and Mn-spins. *Journal of Physics-Condensed Matter* **2008**, 20, (43), 12.

31. Tokunaga, Y.; Iguchi, S.; Arima, T.; Tokura, Y., Magnetic-field-induced ferroelectric state in $DyFeO_3$. *Physical Review Letter* **2008**, 101, (9), 097205.

32. Stroppa, A.; Marsman, M.; Kresse, G.; Picozzi, S., The multiferroic phase of $DyFeO_3$: an ab initio study. *New Journal of Physics* **2010**, 12, 093026.

33. Ikeda, N.; Matsuo, Y.; Mori, S.; Yoshi, K., Electronic ferroelectricity from charge ordering in RFe_2O_4. *IEEE Transactions on Ultrasonics Ferroelectrics and Frequency Control* **2008**, 55, (5), 1043-1045.

34. Yang, H. X.; Zhang, Y.; Qin, Y. B.; Ma, C.; Tian, H. F.; Li, J. Q., Electronic ferroelectricity, charge ordering and structural phase transitions in $LuFe_2O_4(LuFeO_3)(n)$ (n=0 and 1). *Physica Status Solidi B-Basic Solid State Physics* **2010**, 247, (4), 870-876.

35.   Ishihara, S., Electronic Ferroelectricity and Frustration. *Journal of the Physical Society of Japan* **2010**, 79, (1).

36.   Van Aken, B. B.; Palstra, T. T. M., Influence of magnetic on ferroelectric ordering in $LuMnO_3$. *Physical Review B* **2004**, 69, (13), 134113.

37.   Katsufuji, T.; Mori, S.; Masaki, M.; Moritomo, Y.; Yamamoto, N.; Takagi, H., Dielectric and magnetic anomalies and spin frustration in hexagonal $RMnO_3$ (R = Y, Yb, and Lu). *Physical Review B* **2001**, 64, (10), 104419.

38.   Harris, A. B.; Yildirim, T., Charge and spin ordering in the mixed-valence compound $LuFe_2O_4$ *Physical Review B* **2010**, 82, (2), 134417.

39.   Cheong, S. W.; Mostovoy, M., Multiferroics: a magnetic twist for ferroelectricity. *Nature Materials* **2007**, 6, 13-20.

40.   Lemanov, V. V., Improper ferroelastic $SrTiO_3$ and what we know today about its properties. *Ferroelectrics* **2002**, 265, 1-21.

41.   Aizu, K., Consideration of partially ferroelastic and partially antiferroelastic crystal and partially ferroelectric and partially antiferroelectric crystals. *Journal of the Physical Society of Japan* **1970**, 28, (3), 717.

42.   Kubel, F.; Schmid, H., Structure of a ferroelectric and ferroelastic monodomain crystal of the perovskite $BiFeO_3$. *Acta Crystallographica Section B-Structural Science* **1990**, 46, 698-702.

43.   Aizu, K., Possible species of ferromagnetic, ferroelectric, and ferroelastic crystals. *Physical Review B* **1970**, 2, (3), 754.

44.   Kim, K.; Daly, S., Martensite Strain Memory in the Shape Memory Alloy Nickel-Titanium Under Mechanical Cycling. *Experimental Mechanics* **2011**, 51, (4), 641-652.

45.   H., Schmid, Multiferroic Magnetoelectrics. *Ferroelectrics* **1994**, 162, 317.

46.   Ranjan, R.; Senyshyn, A.; Garg, R.; Boysen, H., Magnetic structure and magneto-elastic-structural coupling in Cr-modified SrRuO3: A neutron powder diffraction study. *Journal of Applied Physics* **2011**, 109, (7), 073908.

47.   Baettig, P.; Ederer, C.; Spaldin, N. A., First principles study of the multiferroics $BiFeO_3$, Bi_2FeCrO_6, and $BiCrO_3$: Structure, polarization, and magnetic ordering temperature. *Physical Review B* **2005**, 72, (21), 214105.

48. Khomskii, D., classifying multiferroics: mechanism and effects. *Physics* **2009**, 2, (20).

49. Khomskii, D. I., Multiferroics: Different ways to combine magnetism and ferroelectricity. *Journal of Magnetism and Magnetic Materials* **2006**, 306, (1), 1-8.

50. van den Brink, J.; Khomskii, D. I., Multiferroicity due to charge ordering. *Journal of Physics-Condensed Matter* **2008**, 20, (43), 434217.

51. Ederer, C., Coupling between magnetism and ferroelectricity in multiferroic materials. *Abstracts of Papers of the American Chemical Society* **2005**, 230, 93.

52. Eerenstein, W.; Mathur, N. D.; Scott, J. F., Multiferroic and magnetoelectric materials. *Nature* **2006**, 442, 759-765.

53. Jaiswal, A.; Das, R.; Adyanthaya, S.; Poddar, P., Surface Effects on Morin Transition, Exchange Bias, and Enchanced Spin Reorientation in Chemically Synthesized $DyFeO_3$ Nanoparticles. *Journal of Physical Chemistry C* **2011**, 115, (7), 2954-2960.

54. Kimura, H.; Noda, Y.; Kohn, K., Spin-driven ferroelectricity in the multiferroic compounds of RMn_2O_5. *Journal of Magnetism and Magnetic Materials* **2009**, 321, (7), 854-857.

55. Shen, X.; Xu, C. H.; Li, C. H.; Zhang, Y.; Zhao, Q.; Yang, H. X.; Sun, Y.; Li, J. Q.; Jin, C. Q.; Yu, R. C., Pressure effects on multiferroic $LuFe_2O_4$. *Applied Physics Letters* **2010**, 96, (10), 102909.

56. Ko, K. T.; Noh, H. J.; Kim, J. Y.; Park, B. G.; Park, J. H.; Tanaka, A.; Kim, S. B.; Zhang, C. L.; Cheong, S. W., Electronic Origin of Giant Magnetic Anisotropy in Multiferroic $LuFe_2O_4$. *Physical Review Letters* **2009**, 103, (20), 207202.

57. Phan, M. H.; Frey, N. A.; Angst, M.; de Groot, J.; Sales, B. C.; Mandrus, D. G.; Srikanth, H., Complex magnetic phases in $LuFe_2O_4$. *Solid State Communications* **2010**, 150, (7-8), 341-345.

58. Wang, F.; Li, C. H.; Zou, T.; Liu, Y.; Sun, Y., Electrically driven magnetic relaxation in multiferroic $LuFe_2O_4$. *Journal of Physics-Condensed Matter* **2010**, 22, (49), 496001.

Chapter 1

59. Wen, J. S.; Xu, G. Y.; Gu, G. D.; Shapiro, S. M., Robust charge and magnetic orders under electric field and current in multiferroic LuFe$_2$O$_4$. *Physical Review B* **2010**, 81, (14), 144121.

60. Ederer, C.; Spaldin, N. A., Weak ferromagnetism and magnetoelectric coupling in bismuth ferrite. *Physical Review B* **2005**, 71, (6), 060401.

61. Catalan, G.; Scott, J. F., Physics and Applications of Bismuth Ferrite. *Advanced Materials* **2009**, 21, (24), 2463-2485.

62. Chen, J.; Xing, X. R.; Watson, A.; Wang, W.; Yu, R. B.; Deng, J. X.; Yan, L.; Sun, C.; Chen, X. B., Rapid synthesis of multiferroic BiFeO$_3$ single-crystalline nanostructures. *Chemistry of Materials* **2007**, 19, (15), 3598-3600.

63. Chu, Y. H.; Martin, L. W.; Holcomb, M. B.; Gajek, M.; Han, S. J.; He, Q.; Balke, N.; Yang, C. H.; Lee, D.; Hu, W.; Zhan, Q.; Yang, P. L.; Fraile-Rodriguez, A.; Scholl, A.; Wang, S. X.; Ramesh, R., Electric-field control of local ferromagnetism using a magnetoelectric multiferroic. *Nature Materials* **2008**, 7, (6), 478-482.

64. Chu, Y. H.; Martin, L. W.; Holcomb, M. B.; Ramesh, R., Controlling magnetism with multiferroics. *Materials Today* **2007**, 10, (10), 16-23.

65. Kimura, T.; Kawamoto, S.; Yamada, I.; Azuma, M.; Takano, M.; Tokura, Y., Magnetocapacitance effect in multiferroic BiMnO$_3$. *Physical Review B* **2003**, 67, (18), 180401.

66. Glass, A. M.; Lines, M. E.; Eibschutz, M.; Hsu, F. S. L.; Guggenheim, H. J., Observation of anomalous pyroelectric behaviour in BaNiF$_4$ due to cooperative magnetic singularity. *Communications on Physics* **1977**, 2, (4), 103-107.

67. Murakawa, H.; Onose, Y.; Ohgushi, K.; Ishiwata, S.; Tokura, Y., Generation of electric polarization with rotating magnetic field in helimagnet ZnCr$_2$Se$_4$. *Journal of the Physical Society of Japan* **2008**, 77, (4), 043709.

68. Thiele, C.; Dorr, K.; Bilani, O.; Rodel, J.; Schultz, L., Influence of strain on the magnetization and magnetoelectric effect in La$_{0.7}$A$_{0.3}$MnO$_3$/PMN-PT(001) (A=Sr,Ca).*Physical Review B* **2007**, 75(5), 054408.

69. Hauptmann, J. R.; Paaske, J.; Lindelof, P. E., Electric-field-controlled spin reversal in a quantum dot with ferromagnetic contacts. *Nature Physics* **2008**, 4, (5), 373-376.

70. Srivastava, V.; Song, Y. T.; Bhatti, K.; James, R. D., The Direct Conversion of Heat to Electricity Using Multiferroic Alloys. *Advanced Energy Materials* **2011**, 1, (1), 97-104.

71. Thomas, R.; Scott, J. F.; Bose, D. N.; Katiyar, R. S., Multiferroic thin-film integration onto semiconductor devices. *Journal of Physics-Condensed Matter* **2010**, 22, (42), 423201.

72. Ederer, C.; Spaldin, N. A., Magnetoelectrics - A new route to magnetic ferroelectrics. *Nature Materials* **2004**, 3, (12), 849-851.

73. Bea, H.; Gajek, M.; Bibes, M.; Barthelemy, A., Spintronics with multiferroics. *Journal of Physics-Condensed Matter* **2008**, 20, (43), 726.

74. Bibes, M.; Barthelemy, A., Multiferroics: Towards a magnetoelectric memory. *Nature Materials* **2008**, 7, (6), 425-426.

75. Fiebig, M., Revival of the magnetoelectric effect. *Journal of Physics D-Applied Physics* **2005**, 38, (8), R123-R152.

76. Martin, L.; Crane, S. P.; Chu, Y. H.; Holcomb, M. B.; Gajek, M.; Huijben, M.; Yang, C. H.; Balke, N.; Ramesh, R., Multiferroics and magnetoelectrics: thin films and nanostructures. *Journal of Physics-Condensed Matter* **2008**, 20, (43), 434220.

77. Borisov, P.; Hochstrat, A.; Shvartsman, V. V.; Kleemann, W.; Hauck, P. M., Magnetoelectric Cr_2O_3 for spintronic applications. *Integrated Ferroelectrics* **2008**, 99, 69-76.

78. Hehl, F. W.; Obukhov, Y. N.; Rivera, J. P.; Schmid, H., Magnetoelectric Cr_2O_3 and relativity theory. *European Physical Journal B* **2009**, 71, (3), 321-329.

79. Liu, Y. Y.; Xie, S. H.; Jin, G.; Li, J. Y., The effective magnetoelectric coefficients of polycrystalline Cr_2O_3 annealed in perpendicular electric and magnetic fields. *Journal of Applied Physics* **2009**, 105, (7), 073917.

80. Van Aken, B. B.; Palstra, T. T. M.; Filippetti, A.; Spaldin, N. A., The origin of ferroelectricity in magnetoelectric $YMnO_3$. *Nature Materials* **2004**, 3, (3), 164-170.

81. Kim, J. S.; Cheon, C. I.; Kang, H. J.; Jang, P. W., High temperature properties of multiferroic $BiFeO_3$-$DyFeO_3$-$BaTiO_3$ solid solutions. *Journal of the European Ceramic Society* **2007**, 27, (13-15), 3951-3954.

82. Nan, C. W.; Bichurin, M. I.; Dong, S. X.; Viehland, D.; Srinivasan, G., Multiferroic magnetoelectric composites: Historical perspective, status, and future directions. *Journal of Applied Physics* **2008**, 103, (3), 031101.

83. Zhou, C. C.; Luo, B. C.; Jin, K. X.; Cao, X. S.; Chen, C. L., Magnetic and dielectric properties of $BiFeO_3$-$La_{1/3}Sr_{2/3}MnO_3$ hybrid composite ceramics. *Solid State Communications* **2010**, 150, (29-30), 1334-1337.

84. Ryu, J.; Carazo, A. V.; Uchino, K.; Kim, H. E., Piezoelectric and magnetoelectric properties of Lead Zirconate Titanate/Ni-Ferrite particulate composites. *Journal of Electroceramics* **2001**, 7, (1), 17-24.

85. Gupta, A.; Chatterjee, R., Magnetic, dielectric, magnetoelectric, and microstructural studies demonstrating improved magnetoelectric sensitivity in three-phase $BaTiO_3$-$CoFe_2O_4$-poly(vinylidene-fluoride) composite. *Journal of Applied Physics* **2009**, 106, (2), 024110.

86. Xie, S. H.; Liu, Y. M.; Liu, X. Y.; Zhou, Q. F.; Shung, K. K.; Zhou, Y. C.; Li, J. Y., Local two-way magnetoelectric couplings in multiferroic composites via scanning probe microscopy. *Journal of Applied Physics* **2010**, 108, (5), 054108.

87. Da, H. X.; Li, Z. Y., Optical magnetoelectric effect induced by a moving medium. *Physical Review B* **2007**, 76(1), 012409.

88. Shevchuk, Y. A.; Korchagina, S. K.; Gagulin, V. V.; Bogatko, V. V., Synthesis and investigations of solid solutions based on relaxor ferroelectric-antiferromagnetic $Pb(Fe_{2/3}W_{1/3})O_3$. *Ferroelectrics* **1997**, 199, (1-4), 223-230.

89. Mazumder, R.; Devi, P. S.; Bhattacharya, D.; Choudhury, P.; Sen, A.; Raja, M., Ferromagnetism in nanoscale $BiFeO_3$. *Applied Physics Letters* **2007**, 91, (6), 062510.

90. Jaiswal, A.; Das, R.; Vivekanand, K.; Abraham, P. M.; Adyanthaya, S.; Poddar, P., Effect of Reduced Particle Size on the Magnetic Properties of Chemically Synthesized $BiFeO_3$ Nanocrystals. *Journal of Physical Chemistry C* **2010**, 114, (5), 2108-2115.

91. Ribeiro, J. L., Symmetry and magnetically driven ferroelectricity in rare-earth manganites $RMnO_3$ (R=Gd,Tb,Dy). *Physical Review B* **2007**, 76, (14), 144417.

92. Bak, P.; Jensen, M. H., Theory of helical magnetic structures and phase transitions in MnSi and FeGe. *Journal of Physics C: Solid State Physics* **1980**, 13, 881-885.

93. Uchida, M.; Onose, Y.; Matsui, Y.; Tokura, Y., Real-space observation of helical spin order. *Science* **2006**, 311, (5759), 359-361.

94. Chang, L. J.; Huang, D. J.; Li, W. H.; Cheong, S. W.; Ratcliff, W.; Lynn, J. W., Crossover from incommensurate to commensurate magnetic orderings in $CoCr_2O_4$. *Journal of Physics-Condensed Matter* **2009**, 21, (45), 456008.

95. Anisimov, V. I.; Elfimov, I. S.; Korotin, M. A.; Terakura, K., Orbital and charge ordering in $Pr_{1-x}Ca_xMnO_3$ (x=0 and 0.5) from the ab initio calculations. *Physical Review B* **1997**, 55, (23), 15494-15499.

96. Harris, A. B.; Yildirim, T., Charge and spin ordering in the mixed-valence compound $LuFe_2O_4$. *Physical Review B* **2010**, 81, (13), 134417.

97. Zylberberg, J.; Belik, A. A.; Takayama-Muromachi, E.; Ye, Z. G., Bismuth aluminate $BiAlO_3$: A new lead-free High-T-C piezo-/ferroelectric. *2007 Sixteenth IEEE International Symposium on the Applications of Ferroelectrics*, **2007**,(1-2), 662-663.

98. Tsymbal, E. Y.; Kohlstedt, H., Applied physics - Tunneling across a ferroelectric. *Science* **2006**, 313, (5784), 181-183.

99. Gajek, M.; Bibes, M.; Fusil, S.; Bouzehouane, K.; Fontcuberta, J.; Barthelemy, A. E.; Fert, A., Tunnel junctions with multiferroic barriers. *Nature Materials* **2007**, 6, (4), 296-302.

100. Fennie, C. J.; Rabe, K. M., Ferroelectric transition in $YMnO_3$ from first principles. *Physical Review B* **2005**, 72, (10), 100103(R).

101. Yamasaki, Y.; Sagayama, H.; Goto, T.; Matsuura, M.; Hirota, K.; Arima, T.; Tokura, Y., Electric control of spin helicity in a magnetic ferroelectric. *Physical Review Letters* **2007**, 98, (14), 147204.

102. Chen, C. X., Charge ordering in the perovskite manganites. *Journal of Inorganic Materials* **2005**, 20, (1), 1-12.

103. Efremov, D. V.; van den Brink, J.; Khomskii, D., Bond centered vs. site-centered charge ordering: ferroelectricity in oxides. *Physica B-Condensed Matter* **2005**, 359, 1433-1435.

104. Efremov, D. V.; Van den Brink, J.; Khomskii, D. I., Bond-versus site-centred ordering and possible ferroelectricity in manganites. *Nature Materials* **2004**, 3, (12), 853-856.

105. Rao, C. N. R., Charge, spin, and orbital ordering in the perovskite manganates, $Ln_{1-x}A_xMnO_3$ (Ln = rare earth, A = Ca or Sr). *Journal of Physical Chemistry B* **2000**, 104, (25), 5877-5889.

106. Giovannetti, G.; Kumar, S.; Khomskii, D.; Picozzi, S.; van den Brink, J., Multiferroicity in Rare-Earth Nickelates $RNiO_3$. *Physical Review Letters* **2009**, 103, (15), 156401.

107. Markovich, G.; Fried, T.; Poddar, P.; Sharoni, A.; Katz, D.; Wizansky, T.; Millo, O. In Observation of the verwey transition in Fe_3O_4 nanocrystals, *Materials Research Society Symposium Proceedings.* Symposium on Magnetoelectronics and Magnetic Materials-Novel Phenomena and Advanced Characterization, Boston, **2003**, 746, 151-156.

108. Yamauchi, K.; Fukushima, T.; Picozzi, S., Ferroelectricity in multiferroic magnetite Fe_3O_4 driven by noncentrosymmetric Fe^{2+}/Fe^{3+} charge-ordering: First-principles study. *Physical Review B* **2009**, 79, (21) 212404.

109. Zhou, F.; Ceder, G., First-principles determination of charge and orbital interactions in Fe_3O_4. *Physical Review B* **2010**, 81, (20), 205113.

110. Laverdiere, J.; Jandl, S.; Mukhin, A. A.; Ivanov, V. Y.; Ivanov, V. G.; Iliev, M. N., Spin-phonon coupling in orthorhombic $RMnO_3$ (R=Pr, Nd, Sm, Eu, Gd, Tb, Dy, Ho, Y): A Raman study. *Physical Review B* **2006**, 73,(21), 214301.

111. Uusi-Esko, K.; Malm, J.; Imamura, N.; Yamauchi, H.; Karppinen, M., Characterization of $RMnO_3$ (R = Sc, Y, Dy-Lu): High-pressure synthesized metastable perovskites and their hexagonal precursor phases. *Materials Chemistry and Physics* **2008**, 112, (3), 1029-1034.

112. Munoz, A.; Alonso, J. A.; Martinez-Lope, M. J.; Casais, M. T.; Martinez, J. L.; Fernandez-Diaz, M. T., Magnetic structure of hexagonal $RMnO_3$ (R = Y, Sc): Thermal evolution from neutron powder diffraction data. *Physical Review B* **2000**, 62, (14), 9498-9510.

113. Lee, S.; Pirogov, A.; Kang, M. S.; Jang, K. H.; Yonemura, M.; Kamiyama, T.; Cheong, S. W.; Gozzo, F.; Shin, N.; Kimura, H.; Noda, Y.; Park, J. G., Giant magneto-elastic coupling in multiferroic hexagonal manganites. *Nature* **2008**, 451, (7180), 805.

114. Das, R.; Jaiswal, A.; Adyanthaya, S.; Poddar, P., Origin of Magnetic Anomalies below the Neel Temperature in Nanocrystalline $LuMnO_3$. *Journal of Physical Chemistry C* **2010**, 114, (28), 12104-12109.

115. Waintal A., Capponi J.J., Bertaut E.F., Contré M., François D., Transformation sous haute pression de la forme ferroelectrique de $MnHoO_3$ en une forme perovskite paraelectrique *Solid State Communication* **1966**, 4,(3) 125.

116. A., Waintel; J., Chenavas, Transformation sous haute pression de la forme hexagonale de $MnT'O_3$ (T' = Ho, Er, Tm, Yb, Lu) en une forme perovskite. *Material Research Bulletin* **1967**, 2, 819.

117. Brinks, H. W.; Rodriguez-Carvajal, J.; Fjellvag, H.; Kjekshus, A.; Hauback, B. C., Crystal and magnetic structure of orthorhombic $HoMnO_3$. *Physical Review B* **2001**, 63, (9), 094411.

118. Ishibashi, Y.; Iwata, M.; Janssen, T., On the lattice instability in incommensurate phase transition of K_2SeO_4. *Journal of the Physical Society of Japan* **2001**, 70, (10), 3178-3179.

119. Melnikova, S. V.; Primak, S. V., Cs_2CdI_4 and Cs_2ZnI_4 crystal with incommensurate phases. *Fizika Tverdogo Tela* **1992**, 34, (7), 2173-2177.

120. Ederer, C.; Spaldin, N. A., Recent progress in first-principles studies of magnetoelectric multiferroics. *Current Opinion in Solid State & Materials Science* **2005**, 9, 128-139.

121. Gibbs, A. S.; Knight, K. S.; Lightfoot, P., High-temperature phase transitions of hexagonal $YMnO_3$. *Physical Review B* **2011**, 83, (9), 094111.

122. Johnson, R. D.; Mazzoli, C.; Bland, S. R.; Du, C. H.; Hatton, P. D., Magnetically induced electric polarization reversal in multiferroic $TbMn_2O_5$: Terbium spin reorientation studied by resonant x-ray diffraction. *Physical Review B* **2011**, 83, (5), 054438.

123. Chang, L. J.; Su, Y.; Schweika, W.; Buckel, T.; Chen, Y. Y.; Jang, D. S.; Liu, R. S., Neutron polarization analysis on the multiferroic $TbMn_2O_5$. *Physica B-Condensed Matter* **2009**, 404, (17), 2517-2519.

124. Arima, T.; Goto, T.; Yamasaki, Y.; Miyasaka, S.; Ishii, K.; Tsubota, M.; Inami, T.; Murakami, Y.; Tokura, Y., Magnetic-field-induced transition in the lattice modulation of colossal magnetoelectric $GdMnO_3$ and $TbMnO_3$ compounds. *Physical Review B* **2005**, 72, (10),100102.

125. Cabrera, I.; Kenzelmann, M.; Lawes, G.; Chen, Y.; Chen, W. C.; Erwin, R.; Gentile, T. R.; Leao, J. B.; Lynn, J. W.; Rogado, N.; Cava, R. J.; Broholm, C., Coupled Magnetic and Ferroelectric Domains in Multiferroic $Ni_3V_2O_8$. *Physical Review Letters* **2009**, 103, (8),087201.

126. Mostovoy, M., Ferroelectricity in spiral magnets. *Physical Review Letters* **2006**, 96,(6), 067601.

127. Sosnowska, I.; Peterlin-Neumaier, T.; Steichele, E., Spiral magnetic ordering in bismuth ferrite. *Journal of Physics C: Solid State Physics* **1982**, 15, 4835-4846.

128. Tokura, Y.; Seki, S., Multiferroics with Spiral Spin Orders. *Advanced Materials* **2010**, 22, (14), 1554-1565.

129. Kaushik, S. D.; Rayaprol, S.; Saha, J.; Mohapatra, N.; Siruguri, V.; Babu, P. D.; Patnaik, S.; Sampathkumaran, E. V., Magnetoelectric coupling in Ca_3CoMnO_6. *Journal of Applied Physics* **2010**, 108, (8), 084106.

130. Katsura, H.; Nagaosa, N.; Balatsky, A. V., Spin current and magnetoelectric effect in noncollinear magnets. *Physical Review Letters* **2005**, 95, (5), 057205.

131. Tokura, Y., Multiferroics - toward strong coupling between magnetization and polarization in a solid. *Journal of Magnetism and Magnetic Materials* **2007**, 310, (2), 1145-1150.

132. Michel, C.; Moreau, J. M.; Achenbac.Gd; Gerson, R.; James, W. J., Atomic structure of $BiFeO_3$. *Solid State Communications* **1969**, 7, (9), 701.

133. Thomas, N. W.; Beitollahi, A., Interrelationship of octahedral geometry, polyhedral volume ratio and ferroelectric properties in rhombhhedral perovskites. *Acta Crystallographica Section B-Structural Science* **1994**, 50, 549-560.

134. Bucci, J. D.; Robertso.Bk; James, W. J., Precision determination of lattice parameters and coefficients of thermal expansion of $BiFeO_3$. *Journal of Applied Crystallography* **1972**, 5, 187.

135. Teague, J. R.; Gerson, R.; James, W. J., Dielectric hysteresis in single crystal $BiFeO_3$. *Solid State Communications* **1970**, 8, (13), 1073.

136. Lebeugle, D.; Colson, D.; Forget, A.; Viret, M.; Bonville, P.; Marucco, J. F.; Fusil, S., Room-temperature coexistence of large electric polarization and magnetic order in $BiFeO_3$ single crystals. *Physical Review B* **2007**, 76, 024116.

137. Kamba, S.; Nuzhnyy, D.; Savinov, M.; Sebek, J.; Petzelt, J.; Prokleska, J.; Haumont, R.; Kreisel, J., Infrared and terahertz studies of polar phonons and magnetodielectric effect in multiferroic $BiFeO_3$ ceramics. *Physical Review B* **2007**, 75, (2), 024403.

138. Moreau, J. M.; Michel, C.; Gerson, R.; James, W. J., Ferroelectric $BiFeO_3$ X-ray and neutron diffraction study. *Journal of Physics and Chemistry of Solids* **1971**, 32, (6), 1315.

139. Shvartsman, V. V.; Kleemann, W.; Haumont, R.; Kreisel, J., Large bulk polarization and regular domain structure in ceramic $BiFeO_3$. *Applied Physics Letters* **2007**, 90, (17), 172115.

140. Sergienko, I. A.; Dagotto, E., Role of the Dzyaloshinskii-Moriya interaction in multiferroic perovskites. *Physical Review B* **2006**, 73, 094434.

141. Moriya, T., Anisotropic Superexchange Interaction and Weak Ferromagnetism. *Physical Review* **1960**, 120, (1), 91-98.

142. Ravindran, P.; Vidya, R.; Kjekshus, A.; Fjellvag, H.; Eriksson, O., Theoretical investigation of magnetoelectric behavior in BiFeO$_3$. *Physical Review B* **2006**, 74, (22), 224412.

143. Ederer, C.; Fennie, C. J., Electric-field switchable magnetization via the Dzyaloshinskii-Moriya interaction: FeTiO$_3$ versus BiFeO$_3$. *Journal of Physics-Condensed Matter* **2008**, 20, (43), 434219.

144. Wang, J.; Neaton, J. B.; Zheng, H.; Nagarajan, V.; Ogale, S. B.; Liu, B.; Viehland, D.; Vaithyanathan, V.; Schlom, D. G.; Waghmare, U. V.; Spaldin, N. A.; Rabe, K. M.; Wuttig, M.; Ramesh, R., Epitaxial BiFeO$_3$ multiferroic thin film heterostructures. *Science* **2003**, 299, (5613), 1719-1722.

145. Ederer, C.; Spaldin, N. A., Effect of epitaxial strain on the spontaneous polarization of thin film ferroelectrics. *Physical Review Letters* **2005**, 95,257601.

146. Wang, Y. P.; Zhou, L.; Zhang, M. F.; Chen, X. Y.; Liu, J. M.; Liu, Z. G., Room-temperature saturated ferroelectric polarization in BiFeO$_3$ ceramics synthesized by rapid liquid phase sintering. *Applied Physics Letters* **2004**, 84, (10), 1731-1733.

147. Dho, J. H.; Qi, X. D.; Kim, H.; MacManus-Driscoll, J. L.; Blamire, M. G., Large electric polarization and exchange bias in multiferroic BiFeO$_3$. *Advanced Materials* **2006**, 18, 1445.

148. Popov, Y. F.; Zvezdin, A. K.; Vorobev, G. P.; Kadomtseva, A. M.; Murashev, V. A.; Rakov, D. N., Linear magnetoelectric effect and phase transitions in bismuth ferrite, BiFeO$_3$. *Jetp Letters* **1993**, 57, (1), 69-73.

149. Kadomtseva, A. M.; Zvezdin, A. K.; Popov, Y. F.; Pyatakov, A. P.; Vorob'ev, G. P., Space-time parity violation and magnetoelectric interactions in antiferromagnets. *Jetp Letters* **2004**, 79, (11), 571-581.

150. Kimura, T.; Goto, T.; Shintani, H.; Ishizaka, K.; Arima, T.; Tokura, Y., Magnetic control of ferroelectric polarization. *Nature* **2003**, 426, (6962), 55-58.

151.   Lebeugle, D.; Colson, D.; Forget, A.; Viret, M.; Bataille, A. M.; Gukasov, A., Electric-field-induced spin flop in $BiFeO_3$ single crystals at room temperature. *Physical Review Letters* **2008**, 100, (22), 227602.

152.   Zhao, T.; Scholl, A.; Zavaliche, F.; Lee, K.; Barry, M.; Doran, A.; Cruz, M. P.; Chu, Y. H.; Ederer, C.; Spaldin, N. A.; Das, R. R.; Kim, D. M.; Baek, S. H.; Eom, C. B.; Ramesh, R., Electrical control of antiferromagnetic domains in multiferroic $BiFeO_3$ films at room temperature. *Nature Materials* 2006, 5, (10), 823-829.

153.   Lee, S.; Ratcliff, W.; Cheong, S. W.; Kiryukhin, V., Electric field control of the magnetic state in $BiFeO_3$ single crystals. *Applied Physics Letters* **2008**, 92, (19), 192906.

154.   Rovillain, P.; Cazayous, M.; Gallais, Y.; Sacuto, A.; Lobo, R.; Lebeugle, D.; Colson, D., Polar phonons and spin excitations coupling in multiferroic $BiFeO_3$ crystals. *Physical Review B* **2009**, 79, (18), 180411.

155.   Holmes, L. M.; Hecker, R. R.; Vanuiter.Lg; Hull, G. W., Magnetic behaviour of metamagnetic $DyAlO_3$.*Physical Review B* **1972**, 5, (1), 138.

156.   Holmes, L. M.; Vanuiter.Lg, Magnetoelectric effect and metamagnetic transition in $DyAlO_3$. *Physical Review B* **1972**, 5, (1), 147.

157.   Yamaguchi, T.; Tsushima, K., Magnetic Symmetry of Rare-Earth Orthochromites and Orthoferrites. *Physical Review B* **1973**, 8, (11), 5187-5198.

158.   Yoshii, K., Magnetic properties of perovskite $GdCrO_3$. *Journal of Solid State Chemistry* **2001**, 159, (1), 204-208.

Chapter 2

Effect of Reduced Particle Size on the Magnetic, Raman & Dielectric Spectroscopy of Chemically Synthesized BiFeO$_3$ Nanocrystals: Signatures of Spin-Phonon and Magnetoelectric Coupling
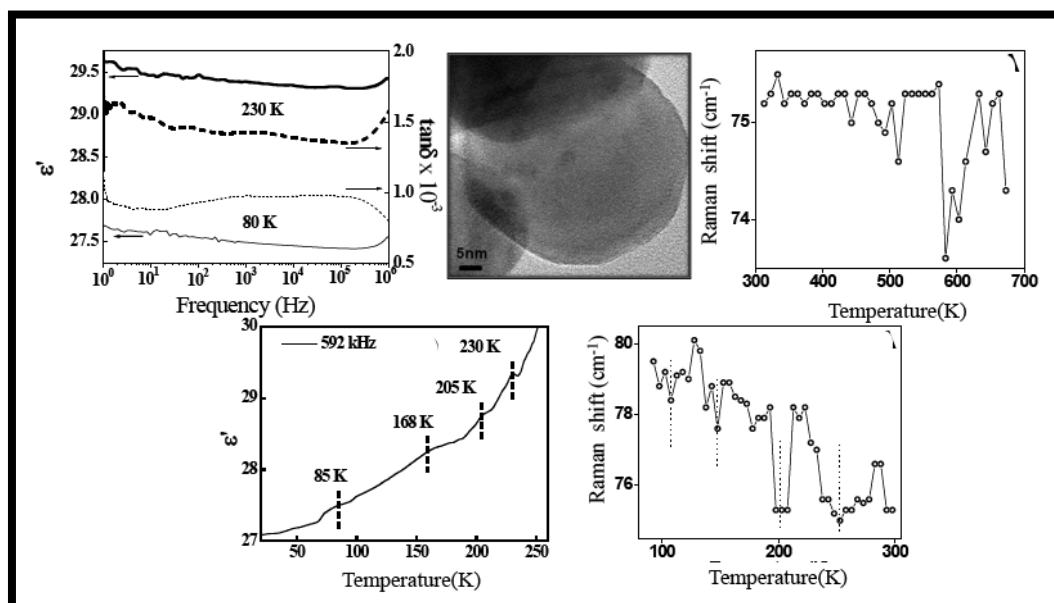
Outline

In this chapter, we report the effect of reduction in particle size on the temperature dependent magnetization, Raman and dielectric spectroscopy of chemically synthesized BiFeO$_3$ nanocrystals with average grain size of 55 nm. Due to the nanosize effect, the M-H loops show a significant coercivity starting from 390 K with an anomaly located in the vicinity of 150 K in our H$_c$ vs. T as well as M$_r$/M$_{s(50\ kOe)}$ vs T curves. At this temperature, both Hc and M$_r$/M$_{s(50\ kOe)}$ undergo minima. Additionally, our results for the first time show the evidence of existence of a low temperature anomaly due to spin-glass transition in the range from 40-44K in the field cooled magnetization curves. In bulk single crystals,

this transition is reported to be situated at around 50 K, however, this transition remained so far undiscovered in the recent studies on BiFeO₃ nanoparticles due to the insufficient temperature resolution. The significant shift in this transition towards lower temperature can be attributed to size dependent effects. The Raman spectroscopy (90 – 700 K) shows two sets of transitions in the lowest Raman E mode, associated with Bi-O bond motion situated in the close proximity to the spin reorientation transitions reported in BiFeO₃, thereby proving the existence of possible coupling between magnons and phonons for the particle size below the helical order parameter (62 nm). These transitions are slightly shifted in temperature in comparison to the bulk single crystals. We also observe a step like behavior in Raman peak position around Nèel temperature suggesting that the phonons are getting influenced by the magnetic ordering in nanosized BiFeO₃.The low temperature (20- 325 K), frequency dependent (1 – 10⁶ Hz) dielectric constant and loss tangent measurements show that the loss tangent (~10⁻³) and ac conductivity values (~ 10⁻⁸ Ohm⁻¹-cm⁻¹) are orders of magnitude lower than the reported values BiFeO₃ ceramics indicating high levels of ionic purity of our samples. The real part of permittivity shows slight reduction in its value (~30) in comparison to the bulk single crystals. Similar to the Stokes Raman shift, its temperature dependent dielectric constant also shows four weak anomalies at~ 85, 168, 205 and 230 K situated in the close proximity with spin reorientation transitions indicating the magnetoelectric coupling.

The work described in this chapter is published as –

➢ **Effect of Reduced Particle Size on the Magnetic Properties of Chemically Synthesized BiFeO₃ Nanocrystals.**
   Adhish Jaiswal, *Raja Das, K. Vivekanand, Priya Mary Abraham, Suguna Adyanthaya, and Pankaj Poddar* **J. Phys. Chem. C** *114 (5), 2108–2115 (2010)*

➢ **Temperature-Dependent Raman and Dielectric Spectroscopy of BiFeO₃ Nanoparticles: Signatures of Spin-Phonon and Magnetoelectric Coupling.**
   Adhish Jaiswal, *Raja Das, Tuhin Maity, K. Vivekanand, Suguna Adyanthaya, Pankaj Poddar* **J. Phys. Chem. C** *114, 12432-12439 (2010)*

2.1 Introduction:

After the initial work by Curie and other researchers on the magnetoelctric effect, where ferroelectric and ferromagnetic/antiferromagnetic order parameters couple in the same phase, there is a recent surge in the development of new synthesis methods as well as to fully understand the physical properties of these multifunctional materials. Among these materials, $BiFeO_3$ (BFO) is one of the most widely studied materials in this class; mostly in bulk single crystal,[1-4] polycrystalline and epitaxially grown thin film forms.[5-7] BFO crystallizes in rhombohedrally distorted perovskite structure with space group *R3c* below its T_c (1100 K).[8] Recently, people have also started investigating the effects on the magnetoelectric coupling after manganese[9], calcium[1], niobium[10] substitution in the lattice to decrease the ac conductivity, increase dielectric constant and magnetization. The usefulness of doping related enhancement in ferroelectric polarization is under a question mark as it may not be truly ferroelectric in origin. Moreover, even in the pure undoped BFO, the bulk phase structural, optical, dielectric and magnetic properties are not completely understood.[1] One of the major reason behind relatively larger attention given to this material is its antiferromagnetic (AFM) nature with reasonably high Neel temperature ($T_N = 380^oC$) and ferroelectric (FE) ordering below its Curie temperature ~ 1100 K[11,12] above which it undergoes a transition from rhombohedral to orthorhombic symmetry and becomes cubic above ~ 1200 K. However, there is a lack of clear understanding as which of these two transitions is truly associated to the FE ordering[13]. The coexistence of FE and AFM ordering at room temperature makes this material one of the most promising candidate for room temperature magnetoelectric (ME) applications. The fascination towards this material is never ending with newer information being added by several groups. Magnetic ordering in BFO is quite complicated because of Dzyaloshinsky-Moriya (DM) interaction which results in a canted AFM ordering of Fe^{3+} spins in the system. These canted Fe^{+3} moments induce a lattice strain which increases the free energy of the crystal. To minimize the free energy of the crystal, spiral spin structure is superimposed on the AFM ordering resulting into rotation of the spins. The order parameter of this helical ordering between two successive planes is found to be around ~ 620Å in the bulk BFO.[14] For bulk BFO, the magnetic hysteresis loop shows a typical AFM behavior with zero coercivity.[15]

Room temperature magnetoelectric (ME) coupling in BFO has also excited a lot of interest in recent years though the origin of this coupling is still debated. In BFO, electrical and magnetic dipole ordering originates in different sublattices; Bi-O orbital hybridization due to Bi $6s^2$ lone pair is the origin of ferroelectricity whereas Fe-O-Fe antisymmetric Dzyaloshinskii-Moriya (DM) exchange interaction gives rise to interesting magnetic ordering. In recent years, the phonon behavior in multiferroic materials has gained interest due to the study of $HoMnO_3$ by Raman and IR spectroscopy[16] and $LuMnO_3$ by transmittance and reflectance measurements[17] which showed the importance of studying phonons in multiferroic materials. Raman studies on epitaxial BFO films and single crystals showed the spin-phonon coupling. Singh et al. reported for the first time, room temperature Raman spectra with phonon mode assignments in epitaxially grown thin films.[18, 19] Haumont et al. showed an anomaly near Nèel temperature in Raman phonon modes (315, 380, and 550 cm^{-1}) in BFO single crystals proving the possible multiferroic character playing the role in the strong phonon anomaly.[20] Kothari et al. and Fukumura et al. showed presence of all the 13 Raman modes predicted by the group theory on single crystal and polycrystalline BFO.[21, 22] Recently, through low temperature Raman measurements, some studies have reported the existence of coupling between ferroelectric and magnetic order parameters in polycrystalline bulk materials.[23]

The dielectric properties of BFO in various forms have also been widely studied in single crystalline,[13] ceramic[13, 24-26] and thin film[27] forms. However, most of these dielectric studies are reported in temperature range higher than room temperature (> 300 K) and do not investigate the relation between magnetic anomalies at low temperature with dielectric parameters which are reported below 300 K only. Recently, Scott et al related low temperature dielectric anomaly and their magnetic coupling in ceramic and single crystalline BFO and reported the existence of coupling between FE & AFM order parameters in single crystal and ceramic BFO.[2-4, 13] The BFO polycrystalline samples showed a decrease in the real part of permittivity (ε') values from 114.4 to 97.2 and loss tangent (tan δ) values from 9.22 to 0.26% when the frequency is increased from 0.01 to 1MHz.[28] The FE behavior of BFO thin films showed high ε' and tan δ values in the low frequency range with continuously decreasing trend at the frequencies higher than 1kHz.[27] The bulk BFO is reported to show relatively low resistivity and high loss tangent

which prevents from studying the polarization loop behavior at and above the room temperature and hinders its potential applications in FE and ME devices.[29] BFO single crystals showed FE hysteresis loop at low temperatures (< 100 K) only, with spontaneous polarization value of P_S= 6.1 $\mu C/cm^2$ which is much lower than expected from the materials with such a high FE transition temperature accompanied with large lattice distortion.[30] On the other hand the observation of orders of magnitude higher P_s in thin films[5] (up to 50-60 $\mu C/cm^2$) accompanied with enhanced magnetization (up to 1 μ_B/unit cell) was attributed to be originating from the higher conductivity and oxygen deficiency in these thin films due to the presence of significant amount of Fe^{2+}.[5, 31] It is therefore non-trivial and a challenging task to synthesize high resistive BFO as the ceramic synthesis and thin film methods usually result in secondary phases such as Fe_2O_3[24, 32], Bi_2O_3[24] and $Bi_2Fe_4O_9$[33] Additionally, the presence of slight non-stiochiometric oxygen in BFO often leads to the presence of Fe^{2+} and lattice defects thereby resulting into unwanted increase in the conductivity at room temperature due to hopping mechanism from Fe^{2+} to Fe^{3+}, significant Maxwell-Wagner type of contributions in the dielectric constant and weak ferromagnetism etc. The high leakage current in bulk BFO synthesized by solid solution methods also leads to serious dielectric breakdown at fields < 100 KV/cm which makes them unsuitable for practical devices.[29] To overcome this problem and to get higher resistive material, people have tried various approaches such as doping with various rare earth and transition metal ions and solid solution of BFO with other ABO_3 perovskite materials but these methods also often result into impure phases.[24] Nanosize effects on the physical properties of both magnetic and ferroelectric counterparts of multiferroics are studied in depth in past several decades due to their potential applications in various nanoscale devices. The observation of Verwey metal to insulator transition and large spin dependent magnetoresistance in chemically synthesized and organically passivated Fe_3O_4 nanoparticles with size as small as 6-8 nm and the shift in the Verwey transition temperature from 120 K (in bulk) to around 90 K (in nanoparticles) is reported.[34, 35] Similarly, the observation of ferroelectric-paraelectric transition in biosynthesized $BaTiO_3$ nanoparticles with size 5-6 nm and the shift of this transition at lower temperature is also reported.[36] Therefore, the interest in the investigation of size dependent properties of multiferroic materials is non-trivial leading

to few recent reports on this topic in BFO. This is largely due the fact that below the particle size ~ 62 nm, there is an enhancement in both ferroelectric and magnetic polarization because of the combined action of exchange and spin-orbit interactions which produces spin canting (away from perfect AFM ordering).[37] Recently, people have reported that below 100 K, nanosized BFO exhibits sizable hysteresis and finite coercivity.[37] Such a deviation from bulk to nano is observed due to the breaking of the helical ordering or incomplete rotation of the spins along the AFM axis which gives rise to higher magnetization. The decrease in particle size below the periodicity of helical ordering gives rise to the suppression of modulated spin structure which improves the magnetization in nanoscale particles.[38] However, in absence of quality magnetization data, some of these studies remain poorly concluded.[37] Moreover, sometimes, the properties of BFO are reported to be masked with presence of the impurity phase of Fe_3O_4.[32]

However, the effect on the reduced size (below the helical order parameter) on the phonons and the dielectric behavior at low temperature (in the vicinity to the spin reorientation transitions) is not studied so far. The temperature dependent Raman and impedance spectroscopy in BFO nanoparticles is required to answer some of the fundamental questions including: (1) what is the temperature dependent frequency behavior of $|\varepsilon|$ and *tan* δ at low temperature in the proximity of magnetic transition in nanosized BFO? (2) Do the relaxation behavior, dielectric constant and loss tangent remain same in nanosize as for bulk BFO? (3) Is there any direct/indirect coupling between the breaking of spiral ordering on the dielectric parameters and FE ordering? (4) What is the fate of FE and AFM ordering transitions and spin-phonon coupling in nanosized BFO?

In this chapter, we have tried to answer some of these questions by doing a careful temperature dependent Raman and dielectric spectroscopy and heat flow measurements on chemically synthesized $BiFeO_3$ nanoparticles with average size ~ 50-60 nm.

2.2 Hydrothermal synthesis of BiFeO$_3$ nanoparticles:

We have developed a modified hydrothermal route to synthesize the BFO nanoparticles based on complexing the metal ions with the citric acid followed by the hydrothermal process. Recently, we applied the similar approach to synthesize GdCrO$_3$ nanocrystals.[39] In contrast to the usual ceramic methods which are used to make bulk BFO and often give impurity phases (most common impurities are Bi$_2$O$_3$ and Fe$_2$O$_3$) and, wet-chemical method adopted by us gave highly pure BFO nanoparticles without any impurity phase due to ionic level mixing. For this purpose, stoichiometric amounts of iron nitrate (Fe(NO$_3$)$_3$.9H$_2$O, Merck, 98%), bismuth nitrate (Bi(NO$_3$)$_3$.5H$_2$O   Merck, 98%), and an equal amount of citric acid (metal/citric acid molar ratio = 1/1) (obtained from Merck, 99.5%) were dissolved in the deionized water by stirring it for 6 h, to complex the metal ions with the citrate ions. This was followed by the dropwise addition of ammonia solution (28 wt. %) to neutralize the unreacted citric acid as well as to raise the pH value of the solution near 9.2 resulting into a sol formation. The sol was transferred to a 200 ml capacity autoclave with Teflon liner followed by the hydrothermal treatment at 150^{0}C for 20 h. The precipitate was in turn filtered, washed with deionized water, re-filtered and finally dried at 160^{0}C for 5 h. The dried powder was calcined at 350°C for 6 h to get crystalline phase and used for further physical property measurements discussed below unless mentioned otherwise. In another case, we calcined the part of these particles at 750°C for 6 hours to study the effect of particle size growth on the magnetic properties.

2.3 Characterization:

2.3.1 X-ray diffraction and Pawley refinements:

In figure 2.1, we have shown the powder x-ray diffraction pattern (XRD) of the as-synthesized BFO nanocrystals recorded by a PANalytical X'PERT PRO instrument using an iron- filtered Cu-Kα radiation (λ=1.5406 Å) in the 2θ range of 10°- 80° with a step size of 0.02°. We used the Materials Studio Software from Accelrys Inc. to perform the Pawley refinement todetermine the lattice parameters of the BFO nanocrystals from the experimental data. The pseudo-Voigt peak shape was selected for these refinements. The refined lattice parameter were calculated as $a = b = 5.574\pm0.001$, $c= 13.850\pm0.002$Å
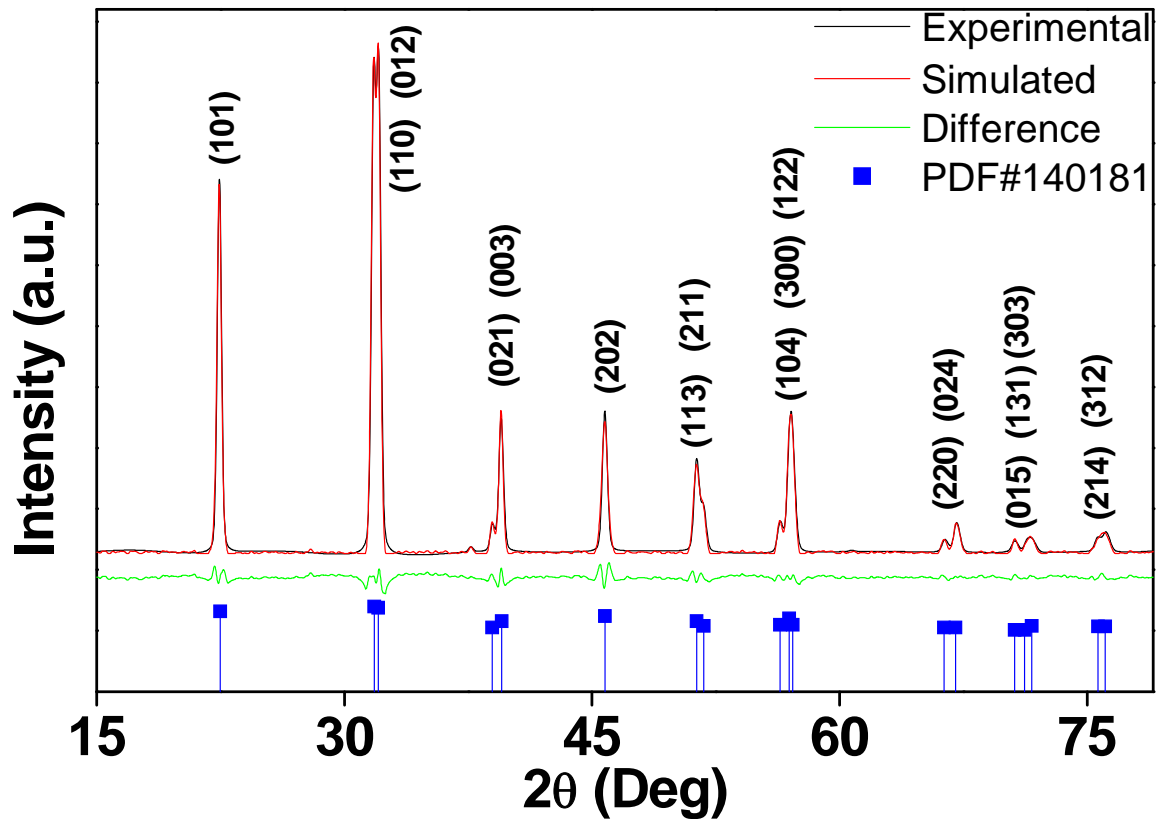
Figure 2.1: Room temperature experimental powder XRD pattern compared with the simulated and difference NPD profiles (using Powley refinement) for BiFeO₃ nanocrystals. The blue lines are the reference values for BiFeO₃ taken from the JCPDS Card No. 140181.

with an excellent Rwp value of 4.94%. The difference in the experimental and simulated data is also shown in figure 2.1. In the supporting information, we have shown the zoom view of different parts of complete XRD profile which clearly shows the absence of any impurity phase (See supporting information). The average crystallite size as calculated using Debye-Scherer formula was found to be around 36 nm.

2.3.2 Determination of shape and size of the $BiFeO_3$ nanoparticles:

To further investigate microstructure and topography, we used the FEI (model Tecnai F30) high resolution transmission electron microscope (HRTEM) equipped with field emission source operating at 300 KV to image BFO nanocrystals on carbon-coated copper TEM grid. The TEM images in figures 2.2 A & B show particles with a quasi
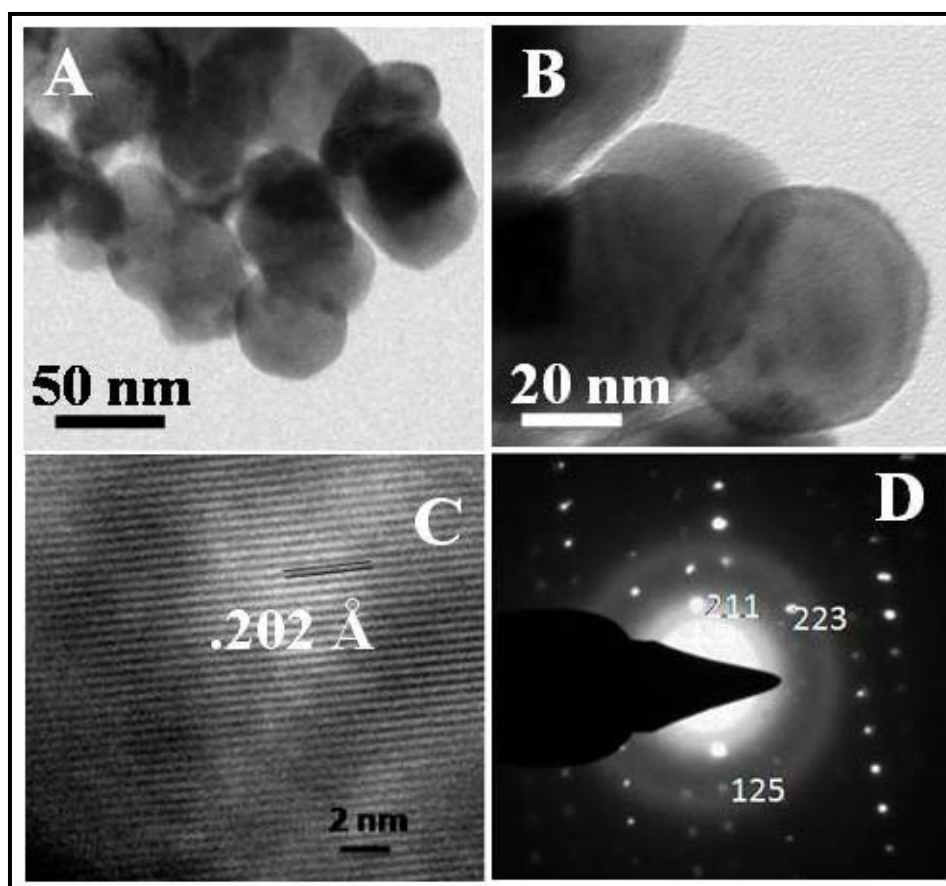
Figure 2.2: *(A,B) Transmission electron micrograph (C) High resolution TEM images showing the lattice fringes (D) Selected Area Electron Diffraction (SAED) pattern of BiFeO₃ nanoparticles.*

spherical morphology and size ranging from 50-60 nm. The average size calculated from TEM images was around 55 nm. In figure 2.2C, we have shown the high resolution TEM image where we could notice well pronounced lattice fringes indicating very good level of crystallinity. The selected area electron diffraction pattern (SAED) in figure 2.2D shows a nice dot pattern that again clearly exhibits highly crystalline nature of BFO nanocrystals. In figure 2.3, we have shown the TEM images of BFO particles recalcined at 750°C for 6 h. These images show that particles that were initially 55 nm in sized have fused together nicely to form larger particles with average size of 0.5 μm.
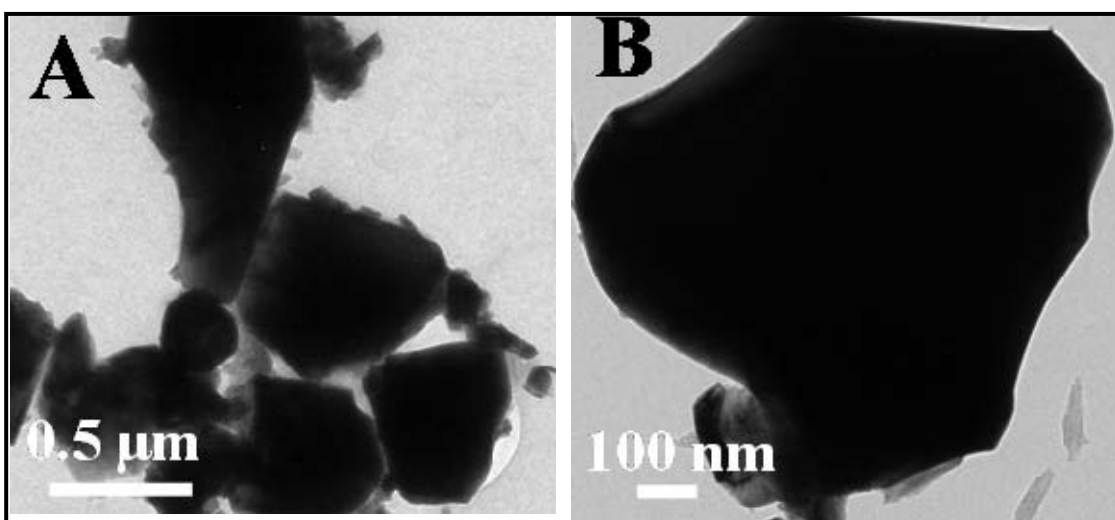
Figure 2.3: *(A, B) Transmission electron micrograph of BiFeO₃ particles calcined at 750°C. Growth of the particl Figure 2.3: (A, B) Transmission electron micrograph of BiFeO₃ particles calcined at 750°C. Growth of the particle size can be clearly seen in comparison to the TEM images in figure 2.2*

2.4 Optical properties:

2.4.1 UV-vis absorption spectroscopy measurements:

In figure 2.4, we have shown the UV–vis -NIR spectra for the BFO nanocrystals in the diffused reflectance mode taken using a Jasco UV-vis-NIR spectrometer (model V570) operated at a resolution of 2 nm. In the UV–vis -NIR spectra, we observed a broad absorption band in the range of 450-600 nm. This absorption is due to two types of electronic transitions. The first excitation is due to the electronic transition from $^6A_1$ state

to $^4T_1$ (^4G) state and the second one is due to the excitation from $^6A_1$---^4E, $^4A_1$(^4G) ligand field transitions and the field transfer band tail.[40] These transitions overlap with each other and give a broad band as seen in figure 2.4. The absorption below 450 nm is associated with charge transfer transition (*d-d*) of Fe^{+3} ions from $^6A_1$ to ^4E (^4D) and $^4T_2$(^4D) level.[40]
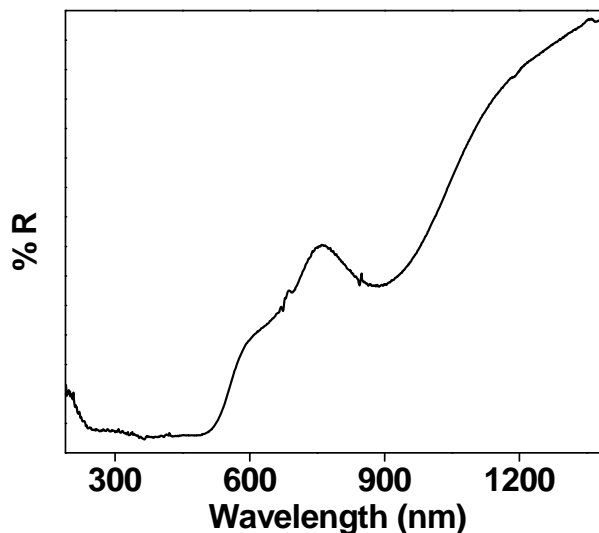
Figure 2.4: *The UV–vis-NIR spectra for BiFeO₃ nanocrystals at room temperature in diffuse reflectance mode.*

2.4.2 X-ray photoelectron spectroscopy measurements:

In figures 2.5 A & B, we have shown the room temperature x-ray photoelectron spectroscopy (XPS) data to confirm the oxidation state of the Bi and Fe to validate the formation of the pure phase. For this purpose the high resolution XPS data was collected by using a VG Microtch, model ESCA 3000 equipped with ion gun (EX-05) for cleaning the surface spectra. The binding energy resolution was 0.1 eV. We used Shirley algorithm for background correction and chemically distinct species were resolved using a nonlinear least square fitting procedure. The core level binding energies were aligned with the carbon binding energy of 285 eV. Figure 2.5A shows the XPS spectra of Fe^{+3}. The deconvoluted peaks are shown in the inset of figure 2.5A. Here, a small peak (referred as pre-peak) at a relatively lower binding energy (around 706 eV) arises probably due to the lattice defects. It is known that for the nanoparticles, it is energetically unfavorable to afford defects in the core of the particles, however, nanoparticle's surfaces can have impurities leading to the generation of this pre-peak. We could also notice two most intense peaks at 711.7 and 723.8 eV which were assigned to the Fe^{+3} $2p_{3/2}$ and $2p_{1/2}$ states.[41] The expanded view in inset of figure 2.5A shows deconvoluted peak pattern of Fe^{3+} $2p_{3/2}$ multiplet which has a great importance due to its sensitivity towards the chemical changes in the neighborhood which reflects in the peak

shape and broadening. We could see that the peak assigned to $2p_{3/2}$ core levels is

unusually broad. Usually, the peak of high spin Fe^{+3} ions is broadened significantly compared to Fe (0 state) and low spin Fe^{+2} state. This broadening is explained by the electrostatic interaction and spin orbit coupling between the $2p$ core hole and unpaired $3d$ electrons of the iron ions and crystal field splitting of the $3d$ orbital into t_{2g} and e_g level.[42] Here, since each iron ion is surrounded by six oxygen ions in an octahedral environment so the oxygen ions create a weak field around the Fe^{3+} ions that makes the system

Figure 2.5: *(A) & (B) XPS spectra for Fe (2p) & Bi (4f) on BiFeO₃ nanoparticles (scatter curves) respectively. The lines represent the deconvoluted peaks. Inset of (A) shows the deconvoluted peaks of Fe (2p).*

high spin with unpaired $3d$ electrons. Another reason behind the observation of relative broadness of almost all the peaks can be due to the reduced coordination number of surface atoms due to the reduced particle size in our BFO nanoparticles. Due to the reduced coordination number, the electron density around the Fe^{3+} ions at the particle surface would be less so the shielding of the iron nucleus is decreased causing the electrons to be pulled closer to it. Such a decrease in the shielding value will require

higher energy to withdraw an electron from the *2p* shell which will result into the peak broadening. In our study, we also found a small peak at 715 eV which is again considered as a surface peak arising due to the decrease in coordination number of Fe^{+3} cations located at the surface. In addition to the broadening of the peak, a small peak was also observed at higher binding energy near 717 eV which is the satellite peak due to shake up process.[43] The observation of such a satellite peak is common in the high spin Fe^{+3} states and arises due to the shake up process in which during the ejection of the *2p* shell photoelectrons, small amount of kinetic energy of photoelectrons is lost thereby promoting the movement of the electrons from the *3d* orbital to the empty *4s* orbital. In figure 2.5 B, we have shown the high resolution core spectrum for Bi *4f*. The two strongest peaks at 158.0 and 164 eV correspond to Bi *4f7/2* and Bi *4f5/2* respectively.[44] The shoulder that appeared at the higher binding energy side corresponds to partially oxidized bismuth ions on the surface. We believed that this is the first detailed x-ray photoelectron spectroscopy study reported so far on the BFO system. This high resolution XPS study rules out any impurity of Fe^{2+} in our samples. Additionally, the ac conductivity values σ_{ac} (at 300K) on our BFO samples were almost three orders of magnitude lower ($\sim 10^{-8}$ Ω^{-1} cm^{-1}) than observed for micron sized polycrystalline samples which is attributed to the very high ionic purity as well as grain effects in our samples as any presence of Fe^{2+} will contribute to larger hopping conduction due electron exchange between Fe^{2+} and Fe^{3+} which is commonly seen in multivalent.[26]

2.4.3 Raman spectroscopy measurements:

Raman spectroscopy is an important tool and has been used by few groups to investigate BFO in single crystals,[3, 22, 45] polycrystalline[21, 23] and thin film[18] forms. The Raman spectra were recorded on a HR 800 Raman spectrophotometer (Jobin Yvon-Horiba, France) using monochromatic radiation emitted by a He-Ne laser (632.8 nm), operating at 20 mW. We observed quite sharp well resolved Raman peaks at 300 K (shown in figure 2.6) with all the 13 Raman modes ($4A_1+9E$) for the rhombohedral R3c structured $BiFeO_3$ nanoparticles. Kothari *et al.* reported all the 13 Raman modes in polycrystalline $BiFeO_3$ with grain size in microns with three strong A_1 peaks at 135, 167,

218 and weak peak at 430 cm^{-1}.[21] In our case, we found strong peaks at 139, 169, 425 and a weak peak situated at 216 cm^{-1}. We could observe all the 9 E Raman modes with strongest situated at 72 cm^{-1}. The peak situated at around 139 cm^{-1} is assigned to the Bi-O vibration modes which is responsible for the coupling between magnetic and electric parameter.[37]

Tables 2.1: *Comparison of the Raman mode positions (cm^{-1}) from our present study on BiFeO$_3$ nanoparticles (figure 2.6), with reported data on bulk polycrystalline BiFeO$_3$ by Kothari et al. and data on single crystalline BiFeO$_3$ by Fukumura et al.*

Raman modes	Our study	Kothari et al.[21]	Fukumura et al.[22]
A$_1$-1	139	135.15±1.38	147
A$_1$-2	169	167.08±0.38	176
A$_1$-3	216	218.11±1.38	227
A$_1$-4	425	430.95±16.69	490
E	260	255.38±0	265
E	276	283.0±0	279
E	348	351.55±8.66	351
E	321	321.47±3.76	375
E	467	467.6±2.46	437
E	529	526.22±2.57	473
E	598	598.84±1.99	525
E	72	71.39±0.11	77
E	98	98.36±3.11	136

The presence of all 13 modes is also clear from table 2.1 where we have compared the positions of the Raman modes seen by us with the earlier reported data on single crystal[22] and polycrystalline samples.[21] Recently, in a temperature dependent Raman studies on these BFO
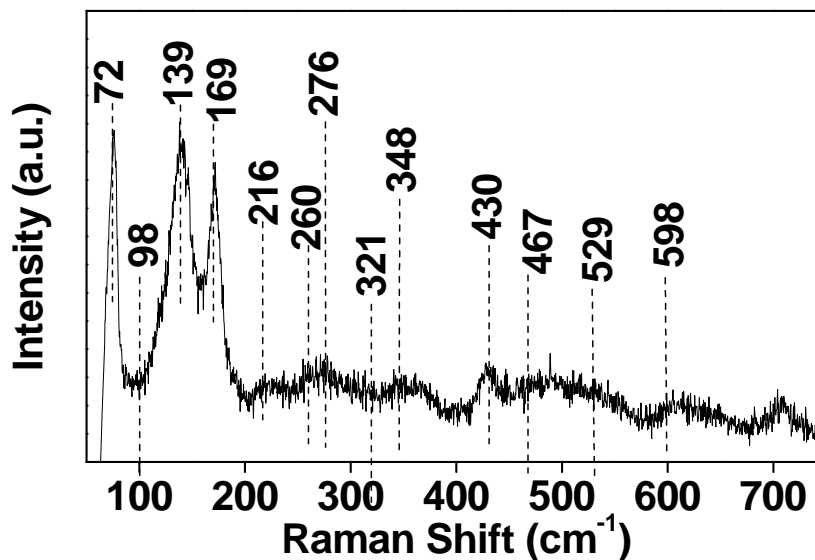
Figure 2.6: *Room temperature raman spectra of BiFeO₃ nanoparticles.*

nanoparticles (80-670 K), we saw the effect of reduced size on Raman spectra of where at low temperature, we observed two sets transitions in the lowest Raman E mode, associated with Bi-O bond motion at temperatures situated in the close proximity to spin reorientation transitions proving a direct indication of coupling between magnons and phonons. These transitions are shifted in temperature in comparison to the bulk single crystals indicating the size effect in BFO. We also observed that there was no change in lowest E mode Raman peak position around bulk Nèel temperature, suggesting the absence of antiferromagnetic ordering due to breaking of helical ordering of Fe^{3+}.[46]

2.5 Magnetic properties measurements:

We performed a detailed DC magnetic susceptibility vs. temperature measurements in field cooled (FC) and zero field cooled (ZFC) conditions as well as magnetic field vs. magnetization (M-H) hysteresis measurements on the BFO nanoparticles using a Physical Property Measurement System (PPMS) from Quantum Design Inc. San Diego, USA equipped with a 7 Tesla superconducting magnet. These measurements were done using a vibrating sample magnetometer attachment of PPMS.
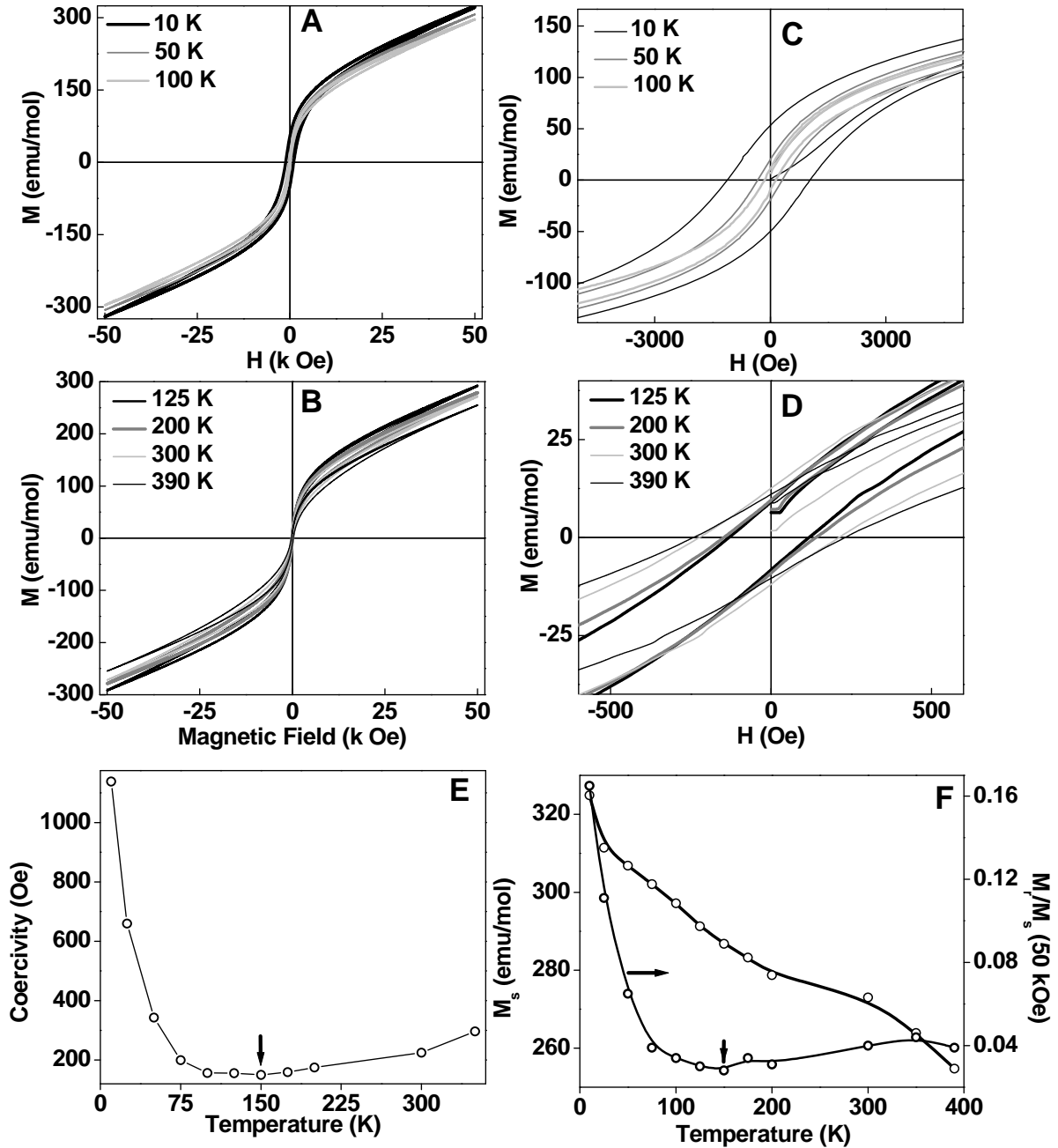
Figure 2.7: *(A, B) M-H loops taken at various temperatures (C,D) zoomed view of A, B respectively (E) variation of coercivity H_C with the measurement temperature (F) temperature dependence of $M_{S(50\,k\,Oe)}$ and $M_r/M_{S(50\,k\,Oe)}$ for BiFeO$_3$ nanoparticles.*

For this purpose, the BFO nanoparticles were packed nicely inside a plastic sample holder which fits into a brass sample holder provide by Quantum Design. The magnetic signal from the sample holder was negligible to affect our data accuracy. We collected M-H loops in a field sweep from -50 k Oe to 50 k Oe at a rate of 25 Oe/sec where data

was collected at every second at the vibrating frequency of 40 Hz. To map various transition regions, we collected the M-H loop of as-synthesized BFO nanoparticles at a range of temperatures. In figures 2.7 A & B, we have shown some representative M-H loops at various temperatures. Figures 2.7 C & D show corresponding zoom views to highlight the opening-up of the hysteresis loops. We can see a significant amount of nonlinearity in the M-H curves starting from 390 K which is accompanied with coercivity of 295 Oe. The coercivity value goes down to 225 Oe at 300 K. In contrast to earlier reports on the bulk polycrystalline and single crystal forms of BFO which showed linear M-H loop with absence of coercivity at room temperature, our results here indicated a clear nanosize effect.[21] As we mention earlier that the size of our BFO nanoparticles was less than size of the spiral ordering which would result in the breaking of the spiral ordering inducing a small ferromagnetism in the antiferromagnetic lattice. In figure 2.7 E, we have plotted a curve showing the coercivity values with temperature. It should be noted that the M-H loop mapping in such a way is not reported in literature for BFO nanoparticles and to the best of our knowledge, for the first time, we could detect a signature of the magnetic transition at around 150 K in the coercivity values which might be associated with the frustrated spins created by the breaking of spiral ordering. It is seen that from 350 K to 150 K there is a decrease in the coercivity value followed by a sharp increase below 150 K. At 300 K, the value of magnetization at 50 k Oe was nearly 7.2 emu/g, which corresponds to the particle size of 50-60 nm as per the magnetization vs. particle size data calculated by Park *et al*. which is in a good agreement with the particle size calculated by us from TEM image.[37] In figure 2.7 F, we have shown the magnetization at 50 k Oe and the $Mr/M_{S(50\ kOe)}$ vs temperature curve. Both the curves shows a series of inflection points indicating various transitions discussed here. To check the change in the magnetic properties for the larger particles, in figure 2.8, we have compared the M-H loops of BFO nanoparticles (~ 55 nm) and the 750°C calcined samples (~ 500 nm). As discussed above, the bulk polycrystalline (average size 500 nm) form of BFO showed linear M-H loop with absence of coercivity at room temperature and down till 10 K. This shows a remarkable change in the magnetic properties of BFO as a function of particle size.
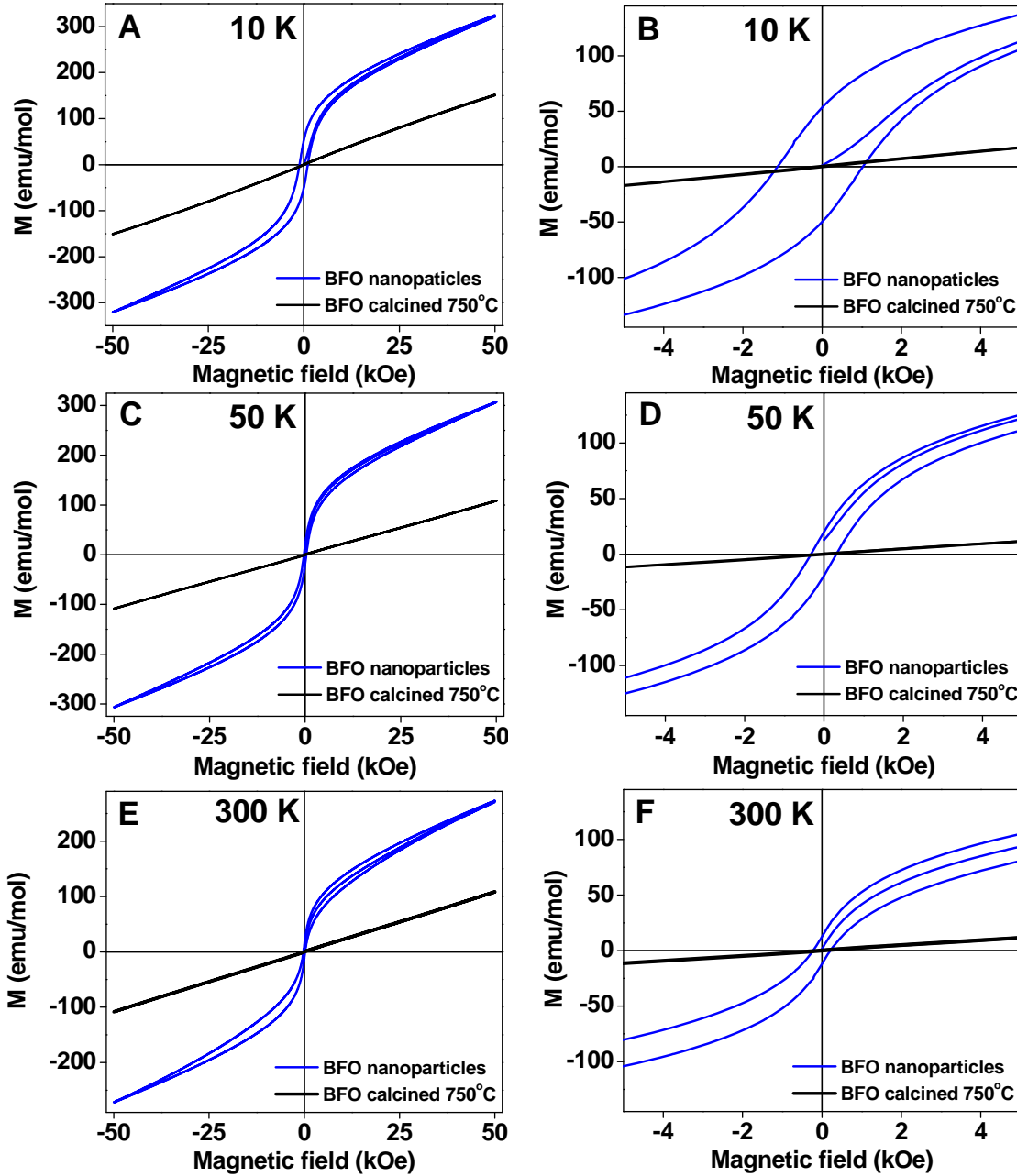
Figure 2.8: *(A, C, E) Comparison of M-H loops taken at 10, 50 and 300 K respectively for BFO nanoparticles and 750°C calcined sample. (D, E, F) Zoomed view of panels A, C and E respectively.*

In figure 2.9A, we have shown the DC magnetization vs. temperature curves for 200 Oe, 500 Oe and 1000 Oe external field in zero field cooled (ZFC) and field cooled modes (FC). For all these measurements, the cooling and heating rate was kept at 1.5 K

per minute and the data was collected at every second after averaging over 40 Hz. A large difference between ZFC-FC curves is observed which is due to the spin-glass type behavior[4] previously seen in bulk single crystals of $BiFeO_3$. However, in contrast to the earlier reports on bulk single crystals, the splitting of these two curves is more pronounced in our nanosized BFO particles and increases at higher field values. Such a deviation is obvious in nanoparticles of BFO because nanosize induces extra strain, coordination distortion and lattice disorder on the surface compared to bulk particles which result in a different frustrated spin structure and high magnitude of magnetic spins - strain interaction.
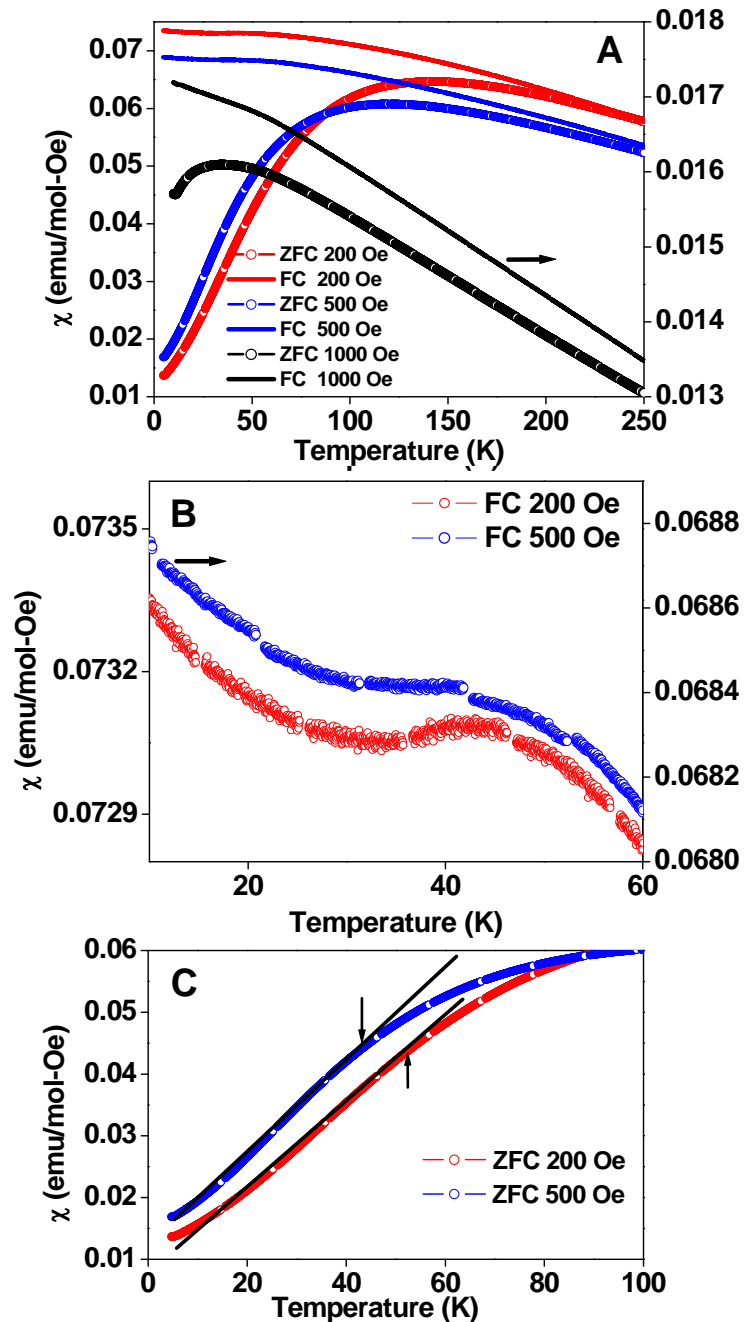
Figure 2.9: *(A) Zero field cooled (ZFC) & field cooled (FC) curves at 200 Oe, 500 Oe and 1000 Oe external field values. (B) field dependenc of spin glass transition (C) field dependence of spin glass transition shown in ZFC curve (line is shown just to indicate the transition point).*

The ZFC curves for all the magnetic field values showed a prominent and broad peak at lower temperatures. The peak temperature decreases with an increase in the applied magnetic field values. Surprisingly, we observed that this behaviour is unique to the nanosize effect of $BiFeO_3$ and absent in bulk single crystal and polycrystalline samples with much larger grain size. It is shown in Figure 2.10A on 750°C calcined sample that such broad peak (spin reorientation transition) is absent in size greater than the critical spiral ordering (62 nm). The origin of this transition (known as spin reorientation transition) is due to the orientation of Fe^{+3} spins which are generated by the breaking of antiferromagnetic spiral ordering and as the orientation of Fe^{+3} spins
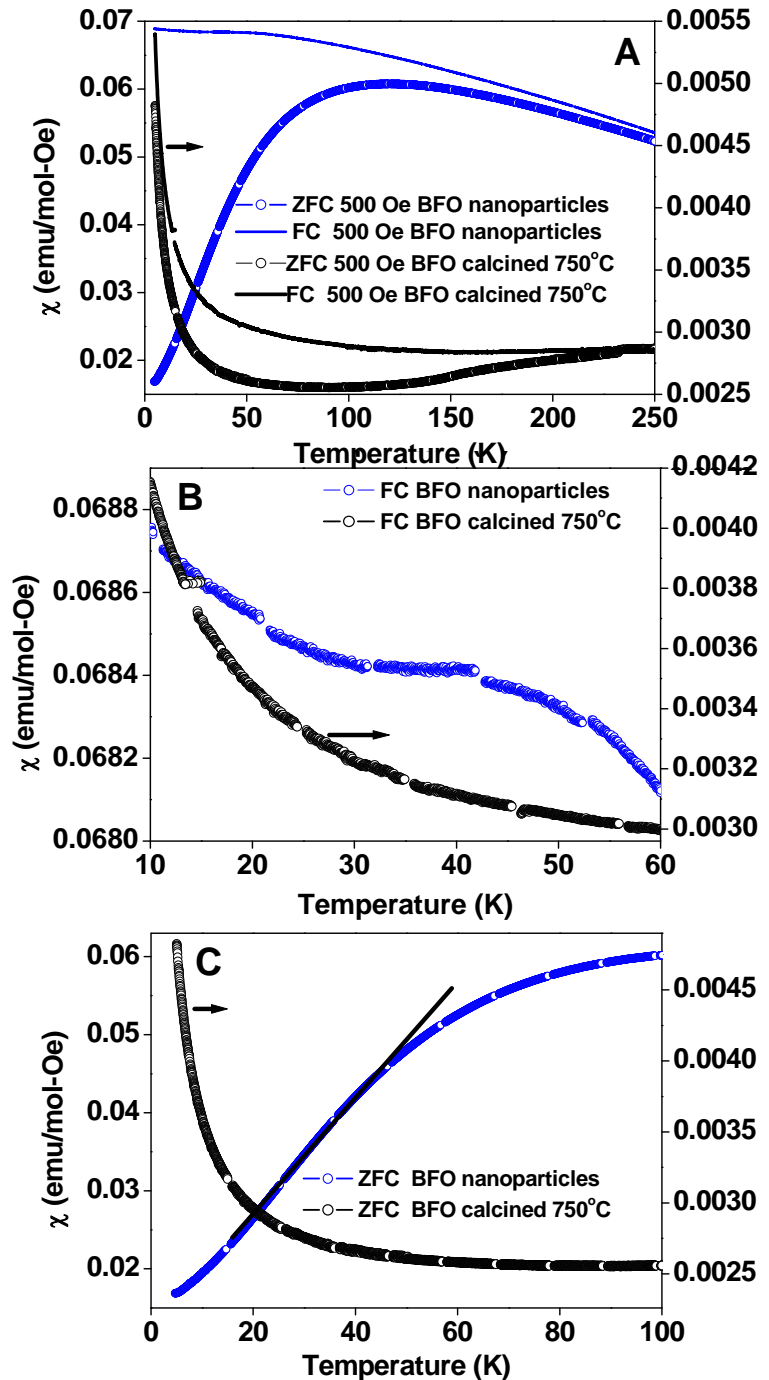
Figure 2.10: *(A) Zero field cooled (ZFC) & field cooled (FC) curves at 500 Oe external field values for both BFO nanoparticles and 750°C calcined samples. (B) spin glass transition in FC curve for BFO nanoparticles and absence in 750°C calcined samples (C) spin glass transition shown in ZFC curve for BFO nanoparticles and absence in 750°C calcined samples.*

are highly field dependent therefore we saw a field dependence in the peak temperature as the external magnetic field would change the orientation of Fe^{+3} spins towards the field direction. Due to this orientation there was an overall decrease in the magnetic susceptibility with an increase in the field and the transition temperature shifted towards lower temperature from 145 K to 110 K. This transition was also reported by Park *et al.* for BFO nanoparticles, however, the dependence of this transition on the applied magnetic field was not reported earlier.[37] In figures 2.9 B & C, we have shown the zoom view of the FC and ZFC curves for 200 Oe and 500 Oe field values respectively. Figure 2.9 B shows a broad and smooth hump in the FC curves for our BFO nanoparticles. For bulk BFO single crystals, this transition has been reported at 50 K as a very sharp cusp.[4] The transformation of a sharp cusp in bulk BFO to a broad, smooth hump clearly reflects the nanosize effect which was not observed previously in BFO nanoparticles. In figure 2.10 B, we have compared FC data of BFO nanoparticles and 750°C calcined BFO which shows clearly that no cusp is present around 50 K in 750°C calcined BFO particles. We believe that the Park *et al.* might have easily missed this transition in their nanosized BFO samples due to the quality of their experimental data where they took the susceptibility measurements at every 10 K temperate steps unlike in our study where the data is collected at every 0.2 K.[37] We also noticed that with the increase in the magnetic field from 200 Oe to 500 Oe, this transition is shifted from ~ 44 K to ~ 40 K (figure 2.9 B). We did not observe this transition at 1000 Oe field values which was large enough to smear-out this weak transition of spin-glass nature.[4] Moreover, a significant shift in this transition from 50 K (seen in bulk single crystal) to the range of 40-44 K is due to the reduced size effect. Surprisingly, in bulk polycrystalline BFO, this transition is not reported. The reasons for which are unknown and point of future study. The zero field cooled curves (200 Oe & 500 Oe) showed this transition as change in the inflection point as shown in figure 2.9 C. In figure 2.10, we have compared the ZFC-FC data of 55 nm particles with the 500 nm particles obtained after recalcination at 750°C for 6 h. A closer look at the ZFC and FC behavior shown in figures 10 B & C reveals remarkable changes in the properties of nanosized BFO in comparison to the bulk samples (calcined at 750°C).

2.6 Magnetoelectric coupling probed by Raman spectroscopy:

The Raman spectra were recorded on a HR 800 Raman spectrophotometer (Jobin Yvon- Horiba, France) using monochromatic radiation emitted by a He-Ne laser (632.8 nm), operating at 20 mW. Temperature dependent Raman spectra have been recorded using LINKAM THMS 600 heating/freezing stage connected to a TP 94 temperature programmer in a temperature range from 90 − 700 K. The Raman spectra recorded at 300 K showed quite sharp and well resolved Raman peaks with all 13 Raman modes $(4A_1+9E)$ for the rhombohedral *R3c* structured BFO nanoparticles in figure 2.6.[47] Kothari *et al.* reported all the 13 Raman modes in polycrystalline BFO with grain size in several microns with three strong

Figure 2.11: *Representative temperature dependent Raman spectra of BiFeO₃ nanoparticles reflecting two sets of spin-glass transitions.*

A_1 peaks at 135±1.38, 167±0.34, 218±0.45 and a weak peak at 430±16.69 cm^{-1}.[21] We could observe all the 9 E Raman modes with strongest peak situated at 74 cm^{-1} at 300 K which confirms the FE phase in BFO as it is associated with the motion of Bi-O bonds which controls the dielectric constant.[48] The modes at 74, 139, 430 cm^{-1} can be attributed to E modes and mode 175 cm^{-1} can be assigned to the A_1 mode. It is known both theoretically and experimentally that the FE ordering in BFO is governed by stereochemically active Bi^{3+} ions with *6s^2* lone pair which take part in relatively lower wavenumber Raman modes in BFO (< 167 cm^{-1}). In figure 2.11, we have plotted the wavenumber variation of three E modes (74, 139, 430 cm^{-1}) and one A_1 mode (175 cm^{-1})

peak position vs temperature curves. In figure 2.12A, the Raman E mode at 74 cm^{-1} showed sudden dips in the peak shift values at temperatures centered around ~ 113, 148, 203 and 253 K (within the error of ± 5 K) respectively. Among them, the observed transitions at ~148 K and 203 K are in the close proximity to the broad magnetic transition of spin reorientation nature.[1] In panels 2.12 B, C and D, we have also plotted
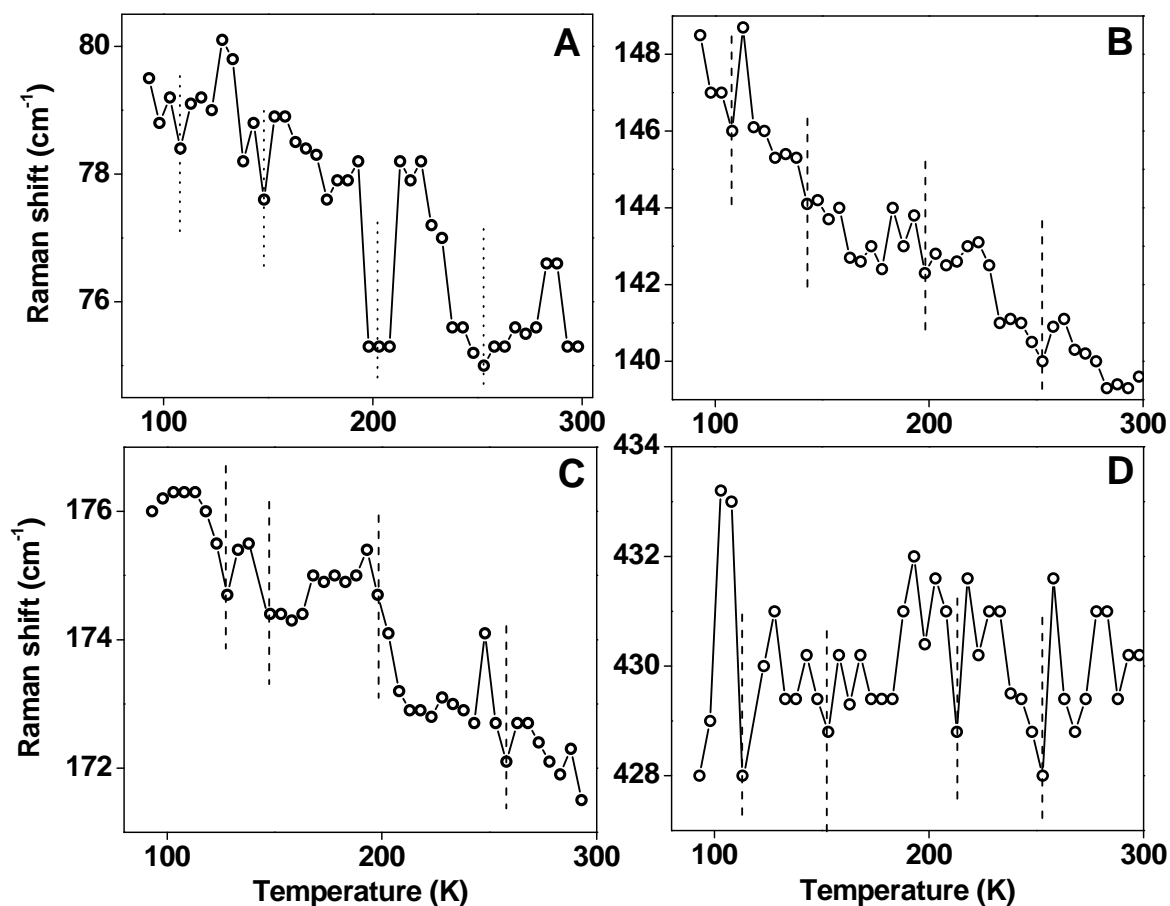
Figure 2.12: *The temperature dependent variation in the Raman peaks of three E mode (74, 139, 430 cm^{-1}) is shown in panels A, B & D and A$_1$ mode (175 cm^{-1}) is shown in panel C for BiFeO$_3$ nanoparticles.*

temperature dependence of Raman peaks of 139, 175, 430 cm^{-1} where some of these transition which were clearly noticed in figure 2.12 A, are either weak or absent. As we

mentioned earlier that the Raman peak situated at 74 cm^{-1}, is most intense and associated with motion of Bi-O bonds and therefore most sensitive to the magnetic transitions as well transitions of dielectric origin. The presence of these anomalies in the Raman shift for this peak (as well as in the magnetic measurements) indicates the coupling between the FE and the spin excitations associated with the magnetic cycloid at 148 K and 203 K in size ~ 55 nm. A recent temperature dependent Raman study on micron sized polycrystalline BiFeO$_3$ (grain size ~ 65.7 μm) showed a sudden drop in intensity of A$_1$ mode (177 cm^{-1}) at nearly 143 K and sudden increase at 193 K due to an additional magnetic transition representing a spin – reorientation.[23] The other two transitions at 113 and 253 K seen in figure 2.12 A could be related to the other set of magnons which were described in incommensurate model of de Sousa.[49] These transitions were reported by Scott et al. at 90 and 240 K on the Raman studies on BFO in bulk single crystal form.[2] These transitions were seen in all other E and A$_1$ modes Raman peaks with little shift in transition position (figure 2.12). We believe that this is the first ever reported indication of existence of the coupling between both the order parameters at nanosize by the coupling between the electric and spin reorientation transitions in nanosized BFO. The significant shift in the transition temperature from 90 K (single crystal) to 113 K (present data) can be attributed to the size dependent effect of BFO. However, till date, there is a lack of clear understanding in literature to explain the origin of these coupling even in the bulk phase. In figure 2.11, we have shown the representative complete Raman spectra in the range of spin reorientation transitions. It has been noted that there is a shift in the all four Raman modes around the spin reorientation temperature.

Next, we did temperature dependent Raman study on the same sample above room temperature (till ~ 670 K). From figure 2.13A, it is clear that the 74 cm^{-1} peak (lowest E mode) show remarkable shift in its position in the vicinity of reported Nèel temperature ~643 K identified with the step like anomaly. This marked anomaly was observed by us in other Raman bands too (figure 2.13B, C & D) though weaker in nature in comparison to 74 cm^{-1} mode. It is known that this magnetic transition in bulk BFO is not accompanied by the structural transition.[50] Earlier Raman studies on bulk BFO single crystals are also consistent with our observation on nanosized BFO where an strong phonon anomaly was observed for the first time around Nèel temperature in form of

similar step like feature.[50] Haumont et al suggested that multiferroicity of BFO may be the reason for the observation of this strong phononic anomaly.[50] High temperature dielectric studies on bulk polycrystalline BFO samples also report very weak anomaly near Néel transition.[51] Our observation clearly shows the presence of AFM ordering transition in our BFO with grain size less than the critical size of 62 nm.
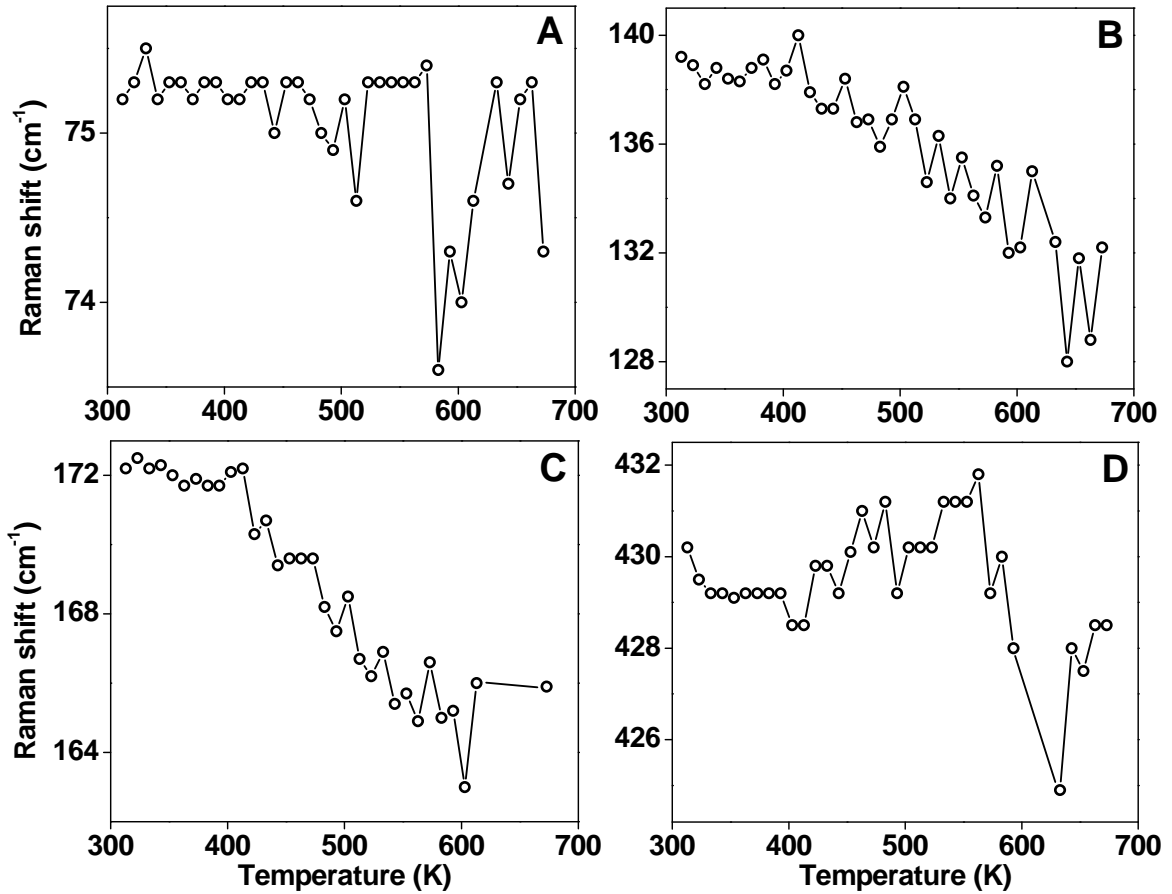
Figure 2.13: Step like anomalies around magnetic Néel transition is shown as the wavenumber variation for E modes (74, 139, 430 cm^{-1}) in panels A, C & D and for A mode (175 cm^{-1}) in panel C as a function of temperature for BiFeO$_3$ nanoparticles.

2.7 Thermal measurements:

To study the existence of FE transition in our BFO nanoparticles, in figure 2.14, we have shown the differential thermal analysis (DTA) results exhibiting the heat flow data in a broad temperature range obtained using SDT model Q600 from TA Instruments,

USA. The data was taken at a heating rate of 10°C/m under a nitrogen flow at 100ml/m. The heat-flow curve on our 55 nm BFO, shows no signature of anomaly in the vicinity of the reported Nèel temperature. However, we found two very sharp well defined peaks situated at 1094 and 1223 K respectively. It is reported that at 1100 K, BFO undergoes a structural transition from rhombohedral to orthorhombic or monoclinic
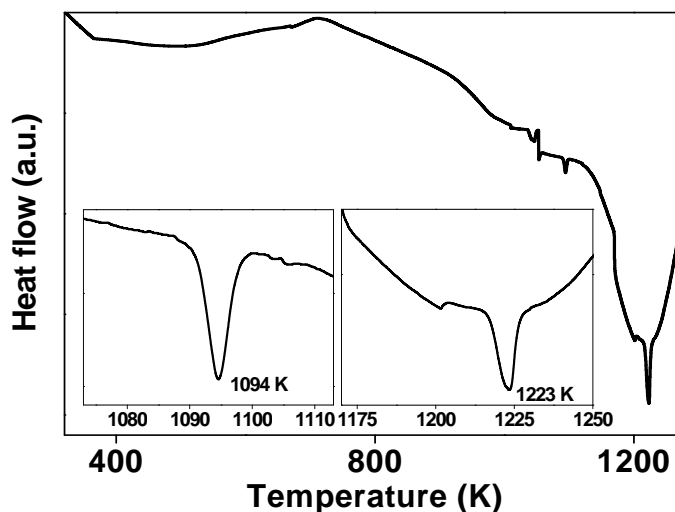
Figure 2.14: Heat flow measurements on 55 nm BiFeO₃ nanoparticles. The inset shows the two endothermic transitions.

phase and at around 1200 K; it transforms into the cubic phase.[13] As we indicated earlier, it is not clear till date, out of these two transitions, which one is the ferroelectric-paraelectric transition. Heating beyond this temperature range leads to the decomposition of BFO. Unfortunately, we could not extend our Raman measurements on BFO nanoparticles around the FE Curie transition due to experimental limitation of our instrument where BFO is supposed to show a complete loss of Raman spectrum above Curie temperature.[50]

2.8 Magnetoelectric coupling probed by dielectric spectroscopy:

To probe the dielectric response in the proximity of the magnetic transitions in BFO at low temperatures, we used a Novocontrol Beta NB Impedance Analyzer with a home-built sample holder to couple with a Janis Inc. helium closed cycle refrigerator. The dielectric response was mapped in a frequency range from 1 to 1 x 10⁶ Hz at 1 volt (rms) and in a temperature range from 20-325 K at a close interval of 1 K (± 0.2 K). A compressed circular pellet, with 13 mm diameter, pelletized by applying 5-6 ton pressure was kept in the customized sample holder to form circular parallel plate capacitor

geometry. In the figure 2.15, the frequency dependent ε' and *tan* δ are plotted at two different representative temperature values.

Overall, the values of ε' at room temperature ($\sim$ 28) are not very much different from reported for ceramic samples with crystallite size in microns[13, 29] but smaller compared to the reported values on bulk single crystals[13] and much smaller in comparison to the
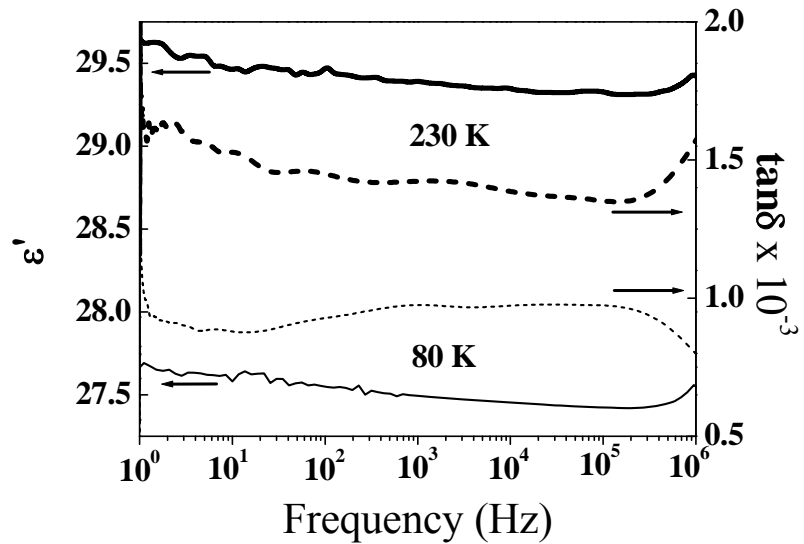
Figure 2.15: *Frequency dependence of real part of permittivity value (ε') and loss tangent (tanδ) for BiFeO₃ nanoparticles for two representative temperature values.*

typical perovskite ferroelectrics such as BaTiO$_3$, and PZT etc.[1] Catalan et al argued that smaller values of dielectric constant in BFO in comparison to the conventional perovskite FE materials might be due to the fact that in BFO the polarization comes from the A site (Bi atoms). On the other hand, in BaTiO$_3$, the polarization is attributed to the B sites (Ti atoms).[1] For most FEs, the domain size varies following the relation: Domain Size α (Particle size)^{m}.[52] It is considered that the decrease in polarization (or dielectric constant) with decreasing particle size is not an intrinsic size effect due to depolarization fields. This decrease might be due to surface effects such as surface tension, strain and increase in porosity. Intrinsic size effects occur below $\sim$15 nm which is material specific and nothing to do with depolarizing field.[53] Recently, we reported a significant decrease in the dielectric constant of 6-8 nm tetragonal phase of BaTiO$_3$ and showed that FE phase does exist in this size range even though the dielectric constant values are quite low in comparison to bulk values.[36] The dielectric constant of nanosized materials might also be slightly underestimated in our studies due to experimental problems such compaction not

being closed to 100% of theoretical density and the contact issues. It should be noted here that several studies on bulk polycrystalline BFO have reported unreasonably high ε' values (as high as 10^4 for 100 Hz and 300 K).[25, 51] Clearly, these values are not intrinsic and probably the effect of presence of oxygen deficiency and Fe^{2+} etc which is a common problem and can be easily noticed from unusually large loss tangent values (sometimes close to 1) due to ionic impurities.[54] These samples with unusually high dielectric constant might also show high degree of polarizability but as a word of caution- high polarization does not always indicate high ferroelectricity or multiferroicity.[55] Similarly, giant dielectric constant values were reported in CuO which might also have originated from the presence of high level of Cu^{3+} impurities.[56] The high level of ionic purity is reflected in the tan δ (between 0.5 x 10^{-3} to 2 x 10^{-3}) values of our samples which are almost 3 orders of magnitude smaller than that for bulk BFO. Due to higher sensitivity of our instrument (tan δ < 10^{-4}) coupled with unique design of our in-house developed sample holder for low temperature measurements, it was possible for us to measure these values accurately. Generally, BFO prepared by solid solution or ceramic methods show much higher dielectric loss due to higher conductivity which causes leakage current. As we discussed earlier, the higher dielectric loss is inherently due to ionic impurities (Fe^{2+}), oxygen nonstoichiometry and lattice defects which is unavoidable in bulk ceramic synthesis. Higher dielectric loss leads to lower ferroelectric polarization in pure material such as spontaneous polarization, remnant polarization and coercive field. Therefore, even though dielectric constant values of our nanocrystalline BFO are in the same range as that of bulk ceramic samples (as discussed earlier) but the surprisingly observation of nearly 10^{-2} to 10^{-3} times lower loss tangent values in our samples are remarkable improvement and shows much lower level of ionic impurity.[13, 27, 29]

In figure 2.15, the ε' value increases slightly as the frequency decreases. We observed that frequency dependence of ε' and tan δ for our samples is quite weak without any resonance peak in the scanned frequency range. The slight increase in the value of ε' at lower frequency is due to the presence of different type of polarization factors such as interfacial, dipolar, ionic, atomic and electronic which becomes significant at low frequencies.[57] Here, the response of grains and their boundaries (interface) at different frequencies plays a crucial role where the contribution from core of nanoparticles will be

significant at higher frequencies and the surface of the particles and their connectivity with neighboring particles will contribute at relatively lower frequency regions.[57] However, in figure 2.15, the fact that the frequency response of ε′ and *tan* δ at different temperature doesn't show any sudden peak or any other feature (often seen in bulk relaxor FE samples) till 1 MHz makes the contributions of particle and its boundary indistinguishable in this range. Higher than 1 MHz dielectric spectroscopy results might show some resonance peaks which is beyond the limit of our instrument at present. It should be noted that several of the earlier dielectric studies done on ceramic samples or thin films showed a strong unusual frequency dependence and Maxwell-Wagner (MW) type of contributions to the dielectric constants due to reasonably high conductivities.[58] In contrast, our results do not show any strong frequency dependence in dielectric constant and loss tangent. In the bulk BFO, the dispersion of dielectric constant and loss tangent with frequency is reported to be high because at lower frequency in the bulk ceramics, oxygen and bismuth vacancy in the lattice mainly contributes in the dielectric constant and loss tangent value.[59] But as we pointed out earlier our wet chemically synthesized   nanocrystalline BFO is likely to have quite less lattice impurities and dislocations, so such high dispersion were not observed in the dielectric constant and loss tangent with frequency.[47]

In the figure 2.16 A, we have shown the variation of ε′ and tan δ with temperature for few representative frequency values here we observed that at high temperatures (> 250 K) there is a significant increase in ε' values. At higher temperatures, the charge carriers are free to move through the lattice causing enhanced polarization which results in high dielectric value. Similar to the anomalies seen in the Raman spectra discussed above, the zoom view of ε′ -T curve (figure 2.16 B) shows four weak anomalies situated at around 85, 168, 205 and 230 K. In bulk single crystals and ceramic BFO, these anomalies were reported which were extremely weak in nature.[13] Redfern et al argued that in BFO since these anomalies are far weaker than those associated with any FE transitions, therefore, they might arise due to the weak coupling with magnetic order parameter.[13] In figure 2.16B, among the four transitions , the observed transitions at ~168 K and 205 K are in close proximity to the broad magnetic transition of spin reorientation nature reported by us on the same material.[47] The observation of transitions shows that

the coupling between FE and cycloid spins exists for particles around 55 nm in size. The other two transitions observed by us (figure 2.16 B) at ~ 85 and 230 K could be related to the other set of spin reorientation transition which was reported by Scott et al. at 90 and 240 K using the Raman studies on bulk single crystal BFO.[2, 13] We believe that this is the first ever reported indication of existence of the coupling between both the order parameters at nano size by the coupling between the electric and spin reorientation
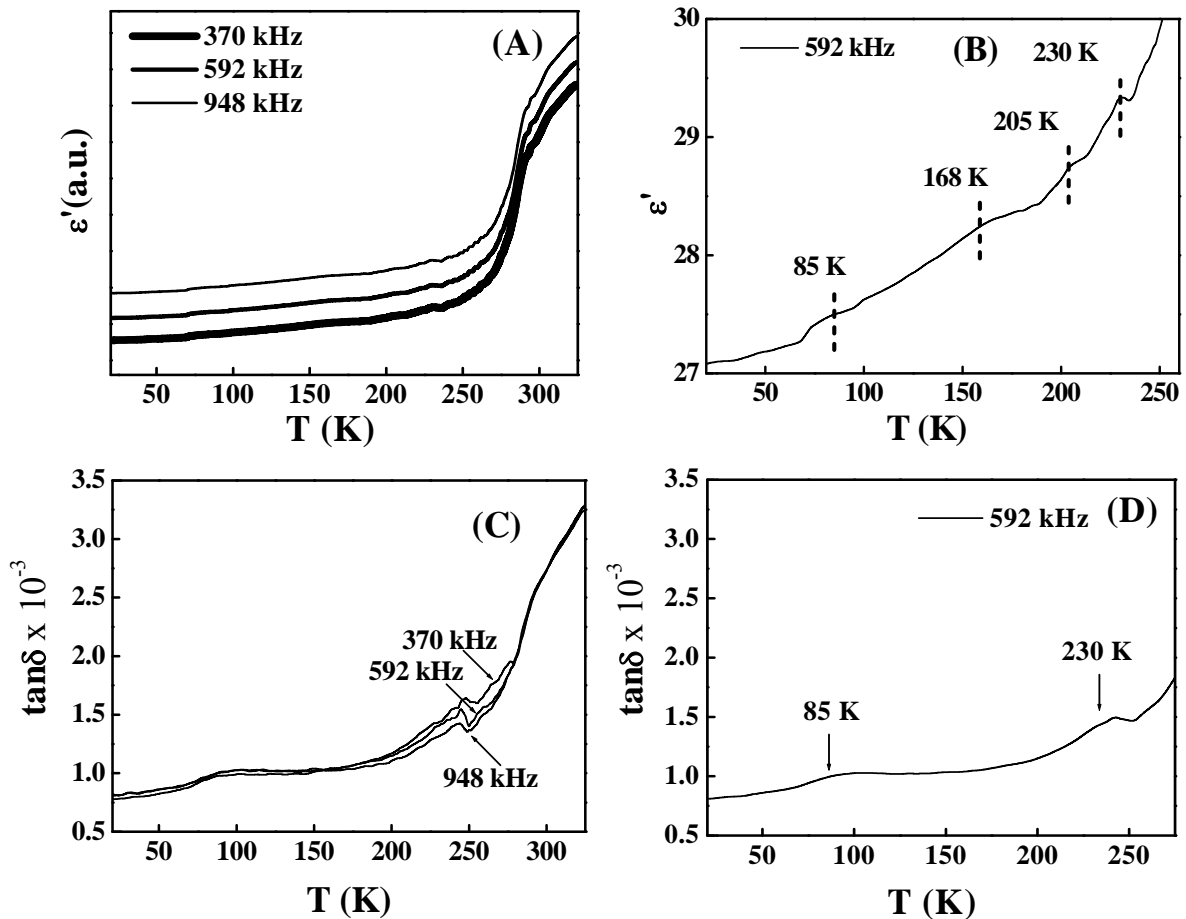
Figure 2.16: *(A & B) Temperature dependent variation of real part of permitivity (ε') and (C&D) loss factor (tan δ) of BiFeO₃ nanoparticles .*

transition in nanosize BFO. It is important to note that out of these four anomalies, two anomalies (90 K and 230 K) were also noticed by us in the tan *δ* - T curves (figure 2.16C). Surprisingly, earlier studies on BFO ceramics failed to see any signature of these spin reorientation anomalies in dielectric loss tangent curves.[13] We believe earlier studies

might have easily missed these transitions due to their subtleness. However, it worth pointing out that in our dielectric measurements did not show anomaly associated with spin-glass transition in the range 40-45 K seen by us in magnetic measurements on 55 nm particles. This transition was reported by Scott's group in ε-T measurements on single crystal (55 K) and in ceramic samples (50K).[13] However, the observation of spin glass transition in BFO is full of mysteries and still not resolved as one recent dielectric measurements as well as ac and dc magnetization study done on BFO single crystal did not find anomaly from 2-120 K.[58]

2.9 Electrical conductivity measurements:

Ionic impurity of mixed valent nature leads to higher dielectric constant (sometime colossal in nature) which may not be always related to the desired ferroelectric polarization.[55] Dielectric and polarization probing may be misleading when ac conductivity and polarizability do coexist in the same material.[55] So it is always important to always check the conductivity values carefully before reaching to any
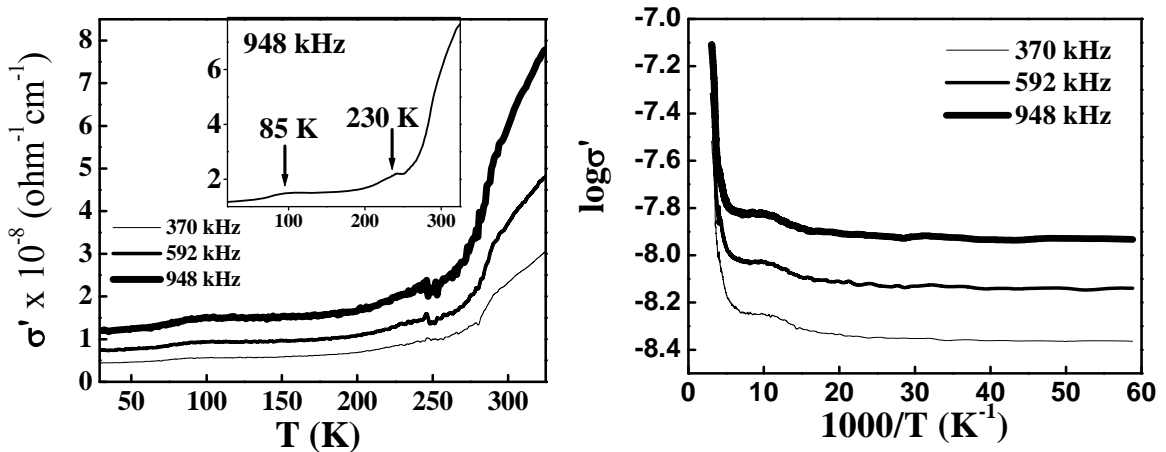
Figure 2.17: *(A)Temperature dependent variation of real part of conductivity (σ') of BiFeO₃ nanoparticles at frequency 370,592, 948 kHz. The inset shows the zoom view of the σ' –T curve at 948 kHz frequency. (B) log σ' vs. 1000/T plot at frequency 370, 592, 948 kHz .*

conclusion about the ferroelectric polarization. The ac conductivity σ_{ac} was calculated by the following relation: $\sigma_{ac}=2\pi f\varepsilon_0|\varepsilon|\tan\delta$. The variation of σ_{ac} with temperature is shown in the figure 2.17 for 948 kHz frequency. For all the frequency values, the σ increases

with temperature. The σ (300K) for our BFO samples was almost three orders of magnitude lower (3 - 6 x 10^{-8} Ω^{-1} cm^{-1}) than observed for micron sized polycrystalline samples which is attributed to the very high ionic purity as well as grain effects in our samples.[26] A slight non-stoichiometric composition of oxygen in BFO creates Fe^{+2} within the iron sublattice. The coexistence of Fe^{+2} and Fe^{+3} in the octahedral sites in the BFO lattice favors the electron hopping conduction from Fe^{+2} to Fe^{+3} via oxygen ions. [25] Much smaller ac conductivity is quite desirable in BFO and its presence in our samples indicates less probability of hopping conduction between Fe^{2+} and Fe^{3+}. The concentration of Fe^{+2} in the lattice is very sensitive to calcinations temperature and it increases with temperature due to increased loss of oxygen. But in our case, we could rule out this possibility due to relatively low annealing temperature. Our high resolution x-ray photoelectron spectroscopy study also did not show any traces of Fe^{+2} impurities.[47] We believe that in BFO nanoparticles, it may the breaking of the spiral ordering which results high value of conductivity for given frequency. When the crystal becomes smaller, the rapid increase of domain wall energy makes the domain configuration unfavorable, thereby promoting single-domain structure in smaller crystals which results more domains and also more domain walls, per unit volume than the bulk. These domain walls will become more technologically important as the particle goes to nanoscale. J. Seidel et al have proved that enhanced conductivity in BFO nanomaterials correlates with structurally driven change in electrostatic potential and local electronic structure which results in the decrease in the band gap at the domain wall.[60] As the frequency increases conductivity value increases for a given temperature (not shown here). In the top panel of figure 2.17 we have observed two peaks around 90 and 230 K which correspond to the reorientation transition in $BiFeO_3$ nano materials. During the reorientation transition, iron spins moves from one crystallographic axis to another which is magnetic origin but again favor the electron-hopping conduction mechanism.

In the lower panel of figure 2.17, we have shown log σ vs. 1000/T for various frequencies. The activation energy E_a varies by orders of magnitude in different temperature regions. At room temperature E_a is around $\sim$ .03 eV. For micron sized BFO particles, the E_a was found to be 0.126 eV at around 290°C and increases 10 times to 1.26 eV as temperature goes high.[24] There are no reports of σ_{ac} below room temperature for

BFO in any form. In our case, the lower values of activation energy and its strong temperature dependence seems to be due to the reduced particle size. The grain boundary does not contribute towards the temperature dependence of activation energy and it is purely due to the conduction mechanism inside the particle.

2.10 Conclusion:

$BiFeO_3$ nanoparticles with average size 50-60 nm were synthesized using modified hydrothermal method. The phase was confirmed using x-ray diffraction study. Pawley refined lattice parameters were a= 5.574±0.001, b=5.574±0.001, c= 13.850±0.002Å with excellent Rwp value of 4.94%. High resolution TEM showed that the particles were of excellent crystallinity. Collectively, our studies on the magnetization measurements indicated new information on this material in form of presence of spin glass transition at lower temperatures and its deviation from the bulk transition temperature. Strong bifurcation in the field cooled and zero field cooled curves was quite similar to bulk single crystals but different then micron sized polycrystalline materials. The origin of these transitions (both in bulk and nanophase) needs to be further studies especially the origin of transition situated between 40-50 K. Temperature dependent Raman study show the existence of two pairs of transitions as dips in the Raman shift vs temperature at three E mode (74, 139, 430 cm^{-1}) and one A_1 modes (175 cm^{-1}) in the close proximity of the spin reorientation transition. These transitions are more pronounced in the lowest E mode (74 cm^{-1}) which has a polar character and controls the dielectric constant. This indicates the coupling between the ferroelectric and spin excitations associated with the magnetic cycloid. These two sets of anomalies were also observed in ε' -T curve with slight shifting in temperature. Out of these four anomalies two anomalies at 90 and 230 K were also observed in our loss tangent and real part of conductivity data. High temperature Raman spectra show remarkable shift in Raman mode for three E modes and A_1 mode around Nèel temperature. Thermal studies did not show any endo/exothermic peak around Néel transition but showed both the ferroelectric-paraelectric transitions. The conductivity of BFO samples at 300K was almost three orders of magnitude lower (3 - 6 x 10^{-8} Ω^{-1} cm^{-1}) than observed for micron sized polycrystalline samples which is attributed to the very high ionic purity as well as grain

effects in our samples. It was further confirmed by the tan δ value which is 10^{-2} to 10^{-3} times lower than the polycrystalline samples. In contrast to bulk BFO which shows strong frequency dependence in ε' and tan δ value, nanocrystalline BFO don't show the relaxation behavior in the frequency range $(1\text{-}10^6$ Hz$)$.

2.11 References:

1. Catalan, G.; Scott, J. F., Physics and Applications of Bismuth Ferrite. *Advanced Materials* **2009,** 21, (24), 2463-2485.

2. Scott, J. F.; Singh, M. K.; Katiyar, R. S., Critical phenomena at the 140 and 200 K magnetic phase transitions in $BiFeO_3$. *Journal of Physics-Condensed Matter* **2008,** 20, (32).

3. Singh, M. K.; Katiyar, R. S.; Scott, J. F., New magnetic phase transitions in $BiFeO_3$. *Journal of Physics-Condensed Matter* **2008,** 20, (25).

4. Singh, M. K.; Prellier, W.; Singh, M. P.; Katiyar, R. S.; Scott, J. F., Spin-glass transition in single-crystal $BiFeO_3$. *Physical Review B* **2008,** 77, (14) 144403.

5. Wang, J.; Neaton, J. B.; Zheng, H.; Nagarajan, V.; Ogale, S. B.; Liu, B.; Viehland, D.; Vaithyanathan, V.; Schlom, D. G.; Waghmare, U. V.; Spaldin, N. A.; Rabe, K. M.; Wuttig, M.; Ramesh, R., Epitaxial $BiFeO_3$ multiferroic thin film heterostructures. *Science* **2003,** 299, (5613), 1719-1722.

6. Chu, Y. H.; Martin, L. W.; Holcomb, M. B.; Ramesh, R., Controlling magnetism with multiferroics. *Materials Today* **2007,** 10, (10), 16-23.

7. Zhao, T.; Scholl, A.; Zavaliche, F.; Lee, K.; Barry, M.; Doran, A.; Cruz, M. P.; Chu, Y. H.; Ederer, C.; Spaldin, N. A.; Das, R. R.; Kim, D. M.; Baek, S. H.; Eom, C. B.; Ramesh, R., Electrical control of antiferromagnetic domains in multiferroic $BiFeO_3$ films at room temperature. *Nature Materials* **2006,** 5, (10), 823-829.

8. Kubel, F.; Schmid, H., Structure of a ferroelectric and ferroelastic monodomain crystal of the perovskite $BiFeO_3$. *Acta Crystallographica Section B-Structural Science* **1990,** 46, 698-702.

9. Palkar, V. R.; Kundaliya, D. C.; Malik, S. K., Effect of Mn substitution on magnetoelectric properties of bismuth ferrite system. *Journal of Applied Physics* **2003,** 93, (7), 4337-4339.

10. Jun, Y. K.; Moon, W. T.; Chang, C. M.; Kim, H. S.; Ryu, H. S.; Kim, J. W.; Kim, K. H.; Hong, S. H., Effects of Nb-doping on electric and magnetic properties in multi-ferroic $BiFeO_3$ ceramics. *Solid State Communications* **2005,** 135, (1-2), 133-137.

11.   Selbach, S. M.; Tybell, T.; Einarsrud, M. A.; Grande, T., The Ferroic Phase Transitions of BiFeO$_3$. *Advanced Materials* **2008,** 20, (19), 3692

12.   Fischer, P.; Polomska, M.; Sosnowska, I.; Szymanski, M., Temperature-dependence of the crystal and magnetic-structure of BiFeO$_3$. *Journal of Physics C-Solid State Physics* **1980,** 13, (10), 1931-1940.

13.   Redfern, S. A. T.; Wang, C.; Hong, J. W.; Catalan, G.; Scott, J. F. In Elastic and electrical anomalies at low-temperature phase transitions in BiFeO$_3$, 15th International Winterschool on New Developments in Solid State Physics, Bad Hofgastein, Germany, Feb 18-22, 2008; Bad Hofgastein, Germany, 2008.

14.   Sosnowska, I.; Zvezdin, A. K., Origin of the long- period magnetic ordering in BiFeO$_3$. *Journal of Magnetism and Magnetic Materials* **1995,** 140, 167-168.

15.   Mazumder, R.; Devi, P. S.; Bhattacharya, D.; Choudhury, P.; Sen, A.; Raja, M., Ferromagnetism in nanoscale BiFeO$_3$. *Applied Physics Letters* **2007,** 91, (6).

16.   Litvinchuk, A. P.; Iliev, M. N.; Popov, V. N.; Gospodinov, M. M., Raman and infrared-active phonons in hexagonal HoMnO$_3$ single crystals: magnetic ordering effects. *Journal of Physics-Condensed Matter* **2004,** 16, (6), 809-819.

17.   Souchkov, A. B.; Simpson, J. R.; Quijada, M.; Ishibashi, H.; Hur, N.; Ahn, J. S.; Cheong, S. W.; Millis, A. J.; Drew, H. D., Exchange interaction effects on the optical properties of LuMnO$_3$. *Physical Review Letter* **2003,** 91, (2), 027203.

18.   Singh, M. K.; Ryu, S.; Jang, H. M., Polarized Raman scattering of multiferroic BiFeO$_3$ thin films with pseudo-tetragonal symmetry. *Physical Review B* **2005,** 72,132101

19.   Singh, M. K.; Jang, H. M.; Ryu, S.; Jo, M. H., Polarized Raman scattering of multiferroic BiFeO$_3$ epitaxial films with rhombohedral R3c symmetry. *Applied Physics Letters* **2006,** 88, (4).

20.   Haumont, R.; Kreisel, J.; Bouvier, P.; Hippert, F., Phonon anomalies and the ferroelectric phase transition in multiferroic BiFeO$_3$. *Physical Review B* **2006,** 73, (13), 132101.

21.   Kothari, D.; Reddy, V. R.; Sathe, V. G.; Gupta, A.; Banerjee, A.; Awasthi, A. M., Raman scattering study of polycrystalline magnetoelectric BiFeO$_3$. *Journal of Magnetism and Magnetic Materials* **2008,** 320, (3-4), 548-552.

22.   Fukumura, H.; Harima, H.; Kisoda, K.; Tamada, M.; Noguchi, Y.; Miyayama, M., Raman scattering study of multiferroic $BiFeO_3$ single crystal. *Journal of Magnetism and Magnetic Materials* **2007,** 310 (2), 367-369.

23.   Rout, D.; Moon, K. S.; Kang, S. J. L., Temperature-dependent Raman scattering studies of polycrystalline $BiFeO_3$ bulk ceramics. *Journal of Raman Spectroscopy* **2009,** 40, (6), 618-626.

24.   Jhih-Cyun, C.; Jenn-Ming, W., Dielectric properties and ac conductivities of dense single-phased $BiFeO_3$ ceramics. *Applied Physics Letters* **2007,** 91, (18), 182903.

25.   Sitchai, H.; Prasit, T.; Teerapon, Y.; Rattikorn, Y.; Santi, M., Dielectric relaxations and dielectric response in multiferroic $BiFeO_3$ ceramics. *Applied Physics Letters* **2009,** 94, (6), 062904.

26.   Jun, Y.-K.; Hong, S.-H., Dielectric and magnetic properties in Co- and Nb-substituted $BiFeO_3$ ceramics. *Solid State Communications* **2007,** 144, (7-8), 329-333.

27.   Yun, K. Y.; Noda, M.; Okuyama, M.; Saeki, H.; Tabata, H.; Saito, K., Structural and multiferroic properties of $BiFeO_3$ thin films at room temperature. *Journal of Applied Physics* **2004,** 96, (6), 3399-3403.

28.   Yuan, G. L.; Or, S. W.; Wang, Y. P.; Liu, Z. G.; Liu, J. M., Preparation and multi-properties of insulated single-phase $BiFeO_3$ ceramics. *Solid State Communications* **2006,** 138, 76-81.

29.   Pradhan, A. K.; Kai, Z.; Hunter, D.; Dadson, J. B.; Loiutts, G. B.; Bhattacharya, P.; Katiyar, R.; Jun, Z.; Sellmyer, D. J.; Roy, U. N.; Cui, Y.; Burger, A., Magnetic and electrical properties of single-phase multiferroic $BiFeO_3$. *Journal of Applied Physics* **2005,** 97, (9), 093903.

30.   Teague, J. R.; Gerson, R.; James, W. J., Dielectric hysteresis in single crystal $BiFeO_3$. *Solid State Communications* **1970,** 8, (13), 1073-1074.

31.   Palkar, V. R.; John, J.; Pinto, R., Observation of saturated polarization and dielectric anomaly in magnetoelectric $BiFeO_3$ thin films. *Applied Physics Letters* **2002,** 80, (9), 1628-1630.

32.   Vijayanand, S.; Potdar, H. S.; Joy, P. A., Origin of high room temperature ferromagnetic moment of nanocrystalline multiferroic BiFeO$_3$ *Applied Physics Letters* **2009,** 94, 182507.

33.   Chen, J.; Xing, X. R.; Watson, A.; Wang, W.; Yu, R. B.; Deng, J. X.; Yan, L.; Sun, C.; Chen, X. B., Rapid synthesis of multiferroic BiFeO$_3$ single-crystalline nanostructures. *Chemistry of Materials* **2007,** 19, (15), 3598-3600.

34.   Poddar, P.; Fried, T.; Markovich, G., First-order metal-insulator transition and spin-polarized tunneling in Fe$_3$O$_4$ nanocrystals. *Physical Review B* **2002,** 65, (17).

35.   Poddar, P.; Fried, T.; Markovich, G.; Sharoni, A.; Katz, D.; Wizansky, T.; Millo, O., Manifestation of the Verwey transition in the tunneling spectra of magnetite nanocrystals. *Europhysics Letters* **2003,** 64, (1), 98-103.

36.   Bansal, V.; Poddar, P.; Ahmad, A.; Sastry, M., Room-temperature biosynthesis of ferroelectric barium titanate nanoparticles. *Journal of the American Chemical Society* **2006,** 128, (36), 11958-11963.

37.   Park, T. J.; Papaefthymiou, G. C.; Viescas, A. J.; Moodenbaugh, A. R.; Wong, S. S., Size-dependent magnetic properties of single-crystalline multiferroic BiFeO$_3$ nanoparticles. *Nano Letters* **2007,** 7, 766-772.

38.   Selbach, S. M.; Tybell, T.; Einarsrud, M. A.; Grande, T., Size-dependent properties of multiferroic BiFeO$_3$ nanoparticles. *Chemistry of Materials* **2007,** 19, (26), 6478-6484.

39.   Jaiswal, A.; Das, R.; Vivekanand, K.; Abraham, P. M.; Adyanthaya, S.; Poddar, P., Magnetic and dielectric properties and Raman spectroscopy of GdCrO$_3$ nanoparticles, *J. Appl. Phys.* **2010,** 107, 013912 .

40.   He, Y. P.; Miao, Y. M.; Li, C. R.; Wang, S. Q.; Cao, L.; Xie, S. S.; Yang, G. Z.; Zou, B. S.; Burda, C., Size and structure effect on optical transitions of iron oxide nanocrystals. *Physical Review B* **2005,** 71, (12), 125411.

41.   Grosvenor, A. P.; Kobe, B. A.; Biesinger, M. C.; McIntyre, N. S., Investigation of multiplet splitting of Fe 2p XPS spectra and bonding in iron compounds. *Surface and Interface Analysis* **2004,** 36, (12), 1564-1574.

42.   Gupta, R. P.; Sen, S. K., Calculation of multiplet structure of core p-vacancy levels. *Physical Review B* **1974,** 10, (1), 71.

43. Yin, L.; Adler, I.; Tsang, T.; Matienzo, L. J.; Grim, S. O., Paramagnetism and shake-up satellites in X-ray photoelectron- spectra. *Chemical Physics Letters* **1974,** 24, (1), 81-84.

44. Yang, X. H.; Wang, X.; Zhang, Z., Synthesis and optical properties of single-crystalline bismuth selenide nanorods via a convenient route. *Journal of Crystal Growth* **2005,** 276, (3-4), 566-570.

45. Fukumura, H.; Harima, H.; Kisoda, K.; Tamada, M.; Noguchi, Y.; Miyayama, M. In Raman scattering study of multiferroic $BiFeO_3$ single crystal, 17th International Conference on Magnetism (ICM 2006), Kyoto, JAPAN, Aug 20-25, 2006; Kyoto, JAPAN, 2006; E367-E369.

46. Adhish Jaiswal,† Raja Das,† Tuhin Maity, K. Vivekanand, Suguna Adyanthaya, and Pankaj Poddar, Temperature-Dependent Raman and Dielectric Spectroscopy of $BiFeO_3$ Nanoparticles:Signatures of Spin-Phonon and Magnetoelectric Coupling, *J. Phys. Chem. C* **2010***, 114, 12432-12439

47. Jaiswal, A.; Das, R.; Vivekanand, K.; Abraham, P. M.; Adyanthaya, S.; Poddar, P., Effect of Reduced Particle Size on the Magnetic Properties of Chemically Synthesized $BiFeO_3$ Nanocrystals. *Journal of Physical Chemistry C* **2010,** 114, (5), 2108-2115.

48. Rovillain, P.; Cazayous, M.; Gallais, Y.; Sacuto, A.; Lobo, R.; Lebeugle, D.; Colson, D., Polar phonons and spin excitations coupling in multiferroic $BiFeO_3$ crystals. *Physical Review B* **2009,** 79, (18) 180411.

49. de Sousa, R.; Moore, J. E., Optical coupling to spin waves in the cycloidal multiferroic $BiFeO_3$. *Physical Review B* **2008,** 77, (1) 012406.

50. Haumont, R.; Kreisel, J.; Bouvier, P.; Hippert, F., Phonon anomalies and the ferroelectric phase transition in multiferroic $BiFeO_3$. *Physical Review B* **2006,** 73, (13).

51. Mazumder, R.; Ghosh, S.; Mondal, P.; Bhattacharya, D.; Dasgupta, S.; Das, N.; Sen, A.; Tyagi, A. K.; Sivakumar, M.; Takami, T.; Ikuta, H., Particle size dependence of magnetization and phase transition near T-N in multiferroic $BiFeO_3$. *Journal of Applied Physics* **2006,** 100, (3), 9.

52. Cao, W.; Randall, C. A., Grain size and domain size relations in bulk ceramic ferroelectric materials. *Journal of Physics and Chemistry of Solids* **1996,** 57, (10), 1499-1505.

53. Scott, J. F., Carlos A. Paz de Araujo, Ferroelectric Memories. *Science*, **1989**, 246,1400

54. Ghosh, M.; Biswas, K.; Sundaresan, A.; Rao, C. N. R., MnO and NiO nanoparticles: synthesis and magnetic properties. *Journal of Materials Chemistry* **2006,** 16, (1), 106-111.

55. Maglione, M.; Subramanian, M. A., Dielectric and polarization experiments in high loss dielectrics: A word of caution. *Applied Physics Letters* **2008,** 93, (3), 032902.

56. Sarkar, S.; Jana, P. K.; Chaudhuri, B. K.; Sakata, H., Copper (II) oxide as a giant dielectric material. *Applied Physics Letters* **2006,** 89, (21), 3.

57. Intatha, U.; Eitssayeam, S.; Wang, J.; Tunkasiri, T., Impedance study of giant dielectric permittivity in $BaFe_{0.5}Nb_{0.5}O_3$ perovskite ceramic. *Current Applied Physics* 10, (1), 21-25.

58. Lu, J.; Günther, A.; Schrettle, F.; Mayr, F.; Krohns, S.; Lunkenheimer, P.; Pimenov, A.; Travkin, V. D.; Mukhin, A. A.; Loidl, A., On the room temperature multiferroic $BiFeO_3$: Magnetic, dielectric and thermal properties. *Europian Physical Journal B* **2010**, 75, 451

59. Yuan, G. L.; Martin, L. W.; Ramesh, R.; Uedono, A., The dependence of oxygen vacancy distributions in $BiFeO_3$ films on oxygen pressure and substrate. *Applied Physics Letters* **2009,** 95, (1), 012904

60. Seidel, J.; Martin, L. W.; He, Q.; Zhan, Q.; Chu, Y. H.; Rother, A.; Hawkridge, M. E.; Maksymovych, P.; Yu, P.; Gajek, M.; Balke, N.; Kalinin, S. V.; Gemming, S.; Wang, F.; Catalan, G.; Scott, J. F.; Spaldin, N. A.; Orenstein, J.; Ramesh, R., Conduction at domain walls in oxide multiferroics. *Nature Materials* **2009,** 8, (3), 229-234.

Chapter 3

Surface Effects on Morin Transition, Exchange Bias Enhanced Spin Reorientation and Dielectric Spectroscopy in Chemically Synthesized DyFeO₃ Nanoparticles
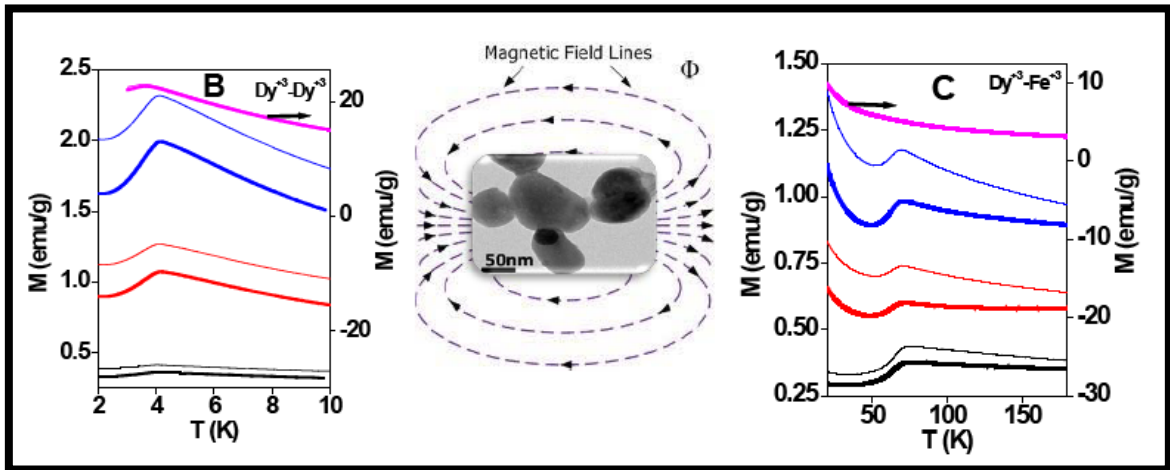
Outline

Giant linear magnetoelectric effect was observed by Y. Tokura's group recently in multiferroic DyFeO₃ which demands a detailed investigation of its magnetic properties. Here, we report the synthesis of DyFeO₃ nanoparticles using a surfactant-less hydrothermal method with a detailed magnetic property measurement and temperature and frequency dependent dielectric spectroscopy and ac magnetic susceptibility. The as-synthesized DyFeO₃ nanoparticles showed excellent crystallinity with average particle size in the range 50-60 nm. Detailed DC magnetization measurements in the temperature range of 3- 350 K could isolate the presence of Dy^{+3}-Fe^{+3} and Dy^{+3}- Dy^{+3} superexchange interactions which showed-up as spin reorientation transitions in various temperature regions due to differing magnitude of their interactions resulting into continuous rotation of antiferromagnetic component of Fe^{+3} spins with cooling of sample. Nanosized DyFeO₃ showed spin-reorientation transitions near 315 and 70 K due to the Dy^{+3}-Fe^{+3}

interaction accompanied with an opening up of the hysteresis loop followed by antiferromagnetic ordering around 4 K due to a possible Dy^{+3}- Dy^{+3} interaction. We also observed significant effect of the particle size reduction on the magnetic properties. The main effects seen by us were in terms of (1) pronounced spontaneous spin reorientation transitions (2) the absence of Morin transition and (3) presence of temperature dependent exchange bias in the $DyFeO_3$ nanoparticles. We present a detailed mechanism to explain these features based on the interplay of Dy^{3+} and Fe^{3+} spins as well surface disorder, anisotropy, canting etc. The measurement of the dielectric properties was carried out in a broad temperature (20-325 K) and frequency ($1–10^6$ Hz) range. The dipolar relaxation phenomenon of non-Debye type was observed in the $DyFeO_3$ (DFO) nanoparticles, as confirmed by the Cole–Cole plots. The higher values of ε´ at the lower frequencies are explained on the basis of the Maxwell– Wagner model. Cole–Cole analysis enabled us to separate the contribution of relaxation times, resistance and capacitance in grain and grain boundaries in $DyFeO_3$ nanocrystals. We found that with increasing temperature, the contribution of grain boundary resistance increases in comparison to the grain resistance. We also performed spin relaxation studies in broad temperature and frequency range. Both the in-phase or real (χ´) and out-of-phase or imaginary (χ´´) components of the ac magnetic susceptibilities of the $DyFeO_3$ shows clear evidence at spin reorientation transition around 70 K and T_N(Dy) around 4K as reported by us in ourlier studyusing the dc magnetic behaviour.

The work in this chapter is published as-

- ➢ **Surface Effects on Morin Transition, Exchange Bias and Enchanced Spin Reorientation in Chemically Synthesized DyFeO₃ nanoparticles.**

  Adhish Jaiswal, *Raja Das, Suguna Adyanthaya, Pankaj Poddar[*] J. Phys. Chem. C 115, 2954–2960 (2011)*

- ➢ **Dielectric and spin relaxation behaviour in DyFeO₃ nanocrystals.**

  Adhish Jaiswal, *Raja Das, Tuhin Maity, Pankaj Poddar (Communicated)*

3.1 Introduction:

The recent surge in the interest in the rare earth orthoferrites emanates from the possible spin-orbital coupling between adjacent antiferromagnetic ions.[1] Among them, the $DyFeO_3$ has been recently reported to show giant linear magnetoelectric (ME) coupling.[2] The orthoferrites with a chemical formula LnFeO$_3$ (Ln = Lanthanide) generally crystallizes in the orthorhombic perovskite structure in which the FeO_6 octahedra get distorted to the extent decided by the size of rare earth ions.[3, 4] An interesting aspect of these rare earth perovskites is that by varying the size of the rare earth ions we might expect not only the variations in A-O and B-O interactions (which results into some distortion of the oxygen polyhedral and finally affects the ferroelectric behaviour) but also the electrical conductivity which decreases with increase in atomic number has been observed.[5, 6]For another well studied perovskite ferrite- $BiFeO_3$, it is the particular orientation of *6s* lone pairs of Bi ions or dangling bonds which creates local electrical dipoles due to which Bi ions will move away from the center of symmetry of oxygen environment, resulting into the lowering of crystal symmetry and inducing ferroelectricity in $BiFeO_3$.[7] If the smaller Dy^{3+} ions replace the larger Bi^{3+} ions in $BiFeO_3$, then to form the close pack structure, the oxygen ions get displaced from their original positions and this displacement deforms the lattice and causes the rotation of the FeO_6 octahedra and results the perovskite structure in $DyFeO_3$ (DFO) to deform.[3, 8] It is well known that the electrical and the magnetic properties of these rare earth ferrites are governed by the Fe^{3+}–Fe^{3+} interaction (spin coupling of the 3d electrons). By introducing rare earth ions (Dy^{3+}) into the lattice, the Dy^{3+}–Fe^{3+} interactions appear (3d–4f coupling), leading to changes in both the electrical and magnetic behavior of the ferrites.[9]

Some of these rare earth orthoferrites, chromites and manganites show quite intriguing magnetic properties evidenced by a series of order-disorder transitions due to the competing magnetic interactions between various cations presenting a complicated picture as the interaction between dissimilar ions is highly dependent upon the size of these cations, temperature and the strength and direction of applied magnetic field.[10] This reflects into a significant decrease in the Néel transition temperature from 740 K for

LaFeO$_3$ to 623 K in LuFeO$_3$ as well as change in the temperatures at which various spin reorientation (SR) transitions are observed in these compounds.[8] Similar features are also observed in chromites where the Néel transition temperature decreasing from 289 K in LaCrO$_3$ to 143 K in YCrO$_3$.[11] This decrease is associated with decrease in the change in the enthalpy and entropy at magnetic transition.[11] Even for the rare earth manganites, a gradual decrease in the antiferromagnetic (AFM) transition is associated with the increase in the size of rare earth ion (from 150 K for LaMnO$_3$ to ~40 K for EuMnO$_3$).[12] These changes in the magnetic transitions perhaps originate from the increased lattice distortion and decreased interionic distances with an increase in the ionic radii of rare earth ions.[13]

Among these compounds, DFO is the only rare earth orthoferrites which shows Morin transition at 35 K[2] followed by three anomalous transitions at temperatures 77, 130, 270 K originating probably due to the field induced spin reorientation (SR) effect originating from competing magnetic interaction between Dy^{3+} and Fe^{3+} ions. The transition observed at very low temperature ~ 4.2 K was explained by the Dy^{+3}- Dy^{+3} antiferromagnetic ordering, similar to the transition at 7 K in GdCrO$_3$ due to Gd^{3+}-Gd^{3+} interaction reported by us and other groups.[10, 14] In DFO, the location of Fe^{3+} ion in a particular plane decide the magnetic interaction with another ion. Despite of showing interesting properties such as giant magnetoelectric effect, DFO is not probed much so far for its magnetic properties (such as magnetic hysteresis loop vs. temperature) even in the bulk phase. The only available magnetic studies were focused on the Mossbauer spectrometry to probe field induced SR transitions in DFO.[14, 15]

The ME effect in these compounds is dictated by the ordering of spins and electrical dipoles where the length scales of these order parameters become important. There are very few materials reported in the literature which exhibit large ferroelectric polarisation and magnetoelectric (ME) coupling. To achieve large ME effect, it is essential that the origin of the ferroelectric polarisation should be magnetic. Recently, Tokura *et al.* reported that single crystal of DyFeO$_3$ (DFO) had gigantic magnetoelectric (ME) phenomena and spontaneous polarisation below ~3.8 K.[16] The origin of the ferroelectric polarization in the multiferroic DyFeO$_3$ phase is supposed to be the exchange striction working between adjacent Fe^{+3} and Dy^{+3} layers with the respective

layered antiferromagnetic components. So the anomalous behaviour of ferroelectric polarisation suggests that in this system, ferroelectric polarisation depends not only on the magnetic structure of Dy^{3+} but also on that of Fe^{3+}.[16] The value of spontaneous polarisation is quite large as for the spin-driven ferroelectrics and also comparable to orthomanganites.[17]

Due to the importance of the length scale, it was realized recently that it was important to understand the change in the physical properties of these materials as a function of particle size to have a tunability over the ferroelectric and magnetic properties in these ME materials for their potential use in nanoscale devices.[18] Recently, we reported size dependent magnetic properties of $BiFeO_3$, where we found that below 100 K, $BiFeO_3$ exhibits sizable hysteresis and finite coercivity.[18] The effect of reduced size on temperature-dependent Raman and dielectric spectroscopy of chemically synthesized $BiFeO_3$ nanoparticles (average size ~50-60 nm) was further studied and observed that the loss tangent, ac conductivity and real part of permittivity values are lower than the reported values for $BiFeO_3$ ceramics, indicating high levels of ionic purity in $BiFeO_3$ nanoparticles.[19] The dielectric and spin relaxation studies of DFO can further provide valuable information about conduction phenomena, frequency dependence of dielectric loss, phase transitions and domain dynamics in nanostructured multiferroic materials. No report, to our knowledge, has so far been made to study the dielectric and ac magnetic susceptibility measurement on nanocrystalline DFO. Keeping in view the importance of DFO as giant magnetoelectric material, in this report, we have investigated DFO nanoparticles using ac impedance spectroscopy and ac magnetic susceptibility techniques. As the electrical properties of such materials largely depend on the grain and grain boundaries so in order to understand them, all electrical parameters such as real and imaginary permittivity, relaxation dynamics, activation energy, its spreading factor and their individual contributions must be separately investigated.

However, the rare earth ferrites, manganites and chromites have not been explored for their size dependent properties as the synthesis of these rare earth complex oxides with a control over particle morphology while maintaining crystallinity is nontrivial. The conventional chemical techniques such as coprecipitation, reverse-

micelle, hot injection etc. are unable to produce the desired phase. Due to this reason, the physical properties of most of these materials are reported mostly in the bulk phases (such as single crystals and polycrystalline form).

3.2 Hydrothermal synthesis of DyFeO$_3$ nanoparticles:

Here, we have successfully developed a modified hydrothermal route[10] to synthesize the DFO nanoparticles based on complexing the metal ions with the citric acid followed by the hydrothermal process. The hydrothermal synthesis process is known to have an edge over other synthesis routes because of its simplicity, low-cost and better yield. Above all, the hydrothermal process is known to produce particles with very good crystallinity and has potential for scaling-up. The rationale behind using this technique in the DFO synthesis is that the high pressure in the reaction vessel helps in stabilizing the crystalline phase which is not possible at ambient pressure. This method was employed by us earlier to synthesize LuMnO$_3$, GdCrO$_3$ and BiFeO$_3$ nanoparticles- three difficult materials in the multiferroic family of compounds to crystallize in nanosize with a proper control over crystallinity.[10, 18, 20] In the present case, the stoichiometric amounts of iron nitrate (Fe(NO$_3$)$_3$.9H$_2$O, Merck, 98%), dysprosium nitrate hydrate (Dy(NO$_3$)$_3$.H$_2$O, Aldrich, 99.9%), and an equal amount of citric acid (metal/citric acid molar ratio = 1/1) (obtained from Merck, 99.5%) were dissolved in the deionized water by stirring it for 6 h, so that the metal ions can be completely complexed to the citrate ions. This was followed by the dropwise addition of ammonia solution (28 wt. %) to neutralize the unreacted citric acid as well as to raise the pH value of the solution near 9.2 resulting into a sol formation. The sol was transferred to a 200 ml capacity autoclave with the Teflon liner followed by the hydrothermal treatment at 150^{0}C for 20 h. The precipitate was in turn filtered, washed with deionized water, re-filtered and finally dried at 160^{0}C for 5 h. Then the dried powder was calcined at 400 ^{O}C for 6 h.

Chapter 3

3.3 Characterisations:

3.3.1 X-ray diffraction measurements:

In figure 3.1, we have shown the powder x-ray diffraction pattern (XRD) of the as-synthesized DFO nanocrystals. The data is compared with the JCPDF data file #470069, which shows the formation of highly crystalline pure phase except one small peak around 29° which could be due to Dy_2O_3. We think that the imbalance of Fe^{3+} ions due to unreacted Fe^{3+} ions could have washed away in the washing process after the synthesis of material.Which is also consistent with the fact that we do not see the peaks for Fe_2O_3 phase.
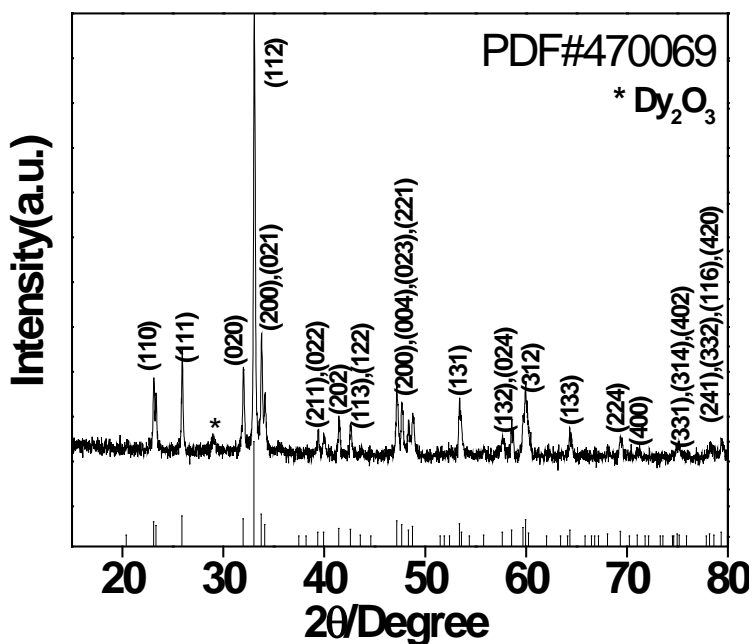
Figure 3.1: A comparison between powder X-ray diffraction pattern of DyFeO₃ nanocrystals with the data from JCPDS Card No. 470069.

The average crystallite size as calculated using Debye-Scherer formula was found to be around ~40 nm.

3.3.2 Determination of shape and size of the nanoparticles:

To further investigate microstructure and topography, we used HRTEM measurements on as-synthesized DFO nanoparticles. In figure 3.2 (A) and 3.2 (B), we have shown two sets of representative TEM images taken on same sample from various part of the grid. In the inset of figure 3.2(B) we have shown the particle size distribution in our sample. Here, we clearly observe the formation of partly faceted, plate-like, with size ranging from 50-60 nm. The average size as seen in TEM image is slightly larger
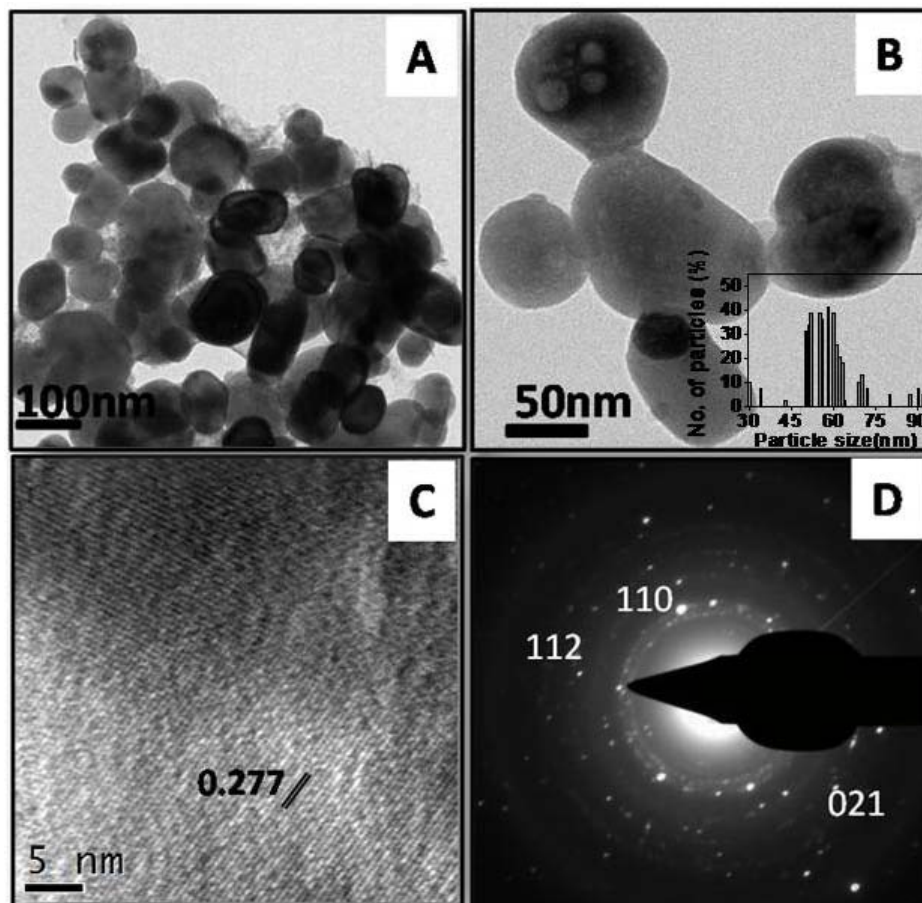
Figure 3.2: *(A), (B) Transmission electron microscopy images of as-synthesized DyFeO₃ nanoparticles. The inset shows particle size distribution graph of DyFeO₃ nano particles. (C) High resolution TEM image showing the lattice fringes (D) Selected area electron diffraction pattern of DyFeO₃ nanoparticles.*

than the crystallite size obtained by the Scherrer equation. We also observe that the particles on the TEM grids overlap at few places (or try to stack-up sometime) after drying out of solvent which is due to the use of surfactant- less synthesis technique as well as the plate like morphology of the particles. In figure 3.2 (C), we have shown the high resolution image where we can notice well pronounced lattice fringes indicating very good level of crystallinity. The selected area electron diffraction pattern (SAED) in figure 3.2 (D) shows a nice dot pattern that clearly exhibit highly crystalline nature of

Chapter 3

DyFeO$_3$ nanocrystals. It is interesting to note the origin of plate like morphologies in as-synthesized particles in DFO. Even, in our previous studies on the synthesis of GdCrO$_3$ and BiFeO$_3$ nanoparticles, we had reported the formation of similar plate like morphologies.[10, 18] We believe that in the formation of plate like nanoparticles in the synthesis adopted by us, the role of nitrate and citrate ions is extremely important and requires a careful investigation which is the subject of our future study. It is known that apart from other factors such as twinning, stacking faults etc., the shape control in the wet-chemical synthesis can also be driven by the preferential binding of ionic ligands, surfactants to the particular lattice facets due to their variable degree of affinity from one facet to another which allows the growth of particular facets while restricting the growth of others. In the case of our hydrothermal synthesis, the strong affinity of both nitrate and citrate ions with metal ions at particular crystalline facets might have promoted the formation of negatively charged anisotropic structures much similar to the role of halide ions in the formation of anisotropic gold nanoparticles.[21-23] However, experimentally, it is quite challenging to prove the role of preferential binding of ionic ligands on the overall morphologies. Careful surface studies using x-ray photoelectron and Raman spectroscopies might provide a clear understanding.

3.4 X-ray photoelectron spectroscopy measurements:

In figures 3.3 (A) & (B), we have shown the room temperature x-ray photoelectron spectroscopy (XPS) data to confirm the oxidation state of the Fe and Dy to validate the purity of the phase formation. Figure 3.3 (A) shows the XPS spectra of Fe^{+3}. There are two most intense peaks at ~711 and ~724 eV which were assigned to the Fe^{+3} 2$p_{3/2}$ and 2$p_{1/2}$ states.[24] In addition to the broadening of the peak, a small peak has also been observed at higher binding energy near 717 eV which is the satellite peak due to shake up process.[25] In figure 3.3 (B), we have shown the high resolution core spectrum for Dy 3d$_{5/2}$ core level. The peak at 1296 eV corresponds to Dy *3d$_{5/2}$* states.[26] This is the first detailed XPS study reported so far on the DFO.
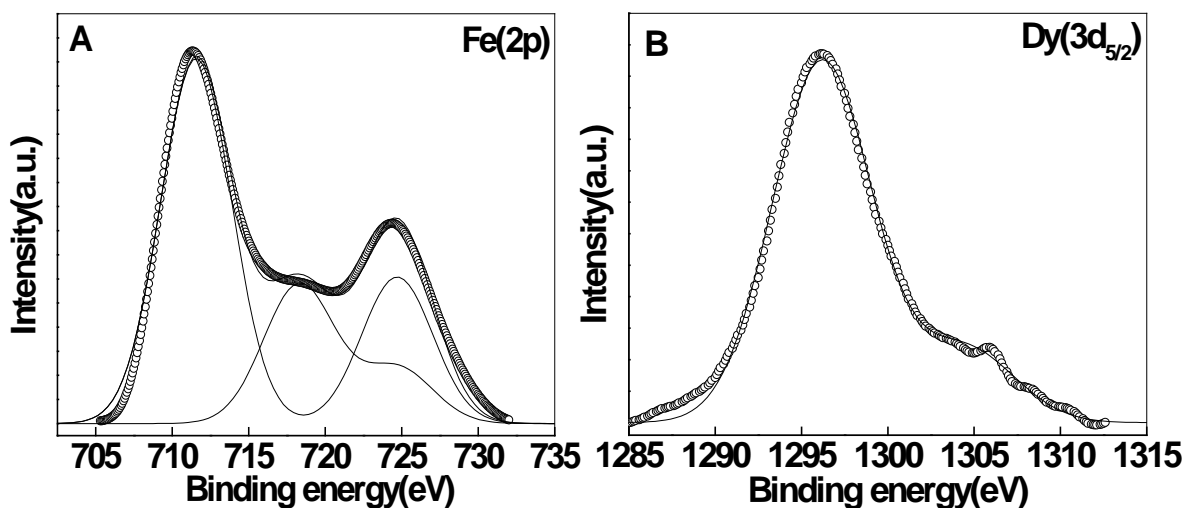
Figure 3.3: *(A) & (B) core level XPS spectra for Fe (2p) & Dy (3d) respectively taken on DyFeO₃ nanoparticles (scatter curves). The lines represent the deconvoluted peaks.*

3.5 Magnetic properties measurement:

As we mentioned earlier, even for the bulk DFO phase, the detailed magnetization studies such as behavior of coercivity, susceptibility as a function of temperature were never reported in literature. Therefore, we performed a detailed DC magnetization vs. temperature measurements as well as magnetic field vs. magnetization hysteresis measurements on the DFO nanoparticles. In figure 3.4 (A), we have shown some representative M-H loops at selected temperature values showing dramatic variation in the shape of the curves with temperature. In the figure 3.4 (B), we have shown the zoom view of the M-H loops at 3, 70, and 370 K. In the figure 3.4 (C) and 3.4 (D), we have plotted the temperature dependence of coercivity (H_c), magnetization at 50 k Oe (M_s) and ratio of remanent magnetization (M_r) and M_s. Our DFO nanoparticles show sizable coercivity of ~ 240 Oe even at 370 K. The coercivity value increases sharply with decreasing temperature[20] and reaches its maximum at 70 K (~ 580 Oe). Further, below 70 K, it shows a decreasing trend and hits minimum at around 4 K (~150 Oe). The coercivity again shoots-up below 4 K as shown in figure 3.4 (C). We will discuss the origin of these features in coming sections. In figure 3.4 (D), there is almost an exponential drop in the M_s value with the increase in temperature. Similar feature around 4K has been
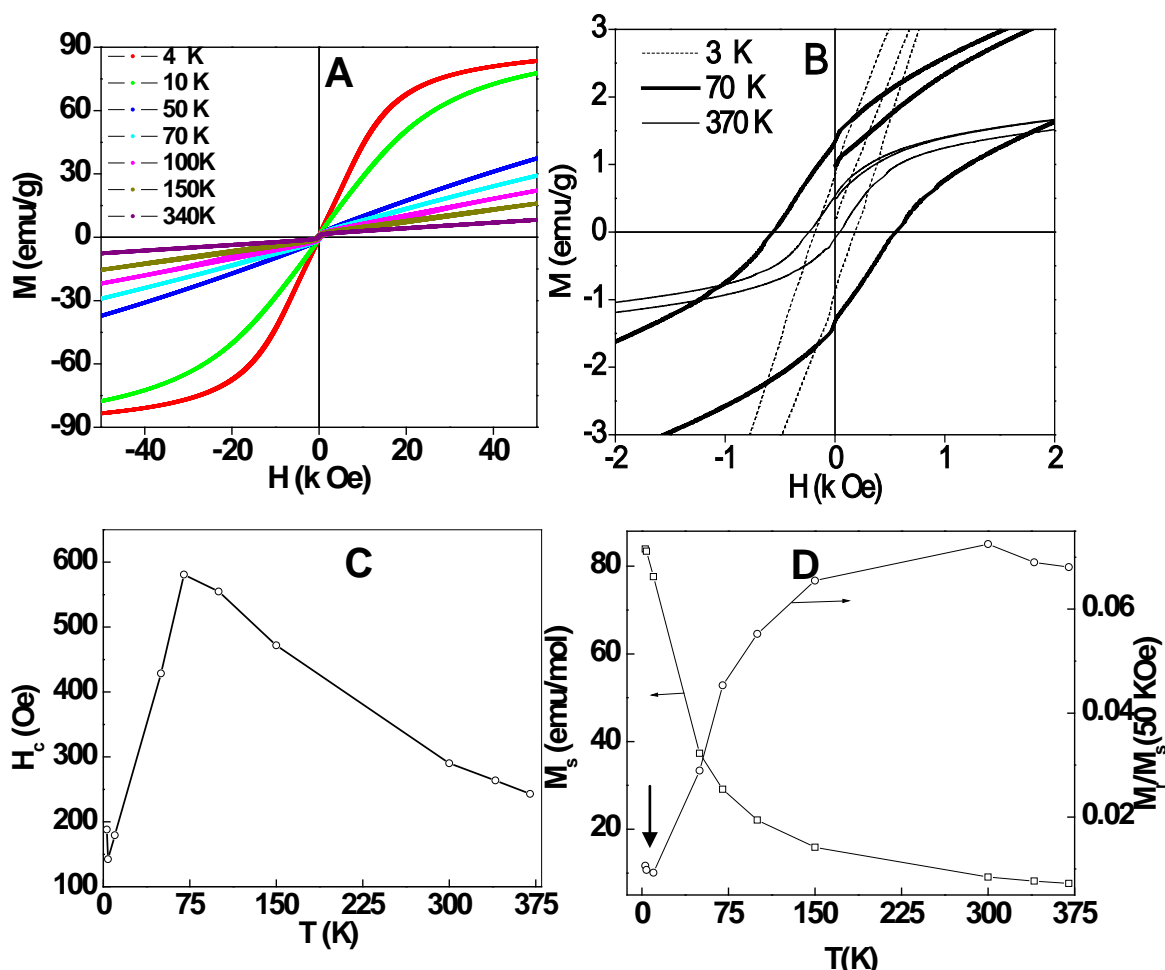
Figure 3.4: *(A) M-H loops taken at various temperatures (B) zoom view of the M-H loops at 3, 70, 370 K (C) variation of coercivity H_C with the temperature. The error in the field measurement was less than ± 25 Oe and the error in temperature measurement was ± 0.1 K. (D) temperature dependence of M_S(50 k Oe) and M_r/M_S(50 k Oe) for $DyFeO_3$ nanoparticles. The M. Std. Err. for moment is in the range of 10^{-6} emu.*

observed in the temperature dependent M_r/M_s behavior. Further, above 4K, M_r/M_s value follows an increasing trend and reaches maximum around 300K. In M-H hysteresis curves, we observed that the M-H hysteresis loops were shifted considerably towards the negative side of the field i.e. the samples showed exchange bias type of signatures. In figure 3.5 (a), we have shown the zoom view of M-H loops at 300 and 100 K where the curve at 300 K showed much larger shift in comparison to the curve at 100 K. In figure
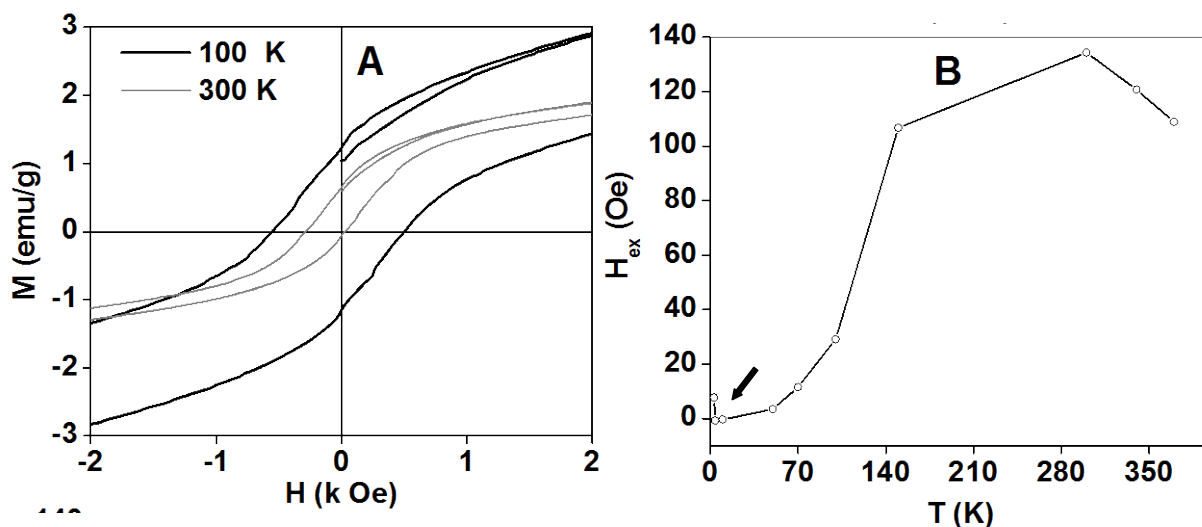
Figure 3.5: *(A) Exchange bias at room temperature (B) variation of exchange field H_{ex} with the temperature for DyFeO₃.*

3.5 (B), we have shown a temperature dependent exchange field which is larger at higher temperature values but goes down sharply at lower temperature.[27] In figure 3.6 (A), we have shown a representative set of FC & ZFC curves taken at 50, 200, 400 and 5000 Oe respectively. Various regions of interest are highlighted in figures 3.6 (B), (C) and (D). Following important features could be summarized: (1) a small hump near 315 K in FC curve which is a first reorientation transition coming out of Dy^{+3} and Fe^{+3} interaction (2) a second reorientation transition near 70 K because of a weak AFM coupling between Dy^{+3} and Fe^{+3} moment (3) a strong AFM coupling between Dy^{+3} and Dy^{+3} moment near 4 K. Most of these features were never seen directly by the DC magnetization measurements by previous researchers. Another important observation by us in the ZFC-FC curves was the absence of Morin transition in our samples which was earlier reported in single crystalline DFO sample by Holmes et al.[28]

Now, let us discuss in detail the possible physical origin of these intriguing features as seen in the M-H and M-T data sets. It is reported that the bulk DFO undergoes an antiferromagnetic transition below its Néel temperature of 645 K.[3] On the basis of their magnetic properties, the rare earth orthoferrites can be divided into two categories.

Chapter 3

In the first category falls those orthoferrites which have diamagnetic rare earth ions (like Y^{+3}) and the magnetic interaction is strongly dependent upon the Fe^{+3}-Fe^{+3} SE(super exchange) interaction and the magnetism is indirectly influenced by the size and lattice
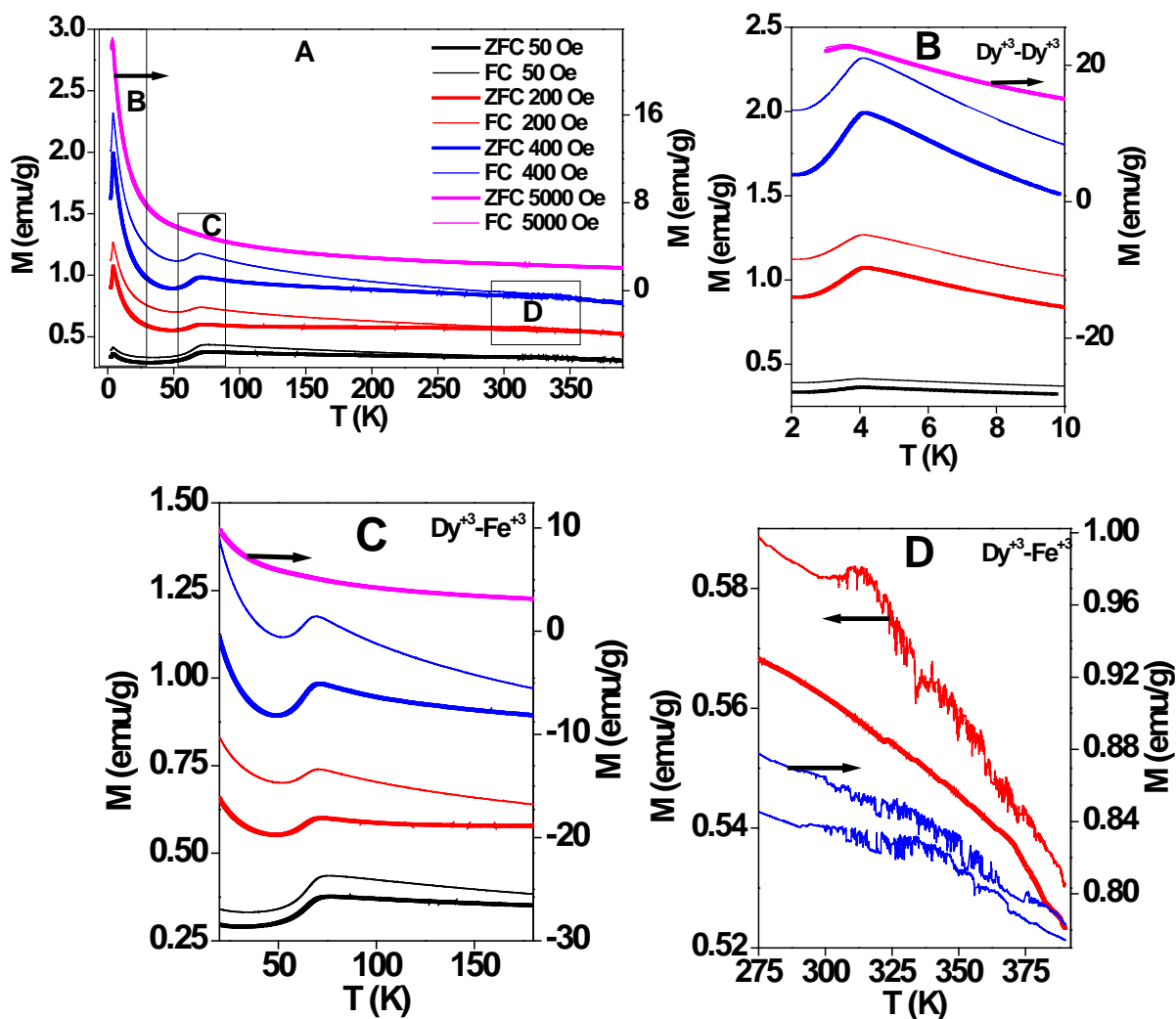
Figure 3.6: *(A) Representative zero field cooled, field cooled curves at 50, 200, 400, 5000 Oe external field. (B), (C), (D) show the zoom views of three different parts of (A).*

spacings of the rare earth ions.[29] The second category consists of those orthoferrites which have magnetic rare earth ions (like Gd^{+3}), the magnetic interactions are not only dependent upon Fe^{+3}-Fe^{+3} exchange interaction but also Gd^{+3}-Fe^{+3} and Gd^{+3}- Gd^{+3} interactions.[30] Here, not only the size of the rare earth ions but their magnetic anisotropies play a crucial role which decide the fate of the spin reorientation transitions.

In comparison to Gd^{3+} ions (paramagnetic nature), Dy^{3+} ions have stronger anisotropy in the crystal which finally results more complex picture of reorientation transition as discussed below.[31] As we mentioned earlier that DFO shows a series of magnetic transitions due to the competing interactions between Dy^{+3}-Dy^{+3}, Dy^{+3}-Fe^{+3}, Fe^{+3}-Fe^{+3} ions. Just below the Néel temperature (645K), the Fe^{3+}-Fe^{3+} interaction dominates and at lowest temperature of measurements, the Dy^{+3}-Dy^{+3} interactions are the dominant ones (figure 3.6 (B)). On the other hand, the Fe^{3+}- Dy^{3+} interactions are observed at the intermediate temperature ranges (figures 3.6 (C) and (D)). In our earlier paper, in the case of $GdCrO_3$, we explained the mechanism behind the competing interactions appearing in different temperature zones.[10] The similar mechanism is applicable in the case of DFO as well. Below the Néel temperature (645 K), the spins of different Fe^{3+} ions interact antiparallely through the SE (super exchange) mechanism and give the G-type of AFM ordering.[8] Here, the Fe^{+3}-Fe^{+3} interactions are much stronger in comparison to Dy^{+3}-Dy^{+3} and Dy^{+3}-Fe^{+3} interactions by the orders of magnitude.[10] In DFO, the Fe^{3+} ions sit in the octahedral geometry surrounded by six O^{2-} ions that leads to the splitting of $3d^5$ orbital into t_{2g} and e_g. The t_{2g} and e_g orbitals are half filled and the half filled e_g orbitals hybridize with $2p$ orbital of O^{2-} where two Fe^{3+} ions interact via O^{2-} ions in 180° position and each Fe^{3+} ion has six Fe^{3+} nearest neighbors and therefore, the total SE interaction is a sum of them. On the other hand, Dy^{3+} and Fe^{3+} ions interact with each other via O^{2-} at 90° position and this interaction is weaker in nature and therefore dominates at lower temperatures only. As each Fe^{3+} ion has eight Dy^{3+} nearest neighbors, the total Dy^{+3}-Fe^{+3} SE interaction will be a sum of them. The Dy^{+3}-Dy^{+3} SE interaction is still one order of magnitude weaker than the SE interaction between Dy^{3+} and Fe^{3+} and shows up around 4 K. We now correlate the influence of these interactions on the features seen by us in the magnetic measurements. At higher temperatures, half filled Fe^{+3} d-orbital (e_g) and O^{2-} p-orbital hybridization is more stable than the Dy^{3+} f-orbital and O^{2-} p-orbital hybridization. However, as the temperature decreases further well below the Néel temperature, f-orbitals in Dy^{3+} ions and p orbitals of oxygen also start interacting, resulting into the onset of Fe^{3+}-O^{2-}- Dy^{3+} interaction. This interaction is weak AFM as here the half filled e_g orbital of Fe^{3+} overlaps with one end of oxygen p-

orbital and the other end of the same overlaps with a more than half filled *f*-orbital of Dy^{3+}. This results into the reorientation of G-type component of Fe^{+3} moment to WFM component around 315 K (figure 3.6 (D)). This weak AFM SE coupling gives rise to opening up of hysteresis loop (shown in figure 3.4 (B)) and consequently the remnant magnetization increases. Here, it should be noticed that it is not just the SE interaction between Fe^{3+} and Dy^{3+} but the Fe^{3+} spins also get canted due to the Dzialoshinski-Moriya (DM) [32] type antisymmetric exchange interaction between Fe^{3+} - Fe^{3+} ions which plays a very important role here.[33] These canted moments of Fe^{3+} induce an opening of the hysteresis loop which continues till 70 K and below this Dy^{+3} moments strongly interact antiferromagnetically with another Dy^{+3} moments which results again in the closing of the hysteresis loop (fig. 3.4 (C)). Below the room temperature, around 70 K Fe^{+3} moments continuously get reoriented from one crystallographic axis to another due to the increased Dy^{+3} - Fe^{+3} interactions and a sharp peak is observed in the ZFC-FC curves at 70K (figure 3.6 (B & C)). Below 70 K, Dy^{+3} moments start ordering antiferromagnetically with other Dy^{+3} moments which results into the decrease in the coercivity which also reflects in the ZFC-FC curves. It is very interesting to note that at low temperature and high magnetic field, DFO shows relatively higher value of magnetization in comparison to the reported values for some other orthoferrites such as $GdFeO_3$, $LuFeO_3$ and $EuFeO_3$. It might be due to the contribution of orbital magnetic moment in the total magnetic moment where *f* orbital electrons play a crucial role for deciding the direction of spins and thereby overall magnetization.[34]

In our nanosized samples, in addition to these intercationic competing SE interactions, the increased surface anisotropy and the amount of uncompensated/canted surface spins due to the increased surface to volume ratio also contributes in the opening up of the sizable hysteresis loop below the Néel temperature as seen in figure 3. 4 (B & C). In case of bulk materials where the particle size is large and the particles are randomly oriented, the contribution of isotropic exchange energy is larger in comparison to the anisotropic energy contribution. Therefore, the weaker magnetic transitions like spin reorientation transitions which are highly dependent upon the direction of spins and

Chapter 3

the applied magnetic field might get a bit suppressed by the isotropic term in bulk phase in comparison to the nanophase. However, as the particle size goes to smaller scale, the surface to volume ratio increases which finally results in to an increase in the surface anisotropy as well as dipolar interaction.[35] To explain the magnetic signature of nanocrystalline DFO, all the energy terms like anisotropic energy, isotropic energy, DM exchange energy, dipolar energy, Zeeman energy and magneto electrostatic energy will contribute significantly.[36] This is the reason why in contrast to the SR transitions seen by us in our nanocrystalline DFO, the Dy^{+3}-Fe^{+3}, Fe^{+3}-Fe^{+3} and Dy^{+3}- Dy^{+3} interactions resulting into various subtle reorientation transitions (as seen in various panels of figure 3.6) can be easily missed in the bulk DFO. The mechanism behind the unique exchange bias feature seen by us in DFO nanoparticles (not observed earlier in bulk BFO) can also be explained by the exchange coupling between the ferromagnetic surface spins and AFM core spins. The change in the AFM character of the core spins with the temperature results into the temperature dependent exchange field as seen in figure 3.5 (B) where all the magnetic transitions reported in ZFC-FC around 315, 70 and 4 K are also observed in the case of temperature dependent exchange field. The exchange field shows a maximum around 315 K and decreases continuously with a small hump near 70 K.Further, below 70 K it again decreases and reaches to zero around 4 K and further it shoots up at 3 K. This type of exchange coupling behavior is quite common in nanosized AFM systems and nicely reviewed by Nogues et al.[27]

At the end, let us discuss the possible reason behind the absence of Morin transition in our nanosized DFO. As we discussed earlier, DFO is the only rare earth orthoferrite which is reported to show Morin transition at 35K in bulk single crystalline form where the AFM vector of coupled Fe^{+3} ions reorient from *a*- axis to *b*-axis in the lattice.[28] The Morin transition, which is also a type of spin-reorientation transition, takes place as a first order transition and widely studied in bulk α-Fe_2O_3 where it occurs at T_M=263 K.[37, 38] The particle size dependence of Morin transition in α-Fe_2O_3 is also reported which is believed to decrease with decreasing particle size and it has been reported that there is no Morin transition above liquid helium temperature in α-Fe_2O_3

particles with diameters smaller than ~20 nm.[37] Below 20 nm, the surface spins deviate strongly from the AFM easy axis.[37] The absence of an anomaly at 35K (Morin transition) in the M-T curve of our nanocrystalline $DyFeO_3$ indicates that the change in the order at this transition is very small. The spin frustration near the nanoparticle surfaces, the finite distribution of particle sizes, and surface strain all might be playing important role to diminish Morin transition in our case.

3.6 Dielectric properties measurement:

To probe the dielectric response in the proximity of the magnetic transitions in DFO at low temperatures, we used Novocontrol Beta NB Impedance Analyzer with a home-built sample holder to couple with a helium closed cycle refrigerator (Janis Inc.). The dielectric response was mapped in a frequency range from 1 to 1 x 10^6 Hz at 1 volt (rms) in the temperature range from 20-325 K at a close interval of 1 K. A compressed circular pellet, with 13 mm diameter was kept in a custom designed sample holder to form circular parallel plate capacitor geometry.

The frequency dependent plots of the real (ϵ') parts of complex dielectric permittivity (ϵ^*) of DFO at few temperature values in 50 to 300 K range are shown in various panels of figure 3.7. The nature of dielectric permittivity related to free dipoles oscillating in an electric field may be described in the following way. At very low frequencies ($\omega \ll 1/\tau$, where τ is the relaxation time), dipoles follow the field and the real part of the dielectric constant $\epsilon' \approx \epsilon_s$ (value of the dielectric constant in a quasistatic field). As the frequency increases ($\omega < 1/\tau$,), dipoles begin to lag behind the field and ϵ' slightly decreases. When frequency reaches the characteristic frequency ($\omega = 1/\tau$,), the ϵ' value drops (relaxation processes). At very high frequencies ($\omega > 1/\tau$,), dipoles can no longer follow the field and $\epsilon' \approx \epsilon_\infty$ (high frequency value of ϵ'). Approximately, this is the behaviour which is observed in figure 3.7(a) where the ϵ' increases with decreasing frequency. In addition to the various types of polarization contribution (interfacial, dipolar, atomic, ionic, electronic) in the dielectric constant, the dielectric behaviour of nanostructured materials is also influenced by enormous number of interparticle

interfaces and defects present at these interfaces which can cause a change of space charge distribution. Under applied ac electric field, these space charges oscillate and can get trapped by these interfacial defects at nanoparticle surfaces, resulting into the formation of additional space charge polarization.[39] Interfaces in nanostructured materials might also have oxygen ion vacancies, which are equivalent to positive charges; giving rise to additional dipole moments. At lower frequencies, the high value of dielectric constant seen by us is mainly due to the space charge polarization.
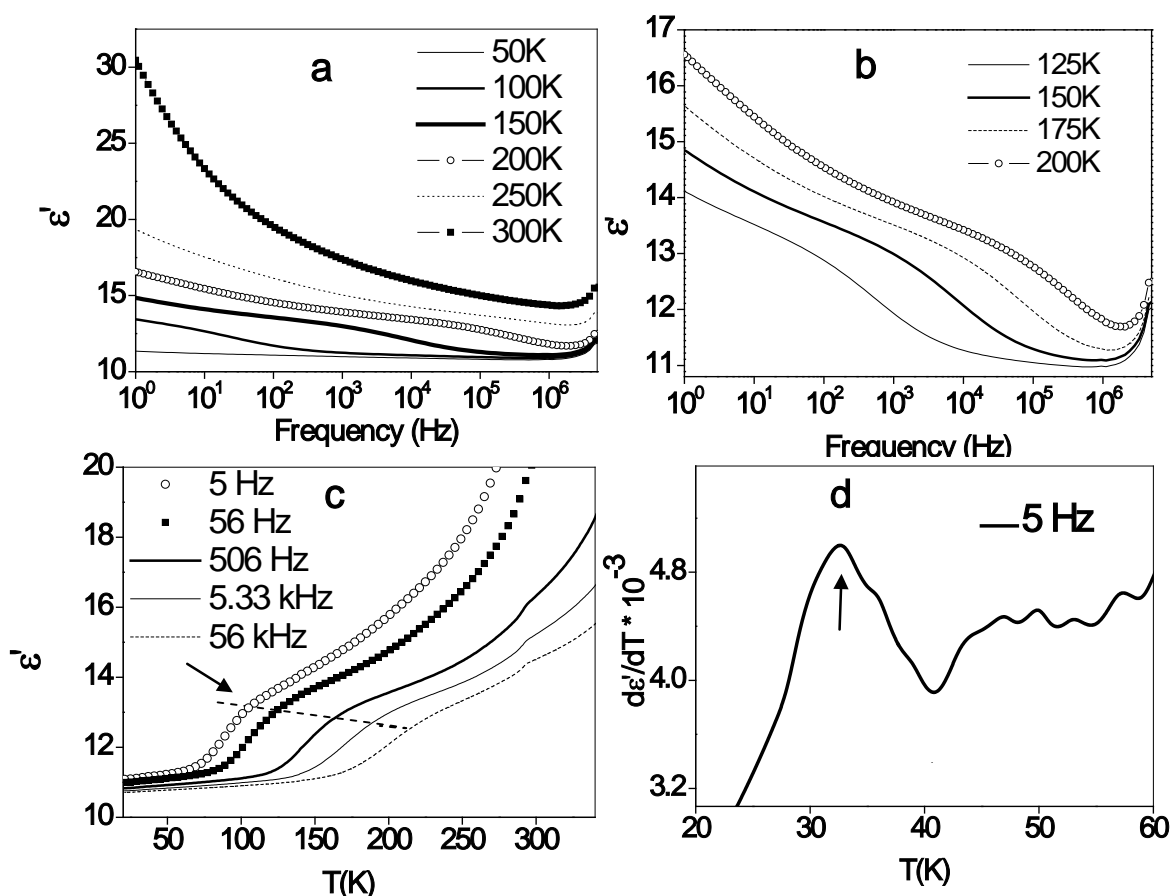
Figure 3.7: *(a) Frequency dependence of real part of permittivity (ε') value at different temperature (b) ε' vs. f curves in 125- 200 K temperature range (c) ε' vs. T curves at different frequencies (d) $d\varepsilon'/dT$ vs. T curves at 5 Hz for $DyFeO_3$ nanoparticles.*

Chapter 3

As the temperature increases, more and more dipoles are oriented in the field direction after overcoming the thermal activation energy barriers, resulting into an increase in the value of the dielectric constant, as observed in figures 3.7a. In figure 3.7 (b), it is noticed that there is a sudden drop in ε' in the temperature range 100 to 200 K where $\omega = 1/\tau$ and with increasing temperature this drop is shifted towards higher frequency side. In figure 3.7 (c), we have shown the temperature dependent dielectric constant for the frequency range 5 Hz to 506 kHz where below 100K, ε' values show a plateau region and above 100K, there is a sudden increase in the ε' value followed by a knee (shown by an arrow) above which ε' gradually increases further at higher temperature values. We also noticed strong frequency dependence in the onset of jump as well as the knee temperature in the ε' values above 100 K with a shift in these features in ε' values towards higher temperatures at high frequencies. It should be noticed that the value of ε' also goes down with increasing frequency. In figure 3.7 (d), we have shown the zoom view of the first derivative of ε′ with temperature shows a peak at around 33 K. At present, the origin of this peak is not clear to us.

Next, we studied the dielectric loss in DFO nanoparticles. The variation of dielectric loss with frequency at different temperatures for DFO nanoparticles is shown in figure 3.8a which shows a strong resonance peak. This peak shifts towards higher frequencies with increasing temperature. We also observed a strong peak in the dielectric loss (*tan δ*) vs. T curves in the temperature range 100–200 K (figure 3.8 b) where the peak temperature shifts towards higher temperature with increasing frequency. In (*tan δ*) vs. T curves, this peak is followed by almost linear increase in *tan δ* at further higher temperatures. There are two opposite factors contributing simultaneously in the value of ε′′ with the increase in temperature. The first factor which results in an increase in *tan δ* value with the increase in temperature is due to an increase in the number of charge carriers in DFO by thermal activation (showing the semiconducting behaviour of the sample) which facilitates the electron hopping from Fe^{+2} and Fe^{+3} at the nanoparticle surfaces. As we indicated earlier, very small amount of Fe^{2+} ions might exist at nanoparticles surface due to oxygen deficiency and reduced coordination number. [19, 40,41]
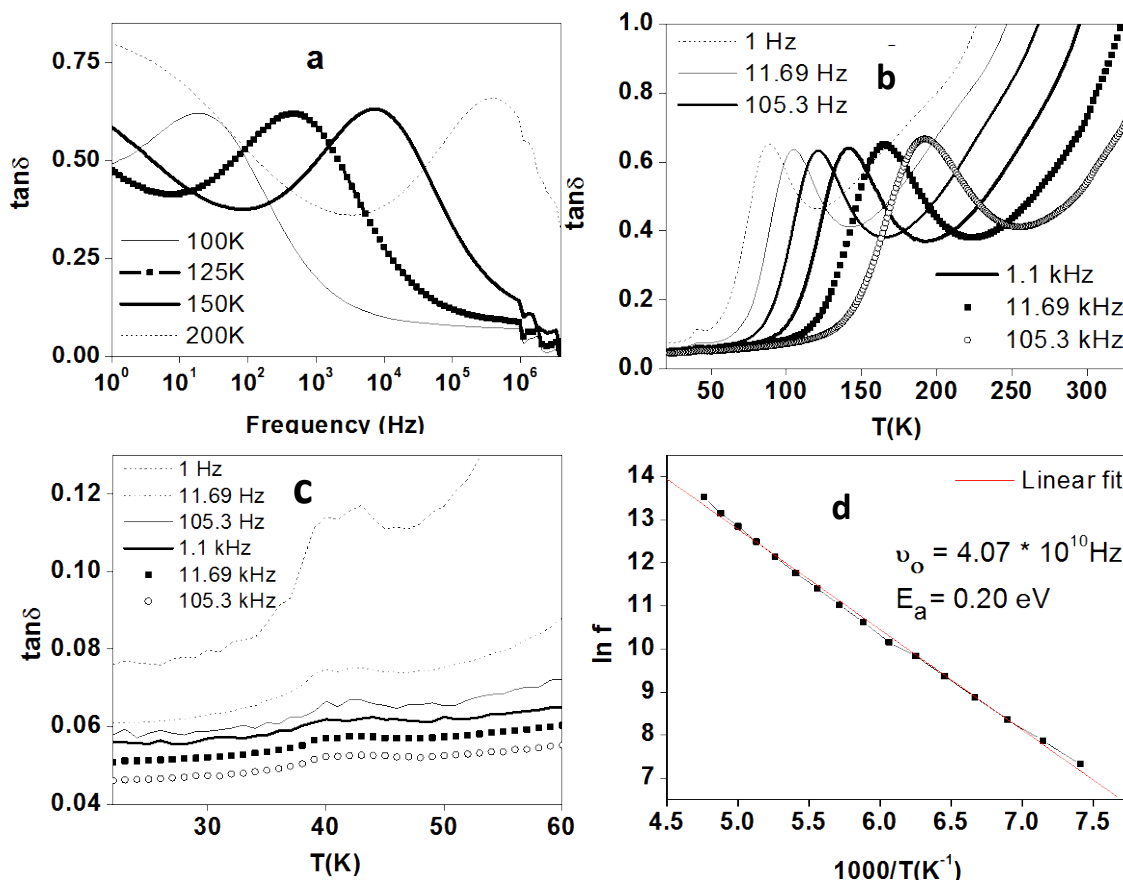
Figure 3.8: *(a) temperature dependent of dielectric loss value at different frequency (b) frequency dependent dielectric loss at different temperature (c) Zoom view of dielectric loss value between temperature range 20-60 K (d) plot of ln f vs. 1000/T for DyFeO₃ nanoparticles.*

The second factor which results in the decrease in *tan δ* value is due to fact that with increased temperature, electrical dipoles can easily align in the field direction and hence the energy spent during polarization decreases with temperature which finally reduce the value of imaginary dielectric constant with increase in temperature. The dielectric loss in low temperature range (30-50K) shows unusual behaviour (figure 3.8c). Firstly, there are apparent peaks at 40 K that do not change position much with change in the frequency. Secondly, as the frequency increases, there is a decrease in the strength of tan δ. For example, for the 1 Hz curve, the maximum value of tan δ is almost 0.11 while it is only about 0.03 at 105.3 kHz.

Chapter 3

To further understand the relaxation behaviour, we calculated the activation energy of the relaxation process. The activation energy (E_a) in a thermally activated relaxation process is generally related to the relaxation time τ by the Arrhenius equation:

$$\tau = \tau_0 \exp\left(\frac{E_a}{k_B T}\right) \tag{1}$$

where, τ is the relaxation time, E_a is the mean activation energy for relaxation, and k_B is the Boltzmann constant. This equation can also be written as (where $f = 1/\tau$):

$$\ln f = \ln f_0 - \frac{E_a}{k_B T} \tag{2}$$

Figure 3.8(d) represents the plot between *lnf* vs. (1000/*T*) which shows a very nice linear fit with the values of E_a and f_o 0.20eV and $4.07 * 10^{10}$ Hz respectively.

It appears clearly that the width of the peak in *tan δ* curves also increases with frequency which shows that there is a possibility of distribution of relaxation process. The width of the relaxation peak in figure 3.8(a, b) cannot be accounted for monodispersive relaxation process and points towards the possibility of distribution of relaxation times. One of the most convenient ways for checking the polydispersive nature of dielectric relaxation is through the complex Argand plane plot of ε″ and ε′ usually called Cole - Cole plot. For the quantitative analysis of dielectric spectra and the relaxation time, the Cole-Cole equation has been described by the empirical relation .[42, 43]

$$\varepsilon^* = \varepsilon' - i\varepsilon'' = \varepsilon_\infty + \frac{\varepsilon_s - \varepsilon_\infty}{1 + (i\omega\tau)^{1-\alpha}} \tag{3}$$

here, ε_∞ is the high frequency limit of ε, ε_s is the low frequency limit of ε, $\varepsilon_s - \varepsilon_\infty$ is a dielectric strength, $\omega = 2\pi\upsilon$ is the angular frequency, τ is the mean relaxation time and α represents the distribution of the relaxation time which in geometric terms represents the displacement of the arc's centre below the real axis. Figure 3.9 shows the plots between real ε′ and imaginary ε″ components of the complex impedance at 175 and 80 K

in the 1 Hz to 1 MHz frequency range. Here, the parameter α characterizes the distribution of relaxation time or spreading factor. It increases with internal degrees of freedom of relaxors, indicating a departure of electrical response from an ideal condition. When α goes to zero, equation (3) reduces to classical Debye's formalism. It is depicted from the Cole-Cole plot in figure 3.9 that the centre of the semicircles arc is below the x axis, therefore, it does not follow the Debye relaxation process (for which $\alpha = 0$). The spreading factor α can be deduced from the angle subtended by the radius of the circle with the ε' axis passing through the origin of the ε" axis. The spreading factor α is measured from the expression for the maximum value of imaginary part of permittivity, given by

$$\varepsilon^{"}_{max} = \frac{(\varepsilon_s - \varepsilon_\infty)\tan\left[\frac{(1-\alpha)\pi}{4}\right]}{2} \qquad (4)$$

where ε" $_{max}$ is the maximum value of imaginary part of permittivity from Cole –Cole plot. From this plot, since centre of the semicircle arc lies below the x-axis so the relaxation process of the DFO is quite different from that of monodispersive Debye-type (where $\alpha = 0$).
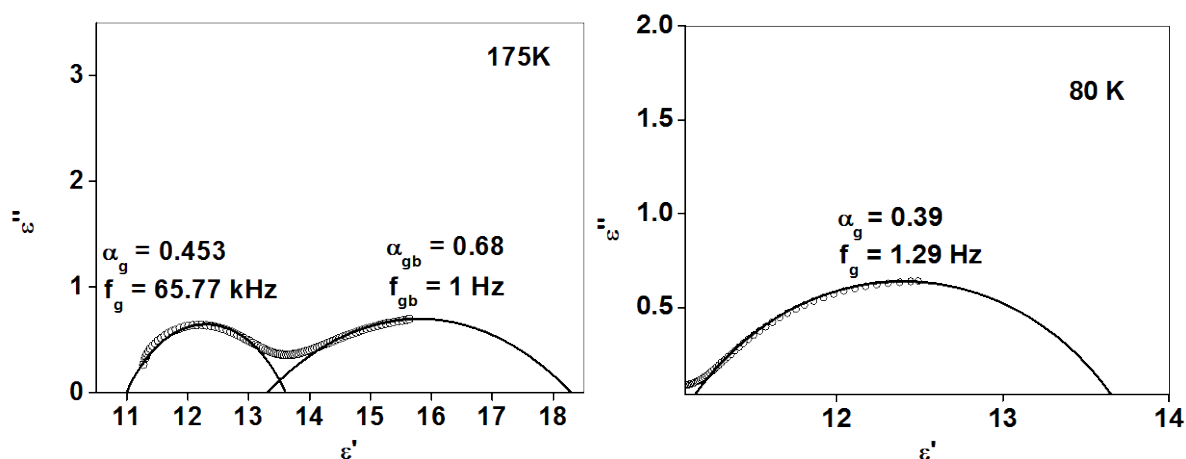
Figure 3.9: Cole-Cole plot of DyFeO₃ nanoparticles at 175K and 80K temperature.

In figure 3.9 (left panel), we have shown two impedance arcs in two separate frequency

ranges at temperature 175 K. This suggests that two different relaxation mechanisms are present in the measured frequency and temperature range. The semicircle in the high-frequency region is representative of the bulk properties of $DyFeO_3$ nanoparticles (contribution from core of the particles). Another semicircle arc in the low frequency region is related to the grain boundaries of these nanoparticles. In both the cases, the centre of semicircles lies below the real axis which shows that the relaxation behaviour is deviating from Debye type. The spreading factor α was calculated from the above equation for both the semi circle arcs and the values for grain and grain boundary were calculated as 0.453 and 0.68 respectively. Therefore, the non-zero value of α confirms the polydispersive nature of dielectric relaxation in the present DFO sample as discussed above. However, it is interesting to note that at lower temperature around 80 K (figure 3.9, right panel), there is only one arc present at higher frequency range which suggests that there is no contribution of grain boundary at this temperature. As temperature increases, a slight amount of oxygen loss can occur which facilitates the appearance of dipoles formed with an adjacent host ion and enlarge the rattling space available for dipole vibration, which as a consequence leads to the short-range hopping of the ions and gives rise to relaxation at lower frequency range and consequently grain boundary contribution increases. The spreading factor α is 0.39 for the semicircle at 80 K. It is clear that α decreases with decreasing temperature. From the Cole- Cole plot we could also calculate several other parameters. The ratio of the diameters of these two arcs indicated that the resistance associated with the bigger arc is much larger than that of the small arc. It suggests that the resistance in the equivalent circuit is dominated by grain boundary resistance.

In figure 3.10a, we have shown the temperature dependent variation of resistance of grain and grain boundary calculated from Cole-Cole plots. We could conclude from the this figure that as the temperature increases from 90 to 170 K, the grain resistance decreases from 2.78 to 2.65 Ω where as grain boundary resistance decreases from 5.41 to 4.85 Ω with increase in temperature from 175 to 260 K.

Chapter 3

Similarly capacitance of grain and grain boundary is calculated using the relation: [44]

$$\omega RC = 1 \qquad (5)$$

where ω is the angular frequency at the maxima of the semicircle for the component and R and C are the resistance and capacitance respectively. Figure 3.10(b) shows the temperature variation of C_g and C_{gb} obtained from Cole–Cole plots. It can be seen that the values of C_g and C_{gb} decrease with the increment in the temperature. Frequency of the top point of the Cole-Cole plot is relaxation frequency of the orientational polarization ($f_r = 1.29$ Hz for 80 K semicircular arc in Fig. 3.9) and at this frequency dielectric value is maximum. The frequency, where the semi-circle crosses with ordinate axis, corresponds to the minimum dielectric losses of applied field. From the peak of each semicircle of the Cole–Cole
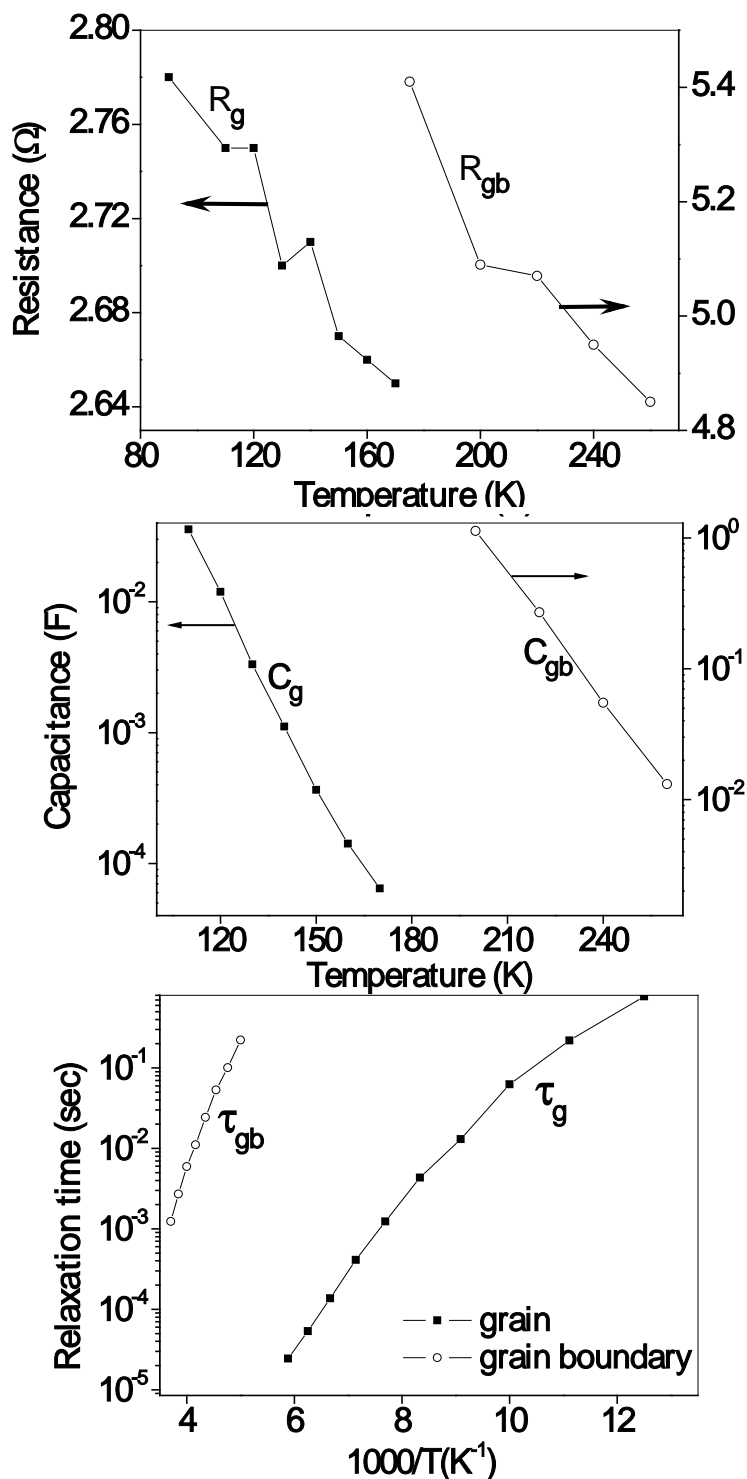
Figure 3.10: *(a), (b), (c) Temperature dependent resistance, capacitance and relaxation time curves for grain and grain boundary contributions respectively.*

plots, the relaxation times due to various effects (grain and grain boundary) were estimated. Figure 3.10c shows the variation of relaxation times τ_g and τ_{gb} with inverse of temperature. These plots are almost linear and obey an Arrhenius relationship:

$$\tau = \tau_0 \exp\left(E_a \middle/ k_B T \right) \tag{6}$$

where E_a is the activation energy for conduction. The values of activation energy due to different contribution as obtained by least squares fitting are $E_g = 0.06$ eV, $E_{gb} = 0.14$ eV.

3.7 Electrical conductivity measurement:

If we assume that all the dielectric loss in the measuring temperature range is due to the conductivity of the sample, then we can calculate the frequency and temperature dependence of ac conductivity (σ) from ε'' using following equation[19]:

$$\sigma = \omega \varepsilon_0 \varepsilon'' \tag{7}$$

where ω is the angular frequency, ε_0 is the permittivity of free space. Figure 3.11a shows the log–log plot of frequency dependence of ac conductivity for DFO at 100 and 150 K temperatures. Conductivity value start increasing around the dielectric loss peak frequency when $\omega \approx \omega_{max}$. As the frequency increases ($\omega \gg \omega_{max}$), $\sigma (\omega)$ exhibits dispersion, increasing in a power-law fashion : $\sigma(\omega) \propto \omega^n$ and log–log plot becoming almost linear. Exponent n represents the degree of interaction between the mobile ions and the lattice around them. However as the temperature increases, the interaction between the charge carriers and the lattice increases which leads to a decrease in n value from 0.95 to 0.77 as the temperature increases from 250 to 350 K. Below 200K, conductivity show a small hump which shifts towards lower frequency with decreasing temperature. It is explained by the space charge polarisation occurring due to oxygen deficiency. It is to be mentioned that at high temperature, some amount of oxygen loss can occur which facilitates the formation of dipoles with an adjacent host ion and enlarge

Chapter 3

the rattling space available for dipole vibration, which as a consequence leads to the short-range hopping of the ions and gives rise to relaxation. The oxygen ions jump between the vacancies, are considered to be responsible for the transition from short-range to long-range hopping and may explain the marked ionic conductivity which shift towards higher frequency side as the temperature increases.

It is seen that σ value decreases with frequency and extrapolation towards lower frequency will give σ_{dc} value which follow Arrhenius law.

$$\sigma_{dc} = \sigma_0 \exp\left(-E_a \middle/ k_B T\right)$$

where σ_o is the pre exponential factor and E_σ, κ_B and T are the activation energy for the conduction, Boltzman's constant, and absolute temperature, respectively. The activation energy for conduction (E_a) was calculated from the slope of the straight lines obtained when σ_{dc} are plotted against 1000/T of samples in figure 3.11b. The activation energy
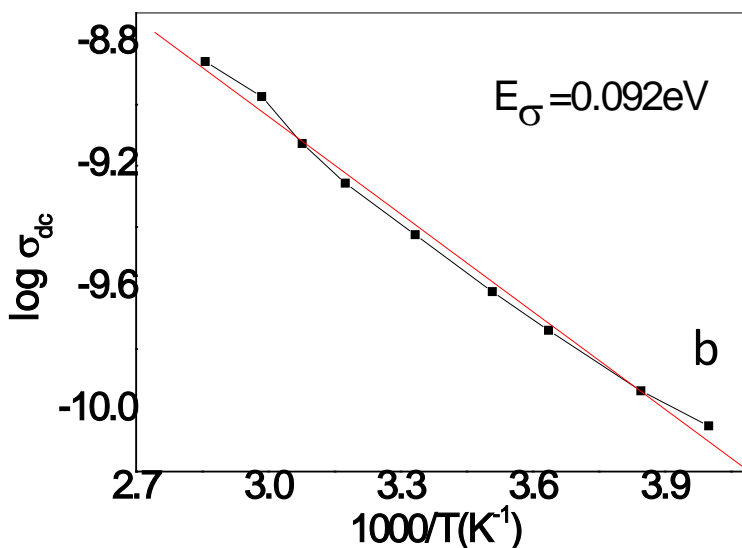
Figure 3.11: *(a) Real part of ac conductivity vs. frequency curves at two temperature values (b) temperature dependent dc conductivity.*

calculated from log σ_{dc} vs 1000/T plot is 0.092eV. Similarly, lower value of activation energy around 0.03eV was also found in nanocrystalline $BiFeO_3$ by us and its strong

temperature dependence seems to be due the oxygen deficiency and reduced particle size.[19] On basis of the summary of conduction mechanisms and associated activation energy values for various semiconductive ferroelectric materials reported by Raymond the conduction mechanism is charge hopping when the activation energy is <0.4 eV. As the activation energy for our material is well below this value we expect this mechanism to apply here as well.[45]

3.8 ac magnetic susceptibility measurement:

To probe the magnetic phase transition and domain dynamics, we performed ac magnetic susceptibility measurement using Physical Property Measurement System
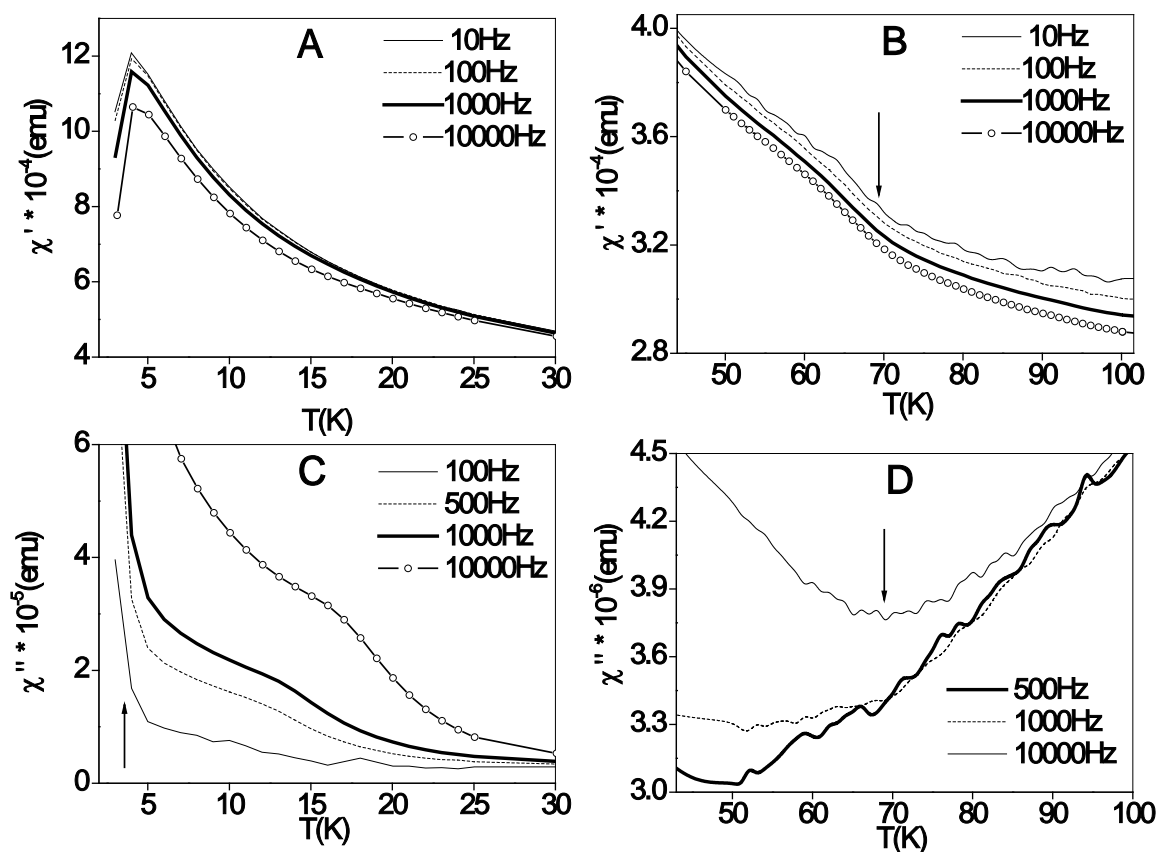
Figure 3.12: Real and imaginary parts of ac magnetization shown in various temperature range for DyFeO₃ nanoparticles.

(PPMS) from Quantum Design Inc., San Diego, CA. Recently we have shown the detail DC magnetization measurements for $DyFeO_3$ nano particle and able to isolate the presence of spin-reorientation transitions near 315 and 70 K due to the Dy^{+3}-Fe^{+3} interaction accompanied with an opening up of the hysteresis loop followed by antiferromagnetic ordering around 4 K due to a possible Dy^{+3}- Dy^{+3} interaction.[46]For detail investigation these magnetic interaction AC magnetic susceptibility is an extremely sensitive technique to detect anomalous behaviour in rare earth ferrite systems such as that caused by spin-reorientation transitions (SRT) which are induced by temperature, magnetic field, domain wall motions, reversible rotation of the magnetic moments or small impurities. To detect these phase transitions at a low temperature, the ac magnetic susceptibility of the $DyFeO_3$ nanoparticles at a lower excitation field (H = 10 Oe) was measured in the temperature range 3-100K and frequency range 10 – 10000 Hz (figure 3.12). The real part of ac susceptibility shows a sudden change in slope at 70 K and imaginary part shows a dip near 70K in figures 3.12 (B, D). This transition temperature corresponds to the spontaneous spin reorientation transition of iron spins T_{SR} due to the coupling between rare earth sublattice with the magnetic moment of Fe sub lattice (Dy - Fe) interaction which was reported by us on the same material using dc magnetization.[46] At lower temperature, the susceptibility χ' increases with decreasing temperature until a sharp peak is observed (figure 3.12A). This sharp peak near 4 K corresponds to the transition from weak ferromagnetic coupling (Dy-Fe), to antiferromagnetic coupling (Dy-Dy) (Néel temperature). This is also consistent with the fact that we did not observe any frequency dependence in this transition temperature (figure 3.12A). Around this antiferromagnetic transition, the imaginary part χ'' (figure 3.12C) starts decreasing where χ' shows a sharp increase before 4 K. At low frequency χ'' shows a single peak at around 10 K at 10 Hz where χ' goes to minima and with increasing frequency this peak shift towards higher temperature side. In general, temperature induced frequency dependent peak in χ'' is associated with dissipation from domain-wall movement, and the drop in χ'' can be understood in terms of pinning of the domain-wall motion in $DyFeO_3$.

3.9 Conclusions:

we have shown that it is possible to synthesize $DyFeO_3$ nanoparticles in single phase using simple hydrothermal process with high crystallinity. Our studies on the magnetization measurements indicate new information on this material in nanosized. Overall, in this case the detailed magnetic properties emphasize the collective as well as individual roles played by the Dy^{3+} and Fe^{3+} ions at various temperatures. Our results for the nanoparticles shows that $DyFeO_3$ undergo reorientation transition at 70 and 315 K where the direction of the net magnetic moment rotates continuously from one crystallographic axis to another due to antisymmetric and anisotropic –symmetric exchange interaction between Fe^{+3} and Dy^{+3}. On further cooling $DyFeO_3$ shows magnetic ordering of the rare earth ions at 4 K. The coexistence of FM and AFM phase at 300 K is supported by the by the shift in hysteresis loop at room temperature which is also explained by the presence of exchange coupling between FM surface and AFM cores at 300 K. we have also studied the dielectric and spin relaxation behavior of the $DyFeO_3$ nanoparticles synthesized by the wet chemical method. We have found from the imaginary part of the impedance spectra that grain and grain boundary both are contributing in relaxation mechanism as further confirmed by the Cole-Cole spectra. An analysis of cole- cole spectra confirm that resistance and capacitance of grain and grain boundary is temperature dependent and continuously decreasing with increase in temperature but relaxation time increases with temperature. All these measurement confirms that relaxation mechanism is governed by Maxwell – Wagner relaxation. Ac magnetic susceptibility measurement shows that spin reorientation transition takes place around 70 K. During this transition temperature there is remarkable change in slope in both the in-phase and the out-of-phase magnetic susceptibility components. Below this temperature around 4 K real component shows a sharp peak for Neel transition and imaginary component shows a dip in value which corresponds to pinning of the domain wall motion.

3.10 References:

1.   Yamaguchi, T.; Tsushima, K., Magnetic Symmetry of Rare-Earth Orthochromites and Orthoferrites. *Physical Review B* **1973,** 8, (11), 5187- 5198.

2.   Tokunaga, Y.; Iguchi, S.; Arima, T.; Tokura, Y., Magnetic-field-induced ferroelectric state in $DyFeO_3$. *Physical Review Letter* **2008,** 101, (9), 097205.

3.   Rykov, A. I.; Pavlukhin, Y. T.; Syrotina, N. I.; Boldyrev, V. V., Structure of amorphous ferrites of Lanthanum, Dysprosium and Bismuth. *Reactivity of Solids* **1989,** 7, (1), 29-42.

4.   Aono, H.; Traversa, E.; Sakamoto, M.; Sadaoka, Y., Crystallographic characterization and NO_2 gas sensing property of $LnFeO_3$ prepared by thermal decomposition of Ln-Fe hexacyanocomplexes, $Ln[Fe(CN)_6]$center dot nH_2O, Ln = La, Nd, Sm, Gd, and Dy. *Sensors and Actuators B-Chemical* **2003,** 94, (2), 132-139.

5.   Rao, G. V. S.; Chandras.Gv; Rao, C. N. R., Are rare earth ortho chromites ferroelectric. *Solid State Communications* **1968,** 6, (3), 177.

6.   Rao, G. V. S.; Wanklyn, B. M.; Rao, C. N. R., Electrical transport in rare earth ortho chromites, ortho manganites and ortho ferrites. *Journal of Physics and Chemistry of Solids* **1971,** 32, (2), 345.

7.   Haumont, R.; Kreisel, J.; Bouvier, P.; Hippert, F., Phonon anomalies and the ferroelectric phase transition in multiferroic $BiFeO_3$. *Physical Review B* **2006,** 73, (13), 132101.

8.   Parida, S. C.; Rakshit, S. K.; Singh, Z., Heat capacities, order-disorder transitions, and thermodynamic properties of rare-earth orthoferrites and rare-earth iron garnets. *Journal of Solid State Chemistry* **2008,** 181, (1), 101-121.

9.   Rezlescu, N.; Rezlescu, E.; Pasnicu, C.; Craus, M. L., Effect of the rare earth ions on some properties of a nickel zinc ferrite. *Journal of Physics-Condensed Matter* **1994,** 6, (29), 5707-5716.

10.   Jaiswal, A.; Das, R.; Vivekanand, K.; Maity, T.; Abraham, P. M.; Adyanthaya, S.; Poddar, P., Magnetic and dielectric properties and Raman spectroscopy of $GdCrO_3$ nanoparticles. *Journal of Applied Physics* **2010,** 107, (1), 013912.

11.   Satoh, H.; Koseki, S.; Takagi, M.; Chung, W. Y.; Kamegashira, N., Heat capacities of $LnCrCO_3$ (Ln=rare earth). *Journal of Alloys and Compounds* **1997,** 259, (1-2), 176-182.

12.   Aliouane, N.; Prokhnenko, O.; Feyerherm, R.; Mostovoy, M.; Strempfer, J.; Habicht, K.; Rule, K. C.; Dudzik, E.; Wolter, A. U. B.; Maljuk, A.; Argyriou, D. N., Magnetic order and ferroelectricity in $RMnO_3$ multiferroic manganites: coupling between R- and Mn-spins. *Journal of Physics-Condensed Matter* **2008,** 20, (43), 12.

13.   Lal, H. B.; Dwivedi, R. D.; Gaur, K., Pyroelectric and dielectric properties of some light rare-earth orthochromites. *Journal of Materials Science: Materials in Electronics* **1990,** 1, (4), 204-208.

14.   Prelorendjo, L. A.; Johnson, C. E.; Thomas, M. F.; Wanklyn, B. M., Spin reorientation transition in $DyFeO_3$ induced by magnetic fields. *Journal of Physics C-Solid State Physics* **1980,** 13, (13), 2567-2578.

15.   Johnson, C. E.; Prelorendjo, L. A.; Thomas, M. F.,Field induced spin reorientation in orthoferrites $DyFeO_3$, $HoFeO_3$ and $ErFeO_3$. *Journal of Magnetism and Magnetic Materials* **1980,** 15-8, (JAN-), 557-558.

16.   Tokunaga, Y.; Iguchi, S.; Arima, T.; Tokura, Y., Magnetic-field-induced ferroelectric state in $DyFeO_3$. *Physical Review Letters* **2008,** 101, (9).

17.   Goto, T.; Kimura, T.; Lawes, G.; Ramirez, A. P.; Tokura, Y., Ferroelectricity and giant magnetocapacitance in perovskite rare-earth manganites. *Physical Review Letters* **2004,** 92, (25).

18.   Jaiswal, A.; Das, R.; Vivekanand, K.; Abraham, P. M.; Adyanthaya, S.; Poddar, P., Effect of Reduced Particle Size on the Magnetic Properties of Chemically Synthesized $BiFeO_3$ Nanocrystals. *Journal of Physical Chemistry C* **2010,** 114, (5), 2108-2115.

19.   Jaiswal, A.; Das, R.; Maity, T.; Vivekanand, K.; Adyanthaya, S.; Poddar, P., Temperature-Dependent Raman and Dielectric Spectroscopy of $BiFeO_3$ Nanoparticles: Signatures of Spin-Phonon and Magnetoelectric Coupling. *Journal of Physical Chemistry C* **2010,** 114, (29), 12432-12439.

20.   Das, R.; Jaiswal, A.; Adyanthaya, S.; Poddar, P., Origin of Magnetic Anomalies below the Neel Temperature in Nanocrystalline LuMnO$_3$. *Journal of Physical Chemistry C* **2010,** 114, (28), 12104-12109.

21.   Jagannathan, R.; Parmar, A. S.; Adyanthaya, S.; Prabhune, A.; Muschol, M.; Poddar, P., In Situ Observation of Antibiotic Mediated Concurrent Growth of Two Distinct Homogeneous Populations of Gold Nanoparticles in Solution Phase. *Journal of Physical Chemistry C* **2009,** 113, (9), 3478-3486.

22.   Jagannathan, R.; Poddar, P.; Prabhune, A., Cephalexin-mediated synthesis of quasi-spherical and anisotropic gold nanoparticles and their in situ capping by the antibiotic. *Journal of Physical Chemistry C* **2007,** 111, (19), 6933-6938.

23.   Younan, X.; Yujie, X.; Byungkwon, L.; Sara , E. S., Shape-Controlled Synthesis of Metal Nanocrystals: Simple Chemistry Meets Complex Physics? *Angewandte Chemie International Edition* **2009,** 48, (1), 60-103.

24.   Grosvenor, A. P.; Kobe, B. A.; Biesinger, M. C.; McIntyre, N. S., Investigation of multiplet splitting of Fe 2p XPS spectra and bonding in iron compounds. *Surface and Interface Analysis* **2004,** 36, (12), 1564-1574.

25.   Yin, L.; Adler, I.; Tsang, T.; Matienzo, L. J.; Grim, S. O., Paramagnetism and shake-up satellites in X-ray photoelectron spectra. *Chemical Physics Letters* **1974,** 24, (1), 81-84.

26.   Han, K. D.; Zhang, Y. J.; Cheng, T.; Fang, Z. Y.; Gao, M. R.; Xu, Z. Y.; Yin, X. B., Self-assembled synthesis and photoluminescence properties of uniform Dy$_2$O$_3$ microspheres and tripod-like structures. *Materials Chemistry and Physics* **2009,** 114, (1), 430-433.

27.   Nogues, J.; Sort, J.; Langlais, V.; Skumryev, V.; Surinach, S.; Munoz, J. S.; Baro, M. D., Exchange bias in nanostructures. *Physics Reports-Review Section of Physics Letters* **2005,** 422, (3), 65-117.

28.   Holmes, L.; Vanuiter.Lg; Hecker, R., Effect of Co on magnetic properties of ErFeO$_3$, HoFeO$_3$, and DyFeO$_3$. *Journal of Applied Physics* **1971,** 42, (2), 657.

29.   Durbin, G. W.; Johnson, C. E.; Thomas, M. F., Direct observation of field induced spin reorientation in YFeO3 by Mossbauer effect. *Journal of Physics C-Solid State Physics* **1975,** 8, (18), 3051-3057.

30.   Durbin, G. W.; Johnson, C. E.; Thomas, M. F., Temperature dependence of field induced spin reorientation in $GdFeO_3$. *Journal of Physics C-Solid State Physics* **1977,** 10, (11), 1975-1978.

31.   Nikolov, O.; Hall, I.; Godfrey, K. W., A mossbauer study of temperature driven spin reorientations in $Dy_{1-X}Ho_XFeO_3$. *Journal of Physics-Condensed Matter* **1995,** 7, (25), 4949-4965.

32.   Moriya, T., Anisotropic Superexchange Interaction and Weak Ferromagnetism. *Physical Review* **1960,** 120, (1), 91-98.

33.   Dzialoshinski, I., A thermodynamic theory of weak ferromagnetism of antiferromagnetics. *Journal of Physics and Chemistry of Solids* **1958,** 4, (4), 241-255.

34.   Berton, A.; Sharon, B., Specific Heat of $DyFeO_3$ from 1.2^0-80^0K. *Journal of Applied Physics* **1968,** 39, (2), 1367-1368.

35.   Poddar, P.; Telem-Shafir, T.; Fried, T.; Markovich, G., Dipolar interactions in two- and three-dimensional magnetic nanoparticle arrays. *Physical Review B* **2002,** 66, (6), 060403(R).

36.   Bidaux, R.; Bouree, J. E.; Hammann, J., Dipolar interactions in rare-earth orthoferrites.1. $YFeO_3$ and $HOFeO_3$. *Journal of Physics and Chemistry of Solids* **1974,** 35, (12), 1645-1655.

37.   Ozdemir, O.; Dunlop, D. J.; Berquo, T. S., Morin transition in hematite: Size dependence and thermal hysteresis. *Geochemistry Geophysics Geosystems* **2008,** 9.

38.   Frandsen, C.; Morup, S., Inter-particle interactions in composites of antiferromagnetic nanoparticles. *Journal of Magnetism and Magnetic Materials* **2003,** 266, (1-2), 36-48.

39.   Maier, J.; Prill, S.; Reichert, B., Space charge effect in polycrystalline, micropolycrystalline and thin film samples- application to AGCL and AGBR. *Solid State Ionics* **1988,** 28, 1465-1469.

40.   Kroger, F. A.; Vink, H. J., Relations between the concentration of imperfections in crystalline solids. *Solid State Physics-Advances in Research and Applications* **1956,** 3, 307-435.

41.   Verwey, E. J.; Haayman, P. W.; Romeijn, F. C., Physical properties and cation arrangement of oxides with spinal structure .2. electron conductivity. *Journal of Chemical Physics* **1947,** 15, (4), 181-187.

42.   Cole, K. S.; Cole, R. H., Dispersion and absorption in dielectrics I. Alternating current characteristics. *Journal of Chemical Physics* **1941,** 9, (4), 341-351.

43.   Cole, K. S.; Cole, R. H., Dispersion and absorption in dielectrics II Direct current characteristics. *Journal of Chemical Physics* **1942,** 10, (2), 98-105.

44.   Suman, C. K.; Prasad, K.; Choudhary, R. N. P., Impedance analysis of $Pb_2Sb_3LaTi_5O_{18}$ ceramic. *Materials Chemistry and Physics* **2006,** 97, (2-3), 425-430.

45.   Raymond, O.; Font, R.; Suarez-Almodovar, N.; Portelles, J.; Siqueiros, J. M., Frequency-temperature response of ferroelectromagnetic $Pb(Fe_{1/2}Nb_{1/2})O_3$ ceramics obtained by different precursors. Part I. Structural and thermo-electrical characterization. *Journal of Applied Physics* **2005,** 97, (8). 084107

46.   Jaiswal, A.; Das, R.; Poddar, P., Surface Effects on Morin Transition, Exchange Bias and Enchanced Spin Reorientation in Chemically Synthesized $DyFeO_3$ nanoparticles. *Journal of Physical Chemistry C* **2011,** 115, 2954–2960.

Chapter 4

Optical, Magnetic, Dielectric and Raman Spectroscopic Study of GdCrO$_3$ Nanoparticles.
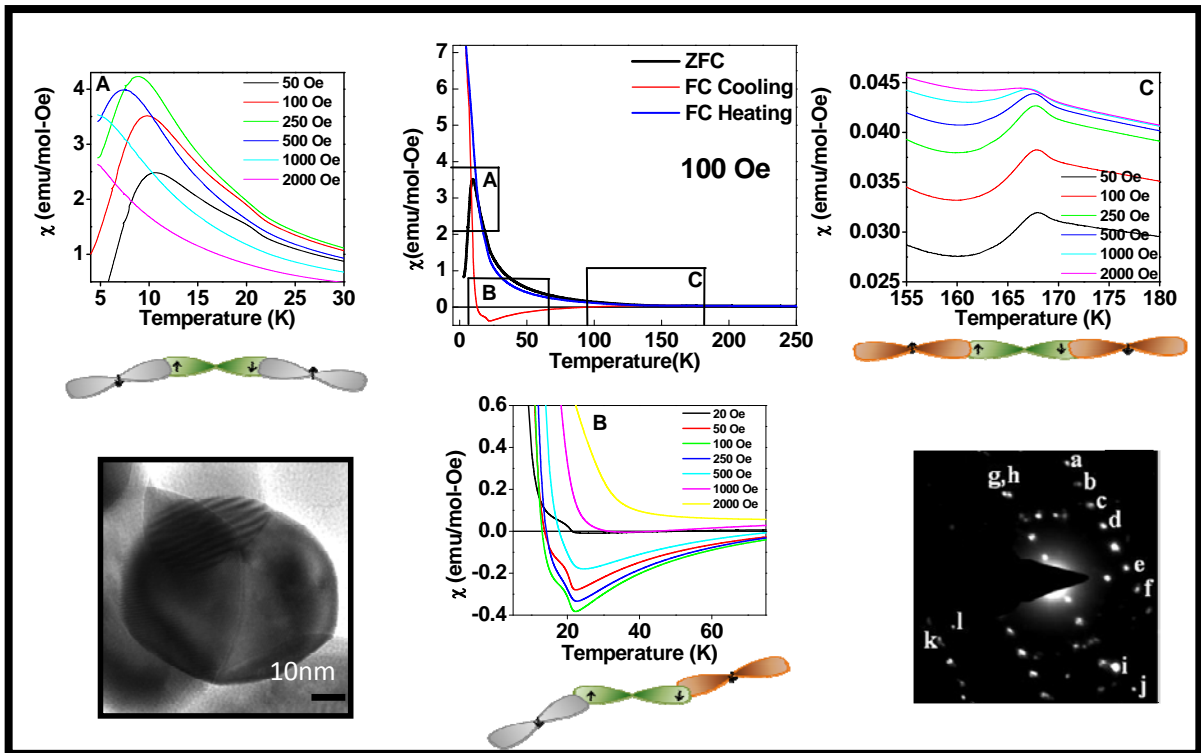
Outline

The rare earth orthoferrites and chromites are extremely interesting due to the richness of their optical dielectric and magnetic properties. In this chapter we have shown the detailed synthesis mechanism of GdCrO$_3$ nanoparticles of size ranging from 40 to 60 nm and study of structural, optical, Raman spectra as well as magnetic & dielectric properties. The magnetic properties are dictated by the Cr^{3+}-Cr^{3+}, Gd^{3+}-Cr^{3+} and Gd^{3+}-Gd^{3+} superexchange interactions in different temperature regions as the magnitude of their interaction differs resulting in to first giving an antiferromagnetic ordering at 167 K

due to the Cr^{3+}-Cr^{3+} followed by a weak ferromagnetism due to the onset of Cr^{3+}-Gd^{3+} interactions (opening up of the hysteresis loop) and at further low temperature, it shows weak antiferromagnetic ordering due to Gd^{3+}-Gd^{3+} interaction. At low temperature (< 95 K) GdCrO₃ nanoparticles showed the presence of negative magnetization due to Gd^{3+} and Cr^{3+} interaction resulting into weak ferromagnetic coupling. Overall, magnetic properties showed excellent markers of the interplay of both Gd^{3+} and Cr^{3+} ions. The Raman spectroscopy shows characteristic Raman shifts indicating that below 450 cm^{-1} Gd^{3+} ions play a dominant role in determining the phonon frequencies of GdCrO₃, and above 450 cm^{-1}, the Cr^{+3} ions dominate. GdCrO₃ is ferroelectric at room temperature. We also present for the first time the low temperature dielectric constant and loss tangent data for the GdCrO3 in the temperature range from 15 - 325 K in a broad frequency range.

The work described in this chapter is published as –

➢ **Synthesis and Optical Studies of GdCrO₃ Nanoparticles.**
  Adhish Jaiswal, *Raja Das, Suguna Adyanthaya, Pankaj Poddar[*] J Nanopart Res 13, 1019 ((2010)*

➢ **Magnetic and dielectric properties and Raman spectroscopy of GdCrO₃ nanoparticles.**
  Adhish Jaiswal, *Raja Das, K. Vivekanand, Tuhin Maity, Priya Mary Abraham, Suguna   Adyanthaya, and Pankaj Poddar *, J. Appl. Phys. 107, 013912 (2010)*

4.1 Introduction:

Since last seven decades or more, binary and ternary oxides of transition and rare-earth elements such as reverse spinel ferrites, manganites have been studied in detail for their rich interplay of spin, charge, orbital ordering, crystal field effect, ferroelectric polarization etc.[1-3] , The famous Verwey transition observed in Fe_3O_4 is an example of existence of both short range and long range charge ordering with interesting size dependent effects.[4-6] Recently, there is a renewed interest in rare earth ferrites, manganites and chromites due to the possible magnetoelectric coupling in these materials.[7-12] One of these compounds- $GdCrO_3$ belongs to the same family of compounds with a general formula of $RCrO_3$ (R=rare earth cations) and is reported to crystallize in a distorted perovskite structure.[13] Rare earth orthochromites show extremely rich magnetic properties due to the interaction between R^{+3} and Cr^{+3} ions leading to various types of magnetic ordering at low temperatures. The antiferromagnetic ordering temperature due to Cr^{3+}-Cr^{3+} is greatly affected by the rare earth ionic radius and goes up linearly with an increase in the ionic radius in the lanthanide series from 135 K for $ErCrO_3$ to 289 K for $LaCrO_3$.[14] This increase in the ordering temperature might be due to the increase in the lattice distortion and an decrease in the Cr^{3+}-O^{2-}-Cr^{3+} distance (thereby varying the intercationic superexchange interaction) with an increase in the size of the rare earth ion.[15, 16] Additionally, the optical properties of these compounds are quite interesting where both rare earth and transition metal ions play an important role. In fact, these materials are not very far from much studied manganites with perovskite structure. However, in contrast to the orthochromites such as $GdCrO_3$ where both Gd^{3+} and Cr^{+3} are magnetic in nature, in some other perovskite materials (general formula ABO_3) such as $BiFeO_3$, $BiMnO_3$, $LaMnO_3$ etc. one of the cations A^{3+} is nonmagnetic and does not participate in the magnetic properties. In such a case, magnetism is governed by the B^{+3} cations. For an example, in $BiFeO_3$, this leads to a Fe–O–Fe antiparallel arrangement giving rise to a (G-type) antiferromagnetic ordering.[17] Similarly in $BiMnO_3$[18], $YMnO_3$[19], the four $3d$ electrons combined with super-exchange interaction should cause an antiferromagnetic

spin arrangement. Materials such as LaMnO$_3$ have an (A-type) antiferromagnetic structure but in the presence of Ca^{2+} or Sr^{2+} ions, they exhibit tunable electrical and magnetic properties.[4,5] As we emphasized earlier, in all such cases, only B^{3+} ion is magnetic in nature. If A^{3+} is replaced by a cations such as Gd^{3+} (half filled 4f^7) ions then these ions will also play a crucial role in deciding the overall magnetic as well as optical properties. Such a system has a magnetic superexchange coupling between both magnetic ions (A & B) and creates an anomalous magnetic behaviour in the system. The coupling between the different magnetic ions reveals an interesting temperature dependent magnetic interaction. Interestingly, it is shown that below certain temperature, almost all the RMO$_3$ compounds are supposed to show the magnetoelectric effect due to the lack of the inversion symmetry where an applied electric field induces a net magnetization in the material which is proportion to the electric field and similarly an applied magnetic field induces an electric polarization which is proportional to the external magnetic field.[20] The fundamental question about the possibility of ferroelectric ordering in some of the polycrystalline rare earth orthochromite with perovskite or distorted perovskite structure was discussed for the first time by C. N. R. Rao and coworkers back in 1967.[21] Based on the resistivity vs. temperature and polarization measurements they suspected the presence of ferroelectric ordering in DyCrO$_3$, HoCrO$_3$, YbCrO$_3$ and LuCrO$_3$.[21] Here, the distortion in the oxygen polyhedral surrounding the Cr^{3+} seems to be the reason behind the ferroelectric behavior.[21] These materials are reported to show p-type extrinsic semiconducting behavior due to the impurities of Cr^{4+} or Cr^{6+} in the lattice.[22] In fact, bulk GdCrO$_3$ shows multiple ferroelectric ordering transitions (Curie temperature); the first one at 360 K and the other at 425 K above which the spontaneous polarization goes to zero.[16] The dielectric properties of this material below room temperature in bulk regime are not reported so for.

However, for any potential application of these materials in small dimensions, it was important to fully understand their properties as a function of the grain size where several times these changes could be undesirable. As an example, BiFeO$_3$, which was being studied in detail for its multiferroic properties in bulk and thin film showed a

sizable hysteresis and finite coercivity in nanosize below 100 K.[23] Such a deviation from bulk to nano size was still being debated and reported to be due to the breaking of helical ordering or incomplete rotation of the spins along the antiferromagnetic axis which could give rise to an enhanced magnetization as the decrease in particle size below the periodicity of helical ordering could led to the suppression of modulated spin structure.[24] However, the rare earth ferrites, chromites and manganites with multiferroic properties have not been explored much for their properties when the grain size is reduced below 100 nm as the synthesis of these rare earth complex oxides with a control over phase purity and crystallinity at nanoscale was quite difficult.[25] The conventional chemical techniques such as coprecipitation, reverse-micelle, hot-injection etc. were unable to produce the desired phase. Due to this reason, the reported physical properties of most of these materials were confined in to the bulk phase.

In this chapter, we have shown that it is possible to use the modified hydrothermal technique to stabilize the $GdCrO_3$ phase in nanosized. To the best of our knowledge, no research has been reported on the synthesis of $GdCrO_3$ nanoparticles so far although solid state methods[26] and flux grown methods[27] have been used previously to synthesize bulk polycrystalline and single crystalline $GdCrO_3$. We have shown the possible mechanism behind the synthesis and a detailed investigation of the magnetic, dielectric properties as well as Raman spectroscopy on $GdCrO_3$ nanoparticles. Additionally, we present a detailed characterization of $GdCrO_3$ nanoparticles using X-ray diffraction (XRD), Transmission electron microscopy (TEM), High-resolution transmission electron microscope (HRTEM), X-ray photoelectron spectroscopy (XPS), UV-vis absorption, photoluminescence and FTIR spectroscopy techniques.

4.2 Hydrothermal synthesis of nanocrystalline $GdCrO_3$:

The wet-chemical synthesis of rare earth complex oxides in nano size is quite challenging and non-trivial. As most of the time, the desired phase is formed at much higher pressure

and temperature. Here, we have used hydrothermal technique to synthesize GdCrO$_3$
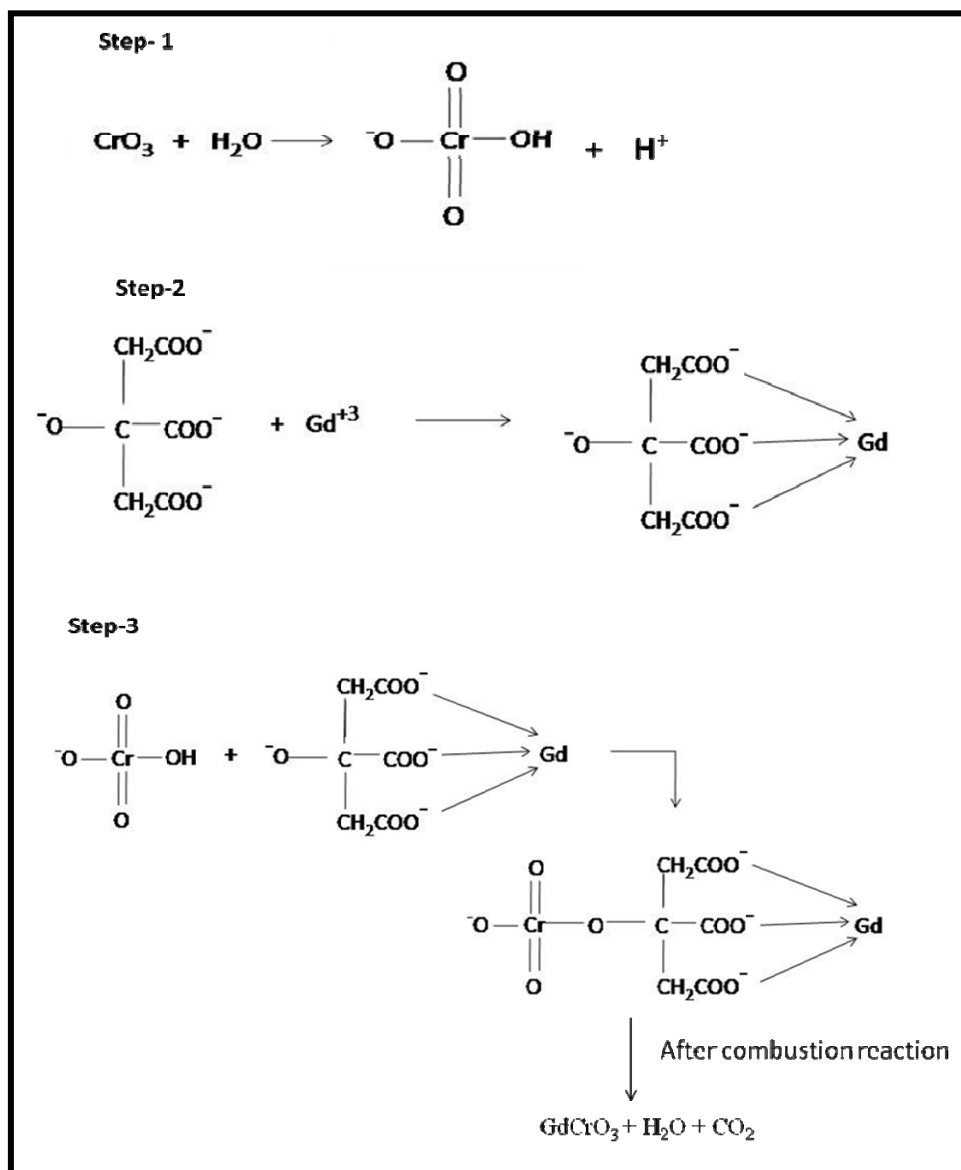
Figure 4.1: Schematic showing the proposed reaction mechanism for the synthesis of GdCrO$_3$ nanoparticles. After the step 3, the material undergoes the hydrothermal process thereby forming the GdCrO$_3$ nanoparticles.

nanoparticles. The rationale behind using high pressure hydrothermal synthesis route over other techniques is that for the synthesis of complex oxide nanomaterials, this technique has an edge over other synthesis routes. For this purpose, stoichiometric

amounts of gadolinium acetate ($Gd(CH_3COO)_3$, Sigma-Aldrich, 99.9%) chromium tri oxide (CrO_3, S. D. Fine-Chem. Pvt. Ltd., 99%) and an equal amount of citric acid (metal/citric acid molar ratio = 1/1)] (obtained from Merck, 99.5%) were dissolved in the deionized water so that the metal ions could be uniformly complexed together. This was followed by the drop-wise addition of ammonia solution (28 wt. %) to neutralize the unreacted citric acid as well as to raise the pH value of the solution near 9.2 resulting into a sol formation due to metal citrate complex. Nearly 150 ml of metal citrate complex was transferred to a 200 ml capacity autoclave with the Teflon liner and heated at 150^0C for 20h. After the completion of the reaction, the precipitate was in turn filtered, washed with deionized water, re-filtered and finally dried at 160^0C for 5 h.[28] In figure 4.1, we have shown a detailed synthesis mechanism which is non-trivial and not reported elsewhere.

4.3 Characterisation:

4.3.1 X-ray diffraction and Pawley refinements:

The $GdCrO_3$ crystallizes in a distorted perovskite type structure with four formula units per unit cell where the distortion is due to the mismatch of Gd—O and Cr—O bond lengths.[13, 26] This distortion further increases with decrease in the ionic radius of the rare earth ion. In figure 4.2, we have shown the powder x-ray diffraction pattern (XRD) of the as-synthesized $GdCrO_3$ nanocrystals recorded by a PANalytical X'PERT PRO instrument using an iron-filtered Cu-Kα radiation (λ=1.5406 Å) in the 2θ range of 10°- 80° with a step size of 0.02^0.

We used the Materials Studio Software from Accelrys Inc. to perform the Pawley refinement to determine the lattice parameters of the $GdCrO_3$ nanocrystals from the experimental data. The pseudo-Voigt peak shape was selected for these refinements. The refined lattice parameters were *a*= 5.30993 ± 0.00221, *b*= 5.51793 ± 0.00226, and *c*= 7.60426 ± 0.00315Å. with an excellent Rwp value of 5.20%. The difference in the experimental and simulated data was also shown in figure 4.2. The average crystallite size as calculated using Debye-Scherrer formula was found to be around 35-40 nm.
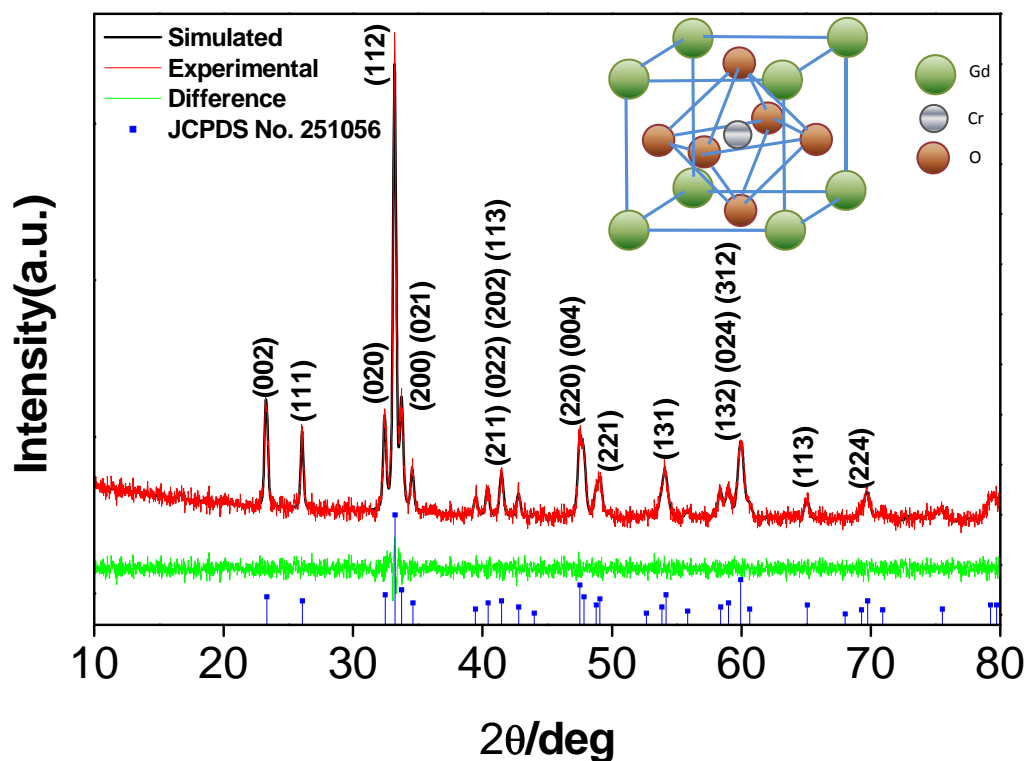
Figure 4.2: Room temperature experimental powder XRD pattern compared with the simulated and difference NPD profiles (using Powley refinement) for GdCrO₃ nanocrystals. The blue lines are the reference values for GdCrO₃ taken from the JCPDS Card No. 251056. The inset shows schematic representation of perovskite structure of GdCrO₃ (lattice distortion is not shown here).

4.3.2 Determination of shape and size of the nanoparticles:

To further investigate the microstructure and morphology of the as-synthesized material, we used the FEI (model Tecnai F30) high resolution transmission electron microscope (HRTEM) equipped with field emission source operating at 300KV to image the drop-coated dilute solution of GdCrO₃ in amyl acetate on carbon-coated copper TEM grids. In figure 4.3 (A, B) we have shown TEM images taken on same sample from various places at varying resolution. We believe that in the formation of plate like nanoparticles in the synthesis adopted by us, preferential binding of both nitrate and
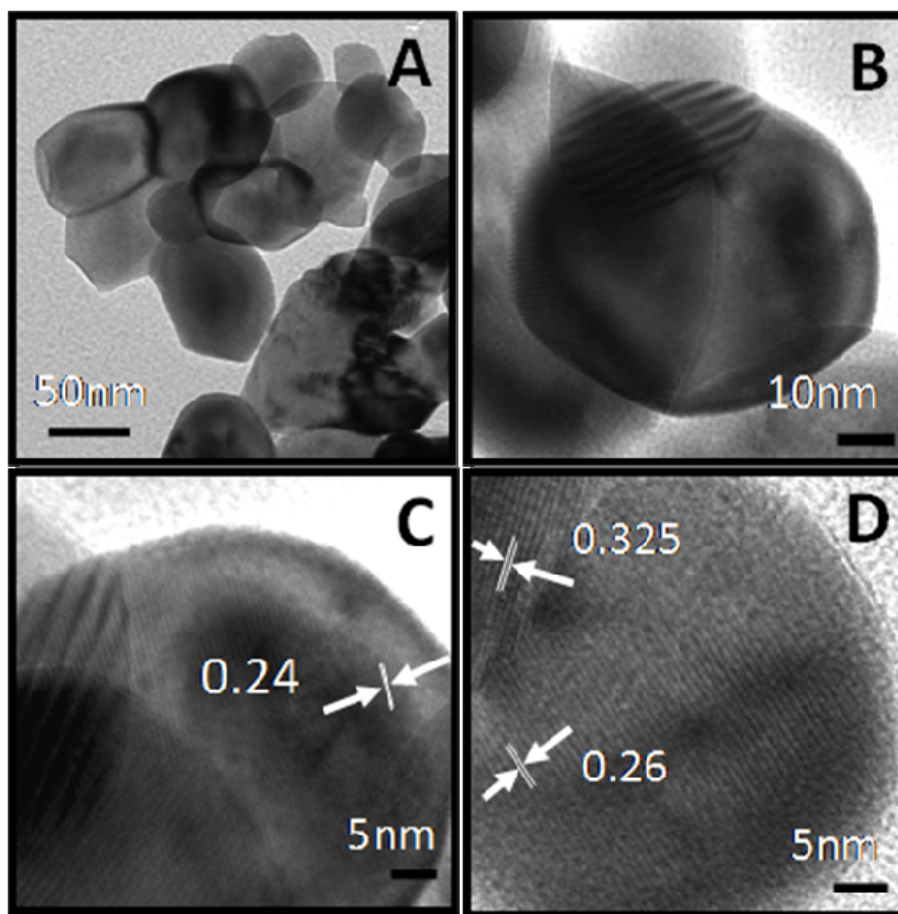
Figure 4.3 Transmission electron micrographs of GdCrO₃ nanoparticles. The d-values calculated in some of these images are in the nanometer units.

citrate ions with metal ions at particular crystalline facets might have promoted the formation of negatively charged anisotropic structures much similar to the role of halide ions in the formation of anisotropic gold nanoparticles.[29] The size obtained from TEM image was slightly larger than the crystallite size obtained by the Debye- Scherrer equation. The particles, after drying out of amyl acetate on the TEM grids, often showed overlapping and stacking due to their plate-like morphology. The panels (C, D) clearly showed presence of lattice fringes reflecting good crystallinity. The d-values calculated from these images (shown in the nm scale) matched with those obtained from powder
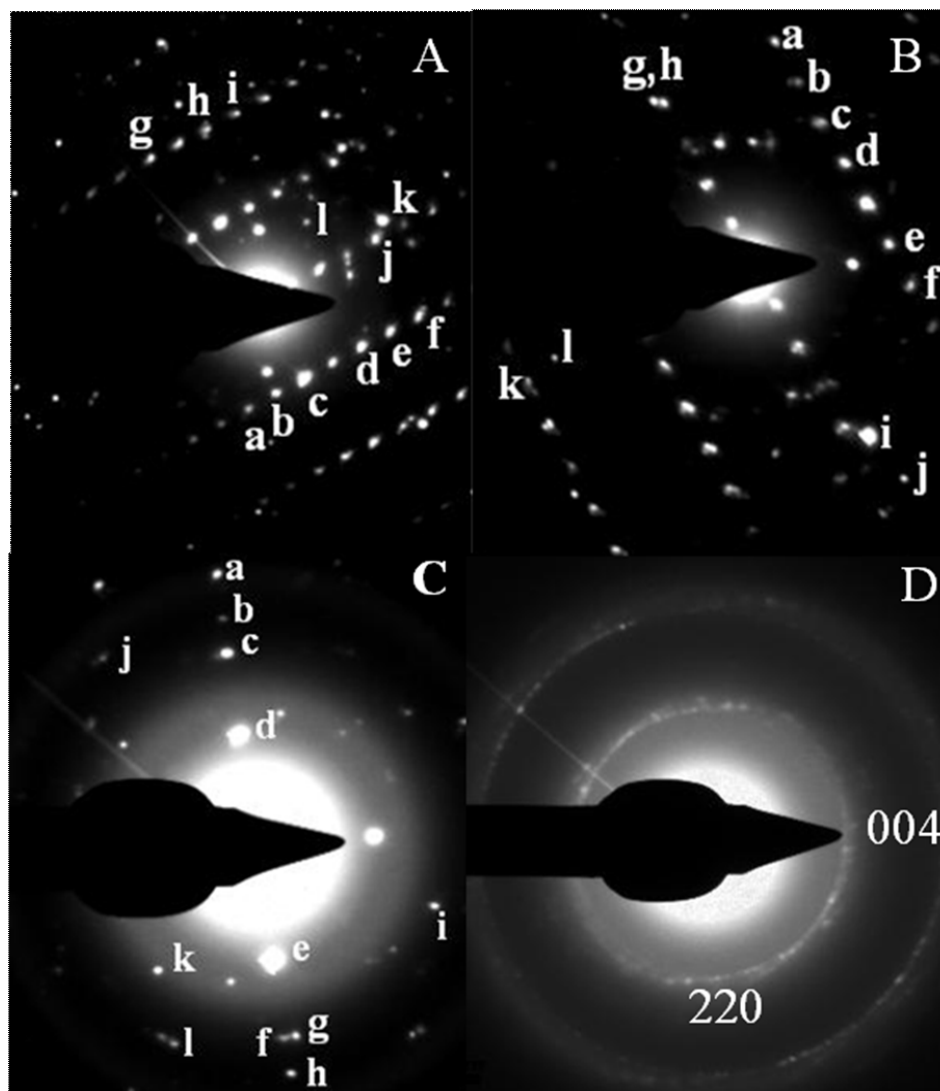
Figure: 4.4 Selected area electron diffraction patterns of GdCrO₃ nanoparticles. The dots representing particular crystalline planes are tabulated in Table 4.1

XRD. In figure 4.4, we have shown various panels showing the selected area electron diffraction patterns (SAED) taken from the same sample at various places. In panels A and B, the nice square patterns clearly showed that majority of particles were defect-free and single crystalline in nature, the ring patterns in the panels C and D were due to the overlap/stacking of the particles. We indexed the electron diffraction patterns and the results are tabulated in table 4.1

Table 4.1: *Lattice planes listed in the table represent the dots shown in the selected area diffraction patterns in panels A, B and C of figure 4.4*

Lattice plane	Panel A	Panel B	Panel C
a	(122)	(041)	(243)
b	(211)	(311)	(142)
c	(021)	(220)	(223)
d	(122)	(022)	(112)
e	(131)	(211)	(112)
f	(133)	(220)	(024)
g	(332)	(024)	(312)
h	(142)	(311)	(400)
i	(225)	(133)	(132)
j	(130)	(421)	(332)
k	(132)	(421)	(004)
l	(021)	(040)	(133)

Chapter 4

4.4 Optical Properties :

4.4.1 UV-vis-IR absorption spectroscopy measurements:

The room temperature optical properties of $GdCrO_3$, such as UV-vis-IR absorption spectroscopy, photoluminescence and infrared spectra are not reported in literature so far (even in the bulk form). In figure 4.5, we have compared the UV–vis -NIR spectra for the $GdCrO_3$ nanoparticles with the precursor used in the synthesis (CrO_3 and gadolinium acetate) in the diffused reflectance mode using a Jasco UV-vis-NIR spectrometer (model V570) operated at a resolution of 2 nm. To our knowledge, this is the
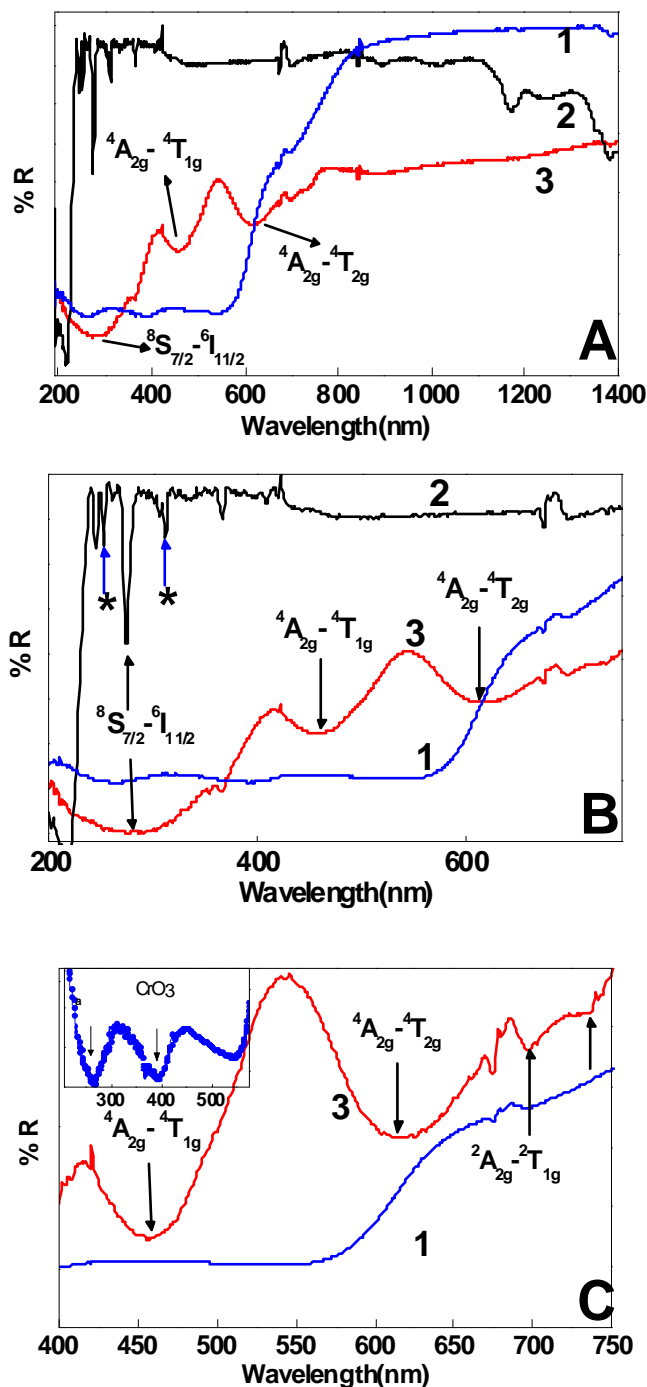
Figure 4.5: The diffuse reflectance UV–vis-NIR spectra for CrO_3 (curve 1), gadolinium acetate (curve 2) and $GdCrO_3$ (curve 3). Panel A shows the complete wavelength range and panels B, C show zoom views of selected regions. In panel B, the transitions in gadolinium acetate (curve 2) $^8S_{7/2}$–^6D_J around 252 nm and $^8S_{7/2}$–$^6P_{7/2}$ at 310 nm are marked with *. In the inset of panel C, we have shown the zoom view to show the electronic transitions in CrO_3.

Ph.D. Thesis   *Adhish Kumar Jaiswal*   *University of Pune*

first report of room temperature UV-vis absorption spectra and its in-depth data analysis for GdCrO$_3$ as mentioned earlier. The rare earth ions such as Gd^{3+} which have half-filled $4f^7$ electronic configuration could have $4f \rightarrow 4f$, $4f \rightarrow 5d$ transitions as well as charge transfer transitions in different energy ranges. Among them, the $4f \rightarrow 5d$ and charge transfer transitions would occur at much higher energies (well beyond the limit of our instrument). The ultraviolet absorptions (240–320 nm) seen in figure 4.5 was related to the electronic transitions in Gd^{3+} ions.[30] The broad dip at 274 nm was due to the $^8S_{7/2} \rightarrow {}^6I_{11/2}$ absorption of Gd^{3+} which was seen as a very sharp absorption in gadolinium acetate as well. Apart from this transition, the precursor- Gd(CH$_3$COO)$_3$ also showed the dominant absorption lines in the UV range for transition $^8S_{7/2} \rightarrow {}^6D_J$ around 252 nm and $^8S_{7/2} \rightarrow {}^6P_{7/2}$ at 310 nm of Gd^{3+} ions (shown as *). However, after the formation of GdCrO$_3$ nanoparticles, these peaks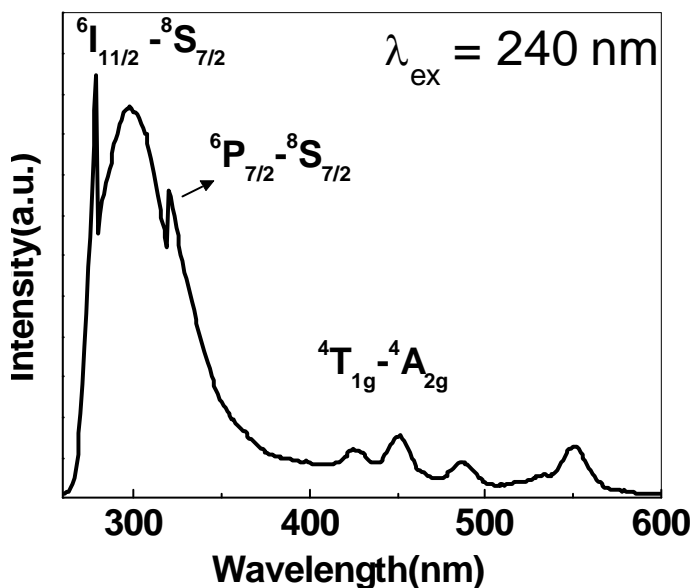 merged and resulted in a broad peak as observed in the curve corresponding to GdCrO$_3$ nanoparticles. In lower panel of figure 4.5, we have shown the zoom view of the top panel in a different energy range to highlight the electronic transitions in Cr^{3+} in GdCrO$_3$ nanoparticles. The peaks for electronic transitions in Cr^{+3} in GdCrO$_3$ nanoparticles (curve 3) were seen at a relatively lower energies at 450, 612 and 698, 736 nm originating from the $^4A_{2g} \rightarrow {}^4T_{1g}$, $^4A_{2g} \rightarrow {}^4T_{2g}$ and $^2A_{2g} \rightarrow {}^2T_{1g}$, $^2A_{2g} \rightarrow {}^2E_{2g}$ transitions respectively.[31] The mechanism responsible for these bands could be explained by the crystal field splitting. The octahedral crystal field around the Cr^{3+} ion was responsible in splitting the $4f$ level into a ground state orbital singlet $^4A_2$ and excited state orbital triplets $^4T_2$ and $^4T_1$. Additionally, due to the crystal field, splitting of the free-ion excited state $2G$ gave rise to level $2E$. The broad absorption bands were due to transitions from level $^4A_2$ to the level $^4T_2$ (band centered at 612 nm) and $^4T_1$ (band centered at 460 nm). Transitions from the ground state $^4A_2$ to the level $2E$ led to narrow absorption band overlapping with the wing of the broad absorption band due to transition from $^4A_2$ to $2E$ (band centered at 735 nm).[32] In comparison to this, the curve corresponding to precursor (CrO$_3$) did not show these transitions (inset in panel C). In contrast to GdCrO$_3$ nanoparticles, the spectrum for CrO$_3$ was characterized by two intense peaks at around 257nm and 386nm which were the characteristic peaks for Cr^{+6} states. These peaks were probably due to the charge transfer transition from oxygen ($2p$)

to $Cr^{+6}(d^0)$ states. During a reaction, such as the reduction of Cr^{+6} states to Cr^{+3} states, the intensity of both the charge transfer transition would decrease.[33]

4.4.2 Photoemission spectroscopy measurements:

In figure 4.6, we have shown the photoemission spectra of $GdCrO_3$ nanoparticles taken at the excitation wavelength of 240 nm. These studies were carried out by Cary Eclipse photoluminescence spectrophotometer from Varian equipped with Xenon flash lamp. In figure 4.6, the emission spectra showed main emission peaks at around 296 nm and 320 nm. As we discussion earlier, these emission peaks were assigned to the $^6I_{11/2}{\rightarrow}^8S_{7/2}$ and $^6P_{7/2}{\rightarrow}^8S_{7/2}$ transitions of Gd^{3+} species presented in the material.[30] The emission spectra from 400 to 600 nm range were assigned to the transition $^4T_{1g}{\rightarrow}^4A_{2g}$ in the Cr^{+3} species.[31]

Figure 4.6: Photoemission spectra of GdCrO₃ nanoparticles with excitation wavelength 240 nm.

4.4.3 Fourier transformed infrared spectroscopy measurements:

In figure 4.7, we have shown the Fourier transformed infrared spectroscopy (FTIR) data on the $GdCrO_3$ nanoparticles and compared it with gadolinium acetate, citric acid, CrO_3 to confirm the formation of phase. As mentioned earlier, the FTIR data for $GdCrO_3$ is not reported earlier even in bulk phase. For the sake of clarity, we have divided the entire spectrum in to three different sections and compared only the relevant precursor with the $GdCrO_3$ data in various panels.

Chapter 4

For FTIR studies, we mixed the samples in KBr and the measurements were done at room temperature using a Perkin–Elmer Spectrum One instrument with resolution of 2 cm^{-1}. In panel A, the GdCrO$_3$ data is compared with gadolinium acetate in 450 – 700 cm^{-1} range. Here, the peaks in the range of 400-600cm^{-1} were attributed to the stretching of Gd-O bond in GdCrO$_3$.The peak shifting and broadening from precursor to product was due to different coordinative arrangement around gadolinium ions. In panel B, we have compared the GdCrO$_3$ data with CrO$_3$ data. As shown in this panel, we also identified several low intensity peaks; among them the peaks at 878 cm^{-1} and 930 cm^{-1} were due to the asymmetric Cr-O stretch, the peak at 839 cm^{-1} was due to the symmetric Cr-O stretch, and the broad peak around 737 cm^{-1} in CrO$_3$
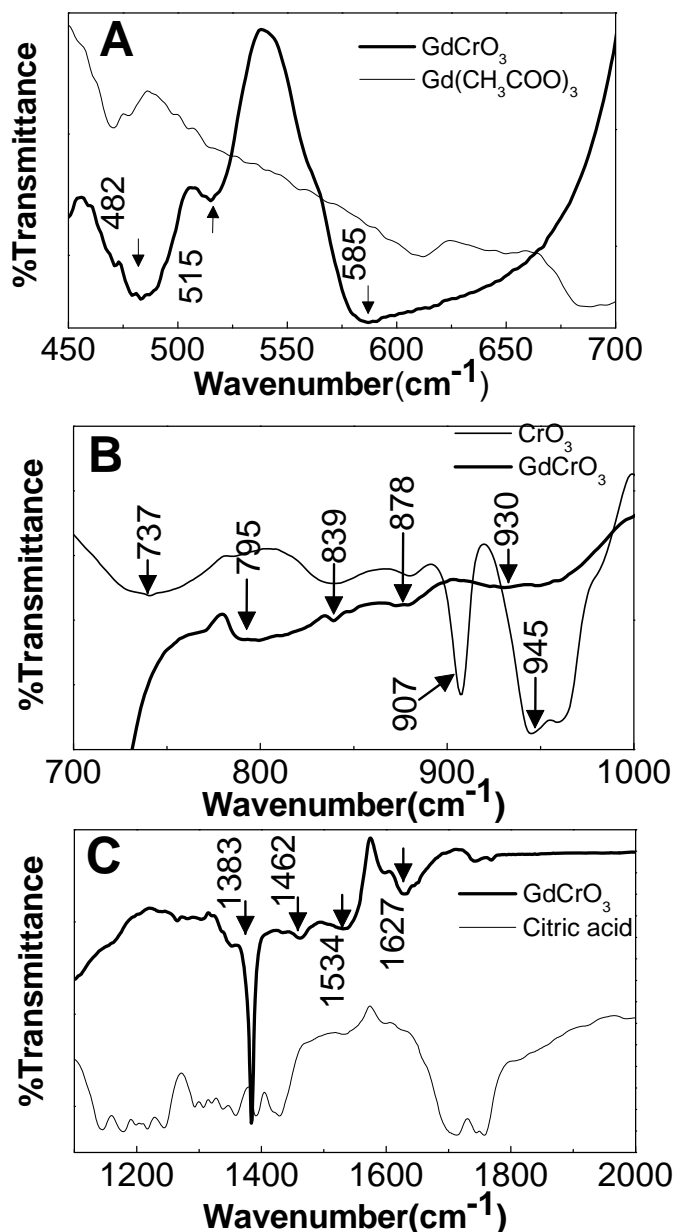

Figure 4.7: A comparison between FTIR spectra of GdCrO$_3$ nanoparticles and precursor as per the relevance. (A) FTIR spectra of GdCrO$_3$ nanoparticles and gadolinium acetate in the range 450-700 cm^{-1}. (B) FTIR spectra of GdCrO$_3$ nanoparticles and CrO$_3$ in the range 700-1100 cm^{-1} (c) FTIR spectra of GdCrO$_3$ nanoparticles and citric acid in the range 1200-2000 cm^{-1}.

was due to Cr-O-Cr bond vibration and 795 cm^{-1} in GdCrO$_3$ showed δ(O-C-O) bond vibration.[34]

The small shift in peaks from CrO$_3$ to GdCrO$_3$ might be due to a lower oxidation state and or different coordinative arrangement of chromium. In panel C, the presence of the sharp peak at 1382 cm^{-1} was due to the ionic nitrates and the peaks at 1466, 1533 cm^{-1} were probably due to the presence of carboxylate ions coming from citric acid. Further the low intense peak at 2340 cm^{-1} was because of the CO$_2$ which might be absorbed at the surface of GdCrO$_3$.

4.4.4 XPS measurements:

We used the room temperature x-ray photoelectron spectroscopy (XPS) to confirm the oxidation state of the Gd and Cr to further validate the formation of the pure phase. For this purpose the high resolution XPS data was
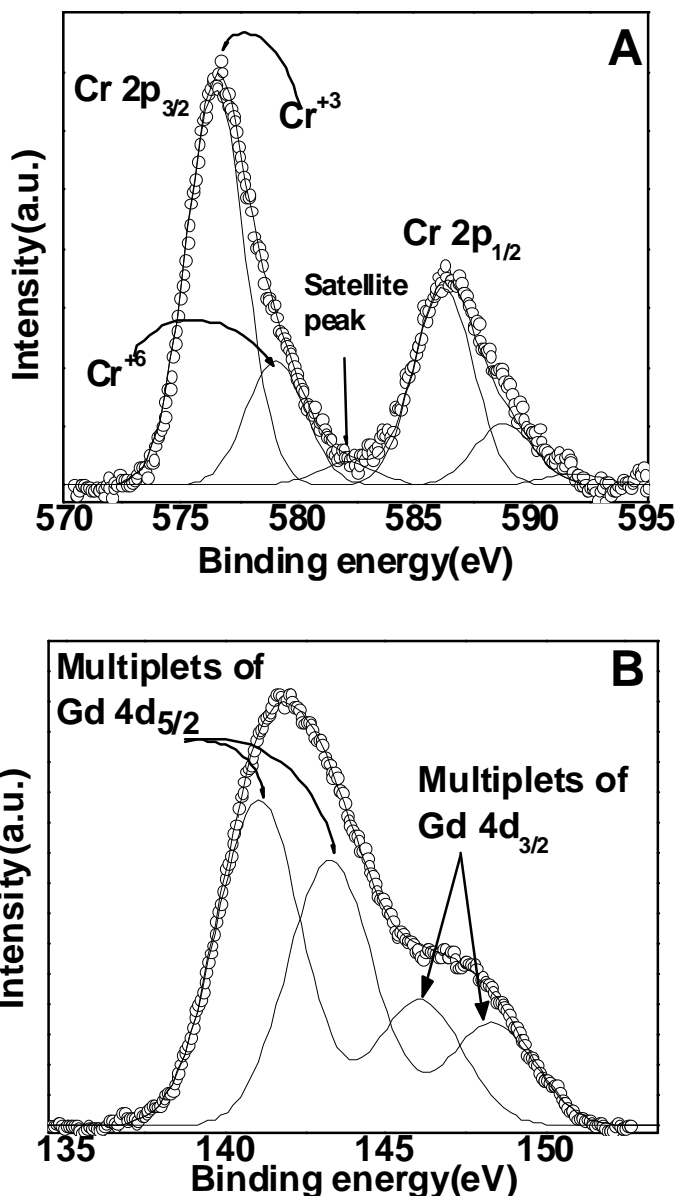
Figure 4.8: X-ray photoelectron spectroscopy spectra of (A) Cr 2p (B) Gd 4d (scatter curves) in GdCrO$_3$ nanoparticles. The lines represent the deconvoluted peaks.

collected by using a VG Microtch, model no ESCA 3000 equipped with ion gun (EX-05) for cleaning the surface spectra. The binding energy resolution was 0.1 eV. We used Shirley algorithm for background correction and chemically distinct species were resolved using a nonlinear least squares fitting procedure.

The core level binding energies were aligned with the carbon binding energy of 285 eV. In figure 4.8A, the peaks at binding energies 576.53 eV and 586.34 eV are associated to the Cr^{3+} $2p_{3/2}$ and Cr^{3+} $2p_{1/2}$ core levels respectively. The other doublet peaks at higher binding energies of 579 eV and 588.8 eV are due to presence of slight Cr^{+6} impurities species coming from the precursor.[35] A small intensity peak was observed at relatively higher binding energy $\sim$ 582 eV which is the satellite peak due to the shake up process. In figure 4.8B, we have shown the XPS spectra of Gd. Here, four clear peaks can be identified for the Gd^{3+} 4d core level binding energies after deconvolution of the experimentally measured curve. The intense peak of Gd $4d_{3/2}$ and Gd $4d_{5/2}$ levels were located at 146.08 eV and 141.06 eV respectively. Two extra peaks in the spectra could be attributed to an additional multiplet structure due to spin-spin interaction.[36] To the best of our knowledge, this is the first ever reported XPS spectra on $GdCrO_3$.

4.4.5 Raman spectroscopy measurements:

Next we characterized the $GdCrO_3$ nanoparticles using Raman spectroscopy. Raman spectroscopy is an excellent and important tool to accurately probe the individually probe the effect of magnetic ordering in the oxides, especially in a material such as $GdCrO_3$ where both Gd^{+3} and Cr^{+3} are playing dominant roles in determining the optical and agnetic properties and display a range of magnetic ordering. In figure 4.9, we have shown the Raman shift for $GdCrO_3$ nanoparticles taken at room temperature. The Raman spectra were recorded on a HR 800 Raman spectrophotometer (Jobin Yvon-Horiba, France) using monochromatic radiation emitted by a Ar^+ laser (514.5 nm), operating at 100 mW. We compared our results with the Raman studies reported previously by Udagawa et al on a bulk single crystal.[34]

Table 4.2: *A comparison of the Raman mode positions between GdCrO₃ nanoparticles (calculated from the current work on GdCrO₃ nanoparticles) and GdCrO₃ single crystal data reported by Udagawa et al[37].*

Raman mode	Present study (cm^{-1})	Udagawa *et al*[37].
A_{1g}	143	141
B_{2g}	165	157
A_{1g}	153	158
B_{1g}	167	161
B_{3g}	246	246
A_{1g}	255	260
B_{2g}	287	282
B_{1g}	290	285
A_{1g}	313	326
A_{1g}	393	390
B_{3g}	408	394
B_{2g}	472	472
A_{1g}	483	480
B_{1g}	476	480
A_{1g}	577	562
B_{2g}	565	568

Chapter 4

In table 4.2, we have tabulated the comparison from which we can conclude that all possible Raman modes in GdCrO$_3$ are present. Below 450 cm^{-1}, it is the Gd^{3+} ions that play a dominant role in determining the phonon frequencies of GdCrO$_3$, and
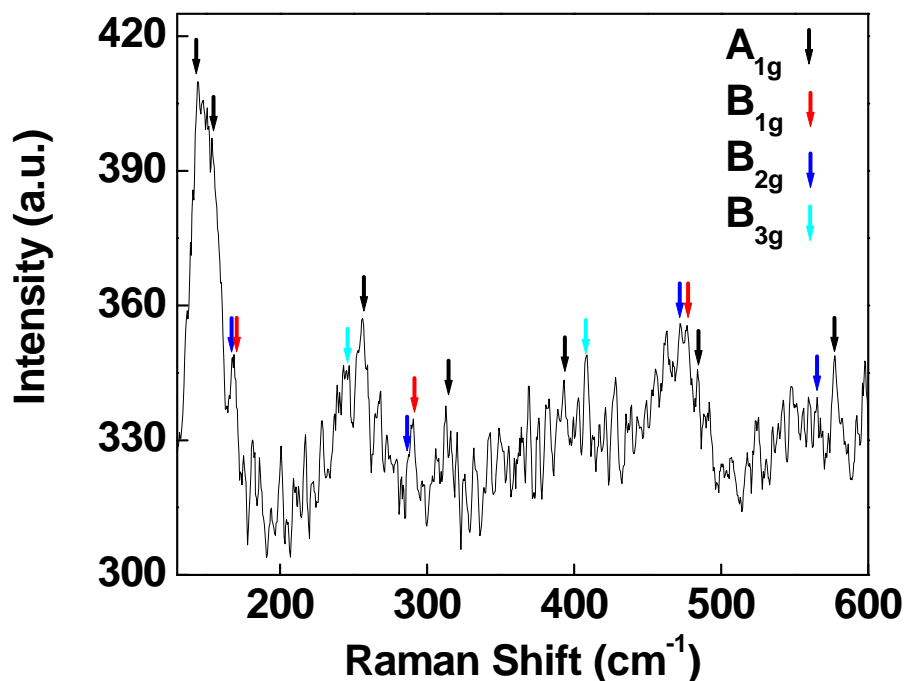

Figure 4.9: Stokes Raman spectra of the GdCrO$_3$ nanoparticles at room temperature.

above 450 cm^{-1}, the Cr^{+3} ions play an important role. For A$_{1g}$ line at 577 cm^{-1} and B$_{2g}$ line at 565 cm^{-1}, the Cr-O-Cr stretching motion plays a determining role and these lines should show a temperature dependent shift[34] at lower temperature due to magnetic ordering below Néel temperature and further as shown below in our magnetic measurements. To understand it further and to correlate it with the magnetic transition (discussed above), we need to do a low temperature Raman study in future.

4.5 Magnetic properties measurement:

We performed a detailed DC magnetization vs. temperature measurements as well as magnetic field vs. magnetization hysteresis measurements on the GdCrO$_3$ nanoparticles using a Physical Property Measurement System (PPMS) from Quantum Design Inc. San Diego, USA equipped with 7 Tesla superconducting magnet. These measurements were done using a vibrating sample magnetometer attachment of PPMS. We collected M-H loops in a field sweep from -50 k Oe to +50 k Oe at a rate of 25 Oe/sec where data was collected at every second at the vibrating frequency of 40 Hz and
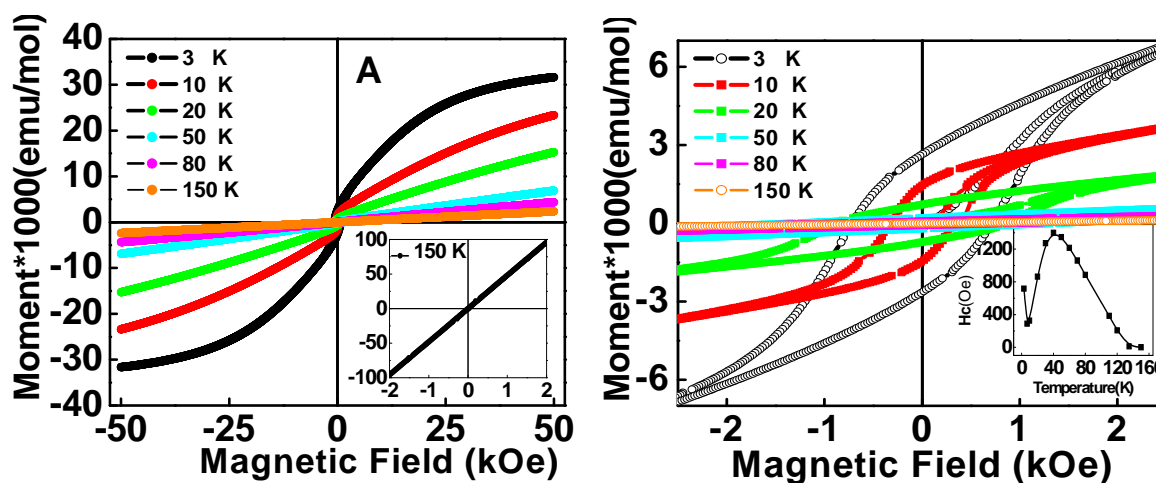
Figure 4.10: (A) M-H loops for GdCrO$_3$ nanoparticles taken at various temperature. Inset shows the zoom view of the M-H curve at 160 K(B) Zoom view of M-H loops shown in the figure 4.9 (A) . Inset shows the coercivity vs. Temperature curve for GdCrO$_3$ nanoparticles.

various temperatures in zero field cooled condition. For this purpose, the sample was demagnetized for each measurement by heating it above Néel temperature. In Figure 4.10A, we have shown some representative M-H loops at selected temperature values to show that magnetization does not saturate up to 50 kOe magnetic field. In the inset of the same figure, we have shown the M-H loops at 150 K, which shows almost a straight line indicating absence of any ferromagnetic ordering. Below 130 K, the coercivity increases sharply and reaches to its maximum at 40 K (~ 1400 Oe). Further, below 40 K, it shows a decreasing trend and hits minimum at around 10 K (325 Oe). The coercivity again shoots-up below 10 K as shown in figures 4.10B. Inset of figure 4.10B showed the temperature dependent of coercivity value. As we mentioned earlier that GdCrO$_3$ shows a series of magnetic transition due to the interactions between Gd^{+3}-Gd^{+3}, Gd^{+3}-Cr^{+3}, Cr^{+3}-Cr^{+3}. Just below the Néel temperatures, the Cr^{3+}-Cr^{3+} interaction dominates and at lowest temperature of measurements, the Gd^{3+}-Gd^{3+} interactions are the dominant ones. On the other hand, the Cr^{3+}-Gd^{3+} interactions are observed at the intermediate temperature ranges. Below the Néel temperature, the spins of different Cr^{3+} ions interact anti-parallelly through the superexchange mechanism and give the antiferromagnetic ordering at ~168 K. Here, the Cr^{3+}-Cr^{3+} interactions are much stronger in comparison to

Gd^{3+}-Gd^{3+} and Gd^{3+}-Cr^{3+} interactions by orders of magnitude. In GdCrO$_3$, the Cr^{3+} ions sit in the octahedral geometry surrounded by six O^{2-} ions that leads to the splitting of 3d^3 orbital into t_{2g} and e_g.[38] The t_{2g} orbital is half filled and e_g is completely empty. The unfilled e_g orbital hybridizes with 2p orbital of O^{2-} where two Cr^{3+} ions interact via O^{2-} ion in 180° position and each Cr^{3+} has six Cr^{3+} nearest neighbors and therefore, the total superexchange interaction is a sum of them. On the other hand, Gd^{3+} and Cr^{3+} ions interact with each other via O^{2-} at 90° position which is weaker in nature and dominates at lower temperatures only. As each Cr^{3+} ion has eight Gd^{3+} nearest neighbors, the total Gd^{3+}- Cr^{3+} superexchange interaction will be a sum of them. The Gd^{3+}- Gd^{3+} superexchange interaction is still one order of magnitude weaker than the superexchange interaction between Gd^{3+} and Cr^{3+} and shows-up below 10 K. At higher temperatures, unfilled Cr^{+3} d-orbital (e_g) and O^{2-} p-orbital hybridization is more stable than the Gd^{3+} f-orbital and O^{2-} p-orbital hybridization. However, as the temperature decreases further, f-orbitals in Gd^{3+} ions and p orbitals of oxygen also start interacting and well below the

Super exchange mechanism:

Step-1

Antiferromagnetic interaction between Cr-O-Cr via super-exchange mechanism at 167 K.
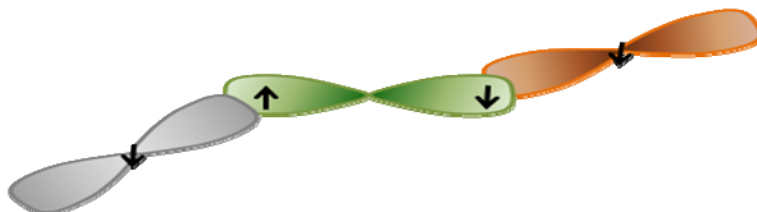

Step-2

Weak antiferromagnetic interaction between Cr-O-Cr because of canted chromium spin below 130 K.

Chapter 4

Step-3

Weak ferromagnetic interaction between Gd-O-Cr between the temperature range 13-130 K.

Step-4

Weak antiferromagnetic interactions start between Gd-O-Gd below 13 K.

Step-5

Weak antiferromagnetic interactions between Gd-O-Gd below 7 K.

Chromium ion   p orbital of oxygen

Gadolinium ion
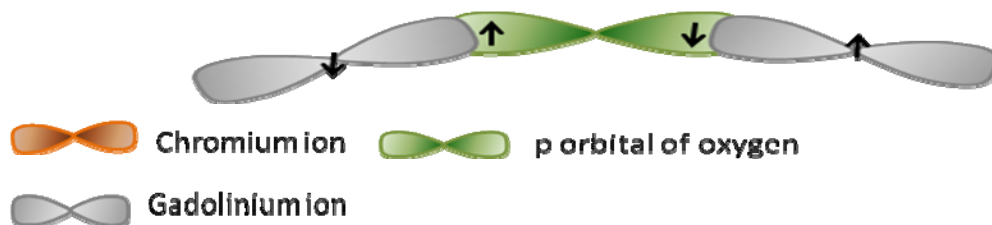
Néel temperature, where the Cr^{3+} spins are fully aligned antiferromagntically, the Gd^{3+}-O^{2-} superexchange interaction also increases, resulting into the onset of Cr^{3+}-O^{2-}-Gd^{3+} interaction. This interaction is ferromagnetic as here the empty e_g orbital of Cr^{3+} overlaps with one end of oxygen p-orbital and the other end of the same overlaps with a half filled f-orbital of Gd^{3+}. This weak ferromagnetic superexchnge coupling gives rise to opening up of hysteresis loop below 130 K (shown in figure 4.10B) with decreasing temperature and the remnant magnetization also increases. Here, it should be noticed that it is not just the superexchange interaction between Cr^{3+} and Gd^{3+} but the Cr^{3+} spins also get canted due to the Dzialoshinski-Moriya type antisymmetric exchange interaction[39, 40] between

Cr^{3+}-Cr^{3+} ions which plays a very important role here. These canted moments of Cr^{3+} induce an overall internal magnetic field at the Gd^{3+} sites (the interionic distance between Gd^{3+} and Cr^{3+} ions is 3.82 Å)[13] which in turn changes the orientation of Gd^{3+} spins in the direction of this induced field. So the average moment is the sum of the canted Cr^{3+} spin and Gd^{3+} spin below 130 K.[27] The average moment is given as

$$\mu_{average} = \mu_{Cr} + \mu_{Gd} \tag{1}$$

Here, if we assume that Gd^{3+} ions follow a Curie-Weiss law, then, this equation can be expressed by

$$\mu_{average} = \mu_{Cr} + \frac{C(H_a - H_i)}{T - \theta} \tag{2}$$

where, μ_{Cr} and μ_{Gd} are the magnetic moments of the canted Cr^{3+} ion and Gd^{3+} ion respectively and C, H_a, H_i, θ are the Curie constant, applied field and induced field (at a gadolinium site due to canted Cr ion) and Weiss temperature, respectively. The Curie constant C can be calculated for free Gd ion from the following equation:

$$C = \frac{Ng^2\beta^2 S(S+1)}{k} \tag{3}$$

The value of C is 7.875 for $g = 2$ and $S = 7/2$. Since the applied field H_a and induced field H_i are opposite to each other so at certain point where $H_a = H_i$, the second term will be zero and average moment will be equal to the canted Cr^{3+} ion. We calculated the moment of canted Cr^{3+} spin and it came out to be -370 ± 50 emu/mole for $GdCrO_3$ nanoparticles which is close to the moments calculated for the bulk phase by Cooke *et al.* and the induced field was calculated as -5.4 ± 0.5 kOe.[27] The negative sign in the induced field indicates that the direction of induced field is opposite to the applied field. Further, as shown in figures 4.10B & its inset, below 10 K, the coercivity increases suddenly with decreasing temperature which can be explained by an onset of antiferromagnetic coupling

between Gd^{3+}-Gd^{3+} ions. We also performed the M-T measurements in various field conditions in a temperature range from 3 K to 300 K. For all these measurements, the cooling and heating rate was kept at 1.5 K per minute and the data was collected at every second at 40 Hz. At first, the desired field was applied at 300 K and data was collected while cooling down to 3 K (in field) and again while heating back from 3 K to 300 K (in field), these two curves will be presented as
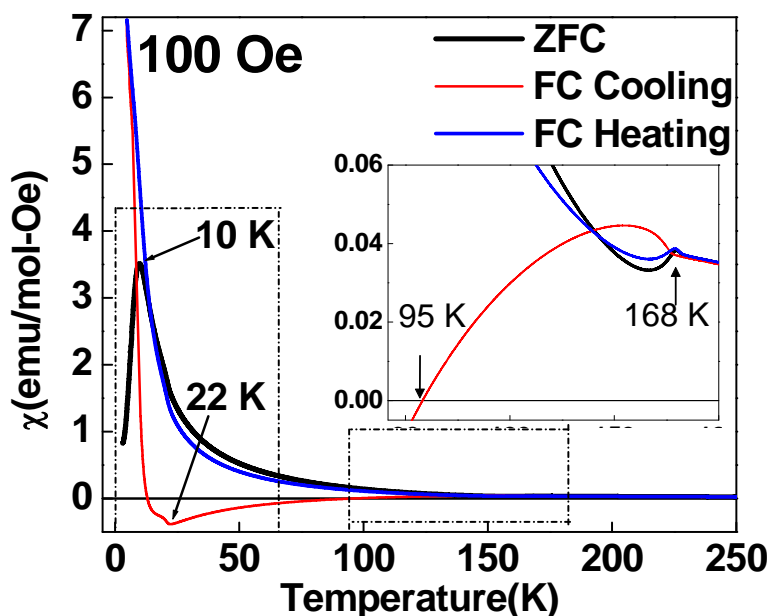
Figure 4.11: *Zero-field cooled, field cooled (both in cooling and heating cycle) curves at 100 Oe field. Inset shows the zoom view of the selected temperature region highlighting the negative magnetization.*

"FC cooling" and "FC heating" here. Next, we removed the magnetic field at 300 K and cooled the sample down to 3 K at the maximum cooling rate of PPMS and after cooling the sample in zero field, the desired field was applied at 3 K and data was collected while heating up to 300 K. This data-set will be presented as "ZFC" here. In figure 4.11, we have shown a representative set of curves with FC cooling, FC heating and ZFC data at taken at 100 Oe. Inset shows the zoom view of the highlighted area in figure 4.11. Following main features can be immediately noticed: (1) a transition at ~ 168 K (2) FC cooling curves go to negative values below 95 K (3) FC cooling curve touches the minimum at around 22 K (4) ZFC curve peaks at 10 K and below which it sharply drops. The sharp transition seen at around 167-168 K is because of the onset of an antiferromagnetic ordering due to the Cr-O-Cr superexchange coupling which is independent of the applied field up to 2000 Oe as the exchange field on any Cr^{3+} spin due to six surrounding nearest Cr^{3+} neighbors will be around 1.2 MOe.[27] The FC cooling

curve deviates considerably from the other two curves immediately below the Néel temperature. While in other two curves the magnetization shows an increasing trend with decreasing temperature, the FC cooling curve the magnetization goes below zero at around 95 K (figure 4.11 inset) and touches minimum at around 22 K (figure 4.11). Negative magnetization behavior is a unique feature in this material and a possible explanation for this behavior can be given by understanding the temperature dependent interaction between Gd^{3+} and Cr^{3+} ions. As we discussed earlier, below 130 K, Cr^{3+} spins get canted and induce a magnetic field on Gd^{3+}. The Gd^{3+} spins get aligned towards the field which is opposite to the canted Cr^{3+} spins (signified by the opening up of the coercivity at this temperature as discussed above and shown in figure 4.10B). The overall moment at any temperature is given by equation 2 where the applied field H_a and induced field H_i play a role apart from temperature. At 100 Oe, the second term in equation 2 is larger (and negative in sign) than the first term below 95 K therefore the net magnetization goes to the negative value. We found that this crossover temperature strongly depends upon the applied magnetic field H_a. We calculated that at 250 Oe, this crossover temperature is at $90^{o}C$ and for 500 Oe, it is situated at $80^{o}C$. For the fields higher than 500 Oe, the H_a is larger than H_i and therefore the second term in the equation 2 remains positive and the FC cooling does not show negative magnetization for applied field of 1000 and 2000 Oe. To further explore the existence of this interesting feature, in figure 4.12 A, we have shown the zoom view of negative magnetization in the FC cooling at various fields. In figure 4.12 D, we have plotted the minimum susceptibility as a function of applied field and in figure 4.12 C we have shown the temperature at which the magnetization shows the minimum value as a function of applied field. As we mentioned earlier that for relatively higher fields such as 1000 and 2000 Oe, the negative magnetization disappears as the applied magnetic field is strong enough to dominate over the induced field giving net positive magnetic moment (figure 4.12 A) which increases further with the decrease in the thermal activation energy. However, at 500 Oe and below, we start observing an overall increase in the value of negative moments as the magnetic field decreases from 500 to 100 Oe. There is very small field dependence in the

$T_{min.}$ as noticed in figure 4.12 C where the T min. goes down with a decrease in the applied field from nearly 23.6 K to below 22 K with an inflection point at 100 Oe. With
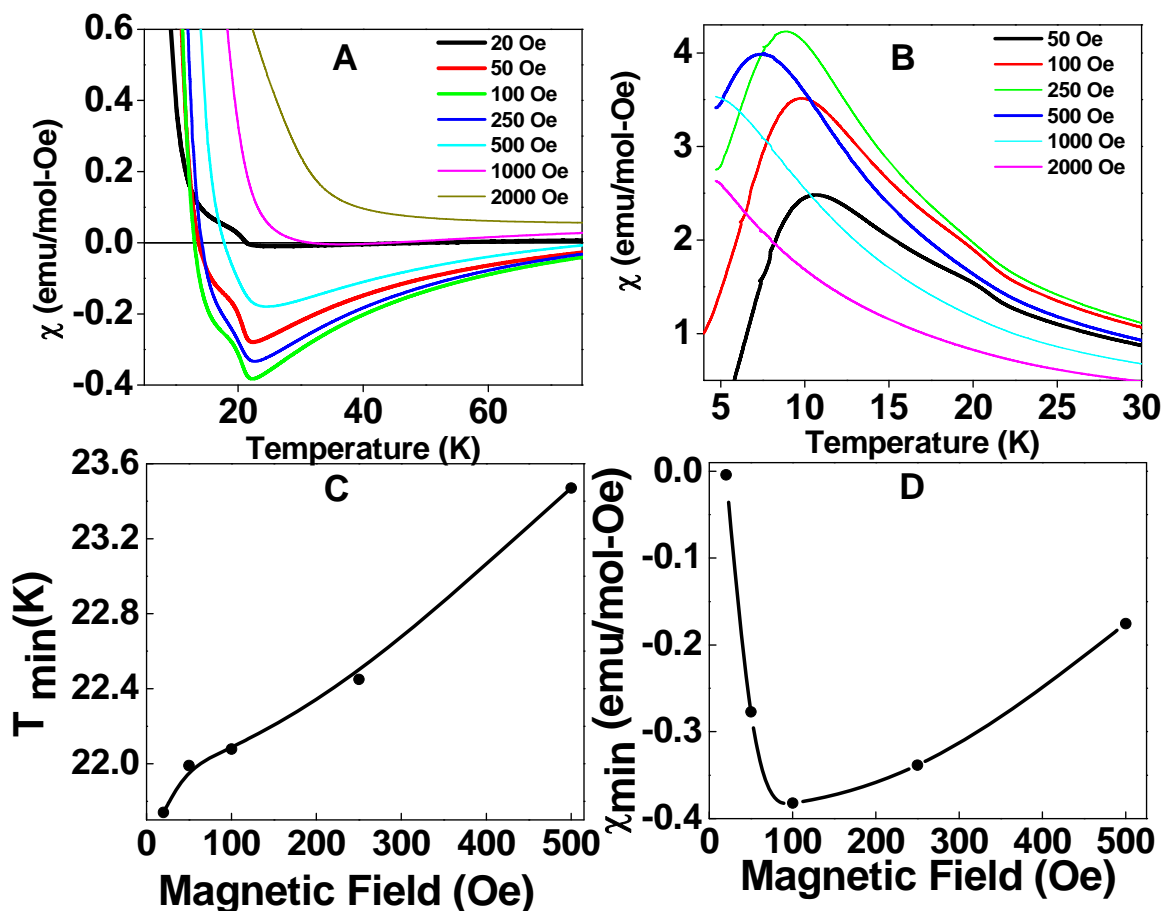
Figure 4.12: *(A) Comparison of magnetic susceptibility vs temperature curves performed in FC cooling mode at various field values to show the negative magnetization. (B) The zoom view of the second Néel temperature due to Gd^{3+}-Gd^{3+} ordering shown by the zero field cooled curves at various fields. The field dependence of the ordering temperature is clearly seen here which is due to a weak superexchange interaction between Gd^{3+}-Gd^{3+} spins. (C) $T_{min.}$ vs. applied magnetic field curve. (D) maximum negative susceptibility plotted against the applied magnetic field.*

further cooling below 20 K, the FC cooling curve again increases and reaches to zero value around 13 K. At this point the canted chromium moment and induced gadolinium moment are equal and opposite to each other so the net magnetization exhibits zero value (*i.e.* the first and second term in equation 2 are equal in magnitude but opposite in sign). Below 13 K, a sudden orientation of spins gives rise to the increase moments and we see a sharp rise in the moments with decreasing temperature. At the end, the magnetic signature of the Gd^{3+} - Gd^{3+} superexchange interaction is also picked up in the zero field cooled curves (apart from the sharp change in the coercivity in M-H loops). Below 10 K, a sharp decrease in the moments is observed accompanied by a sudden increase in the coercivity as well. This is explained by the onset of a weak Gd^{3+} - Gd^{3+} antiferromagnetic ordering which is of second order which was confirmed on the specific heat measurements on $DyFeO_3$ belonging to same rare earth orthoferrite/chromite family.[41] Due to this interaction being much weaker in nature, this antiferromagnetic ordering shows a dependence on the applied magnetic field (unlike the antiferromagnetic ordering between Cr^{3+}-Cr^{3+}). We have shown the field dependence of the this ordering in figure 4.12 B where the ordering temperature is at 10.5 K at 50 Oe and it goes down to 7.3 K for the applied field of 500 Oe. For the fields higher than 500 Oe, we do not see this antiferromagnetic ordering as the exchange field on Gd^{3+} is much weak.

4.6 Maxwell–Wagner relaxation behaviour in GdCrO$_3$ nanoparticles:

As we discussed earlier that almost all the RMO_3 compounds (R=rare earth ions and M=Cr, Fe, Mn) are supposed to show the coupling between the magnetic order and electric dipolar order parameters due to the lack of the inversion symmetry where an applied electric field induces a net magnetization in the material which is proportion to the electric field and similarly an applied magnetic field induces an electric polarization which is proportional to the external magnetic field.[20] To probe the dielectric response in the proximity to the magnetic transitions, we also studied the frequency and temperature
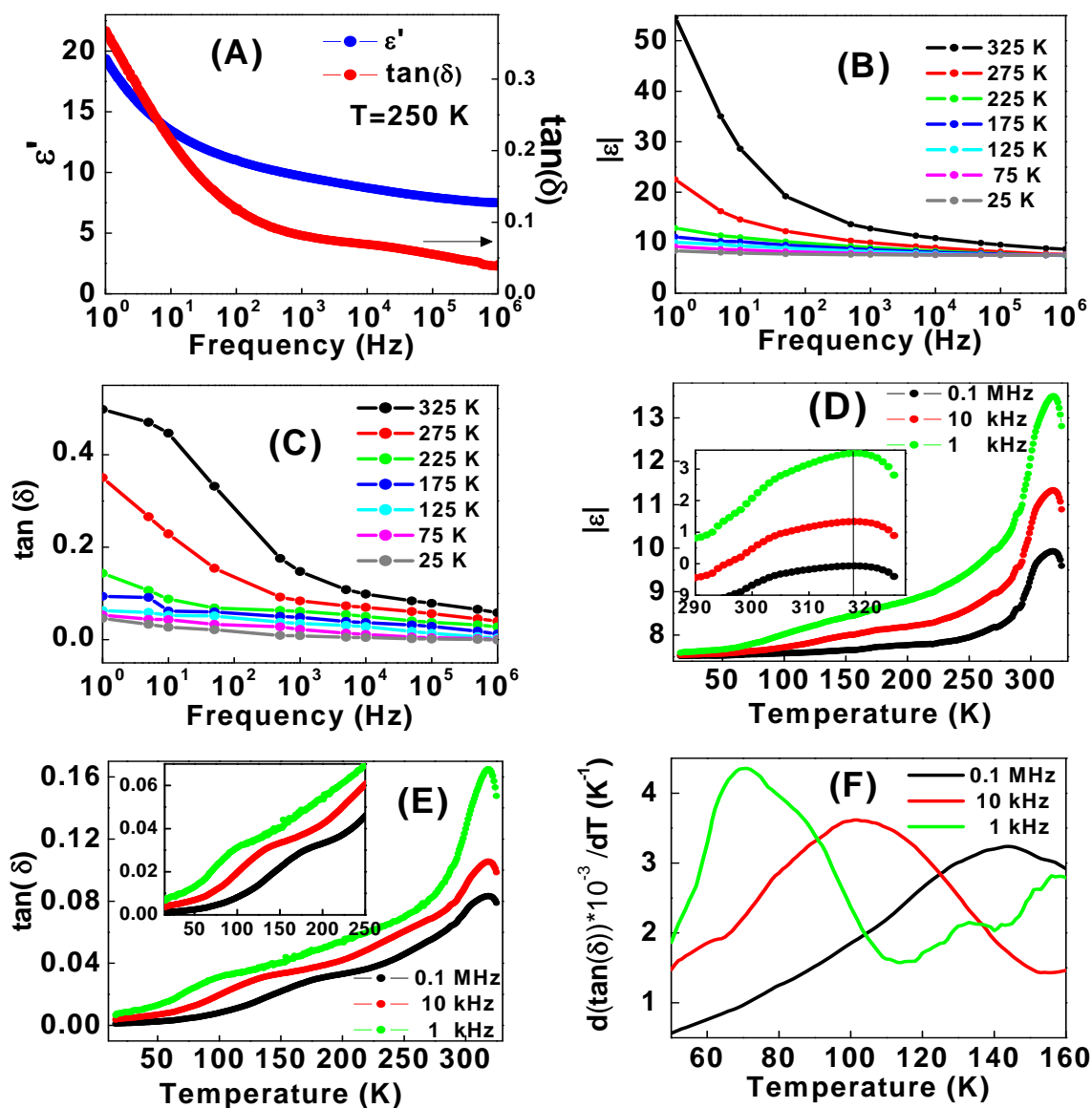
Figure 4.13: *(A) Representative curves of dielectric constant ε' and tan δ vs. frequency at T=250 K.(B) depicts the sigmoidal variation of the dielectric constant ε as a function of frequency at various temperatures. (C) represents the corresponding loss values in relation to the curves in (B).(D) represents the dielectric constant ε vs T curves. The inset shows zoom view. (E) tan δ vs. T curves with inset showing the zoom view. (F) d(tan δ)/ dT curves.*

dependent dielectric and loss tangent behavior on $GdCrO_3$ nanoparticles. To the best of our knowledge this is the first complete study of dielectric constant and loss tangent

below room temperature for $GdCrO_3$. There is no previous report even for the bulk dielectric behavior below the room temperature (in the proximity to magnetic ordering temperature range). For this purpose, we used Novovcontrol Beta Impedance Analyzer with a home-built sample holder to couple with a Janis Inc. helium closed cycle refrigerator in a frequency range from 0.1 Hz to 1 x 10^6 Hz at 1 volt (rms) and with no dc bias. The data was taken in a temperature range from 15-325 K at each 1 K step size. A compressed circular pallet, with 5 mm diameter, was kept in a custom designed sample holder to form a circular parallel plate capacitor geometry.

The complete frequency spectrum of ε' and *tan (δ)* at T=250 K is shown in figure 4.13 (A) which shows a sharp decrease in the *ε'* and *tan (δ)* values with increasing frequency. From figure 4.13 (B) this sharp or sigmoidal variation of the dielectric constant in the low frequency is observed for all temperatures followed by saturation in the high frequency region. For a particular temperature, the observed high values of the dielectric constant at low frequencies and vice versa at higher frequencies indicate large dispersion due to the Maxwell–Wagner type of interfacial polarization which is in agreement with Koop's phenomenological theory[42-44]. This is due to the inability of the electric dipoles to be in accordance with the frequency of the applied electric field. Therefore from figure 4.13 (C) we see that the losses are significantly high at low frequencies than at high frequencies. From both figure 4.13 (B) and (C) we notice similar dispersion profiles at all temperatures but with reducing strength with decreasing temperature. In figure 4.13 (D), we have shown the temperature dependence of *ε* which shows a sharp increase in the dielectric constant with an increase in the temperature above 300K. A peak is observed at around 320 K and above that there is a decrease in the dielectric constant (as shown in the inset of figure 4.13 (D)). This behavior overlaps quite nicely with the dielectric constant behavior reported for bulk $GdCrO_3$ in a temperature range from nearly 295 to 460 K which also shows a peak centered around 320 K and a minimum at around 425 K above which the spontaneous dielectric polarization goes to zero.[16] The origin of the peak at 320 K is not known at present. We found that At 300 K and 1 k Hz, the value of ε is nearly 12 which is much lower than 23

reported for bulk polycrystalline samples.[22] The size dependent effects, amount of compaction of pellet and sintering effects (in polycrystalline samples) together can be attributed to the difference between these values.In figure 4.13 (E), we have plotted the loss tangent vs. temperature curves which again shows a sharp decrease with decreasing temperature with a broad hump as highlighted in the inset of the figure. The values of the loss tangent are quite low for $GdCrO_3$. In figure 4.13 (F), we present the temperature derivative of loss tangent showing a broad peak with a very strong frequency dependence. The fact that this temperature range is in the vicinity of the magnetic transitions in $GdCrO_3$ nanoparticles, therefore, it will be interesting to explore whether both the effects are coupled with each other as seen in other multiferroic nanomaterials.[25]

4.7 Conclusions:

In this chapter, Single-phase and high purity $GdCrO_3$ perovskite crystallites with particle size around 50-60 nm were successfully synthesized in a Teflon liner hydrothermal cell using gadolinium acetate, chromium tri oxide as a precursor and citric acid as a complexing agent. Compared with the conventional solid-state reaction process, the size and shape of the $GdCrO_3$ is well controlled in the hydrothermal reaction. The growth of $GdCrO_3$ nanocrystals in a hydrothermal cell was explained by dissolution–crystallization process. The x-ray diffraction showed phase purity of $GdCrO_3$ nanoparticles. The UV-vis absorption and emission spectra showed interesting optical properties. we have presented the detailed magnetic, dielectric and Raman studies for the first time for $GdCrO_3$ nanoparticles which emphasize the collective as well as individual roles played by the Gd^{3+} and Cr^{3+} ions at various temperatures. The Raman spectra shows that below 450 cm^{-1}, it is the Gd^{3+} ion that play a dominant role in determining the phonon frequencies of $GdCrO_3$, and above 450 cm^{-1}, the Cr^{+3} ions play an important role. The low temperature frequency dependent dielectric studies show interesting transition at 320 K with significantly lowered dielectric value due to size effects. The loss tangent reveals a strong transition at lower temperature with strong frequency dependence probably due to coupling with magnetic order parameter.

4.8 References:

1. Anderson, P. W., Antiferromagnetism- theory of superexchange interaction. *Physical Review* **1950,** 79, (2), 350-356.

2. Wollan, E. O., Magnetic coupling in crystalline compounds- a phenomenological theory of magnetism in 3D metals. *Physical Review* **1960,** 117, (2), 387-401.

3. Anderson, P. W., New approach to the theory of superexchange interactions. *Physical Review* **1959,** 115, (1), 2-13.

4. Verwey, E. J. W.; Haayman, P. W., Electronic conductivity and transition point of magnetite ("Fe$_3$ O$_4$"). *Physica* **1941,** 8, 979-987.

5. Poddar, P.; Fried, T.; Markovich, G., First-order metal-insulator transition and spin-polarized tunneling in Fe$_3$O$_4$ nanocrystals. *Physical Review B* **2002,** 65, (17), 172405.

6. Poddar, P.; Fried, T.; Markovich, G.; Sharoni, A.; Katz, D.; Wizansky, T.; Millo, O., Manifestation of the Verwey transition in the tunneling spectra of magnetite nanocrystals. *Europhysics Letters* **2003,** 64, (1), 98-103.

7. Kimura, T.; Goto, T.; Shintani, H.; Ishizaka, K.; Arima, T.; Tokura, Y., Magnetic control of ferroelectric polarization. *Nature* **2003,** 426, (6962), 55-58.

8. Ederer, C.; Spaldin, N. A., Magnetoelectrics - A new route to magnetic ferroelectrics. *Nature Materials* **2004,** 3, (12), 849-851.

9. Chu, Y. H.; Martin, L. W.; Holcomb, M. B.; Ramesh, R., Controlling magnetism with multiferroics. *Materials Today* **2007,** 10, (10), 16-23.

10. Ederer, C., Coupling between magnetism and ferroelectricity in multiferroic materials. *Abstracts of Papers of the American Chemical Society* **2005,** 230, 93-PHYS.

11. Eerenstein, W.; Mathur, N. D.; Scott, J. F., Multiferroic and magnetoelectric materials. *Nature* **2006,** 442, 759-765.

12. Fiebig, M., Revival of the magnetoelectric effect. *Journal of Physics D-Applied Physics* **2005,** 38, (8), R123-R152.

13. Geller, S., Crystallographic Studies of Perovskite-Like Compounds. IV. Rare Earth Scandates, Vanadites, Galliates, Orthochromites. *Acta Crystallographica* **1957,** 10, 243-248.

14. Satoh, H.; Koseki, S.; Takagi, M.; Chung, W. Y.; Kamegashira, N., Heat capacities of LnCrCO$_{(3)}$ (Ln=rare earth). *Journal of Alloys and Compounds* **1997,** 259, (1-2), 176-182.

15. Rao, G. V. S.; Ramdas, S.; Mehrotra, P. N.; Rao, C. N. R., Electrical transport in rare-earth oxides. *Journal of Solid State Chemistry* **1970,** 2, (3), 377-384.

16. Lal, H. B.; Dwivedi, R. D.; Gaur, K., Pyroelectric and dielectric properties of some light rare-earth orthochromites. *Journal of Materials Science: Materials in Electronics* **1990,** 1, (4), 204-208.

17. Ederer, C.; Spaldin, N. A., Influence of strain and oxygen vacancies on the magnetoelectric properties of multiferroic bismuth ferrite. *Physical Review B* **2005,** 71, 224103.

18. Belik, A. A.; Takayama-Muromachi, E., Magnetic properties of BiMnO$_3$ studied with dc and ac magnetization and specific heat. *Inorganic Chemistry* **2006,** 45, 10224-10229.

19. Munoz, A.; Alonso, J. A.; Casais, M. T.; Martinez-Lope, M. J.; Martinez, J. L.; Fernandez-Diaz, M. T., The magnetic structure of YMnO$_3$ perovskite revisited. *Journal of Physics-Condensed Matter* **2002,** 14, (12), 3285

20. Yamaguchi, T.; Tsushima, K., Magnetic Symmetry of Rare-Earth Orthochromites and Orthoferrites. *Physical Review B* **1973,** 8, (11), 5187- 5198.

21. Subba Rao, G. V.; Chandrashekhar, G. V.; Rao, C. N. R., Are rare earth orthochromites ferroelectric? *Solid State Communications* **1968,** 6, (3), 177-179.

22. Tripathi, A. K.; Lal, H. B., Electrical transport in light rare-earth orthochromites. *Journal of Materials Science* **1982,** 17, (6), 1595-1609.

23. Park, T. J.; Papaefthymiou, G. C.; Viescas, A. J.; Moodenbaugh, A. R.; Wong, S. S., Size-dependent magnetic properties of single-crystalline multiferroic BiFeO$_3$ nanoparticles. *Nano Letters* **2007,** 7, 766-772.

24.   Selbach, S. M.; Tybell, T.; Einarsrud, M. A.; Grande, T., Size-dependent properties of multiferroic BiFeO$_3$ nanoparticles. *Chemistry of Materials* **2007,** 19, (26), 6478-6484.

25.   Kharrazi, S.; Kundaliya, D. C.; Gosavi, S. W.; Kulkarni, S. K.; Venkatesan, T.; Ogale, S. B.; Urban, J.; Park, S.; Cheong, S. W., Multiferroic TbMnO$_3$ nanoparticles. *Solid State Communications* **2006,** 138, (8), 395-398.

26.   Yoshii, K., Magnetic properties of perovskite GdCrO$_3$. *Journal of Solid State Chemistry* **2001,** 159, (1), 204-208.

27.   Cooke, A. H.; Martin, D. M.; Wells, M. R., Magnetic interactions in gadolinium orthochromite, GdCrO$_3$ *Journal of Physics C: Solid State Physics* **1974,** 7, 3133-3144.

28.   Niu, J. R.; Deng, J. G.; Liu, W.; Zhang, L.; Wang, G. Z.; Dai, H. X.; He, H.; Zi, X. H., Nanosized perovskite-type oxides La$_{1-x}$Sr$_x$MO$_3$-delta (M = CO, Mn; x=0, 0.4) for the catalytic removal of ethylacetate. *Catalysis Today* **2007,** 126, (3-4), 420-429.

29.   Jagannathan, R.; Poddar, P.; Prabhune, A., Cephalexin-mediated synthesis of quasi-spherical and anisotropic gold nanoparticles and their in situ capping by the antibiotic. *Journal of Physical Chemistry C* **2007,** 111, (19), 6933-6938.

30.   Liang, H. B.; Su, Q.; Tao, Y.; Xu, J. H.; Huang, Y., The VUV-vis spectroscopic properties of phosphors Ca$_3$Gd$_{2((1-x))}$Ln$_{(2x)}$(BO$_3$)$_4$ (Ln($^{3+}$) = Ce, Sm, Eu, Tb). *Materials Research Bulletin* **2006,** 41, (8), 1468-1475.

31.   Xu, H. T.; Lou, T. J.; Li, Y. D., Synthesis and characterize of trivalent chromium Cr(OH)$_3$ and Cr$_2$O$_3$ microspheres. *Inorganic Chemistry Communications* **2004,** 7, (5), 666-668.

32.   Bhatt, R.; Kar, S.; Bartwal, K. S.; Wadhawan, V. K., The effect of Cr doping on optical and photoluminescence properties of LiNbO$_3$ crystals. *Solid State Communications* **2003,** 127, (6), 457-462.

33.   Bensalem, A.; Weckhuysen, B. M.; Schoonheydt, R. A., In situ diffuse reflectance spectroscopy of supported chromium oxide catalysts: Kinetics of the reduction

process with carbon monoxide. *Journal of Physical Chemistry B* **1997,** 101, (15), 2824-2829.

34. Omotoso, O. E.; Ivey, D. G.; Mikula, R., Hexavalent chromium in tricalcium silicate - Part II - Effects of Cr-VI on the hydration of tricalcium silicate. *Journal of Materials Science* **1998,** 33, (2), 515-522.

35. Sohn, J. R.; Ryu, S. G.; Park, M. Y.; Pae, Y. I., Preparation and characterisation of chromium oxide supported on zirconia. *Bulletin of the Korean Chemical Society* **1992,** 13, (6), 605-612.

36. Talik, E.; Neumann, M.; Mydlarz, T., Photoemission study and magnetization of Gd_3Pd intermetallic compound. *Journal of Magnetism and Magnetic Materials* **1998,** 189, (2), 183-188.

37. Udagawa, M.; Kohn, K.; Koshizuka, N.; Tsushima, T.; Tsushima, K., Influence of magnetic ordering on the phonon raman spectra in $YCrO_3$ and $GdCrO_3$. *Solid State Communications* **1975,** 16, 779-783.

38. Blazey, K. W.; Burns, G., Exchange of Cr^{3+} in $GdAlO_3$. *Proceedings of the Physical Society* **1967,** 91, (3), 640-644.

39. Moriya, T., Anisotropic Superexchange Interaction and Weak Ferromagnetism. *Physical Review* **1960,** 120, (1), 91-98.

40. Dzialoshinski, I.,A thermodynamic theory of weak ferromagnetism of antiferromagnetics. *Journal of Physics and Chemistry of Solids* **1958,** 4, (4), 241-255.

41. Berton, A.; Sharon, B., Specific Heat of $DyFeO_3$ from 1.2^0-80^0K. *J. Appl. Phys.* **1968,** 39, (2), 1367-1368.

42. Maxwell, J. C., *Electricity and Magnetism Vol 1.* (Oxford:Oxford University Press) Section 328: Vol. 1.

43. Koops, C. G.,On the dispersion of resistivity and dielectric constant of some semiconductors at audiofrequencies. *Physical Review* **1951,** 83, (1), 121-124.

44. Uniyal, P.; Yadav, K. L., Observation of the room temperature magnetoelectric effect in Dy doped BiFeO3. *Journal of Physics-Condensed Matter* **2009,** 21, (1) 405901.

Chapter- 5

Outlook

This chapter details the salient features of the work presented in the thesis and emphasizes on potential avenues for future work.

Chapter 5

5.1 Summary of the Work:

The interplay of charge, spin and orbital ordering etc. and their signatures in the optical, magnetic and dielectric properties have enriched the condensed matter physics since more than five decades and have been exploited into various technologies. Several of the rare earth transition metal oxides (with general formula: ABO_3, AB_2O_5 where A = rare earth ions and B= (Fe, Cr, Mn) have been studied along with some other perovskites materials such as $BiFeO_3$ and $BiMnO_3$ for their potential multiferroic properties where the magnetic, ferroelectric and ferroelastic order parameters couple together resulting into a range of often puzzling signatures in the temperature dependent Raman spectroscopy, UV-Vis absorption spectroscopy, magnetization and dielectric properties. However, these materials have not been explored for their size dependent properties as the synthesis of these rare earth complex oxides with excellent control over particle morphology while maintaining crystallinity at nanoscale is quite difficult. The conventional chemical techniques such as co-precipitation, reverse-micelle, hot-injection etc. are unable to produce the desired phase. Due to this reason, the physical properties of most of these materials are reported in bulk size only. I propose to synthesis a range of rare earth ferrites and chromites such as $GdCrO_3$, $DyFeO_3$, $BiFeO_3$ etc. in orthorhombic and rhombohedral crystalline form in a varying size range to study the coupling between their structural, magnetic, dielectric, thermal and optical behaviour using a host of advanced tools for a variety of application in electronic devices.

In $BiFeO_3$, some interesting size dependent effects are observed in the dielectric, magnetic properties as well as Raman spectra. Due to the nanosize effect, our results show the evidence of existence of a low temperature anomaly due to spin-glass transition in the range from 40-44 K in the field cooled magnetization curves which is reported at 50K in bulk single crystal. The origin of the size dependent feature observed by us in the dielectric properties are not well understood but size dependent changes below 60 nm in the magnetic and Raman properties supposed to originate from the breaking of the helical ordering or incomplete rotation of spins along the antiferromagnetic axis. However, the

effect on the reduced size (below the helical order parameter) on the phonons and the dielectric behaviour at low temperature (in the vicinity to the spin reorientation transitions) has not been studied so far. To answer these questions we have shown 'Temperature-Dependent Raman and Dielectric Spectroscopy of $BiFeO_3$ Nanoparticles' and triggered the Spin-Phonon and Magnetoelectric Coupling. Temperature-dependent Raman and dielectric spectroscopy shows the existence of two pairs of transitions in a close proximity to the spin reorientation transition, indicating magnetoelectric coupling. This indicates the coupling between the ferroelectric and spin excitations associated with the magnetic cycloid for particle size below the helical order parameter (62 nm). The electrical conductivity of $BiFeO_3$ at room temperature was 3 orders of magnitude lower than the micron sized polycrystalline particles which are attributed to the very high ionic purity as well as grain effects in our samples.

The current revolution in the field of multiferroics began with the discovery of high magnetic tuneability of electric polarization or magnetoelectric effect. To achieve large Magnetoelectric coupling effect, it is essential that the origin of the electrical polarisation should be magnetic. In BFO, electrical and magnetic dipole ordering originates in different sublattices; Bi-O orbital hybridization due to Bi $6s^2$ lone pair is the origin of ferroelectricity whereas Fe-O-Fe antisymmetric Dzyaloshinskii-Moriya (DM) exchange interaction gives rise to interesting magnetic ordering. The magnetoelectric coupling behavior in $BiFeO_3$ system is quite low because the origin of ferroelectricity and magnetic ordering involves different sub-lattice. To solve this problem, we have chosen $DyFeO_3$ as a model system in which giant magnetoelectric coupling behavior has been observed due to interplay of both the magnetic ions. In this regard, we have shown 'Surface Effects on Morin Transition, Exchange Bias and Enchanced Spin Reorientation in Chemically Synthesized $DyFeO_3$ nanoparticles'. This material shows gigantic magnetoelectric (ME) phenomena and spontaneous polarization due to be the exchange striction working between adjacent Fe^{+3} and Dy^{+3} layers with the respective layered antiferromagnetic components. We have observed three significant features in the

magnetisation vs temperature curve such as (1) pronounced spontaneous spin reorientation transitions, (2) the absence of Morin transition, and (3) presence of temperature-dependent exchange bias which clearly indicates the effect of particle size on on magnetic properties. Keeping in view the importance of DFO as giant magnetoelectric material, in this report, we have investigated DFO nanoparticles using ac impedance spectroscopy and ac magnetic susceptibility techniques. As the electrical properties of such materials largely depend on the grain and grain boundaries so in order to understand them, all electrical parameters such as real and imaginary permittivity, relaxation dynamics, activation energy, its spreading factor and their individual contributions has been separately investigated.

The rare earth orthochromites are extremely interesting due to the richness of their optical, dielectric, and magnetic properties as well as due to their multiferroic properties at low temperature which make them suitable materials to study in the nanoregime. $GdCrO_3$, belongs to the same family of compounds as $DyFeO_3$ and crystallize in a distorted perovskite structure.

A detailed synthesis mechanism of $GdCrO_3$ nanoparticles using a surfactant-less hydrothermal method with average particle size around 50–60 nm is investigated. We have shown a detailed study of their structural and optical properties which provide optical signatures of the formation of $GdCrO_3$ where both Gd^{3+} and Cr^{3+} play dominant role in different frequency regions. We have presented a detailed investigation of the magnetic and dielectric properties as well as Raman spectroscopy on $GdCrO_3$ nanoparticles which emphasize the collective as well as individual roles played by the Gd^{3+} and Cr^{3+} ions at various temperatures.

We have reported the formation of similar plate like morphologies in as-synthesized particles like $DyFeO_3$, $BiFeO_3$ and $GdCrO_3$. We believe that, in the formation of plate like nanoparticles in the synthesis adopted by us, the role of nitrate and citrate ions is extremely important. In the case of our hydrothermal synthesis, the strong affinity of both nitrate and citrate ions with metal ions at particular crystalline facets might have promoted the formation of negatively charged anisotropic structures much similar to the role of halide ions in the formation of anisotropic gold nanoparticles.

Overall, new experimental observations are adding to the current understanding as well as creating new excitement and opportunities for researchers in this more than six decade old field.

5.2 Scope for future work:

There is an ever increasing demand for improved computer performance in terms of speed and data storage capacity. The information technology industry has so far been able to keep up with the evolution predicted by the famous Moore's law, which states that the performance of computers will double every other year. Coexistence of e.g. ferroelectricity and ferromagnetism in multiferroic materials enables "four-state memories" based of magnetoresistance and electroresistance, due to the four different combinations of magnetisation and polarisation, which could dramatically enhance the data storage density. Even more interesting is the possibility of a magnetoelectric memory. Improvements of magnetoelectric multiferroic materials are so vast that this field in the recent few years has become one of the hottest of materials science, inspiring numerous reviews in the last few years. Most multiferroic materials investigated are oxides, particularly hexagonal manganites and Bi-containing perovskites in single crystal and polycrystalline materials for technological applications. Moreover, understanding the behaviour of ferroic ordering phenomena at the nano-scale is of outmost importance to the ever ongoing miniaturisation of electronic devices. Most of the known single phase, bulk multiferroic materials don't exhibt strong magnetoelectric (ME) coupling and have a Neel and Curie temperature far below room temperature. These limitations have to be overcome for practical technological application of these materials which include dual purpose sensors and transducers where both electric and magnetic field could be sensed. To solve this problem many more materials should be investigated with the reduction of the particle size.

There has been also considerable recent interest in the synthesis and characterization of one dimensional (1D) nanostructures such as nanotubes, inorganic

nanorods, and nanowires. 1D nanostructure systems offer the opportunity for investigating the influence of size and dimensionality of materials with respect to their collective optical, magnetic and electronic properties because they exhibit physical and chemical properties different from their bulk counterparts. These one dimensional nanostructures are also promising candidates for realizing nanoscale electronic, optical, and mechanical devices because they retain wire-like connectivity despite their nanoscale radial dimension. Most technologically important ferroelectrics are transition metal oxides with a perovskite structure, because that structure has a wide capacity characterized by a tolerance factor. These oxides exhibit large nonlinear optical coefficients and large dielectric constants, which are responsible for their widespread applications in the manufacture of thermostats, multilayer capacitors, and electro-optical devices, electromechanical devices, transducers, capacitors, actuators, high-k dielectrics, dynamic random-access memory, and field-effect transistors. Further, there is a scope of blending the piezo/ferroelectric materials with excellent properties with the ferromagnetic materials as well as piezoelectric polymers so that the composite material will have advantages of both the materials. To investigate this issue, we have synthesized $GdCrO_3$, $LuMnO_3$, $DyFeO_3$, $TbMnO_3$, $BiFeO_3$, $YbMnO_3$, $HoMnO_3$, $GdMnO_3$ etc. in nano size via hydrothermal and sol-gel route and study its magnetic and dielectric properties. We found that, on application of magnetic field they have anomalous magnetic transition (spin reorientation or glass transition) which is absent in ceramics and single crystal. Despite intensive experimental efforts, however, a general method to synthesize well-isolated crystalline nanostructures (nano rods and nanotubes) of perovskite oxides has been lacking, which has hindered detailed experimental investigations on the size-dependent properties of these oxides.

During my PhD work there was unanswered question which need advanced tools to further characterise. In $BiFeO_3$, we have observed some interesting size dependent effects in the dielectric, magnetic properties as well as Raman spectra but some question regarding the origin of these transitions (spin reorientation and glass transition) both in bulk and nano phase needs to be further studies especially the origin of transition situated between 40-50 K. We have proposed that the breaking of the spiral

ordering for the particles size less than 62 nm are responsible for anomalous magnetic transition but still there is no alternative evidence to again confirm this theory. Is there any direct/indirect coupling between the breaking of spiral ordering on the dielectric parameters and FE ordering? What is the fate of FE and AFM ordering transitions and spin-phonon coupling in nanosized BFO. It has been reported that at 1100 K, BFO undergoes a structural transition from rhombohedral to orthorhombic or monoclinic phase, and at around 1200 K, it transforms into the cubic phase. As we indicated earlier, it is not clear to date, out of these two transitions, which one is the ferroelectric-paraelectric transition.

We have performed detailed magnetic investigation in chemically synthesized $DyFeO_3$ nanoparticle but the absence of an anomaly at 35K (Morin transition) in the M-T curve of our nanocrystalline $DyFeO_3$ is still not clear. The Morin transition is a kind of reorientation transition which has been observed in single crystal $DyFeO_3$ around 40K. In the present study we have shown the spontaneous spin reorientation transitions in $DyFeO_3$ nanoparticles which are absent in single crystal. We have shown the possible origin of this transition is the finite size effect and Dy^{+3}- Fe^{+3} interaction but still it is not understood which effect is dominant. This material shows gigantic magnetoelectric (ME) phenomena and spontaneous polarization due to be the exchange striction but the magnetoelectric coupling behavior below 4K in nano scale is still unanswered. In the real part of dielectric susceptibility vs temperature behavior we have observed a peak at around 33 K. At present, the origin of this peak is not clear to us.

The synthesis of these rare earth complex oxides with excellent control over particle morphology while maintaining crystallinity at nanoscale is quite difficult. We have shown the particle size around 50-60 nm synthesized by modified hydrothermal method but still controlling the shape of these rare earth ferrites and chromites is again challenging job for material scientist. We obtained plate type morphology of these ternary metal oxide after the hydrothermal synthesis but the clear evidence of role of nitrates or citrates for such kind of two dimensional structure, need further investigation.

List of publication:

(1) Magnetic and dielectric properties and Raman spectroscopy of $GdCrO_3$ nanoparticles.
Adhish Jaiswal, Raja Das, K. Vivekanand, Tuhin Maity, Priya Mary Abraham, Suguna Adyanthaya, and Pankaj Poddar *Journal of Applied Physics* **2010,** 107, 013912 .

(2) Synthesis and optical studies of $GdCrO_3$ nanoparticles.
Adhish Jaiswal, Raja Das, Suguna Adyanthaya, Pankaj Poddar, *Journal of Nanopartical Research*, **2010**,13,1019 .

(3) Effect of Reduced Particle Size on the Magnetic Properties of Chemically Synthesized $BiFeO_3$ Nanocrystals .
Adhish Jaiswal, Raja Das, K. Vivekanand, Priya Mary Abraham, Suguna Adyanthaya, and Pankaj Poddar *Journal of Physical Chemistry C* **2010**, 114, 2108-2115.

(4) Temperature-Dependent Raman and Dielectric Spectroscopy of $BiFeO_3$ Nanoparticles: Signatures of Spin-Phonon and Magnetoelectric Coupling.
Adhish Jaiswal, Raja Das, Tuhin Maity, K. Vivekanand, Suguna Adyanthaya, and Pankaj Poddar *Journal of Physical Chemistry C* **2010**, 114, 12432-12439.

(5) Surface Effects on Morin Transition, Exchange Bias and Enchanced Spin Reorientation in Chemically Synthesized $DyFeO_3$ nanoparticles.
Adhish Jaiswal, Raja Das, Suguna Adyanthaya, Pankaj Poddar *Journal of Physical Chemistry C* **2011**, 115, 2954–2960.

(6) Origin of Magnetic Anomalies below the Neel Temperature in Nanocrystalline $LuMnO_3$.
Raja Das, **Adhish Jaiswal**, Suguna Adyanthaya, and Pankaj Poddar *Journal of Physical Chemistry C* **2010**, 114, 12104-12109.

 (7) Grain growth related effect on spin and phonon behavior in $TbMnO_3$ nanoparticles
Raja Das, **Adhish Jaiswal**, Suguna Adyanthaya, Pankaj Poddar *Journal of Applied Physics*, **2011**, 109, 064309 .

 (8) Dielectric and spin relaxation behaviour in $DyFeO_3$ nanocrystals.
Adhish Jaiswal, Raja Das, Tuhin Maity, Pankaj Poddar (Communicated)

(9) Interplay of Gd^{3+} and Mn^{3+} spins in $GdMnO_3$ nanoparticles.
Raja Das, **Adhish Jaiswal**, Suguna Adyanthaya, Pankaj Poddar (Communicated)

(10)Synthesis and magnetic properties of $DyMnO_3$ nanocrystal.
Raja Das, **Adhish Jaiswal**, Pankaj Poddar (Communicated)